Preparation and Characterization of LLDPE-Polybenzoxazine-Ferrite Nanoparticle based Flexible Magnetic Nanocomposites

THESIS

Submitted in partial fulfillment

of the requirements for the degree of

DOCTOR OF PHILOSOPHY

by

RAJPUT AMIT BALSING

Under the Supervision of

Dr. Narendra Nath Ghosh

and

Co-supervision of

Dr. Pravin Madanrao Singru

BIRLA INSTITUTE OF TECHNOLOGY AND SCIENCE, PILANI

2013

BIRLA INSTITUTE OF TECHNOLOGY AND SCIENCE, PILANI

CERTIFICATE

This is to certify that the thesis entitled **"Preparation and Characterization of LLDPE-Polybenzoxazine-Ferrite Nanoparticle based Flexible Magnetic Nanocomposites"** and submitted by **Rajput Amit Balsing,** ID No. 2010PHXF438G for award of Ph.D. Degree of the Institute, embodies original work done by him under my supervision.

Signature in full of the Supervisor:

Name in capital block letters: **DR. NARENDRA NATH GHOSH**

Designation: Associate Professor

Signature in full of the Co-supervisor:

Name in capital block letters: **DR. PRAVIN MADANRAO SINGRU**

Designation: Associate Professor

Date:

Dedicated to my loving "Papa"

Late Mr. Balsing B. Rajput

For his endless love, blessing and encouragement

Acknowledgements

ABSTRACT

Recently, magnetic nanocomposites, which are composed of magnetic nanoparticles and polymers, have attracted immense interest because of their light weight and tunable physical properties (e.g., magnetic, electrical, mechanical and thermal properties). These nanocomposites are potential candidates for a plethora of applications, including electronic devices, magnetic data storage, antistatic coatings, rechargeable batteries and corrosion inhibitors. Ferrites are well-known magnetic materials and possess interesting magnetic and electrical properties. In this research work, a simple method for the preparation of magnetic nanocomposites consisting of magnetic nanoparticles (MNPs), polybenzoxazine (PB), linear low density polyethylene (LLDPE) and LLDPE-g-Maleic anhydride (LgM) is described. $CoFe_2O_4$ (CF), $BaFe_{12}O_{19}$ (BHF) (hard ferrite) and $NiFe_2O_4$ (NF), $Ni_{0.8}Zn_{0.2}Fe_2O_4$ (NZF) (soft ferrite) were used as MNPs. Composites were prepared by first forming benzoxazine-MNPs composite followed by melt blending with LLDPE and thermal curing of benzoxazine. Prepared composite materials have been characterized using X-ray diffraction analysis (XRD), Differential scanning calorimetry (DSC), Thermogravimetric analysis (TGA), Fourier transform-infrared (FT-IR) spectroscopy, Transmission Electron microscope (TEM), Particle size analyzer (PSA), Universal testing machine (UTM), Scanning electron microscopy (SEM) and Vibrating sample magnetometry (VSM). XRD analysis of the final composites confirms the presence of pure single phase ferrites (CF, BHF, NF and NZF) in the composite. TGA analysis reveals that the thermal stability of the composites increased by increasing amount of polybenzoxazine in the composition. Tensile testing of the composites revealed that the composites consisting of LLDPE, PB and 5 wt% LgM possessed higher tensile strength than pure LLDPE and a greater elongation at break than pure PB. Incorporation of MNPs in the composites resulted in decrease in the tensile properties of composites, but variation of loading of MNPs (from 14.25 wt% to 33.25 wt%) did not affect much in the tensile properties. From flexural tests it was observed that L-LgM-PB-MNPs composites possessed a higher flexural strength than that of pure LLDPE and toughness of the final composites was higher than that of the pure PB, pure LLDPE and 47.5L-5LgM-47.5PB blend. The incorporation of MNPs in the composites introduced magnetic property of the composites. It was observed that the mechanical properties of the composites did not vary much with the nature of magnetic nanoparticles (CF, BHF, NF and NZF). However, a magnetic property of the composites mainly depends on the nature of MNPs and also with the

wt% of MNPs in the composite. So, the mechanical and magnetic properties of these composites can easily be tailored by the judicious choice of the nature of MNPs and their loading level in the composites.

Advantages offered by these prepared LLDPE-LgM-PB-MNPs composites that make them attractive are:

(i) Composites were prepared by blending LLDPE with polybenzoxazine in presence of a compatibilizer (LLDPE-g-MA) by employing a simple melt blending method.

(ii) Reported method is very simple and cheap LLDPE was used to blend with polybenzoxazine. So, these composites can easily be prepared in large scale.

(iii) Prepared composites possess good mechanical flexibility along with good thermal stability; these composites have the potential to be used in preparation of complex structures.

(iv) As the sheets of these composites showed structural flexibility along with magnetic properties, so these composites have the potential of being used in complex device applications and coatings.

TABLE OF CONTENT

2. Preparation and characterization of flexible polybenzoxazine-LLDPE composites

3. Synthesis, characterization and properties of pure single phase $CoFe_2O_4$ and LLDPE-LgM-Polybenzoxazine-$CoFe_2O_4$ flexible magnetic nanocomposites

4. Synthesis, characterization and properties of pure single phase BaFe$_{12}$O$_{19}$ and LLDPE-LgM-Polybenzoxazine-BaFe$_{12}$O$_{19}$ flexible magnetic nanocomposites

5. Synthesis, characterization and properties of pure single phase NiFe$_2$O$_4$ and LLDPE-LgM-Polybenzoxazine-NiFe$_2$O$_4$ flexible magnetic nanocomposites

List of Figures

List of Tables

List of Schemes

List of Abbreviations

Abbreviation	Description
ATBN	Amine terminated butadiene/acrylonitrile rubber
ASTM	American Society for Testing and Materials
B-a	6,6'-(propane-2,2-diyl)bis(3-phenyl-3,4-dihydro-2H-benzo[e][1,3]oxazine)
BA	Benzoxazine
BHF	Barium hexaferrite
B-m	6,6'-(propane-2,2-diyl)bis(3-methyl-3,4-dihydro-2H-benzo[e][1,3]oxazine)
CTBN	Carboxyl terminated butadiene/acrylronitrile rubber
CNT	Carbon nanotubes
CF	Carbon-fiber
CMNC	Ceramic matrix nanocomposites
CF	Cobalt ferrite
DMA	Dynamic mechanical analysis
DLS	Differential light scattering
DSC	Differential scanning calorimeter
EDTA	Ethylenediaminetetraaceticacid
EMR	Electromagnetic radiation
EMI	Electromagnetic interference
FT-IR	Fourier-transform infrared spectroscopy
GPa	Gigapascal
H_c	Coercivity
IUPAC	International Union of Pure and Applied Chemistry
ICDD	International Centre for Diffraction Data
JCPDS	Joint Committee on Powder Diffraction Standards
LLDPE	Linear Low Density Polyethylene
LgM	Linear Low Density Polyethylene-g-Maleic anhydride
MNPs	Magnetic nanoparticles
MMNC	Metal Matrix Nanocomposite
MMA	Methyl Methacrylate
MMT	Montmorillonite

MPa	Megapascal
M_s	Saturation magnetization
NMR	Nuclear Magnetic Resonance
NF	Nickel ferrite
NZF	Nickel-Zinc ferrite
OMMs	Organically modified montmorillonites
P-a	N-phenyl-3,4-dihydro-2H-1,3-benzoxazine
PMNC	Polymer matrix nanocomposite
PMMA	Poly(methyl methacrylate)
PC	Polycarbonate
PU	Polyurethane
PCL	Poly(ε-caprolactone)
PB	Polybenzoxazine
RAMs	Radio-absorbing materials
SEM	Scanning Electron Microscopy
SPM	Superparamagnetism
THF	Tetrahydrofuran
TIPO	Titanium isopropoxide
TGA	Thermo-gravimetric analysis
TEM	Transmission Electron Microscope
$T_{5\%}$	Temperature at 5% weight loss
$T_{10\%}$	Temperature at 10% weight loss
T_g	Glass transition temperature
UTM	Universal Testing Machine
VSM	Vibrating Sample Magnetometer
XRD	X-Ray Diffraction

CHAPTER 1

Introduction

1.1 Scope of Research Work

The focus of this research work is the preparation and characterization of polybenzoxazine based flexible magnetic nanocomposite. In particular, this work is divide in three steps: first the synthesis of nanostructured hard and soft ferrites by employing a simple and cost-effective EDTA based chemical method, second step is preparation of polybenzoxazine-magnetic nanocomposite and third step is preparation of flexible nanocomposite sheet, composed of polybenzoxazine, LLDPE and magnetic nanoparticles.

1.2 Introduction to Nanocomposite

Nanocomposite science and technology is a rapidly growing field of research, initiated in Toyota Research Laboratories in Japan in the 1980s [1, 2]. Nanocomposites are multiphase materials in which one of the phases has characteristic dimensions at the nanometer scale [3, 4]. In general they are expected to display improved properties emerging from the combination of each component. According to the International Union of Pure and Applied Chemistry (IUPAC), a composite material is defined as "a multicomponent material comprising multiple different (non-gaseous) phase domains in which at least one type of phase domain is in a continuous phase". IUPAC also extends its definition to nanocomposite materials as those composites "in which at least one of the phases has at least one dimension of the order of nanometers" [5]. Overall, nanocomposites can be engineered to have a variety of unique properties, by controlling the chemical composition, physical properties and morphology of the chosen components. It is possible to tune physical properties of nanocomposites across a wide spectrum, from mechanical [6], optical [7], thermal [8], to electrical [9], chemical [10] and magnetic properties [11]. This broad spectrum of unique physical and chemical properties lends nanocomposites to various applications from radiation sensors [12] to biomedicines [13]. According to their matrix materials, nanocomposites can be classified as ceramic matrix nanocomposites (CMNC), metal matrix nanocomposites (MMNC), and polymer matrix nanocomposites (PMNC). Further polymer matrix nanocomposite can be broadly classified into three categories based on the dimensions of the nanosized components dispersed in the polymeric matrix: such as nanosheets dispersed in

polymeric matrix, nanotubes/nanorods/nanowires in polymeric matrix and nanoparticles in polymeric matrix (Scheme 1.1).

Nanocomposites

Metal matrix nanocomposites (MMNC) Examples: Fe-Cr/Al_2O_3, Ni/Al_2O_3, Co/Cr, Fe/MgO, Al/CNT, Mg/CNT	Polymer matrix nanocomposites (PMNC) Examples: Thermoplastic/thermoset polymer/layered silicates, polyester/TiO_2, polymer/CNT, polymer/layered double hydroxides.	Ceramic matrix nanocomposites (CMNC) Examples: Al_2O_3/SiO_2, SiO_2/Ni, Al_2O_3/TiO_2, Al_2O_3/SiC, Al_2O_3/CNT

Nanosheets Based Nanocomposites Example: Epoxy resin/graphite nanosheet nanocomposite.	Nanorods/Nanowires/ Nanotubes Based Nanocomposites Example: Polyaniline-CNT, MMA-CNT, Epoxy-CNT	Nanoparticles Based Nanocomposites Example: Epoxy vinyl ester/γ-Fe_2O_3, Polyimide/SiO_2, polycarbonate / SiO_2 and poly (amide-imide)/TiO_2

Scheme 1.1 Classifications of Nanocomposites.

1.2.1 Methods of Polymer Nanocomposite Preparation

One of the major challenges in preparing nanoparticles/polymer composite is achieving homogeneous dispersion of the nanoparticles in a polymer matrix. This criteria is very important because good dispersion of the individual nanoparticles in the polymer matrix is the basis for obtaining desired properties [14]. Many methods have been reported for the preparation of polymer nanocomposites. Some of them are

(a) In-situ polymerization

The first nanoclay/polymer (Nylon-6/MMT) composite reported by the scientists of Toyota Research Group was prepared by in-situ polymerization [15-17]. It is a developing technique for CNTs composite preparation. The method starts by dispersing nanotubes in monomer followed by polymerizing the monomers [18-21]. The in-situ polymerization process is useful for polyamide and epoxy-based composites [22-24], and it enables covalent bonding between the polymer macromolecules and the nanoparticle surfaces [25-27]. However, the application of this method is not general to other kinds of polymers. This technique also requires

extended processing time as well as a solvent while polymerizing certain types of polymer. These concerns limit the application for in-situ polymerization to industrial practice.

(b) Sol-gel process

The sol-gel process is a versatile method for the preparation of homogeneous inorganic oxides for conventional inorganic glasses at ambient temperatures. Hence, growing inorganic ceramic networks within a polymer matrix through the sol-gel process becomes a convenient technique, and allows the production of organic/inorganic hybrids even at the molecular level [28]. Accordingly, various organic/inorganic hybrids have been reported prepared using the sol-gel process [29, 30].

(c) Solution polymerization

In the solution radical polymerization technique, the grafting of polymers into clay interlayer depends on the swelling of the organophilic-modified clay promoted by a solvent. Swelling is manifested due to solvation of interlayer cations thus; inclusion of the vinyl monomer between the layers of the clays can be maximized by the use of appropriate solvent. The interlayer distance can be increased remarkably in the solvent, which have strong attractive forces between the intercalated monomer of clay and solvent molecules. Nanocomposites based on high density polyethylene, polyimide and nematic liquid crystal polymers have been synthesized by this method. The major advantage of this method is that it offers the possibility to synthesize intercalated nanocomposites based on polymers with low or even no polarity [31, 32].

(d) Melt blending

Melt blending for attempting to disperse nanoparticles into polymer matrices is now the best scalable method for industrial applications and it is also economical and environmentally friendly. The melt blending process generally involves the melting of polymer pellets to form a viscous liquid. The nanoparticles are dispersed into the polymer matrix by high shear rate combined with diffusion at high temperature [33-35]. The problem with this method is that good dispersion is usually hard to obtain, especially in non-polar polymers. Although using polypropylene oligomers (polypropylene-*g*-malic anhydride) as a compatibalizer, the exfoliation of nanoclay within the polypropylene matrix was improved, the elongation at break greatly decreased and the composite changed from flexible material to brittle material [36]. In addition, the properties of the composites failed to increase at a high nanoparticle

loading (>10 wt%) due to the aggregation of nanoparticles [37]. Hence, although melt compounding has shown some promise for producing composites with improved properties, it does not provide a general means applicable to all polymers. Furthermore, we can expect an improvement of properties of about 100% at 5 to 6 wt% but little improvement with further loading levels [38]. The improvement in composite properties such as modulus is significantly below what is expected theoretically [39].

(e) Emulsion polymerization

The emulsion polymerization is recently introduced technique for nanocomposite synthesis [40-43]. The disadvantage of intercalation process is the lack of affinity between hydrophilic silicate interlayer and hydrophobic polymer and they can be applied only to pretreated silicate layer swellable with organic ions by ion exchange between organic onium ions salt and interlayer cation of clay [44-46]. Emulsion polymerization is a heterogeneous reaction system. In this process, reacting monomer is dispersed in a water phase and polymerized with a water soluble radical initiator in presence of Na^+ montmorillonite.

In this present work, we are concentrating on preparation of polymer based magnetic nanocomposites. The composites composed of linear low density polyethylene, polybenzoxazine and ferrite nanoparticles. For preparation of polymer based magnetic nanocomposites, a melt blending method was employed.

1.3 Introduction to Polymer-ferrite based Nanocomposite

Ferrites are by far the best example of magnetic materials that have been extensively studied over the years owing to their high thermal stability and interesting physical properties (e.g., thermal, electrical, and magnetic). Ferrite materials are used in a wide range of applications starting from household materials to high-tech space applications [47]. But their brittleness sometimes limits their applications. In comparison, polymeric materials exhibit elastic properties but generally possess less thermal stability. In this context, polymer-ferrite nanocomposites, with their tailored compositions, are appropriate for various applications where the useful properties of both the components remain preserved to a large extent. Thus, the hybridization of ferrite with organic polymer has attracted interest of the researchers. These hybrid materials can combine the best attributes of the two components. In case of traditional composites, the adhesion between inorganic and the polymer is often poor because

they are combined in a macroscopic scale. Therefore, they do not offer the desired reinforcement effect to the hybrid materials [48-51].

Recently, there has been an intense interest to design polymer composites containing magnetic nanoparticles. It is now a well-established fact that nanoparticles exhibit unusual properties, including magnetic, electrical, optical, and mechanical, in comparison with bulk materials. In polymer-magnetic nanocomposites, it is possible to manipulate their physical properties by controlling the particle size of the nanoparticles and their weight ratio in the composition. These nanocomposites have been found to demonstrate unique physical and chemical properties even more than their constituents and are far different from conventional macro- or micro-composites.

1.3.1 Literature Survey

In recent years the incorporation of magnetic nanoparticles in polymer matrices have attracted much attention by material scientists and engineers. There have been certain reports based on the study of nanoparticles of Co, Fe, Fe_2O_3 and Mn-Zn ferrite, Ni-Zn ferrite, $BaFe_{12}O_{19}$, $CoFe_2O_4$ dispersed in polymeric matrix. The polymer-ceramic nanocomposites for magnetic applications, metals and metal alloys (e.g. Fe) [52] or (CoPt) [53], oxides (e.g. ferric oxide) [54] and ferrite [55] are used as inorganic nanofillers. Chen et al., [56] have reported core/shell structure of porous Fe_3O_4/Fe/SiO_2 nanorods with a length of 80 nm and 1 mm for electromagnetic wave absorption applications. Kim et al., reported the EM wave absorption of $Ni_{0.5}Zn_{0.4}Cu_{0.1}Fe_2O_4$ ferrite nanoparticles embedded in the PMMA matrix [57]. Yang et al., have reported nanotube-PS foam composite as an effective EMI shielding material [58]. The efficiency of magnetic polymer composites with multicomponent fillers has been studied by Lopatin et al., [59] from the viewpoint of application of such composites as radio-absorbing materials (RAMs). Srikanth et al., have synthesized polystyrene coated Fe nanoparticles by microwave plasma polymerization and studied the impact of polymer coating on their magnetic response [60]. Magnetic nanocomposites containing γ-Fe_2O_3 embedded in a polymer matrix of sulphonated polystyrene and divinyl benzene prepared by an ion exchange method have been studied by Malini et al., [61]. Kiskan et al., [62] reported carboxylic acid functional benzoxazine that is easily coated on neat magnetite and forms polybenzoxazine-nanomagnetite nanocomposites via thermally activated ring opening polymerization. The nanoparticles showed typical ferromagnetic characteristics and the magnetic properties were preserved after curing. Rubber ferrite composites containing different mixed ferrites with various loading levels have been studied by Anantharaman et al., [63]. Jiang et al., introduced a novel poly

(aniline-co-o-toluidine)/$BaFe_{12}O_{19}$ composite, which was successfully synthesized by a facile, general and inexpensive in-situ polymerization method [64]. Ting et al., had reported the microwave absorption of the polyaniline/$BaFe_{12}O_{19}$ and noticed that microwave absorbing properties can be modulated simply by controlling the content of polyaniline on the samples for the required frequency bands [65]. Deng et al., have studied the synthesis of magnetic and conducting Fe_3O_4-crosslinked polyaniline nanoparticles with core-shell structure by using a precipitation-oxidation technique [66]. Xu et al., have reported an in-situ polymerization process to obtain polyaniline/$BaFe_{12}O_{19}$ nanocomposites and their microwave absorption properties were investigated [67].

1.3.2 Applications of Polymer-ferrite based Nanocomposites

Ferrite nanoparticles incorporated polymeric composites find number of applications. Such as in microwave absorption, electromagnetic interference (EMI) shielding, radio-absorbing materials (RAMs), molecular electronic, antistatic coatings, rechargeable batteries, corrosion inhibitors, etc. Hence, Polymer-ferrite nanocomposites are emerging as new materials for variety of hi-tech applications. Table 1.1 presents some of the applications of polymer-ferrite nanocomposites.

Table 1.1 Applications of polymer-ferrite based nanocomposites.

Polymer matrix	Magnetic nanoparticles	Applications	Ref
Polymethyl methacrylate	$(Ni_xR_{1-x})_{0.5}Zn_{0.5}Fe_2O_4$ R= Mn,Co,Cu; x = 0, 0.5	Electromagnetic interference (EMI) shielding	[68]
Epoxy	Ni-Zn ferrite	Electronic applications	[69]
Natural Rubber matrix	$NiFe_2O_4$	Microwave absorption	[70]
Epoxy	$Ni_{1-x}Zn_xFe_2O_4$ x = 0.2, 0.4, 0.5	Suppression of EMI in microwave circuits	[71]
Polyaniline	$Co_{0.5}Zn_{0.5}Fe_2O_4$	Microwave absorption	[72]
Polyvinyl Chloride	$Ni_{0.33}Zn_{0.67}Fe_2O_4$	RF electromagnetic wave absorbing material	[73]
Polyaniline	$MnFe_2O_4$	Microwave absorption	[74]
Paraffin	$Co_xMn_{1-x}Fe_2O_4$	EMI shielding	[75]
Polyaniline	γ-Fe_2O_3	Microwave absorption	[76]
Polyethylene	Hexaferrite ($BaFe_{12}O_{19}$ or $SrFe_{12}O_{19}$)	Electromagnetic wave absorbers in the U-band	[77]

1.4 Introduction to Ferrite and their Synthesis Methods

Ferrites are ceramic materials, black or dark grey in appearance and very brittle and hard. Ferrites are a group of technologically important ferrimagnetic materials [78, 79]. Ferrite nanoparticles are currently being investigated for a wide range of applications in the field of inductor and transformer cores, antenna cores, magnetic amplifiers, deflection yokes in television sets, hearing aids, computer peripherals, memory and switching applications in digital computers and data processing circuits, modulators, circulators, isolators, phase shifters, other high frequency devices, high-density magnetic and magneto-optic recording media, magnetic fluids, fabrication of permanent magnets, etc [47, 80, 81]. Now-a-days some ferrites are explored for use as microwave or radar adsorbing materials (mostly in the form of coating or films), which are important in military technology [82, 83]. Other applications of ferrites involve the use in temperature sensors, magnetostrictive decay lines, magnetic resonators, and ferrite filters [84], ferrite radiators [85] ferrite power limiters and so on. They are usually employed in the ceramic form. These ceramic magnets have the inherent drawback that they are not easily machinable to obtain complex shapes. Magnetically, ferrites are classified into two groups, namely, soft and hard [86]. Further, depending on its symmetry, the magnetic ferrites fall mainly into two groups, cubic and hexagonal [87].

1.4.1 Types of Ferrite Materials

Based on the magnetic property ferrites are classified as hard ferrite (e.g. $CoFe_2O_4$, $BaFe_{12}O_{19}$, $SrFe_{12}O_{19}$ etc) and soft ferrite ($NiFe_2O_4$, $NiZnFe_2O_4$ etc) [88, 89].

(a) Soft Ferrite

Ferrite material in which the ferromagnetism emerges only when a magnetic field is applied (means temporary) is called the soft ferrite [78]. The general formula is $MOFe_2O_3$, where M is a divalent metal ion like Mn, Ni, Fe, Mg etc [87, 90]. These ferrites have good magnetic properties with extremely high electrical resistivity, so, they can operate with almost no eddy current loss at high frequencies. This fact accounts for all the applications of soft ferrites [87]. There are many other significant applications [91] of soft ferrites such as antenna rods, recording heads, humidity sensors, proximity sensors, interference suppression cores, etc [87].

7

(b) Hard ferrite

Ferrite materials exhibit ferromagnetism even in the absence of an external magnetic field is called hard ferrites [78]. Hard ferrites have hexagonal crystal structure. The general formula is $MO6Fe_2O_3$, where M is a divalent metal ion like Ba, Sr and Pb [87, 92]. In the group of hard ferrites, magnetoplumbites or M-type hexagonal ferrites ($MO6Fe_2O_3$) are extensively used in many technological applications due to their superior magnetic properties [87]. Hard ferrite materials are used as permanent magnets for various kinds of electric meters, loudspeakers and in other apparatus for which high remanence, large hysteresis loss, and high coercivity are desirable [87, 93].

1.4.2 Different Methods for Preparation of Ferrites

The preparation method plays a key role in determining the particle size and shape, size distribution, surface chemistry and therefore the properties and applications of the material. Many synthesis routes have been developed to achieve proper control of particle size, polydispersity, crystallinity, shape and the magnetic properties of these materials [78]. Some of the common methods adopted for the preparation of ferrites are discussed below:

(a) Ceramic Method [94-96]

The oldest and the most common method, for preparing multiphase component solid materials is by the direct reaction of solid components at high temperatures. Since solids do not react with each other at room temperatures even if it is thermodynamically favorable, high temperatures are necessary to achieve appreciable reaction rates. The heat treatment causes diffusion of constituent starting materials and the growth of crystallites occurs due to solid sate reaction. To obtain the good homogeneity, sometimes, the calcined powders are again crushed and milled. The advantage of solid state reaction is the ready availability of precursors and the low cost for production on the industrial scale. Generally, the oxides of the different metal components are fine grind, to maximize surface areas to improve reaction rates. The powder is pressed into a pellet to ensure intimate contact between the grains. The pellets are heat treated at high temperatures for long durations.

(b) Co-precipitation Method [97-107]

This is a wet chemical method, where ferrites with desired chemical compositions are simultaneously precipitated from aqueous solutions of metal ions. The reaction of metal ions solutions with precipitating agents like alkaline solutions of carbonates, hydroxides, ammonia

or amines results in co-precipitation. The precipitate contains ferrous and of the metal carbonates or hydroxides, which decompose to oxides when calcined at 500-800 ^{0}C. The method gives precise control over the chemical compositions of the product. The materials produced by this method are not exceptionally homogenous and in some cases the reproducibility is also poor. The method also suffers from drawbacks like retention of impurities and difficulty in separation in case of gelatinous precipitate. The properties of synthesized ferrites depend on concentration of metal ions, base solutions, composition of base solution, digestion time, type and degree of mixing of the metal ions and base solutions for co-precipitations.

(c) Sol-Gel Method [108-114]

In this method, acid or base catalyzed hydrolysis of organometallic compounds like, alcoholate, carboxylate or chelates of different metals, is followed by condensation and poly-condensation reaction in an organic solvent producing a gel. The gel is then calcined at around 300-800 ^{0}C in the presence of oxygen to yield desired ferrites. Sol-gel technique is generally employed to prepare finely divided powders that are useful particularly in the manufacture of coating compositions, intricately shaped and fine-grained ceramics, and cermets. Use of expensive metal alkoxides or complex metal compounds is the main limitation of this method.

(d) Hydrothermal Method [115-124]

The method finds application where the resulting ferrite particles are required to be uniformly disperse, as in the case of high density recording materials. A mixture of aqueous solutions of metal ions and/or aqueous slurry of metal hydroxides is mixed with alkaline solution and the mixture is autoclaved between 100 and 400 ^{0}C. This method requires comparatively low temperature treatment, which results in a uniform mixture of the metals to form ferrites with the required chemical composition. This process is found to be superior to the conventional high temperature process because it avoids the sintering or agglomeration of ferrite grains. Although hydrothermal technique is very versatile, one of the main drawbacks of the conventional hydrothermal method is the slow reaction kinetics at any given temperature.

(e) Precursor Based Method [125-134]

This method involves the preparation of a "precursor" compound which is a complex combination of cations and a polymeric/chelating agent. The pyrolysis of the precursor at

various temperatures gives rise to nanoscale particles of the desired single or mixed oxide system. Various organo-metallic complexes, metal hydroxides/oxalates/citrates/hydrazine carboxylates etc. are some of the commonly used precursor compounds. The precursor method permits good control of the product stoichiometry, especially for multicomponent systems. However, it is not always easy to choose a suitable precursor to synthesize a particular compound.

(f) Combustion Method [135-141]

The method utilizes a precursor that ignites at a low temperature and leads to a gas producing exothermic reaction that is self-propagating and yields voluminous fine oxides in a few minutes. Various organo-metallic complexes, metal hydroxides/oxalates/citrates/hydrazine carboxylates etc. are some of the commonly used precursor compounds. This method is also known as the "self-sustaining/propagating synthesis process." The process is rapid and may approach direct conversion from the molecular mixture of the precursor solution to the final oxide product. The disadvantage is that sometimes the exothermic reaction might be difficult to control especially when being performed on a large-scale.

(g) Reverse Micelle Method [142]

A reverse micellar system consists of nanometer sized water droplets that are dispersed in an oil medium and stabilized by a surfactant. In this method, tiny droplets of water are encapsulated as a reverse micelle. The structure of a reverse micelle is characterized by a polar core formed by hydrophilic heads of the surfactant and a non-polar shell formed by hydrophobic tails of the surfactant. The droplet size of reverse micelles can be readily modulated in the nanometer range particularly by controlling the water: surfactant ratios. The reverse micelle method leads to the controlled synthesis of ceramic materials and metals having a tailored shape, size and composition. The method can be used to synthesize the monodispersed nanoparticles with various morphologies. However, this method requires a large amount of organic solvent and also the yield is low.

1.5 Introduction to Polybenzoxazine

Polybenzoxazine is a recently developed new type of addition polymerized phenolic resins [143]. Though common phenolic or epoxy resins have myriad applications in diverse fields, a number of shortcomings are also associated with these materials. Some of the limitations include brittleness, poor shelf life, use of acid or base catalysts, release of byproducts,

formation of micro voids during curing, and so forth. To overcome these limitations, a new type of addition-cure phenolic system, polybenzoxazine, has recently been developed. The advantages offered by polybenzoxazine-based materials are (i) near-zero volumetric change upon curing, (ii) low water absorption, (iii) much higher T_g than cure temperature, for some polybenzoxazines, (iv) better thermal stability, (v) high char yield, (vi) no release of toxic by-products during curing, and (vii) no requirement of strong acid catalysts for curing. The molecular structure of polybenzoxazines offers enormous design flexibility, which allows the properties of the cured materials to be tailored for a wide range of applications [144, 145].

1.5.1 Unique Properties of Polybenzoxazines

(i) Near-Zero Volume Change

Benzoxazine resin display near-zero shrinkage with high mechanical integrity. The majority of the monomers changed their volume with ±1% upon polymerization. Polybenzoxazine have various hydrogen bonds that may restrict the freedom of the chain and further stiffen the chains leading to poor molecular packing. This may results in high free volume which can be one of the factors responsible for very low shrinkage or even expansion during curing [146].

(ii) Low Water Absorption

One of the common problems of polyesters, vinylester, phenolics and epoxy resins is their relatively high water absorption. Both phenolics and epoxy resin absorb as much as 3-20% by weight upon. This relatively high water absorption is due to the presence of polar groups in these resins. Polybenzoxazine also contains polar groups, such as phenolics OH and mannich base in each chemical repeating unit. This may result of hydrogen bonding between phenol and nitrogen; the conformationally preferred acid base interaction competes with water and reduces the water uptake [147].

(iii) High Glass Transition Temperature (T_g)

Crosslinked polybenzoxazines shows surprisingly high glass transition temperatures ranging from approximately from 150 to 350 ^{0}C. Polybenzoxazines have low crosslinking densities but high T_g's. But in general, higher the degree of crosslinking, the higher is the T_g. It has been proposed by Wirasate et al., that hydrogen bonding may contribute to the stiffness of the chain and so may influence the T_g [148].

(iv) High Thermal Stability

Thermal stability of polymers depends on the bond energy. As temperature increases, vibrational energy increases which leads to bond breakage. Studies on the thermal

decomposition of polybenzoxazines have revealed that polybenzoxazines decomposed by volatilizing aniline fragments during thermal degradation [149]. Thermal stability of polybenzoxazine thus depends on the stability of aniline fragments.

(v) High Char yield

Char formation decreases the flammability by forming a barrier for oxygen supply. Many polymers show low char yield when the reaming weight is examined under nitrogen at 800 ^{0}C. This char yield is 5-15% for epoxy resins, and 30-55% for phenolic resins. Phenolic resins show one of the highest char yields among processable polymers. Char formation usually increases with increased content of benzene groups, although there is no direct relationship between the benzene content and char yield. This is well expressed by the fact that despite a high content of aliphatic groups in polybenzoxazines, their char yield, generally high (35-70%), is higher than traditional phenolic resins [150].

1.6 Benzoxazine Monomer and their Processibility

Benzoxazine is a single benzene ring fused to another six-membered heterocycle containing one oxygen atom and a nitrogen atom. There are a number of possible isomeric benzoxazines exists depending on the relative positions of the two heteroatoms of this oxazine ring system, and 1,3-benzoxazine is the kind of isomer used for polymerization [143-145].

1.6.1 Synthesis of Benzoxazine Monomers

Though benzoxazine was first synthesized by Cope and Holly in 1940s [151] by using condensation reaction of primary amines with formaldehyde and phenol, the potency of polybenzoxazines has been recognized much later. In 1949, Burke found that the benzoxazine ring reacts preferentially with the free ortho positions of a phenolics compound and forms a Mannich bridge [152]. Riess et al., [153] confirmed this regioselectivity in model compounds by following the kinetics of polymerization for thermally activated and substituted-phenol initiated monofunctional benzoxazines. Typically, benzoxazine monomers are synthesized by using phenol, formaldehyde, and amine (aliphatic or aromatic) as starting materials [154] (Scheme 1.2). Ishida and coworkers [155] have popularized the synthesis of benzoxazine monomers by inventing a solventless method. Using various types of phenols and amines, having different substitution groups attached, several types of benzoxazine monomer can be synthesized. These substituted groups can provide additional polymerizable sites and also affect the curing process. The potential exists to obtain polymeric materials, with desired

properties, by tailoring the benzoxazine monomer with different functionality and a wide variety of monomers can be synthesized by using judiciously chosen phenol and amine. Here also, selection of starting materials play critical role. For example, presence of electron withdrawing functional group (-COOH, -CN) with amine was found to be responsible for reduction in yields. Also, it is hard to synthesize benzoxazine monomers containing free phenolic -OH groups employing conventional method.

Bisphenol A

Benzoxazine monomer (BA)
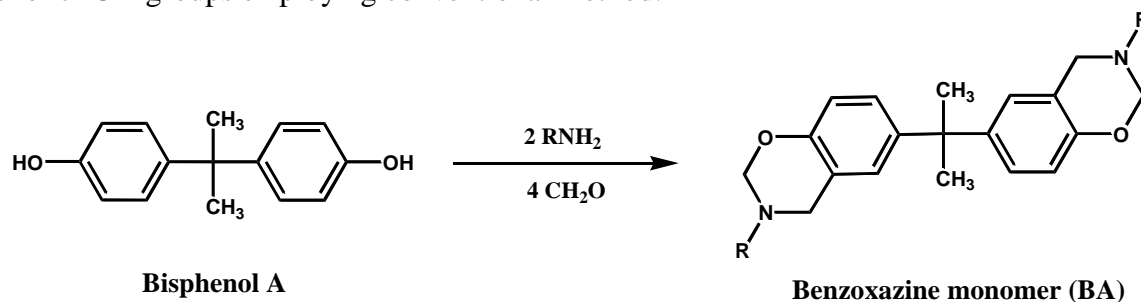
Scheme 1.2 Synthesis of benzoxazine monomer (BA).

1.6.2 Processibility and Film Formation

Polybenzoxazines prepared from the monomers precursor are associated with some limitations on their use in practical applications. The monomers are usually powder and processing into thin films is rather difficult. Additionally, the formed polymers are brittle as a consequence of the short molecular weight of the network structure. Addition of elastomeric materials to brittle resins is a well-known approach to improve the ductility. Although, improvement in ductility of benzoxazine may be achieved using this approach, it sacrifices the intrinsic advantages of thermosetting resins. The possibility of adjusting polybenzoxazine properties due to a rich design flexibility of molecular architectures opens wide opportunities to further enhance the properties over the monomeric benzoxazine resins. Therefore, a different molecular design to achieve the ductility without resorting to the thermally weak elastomeric materials has been adopted [145]. To improve the processibility and mechanical properties, several researchers have attempted various strategies, such as:

    (a) Preparation of modified monomers with additional functionality.

    (b) Synthesis of novel polymeric precursors.

    (c) Blending with a high-performance polymer or filler and fiber.

(a) Preparation of modified monomers with additional functionality [145]

In this approach, the introduction of ethynyl or phenyl ethynyl [156, 157], nitrile [158], propargyl [159] etc. groups can offer additional cross-linking sites during polymerization,

and were found to be acceptable choices for that purpose [143]. Some of the modified benzoxazine monomers with additional functionalities are listed below in Table 1.2.

Table 1.2 Benzoxazine Monomers with Additional Functionalities [145].

Functional Monomers		References
Allyl functionalized monomers (P-ala)		[160]
Acetylene functionalized monomers (Ph-apa)		[161]
Nitrile functionalized monomers		[162]
Phenyl propargyl functionalized monomers		[163]
Coumarine-containing benzoxazine		[164]
Malemide functionalized monomers		[165]

(b) Synthesis of novel polymeric precursors

Novel polymeric-based precursors have been synthesized by incorporating benzoxazine units either as side chain or as end chain or in main chain of polymer. It is expected that the crosslinked network structure, formed from polymer and polymerization of benzoxazine will exhibit enhanced mechanical property while retaining the beneficial properties of polybenzoxazine. Polymeric precursors offer the ability to prepare a varnish with low solid content that forms good quality films [145].

(i) Side-Chain Precursors [145]

Side chain polymer strategy is a way to incorporate benzoxazine groups into a polymer backbone to achieve a highly dense network. Curing of many repeating benzoxazine units resulted in crosslinking of polymer chains. There are various synthetic methods to obtain side chain polymers [166, 167]. Some include postpolymer modification like click chemistry or polymerizing suitable molecules (Scheme 1.3) [145]. Recently, Kiskan et al. have synthesized postpolymer-grafted benzoxazine with several polymers, for example, PVC, polystyrene, polybutadiene, by using ''click chemistry'' [168, 169].
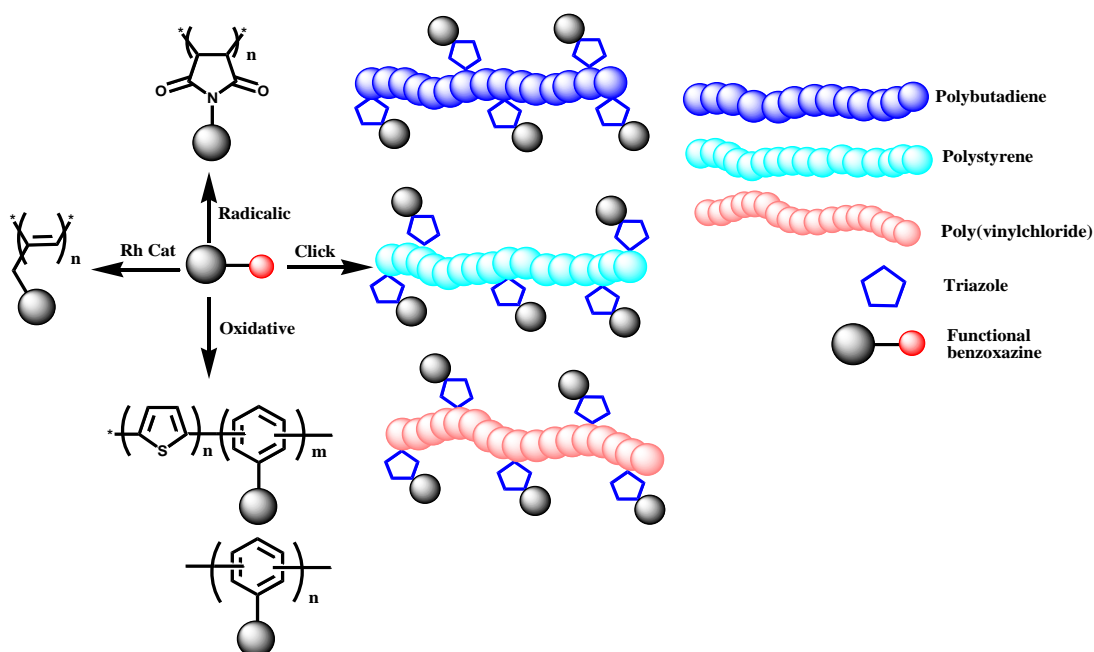
Scheme 1.3 Side chain polymer strategy to incorporate benzoxazine groups into a polymer [145].

(ii) Crosslinkable Telechelics with Benzoxazine Moiety at the Chain End [145]

In this approach, benzoxazine ring has been anchored to the end of a polymer [170, 171]. Here a polymeric structure act as backbone structure, which are end capped with benzoxazine. Telechelics with relatively large molecular weight oligomers possess thermoplastic-like properties, while allowing later crosslinking for dimensional stability, chemical resistance, and high-temperature stability. A unique synthetic route was reported by Kiskan et al., [170] for synthesis of a macromonomer where benzoxazine ring was anchored to the polysterene polymer.

A very interesting network structure can be achieved from polymeric precursors with benzoxazine end chain. When these monomers undergo thermal curing, benzoxazine groups

can form domains by polymerizing together and polymer macromolecules can hang as dangling chain. In another case, when benzoxazines attached as end group of both ends of a long chain polymer, small domains of polybenzoxazine form, by ring opening polymerization of benzoxazine, and these domains are covalently attached to the polymer chains. As a result, a crosslinked structure forms which contains small domains of polybenzoxazine.

(iii) Main-Chain Precursors [145]

Liu and Ishida reported the concept of oligomeric benzoxazine resins where oxazine rings are in the main chain [172]. Takeichi et al [173] and Ishida and coworkers [174] have independently reported a synthetic approach for the preparation of polymers containing benzoxazine moieties in the main chain. High-molecular weight polybenzoxazine precursor was synthesized from aromatic or aliphatic diamine and bisphenol-A with paraformaldehyde [173]. The major problems associated with the preparation of such main-chain benzoxazine precursor polymers are low molecular weight and crosslinking arising from the Mannich reactions of multiple functional groups [145]. Different types of benzoxazine based main-chain polymeric precursors have been described in Scheme 1.4.
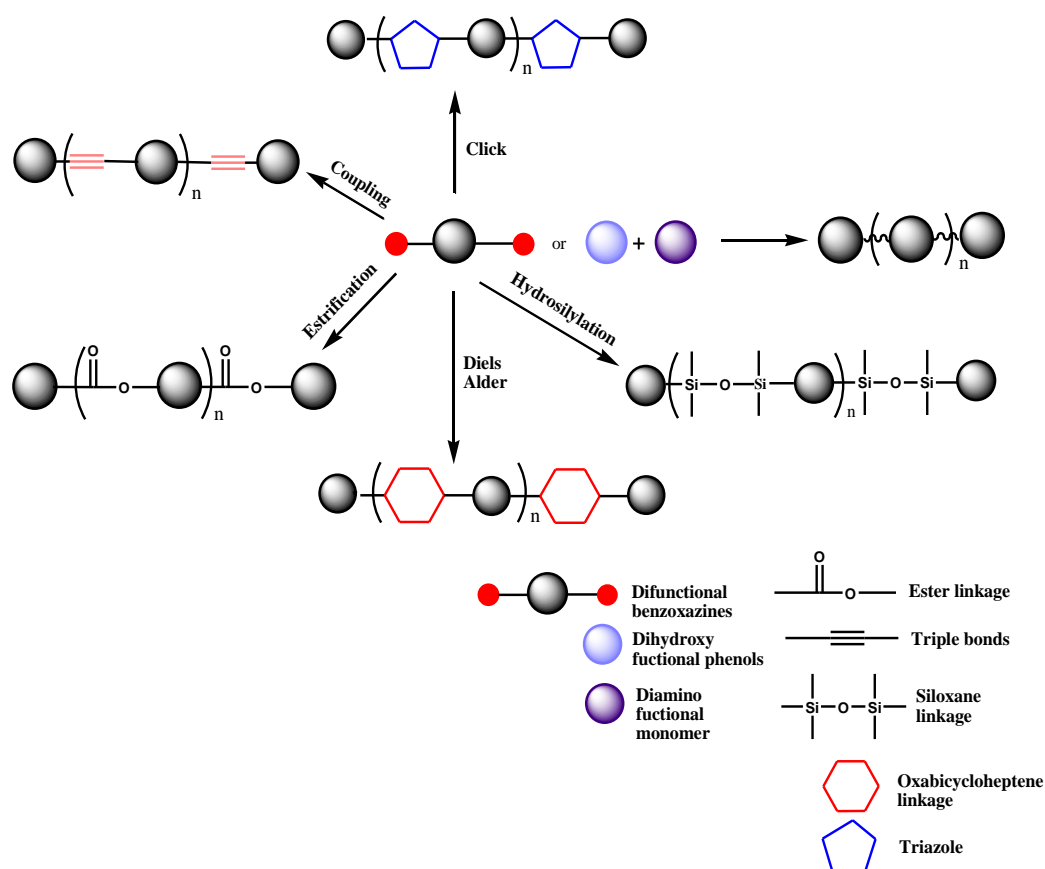
Scheme 1.4 Different types of benzoxazine based main-chain polymeric precursors [145].

All the above described approaches are also associated with some limitations. For example, (i) modified monomers with additional functionality are difficult to synthesize and preparation of flexible film has not yet accomplished, (ii) in case of novel polymeric precursors, though the polymeric chain contributes toward the improvement of mechanical property and processibility of the resulting polymer but it sacrifices the thermal property of polybenzoxazines as well as these composites difficult to prepare in large scale [145].

(c) Blending with a high-performance polymer or filler and fiber

Apart from the strategy discussed above a variety of blends, alloys and composites have been prepared by mixing benzoxazine with different resins (e.g., polyurethane, epoxy, polycarbonate, rubber, etc.) to manipulate the properties in terms of mechanical, thermal, flame retardant, and so forth [143, 144]. Some examples of benzoxazine-based composites are listed below in Table 1.3.

Table 1.3 Benzoxazine-based composites [143, 144].

System	Process	Remark	Ref
Polyurethane/ benzoxazine composite	Solution blending	PU/benzoxazine films were prepared by blending solutions of PU prepolymer and BA-a in tetrahydrofuran (THF) solvent with various weight ratios of PU and BA-a. The films were then thermally cured using a cure cycle. The cured PU/BA-a films were transparent, suggesting good compatibility between the PU and BA-a components. All the PU/BA-a films had only one T_g. The thermal stability of PUs was greatly enhanced even with the incorporation of a small amount of BA-a. It was observed that increasing the BA-a content led to a higher decomposition temperature.	[175]
Epoxy/polybenzoxazine composites	Solution blending	Chain-extended epoxy (40 mol%) and benzoxazine (60 mol%) were thoroughly mixed at 85 ^{0}C. Acetone was used as diluent to facilitate mixing. Then, the material was subjected to a curing cycle. Ring-opening reactions of benzoxazine produce phenolic hydroxyl groups, which can react with epoxy resins and provide additional crosslinking points in the resulting network structure. This increase in the crosslink density of a thermosetting matrix will strongly influence the mechanical and thermal properties.	[176]

Polycarbonate-blend-polybenzoxazine	Solution blending	Solution blending of PC and BA-a was performed using chloroform as solvent to obtain a transparent yellow solution. After complete removal of solvent, the samples were isothermally polymerized in an air-circulated oven at 180 ^{0}C for various periods of time. Due to its relatively high toughness and ability to form intermolecular hydrogen bonds with polybenzoxazine main chains, polycarbonate was chosen as a blending material to improve the toughness of polybenzoxazine.	[177]
Poly(ε-caprolactone)-blend-polybenzoxazine	Melt-blending	Various concentrations of poly(ε-caprolactone) were added to BA-a at 120 ^{0}C. After thorough mixing, a clear homogeneous mixture was obtained. This mixture was then step-cured in a compression moulder after degassing. PCL is considered to be a potential candidate for blending with polybenzoxazine to achieve easy processibility and improved thermal properties.	[178]
Rubber/polybenzoxazine composites	Melt-blending	Rubber modification of polybenzoxazine was carried out by adding liquid rubber to molten monomer at 120 ^{0}C and by mixing with a mechanical stirrer. A common approach to improve the toughness of a brittle material is by adding tough materials such as rubber and thermoplastics. Two liquid rubbers, namely amine terminated butadiene/acrylonitrile rubber (ATBN) and carboxyl terminated butadiene/acrylronitrile rubber (CTBN), were studied for the purpose of improving the toughness of polybenzoxazine.	[179]
Carbon fibre/polybenzoxazine composites	Hand-layup process	Laminates were compression-moulded by placing the prepreg stacks into a flat metal die at room temperature and then inserting the die into the compression moulder. These materials exhibit excellent mechanical properties, ablation resistance, good flame retardance and low smoke generation.	[180]
Titania/polybenzoxazine hybrids	Sol-gel process	Produced polybenzoxazine and titania hybrids with BA-a monomer and titanium isopropoxide (TIPO) by adding dropwise a desired amount of THF solution of TIPO to a stirred solution of BA-a in THF. T_g of these hybrid materials were shifted to higher temperature compared to pure polybenzoxazine. Thermal stability and flame-retardant properties of polybenzoxazine were greatly improved by hybridization with TiO_2.	[181]

| Clay/polybenzoxazine composites | Melt blending | OMMs were prepared by surface treatment of montmorillonite with octyl-, dodecyl- or stearylammonium chloride. BA-a and OMM were blended together by melt blending in various weight ratios at 100 ^{0}C. The presence of montmorillonite nanolayers improved the thermal stability of nanocomposites in comparison with the pure polybenzoxazine. | [182] |
| Silica fiber/polybenzoxazine composites | Solution blending | Silica fiber/polybenzoxazine composites were prepared by mixing a solution of benzoxazine monomer in acetone with silica fibers, followed by thermal curing. | [183] |

1.7 Reaction Mechanism of Ring opening polymerization of Benzoxazine

The ring opening reaction of the benzoxazine was first reported by Burke et al. [184]. A mono-oxazine ring containing benzoxazine is a distorted semi-chair structure, with the nitrogen and the carbon between the oxygen and nitrogen on the oxazine ring sitting, respectively, above and below the benzene ring plane. The resulting ring strain from this molecular conformation helps this type of six-membered ring undergo ring-opening reaction under specific conditions. In addition, due to their high basicity (by Lewis definition) both the oxygen and the nitrogen of the oxazine ring can act as potential cationic polymerization initiation sites and makes the ring very likely to open via a cationic mechanism [185, 186]. The electron charge calculation after energy minimization predicts that oxygen might be the preferred polymerization site over nitrogen due to its high negative charge distribution (O, -0.311; N, -0.270). In the reaction of 1,3-dihydrobenzoxazine with a phenol, having both ortho and para positions free, aminoalkylation occurred preferentially at the free ortho position to form a Mannich base bridge structure, along with small amount reaction at para position. To explain this ortho preference the formation of an intermolecular hydrogen-bonded intermediate species was proposed. Riese et al. also observed the high reactivity of the ortho position when following the kinetics of monofunctional benzoxazines with 2,4-di-tert-butylphenol catalyst [187]. Ring opening mechanism by protonation of the oxygen atom to form an iminium ion, followed by electrophilic aromatic substitution, as shown in Scheme 1.5 was proposed by Dunkers and Ishida [188].
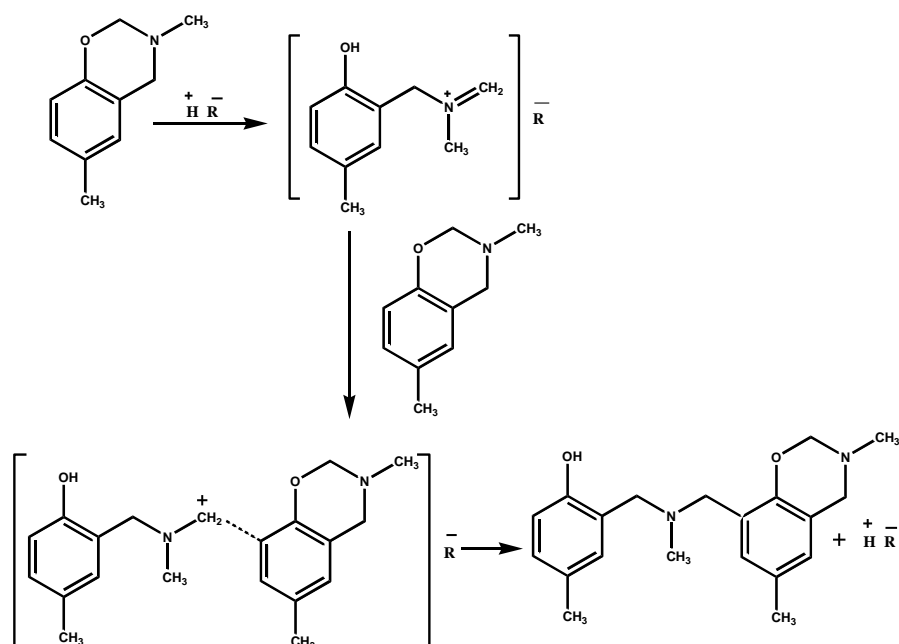
Scheme 1.5 Acid catalyst ring opening polymerization of 3,4-dihydro-2-H-1,3-benzoxazines [143].

(a) Cationic Polymerization of Benzoxazine

(i) Acid catalyzed polymerization of benzoxazine

Some investigations on catalyst assisted benzoxazine curing showed that the presence of catalysts influence to reduce the induction time and accelerate the reaction rate [189]. However, no significant polymerization was observed below 100 ^{0}C. Ishida and Rodriguez [190] have surveyed various acids ranging from strong acids to weak carboxylic acids to phenols as catalyst for this type of polymerization reaction. It has been observed that polybenzoxazines cured with strong carboxylic acids were inferior to those cured with weak carboxylic acids [188]. Several initiators, such as PCl$_5$, PCl$_3$, POCl$_3$, TiCl$_4$, AlCl$_3$ and MeOTf, were also reported as effective catalyst for polymerization which provides polybenzoxazines with high T$_g$ and high char yield [185, 191]. From the investigations on use of various cationic, anionic and radical initiators it has been proposed that the ring opening polymerization of the benzoxazine proceeds through a cationic mechanism [185, 186, 192, 193]. McDonagh and Smith [194] reported that 3,4-dihydro-2H-1,3-benzoxazine exhibits ring/chain tautomerism when protonated, by migration of the proton from the nitrogen to the oxygen atom, and thereby produce iminium ions in the chain form. Different mechanisms for cationic polymerization of benzoxazine and substituted benzoxazine were proposed by Wang and Ishida [186] to explain the dependency of formation of different polymeric structures on

the number and the position of the substitutions in the benzene ring of the monomer. The proposed reaction mechanisms are shown in schemes 1.6 and 1.7.
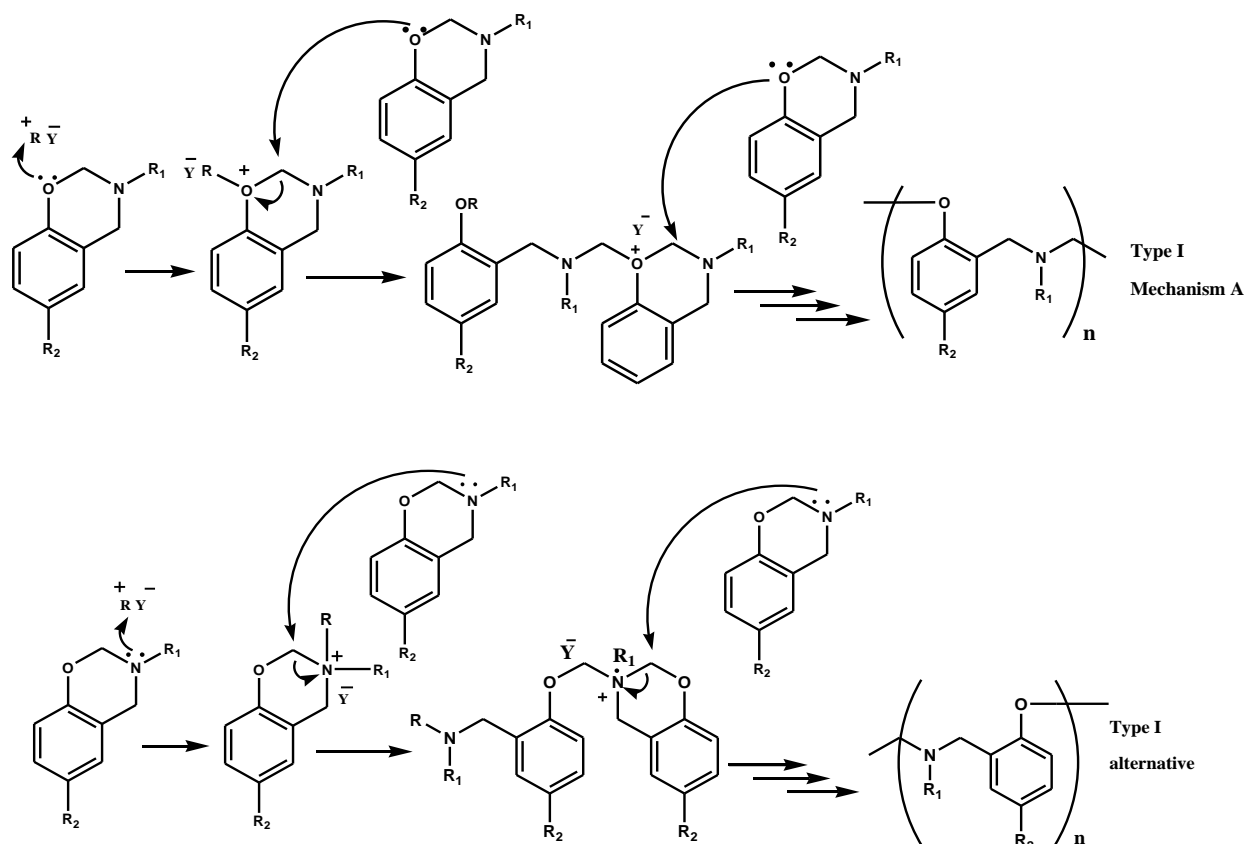
Scheme 1.6 Cationic ring opening mechanisms of 3,4-dihydro-2H-1,3-benzoxazines (Type I) [143].
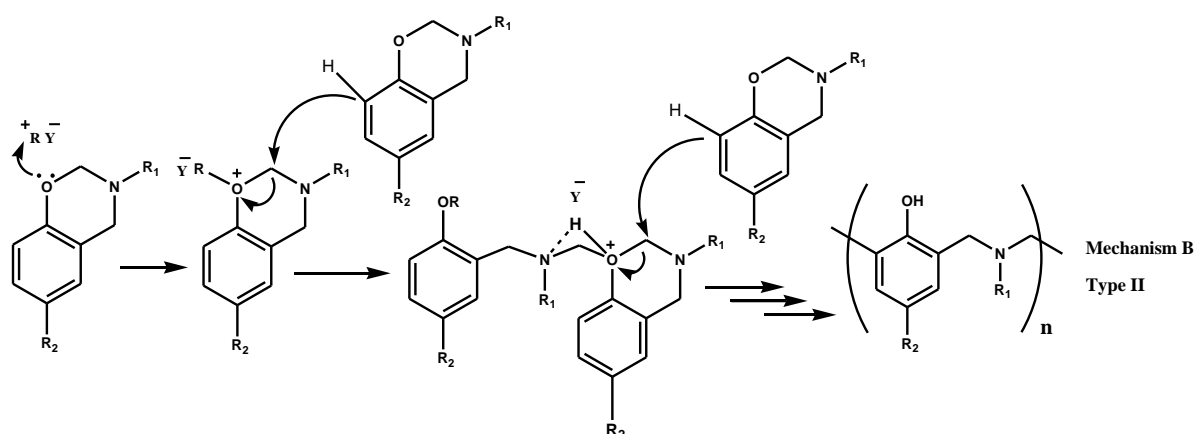
Scheme 1.7 Cationic ring opening mechanisms of 3,4-dihydro-2H-1,3-benzoxazines (Type II) [143].

(ii) Photoinitiated polymerization of benzoxazine

The photoinitiated ring-opening cationic polymerization of a mono-functional benzoxazine, 3- phenyl-3,4-dihydro-2H-1,3-benzoxazine (P-a), with onium salts such as diphenyliodonium hexafluorophosphate and triphenylsulfonium hexafluorophosphate as initiators was investigated by Kasapoglu et al [195].

The typical method of polymerization of benzoxazine monomers is thermal curing without using any catalyst [196-199]. It should be emphasized that the polymerization mechanism of benzoxazine resins is still not well established.

In this present work, we have used the thermal polymerization route to cure the benzoxazine monomer, so we are concentrating on thermal polymerization of benzoxazine.

(b) Thermal Polymerization of Benzoxazine

A cross-linked network structured polybenzoxazines, with higher T_g and degradation temperature, can be obtained when difunctional or multifunctional benzoxazines undergo polymerization. The polymeric structures form due to curing of monofunctional and difunctional benzoxazines are shown in Scheme 1.8 [200-202].
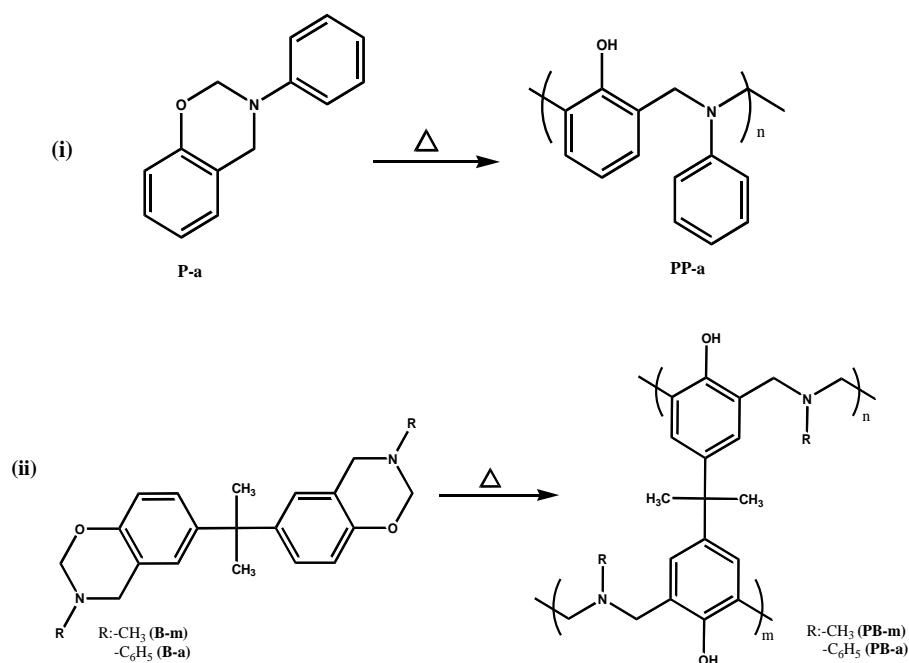
Scheme 1.8 Curing of (i) monofunctional and (ii) difunctional benzoxazines [143].

In the DSC thermogram of a mono-functional benzoxazine, P-a, a sharp exotherm was observed with onset and maximum temperatures of the exotherm at 202 and 230 ^{0}C, respectively, corresponding to the ring-opening polymerization, and an exotherm for P-a of 62 cal/g. In case of difunctional benzoxazine, B-a, DSC showed an exotherm onset at ca. 223 ^{0}C and maximum at a 249 ^{0}C corresponding to the ring-opening polymerization of benzoxazine. The amount of exotherm for B-a was 79 cal/g [200].

It has been reported that during synthesis of a difunctional benzoxazine (from bisphenol A, formaldehyde and methyl amine) not only bisphenol-A based benzoxazine (B-m) monomer forms as major product, but also dimers and small oligomers form by the subsequent reactions between the rings and ortho position of bisphenol A hydroxyl groups. These free phenolic hydroxy structure containing dimers and oligomers trigger the monomer to be self-initiated towards polymerization and crosslinking reactions [203]. Attempts have been made to understand the cure mechanism and kinetics of the thermal curing of mono and difunctional benzoxazines utilizing DSC, FTIR, DMA, ^{13}C and ^{15}N solid sate NMR spectroscopic measurements [204-211]. It has been proposed that the ring-opening initiation of benzoxazine results the formation of a carbocation and an iminium ion, which exist in equilibrium [205] (Scheme 1.9).
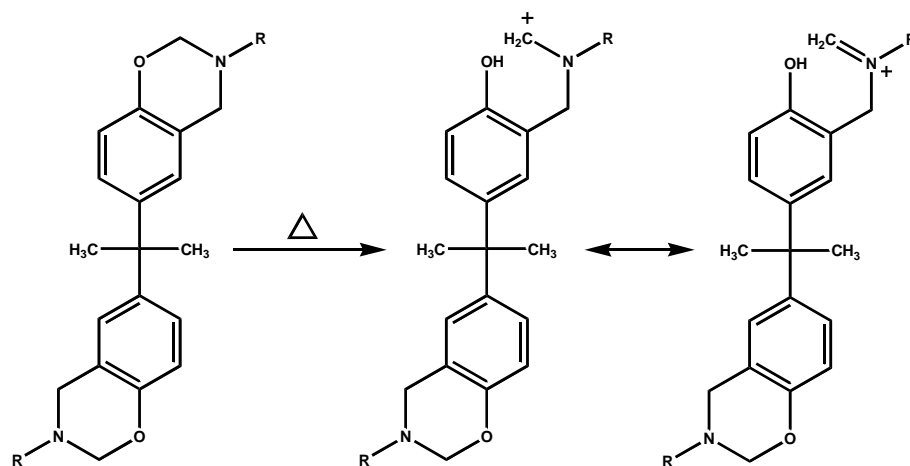
Scheme 1.9 Initiation of ring-opening polymerization of benzoxazines [143].

Polymerization proceeds via the electrophilic substitution by the carbocation to the benzene ring. This transfer occurs preferentially at the free ortho and para position of the phenol group. The stability of the iminium ion greatly affects the propagation rate because carbocation is responsible for propagation. Further, the reactivity of the equilibrium pair depends on the basicity of the amine group. The more basic the amine, with more the free

electron density of the nitrogen, has the capability to stabilize more the positive charge of the iminium ion. If the iminium ion is more stable, the equilibrium shifts toward it, causing lowering in propagation rate. If the iminium ion is unstable, the equilibrium will be shifted toward the carbocation, resulting in a higher propagation rate. It should be noted that since the propagation reaction involves chain transfer to a benzene ring temperature should have a great impact on the rate of propagation. Kinetic study indicated that in the early stages of polymerization, the reaction might be relatively independent of the cure temperature. As the reaction proceeds, the temperature effect on propagation becomes more evident in the reaction kinetics. Curing reactions at two different temperatures, below and above T_g temperature, demonstrate that the kinetics are significantly different for the two cure temperatures. Vitrification occurs sooner at higher cure temperature than the lower cure temperature, especially below the T_g. As vitrification causes a large increase in the viscosity of the system, at the reaction becomes largely diffusion controlled, and greatly affect the curing kinetics [205]. Scheme 1.10 illustrates the thermal polymerization of BA-a through cationic mechanism [143].
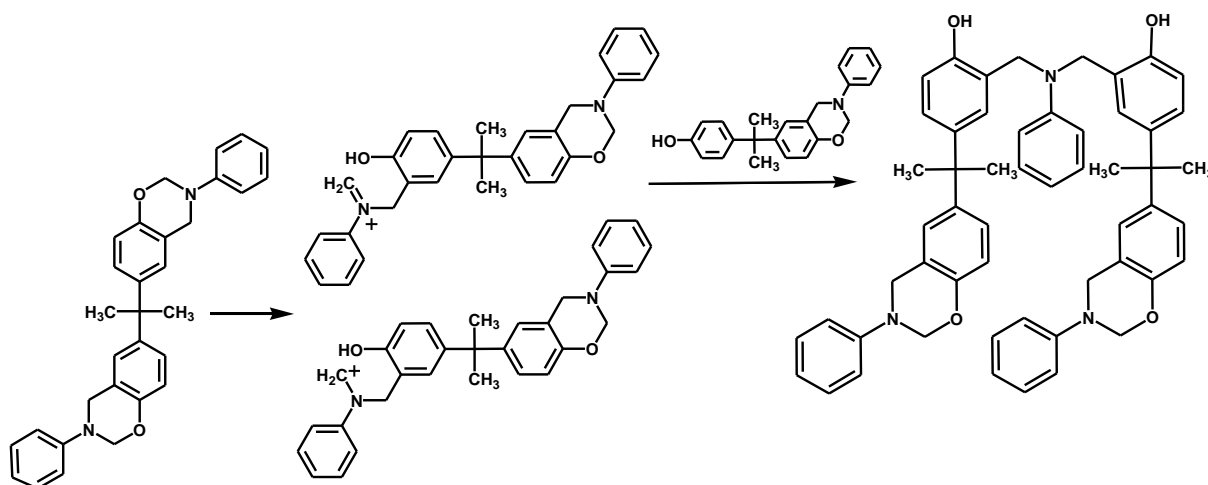
Scheme 1.10 Thermal polymerization of BA-a through cationic mechanism [143].

Solid State ^{15}N-NMR study identified the formation of a structure generated possibly due to the electrophilic substitution reaction between ortho position of the aniline and carbocation. Similar to phenol, the electron-donating nature of nitrogen of the aniline makes its ortho and para position as possible sites for electrophilic substitution with the carbocation. The formation of this structure is shown in Scheme 1.11 [206].
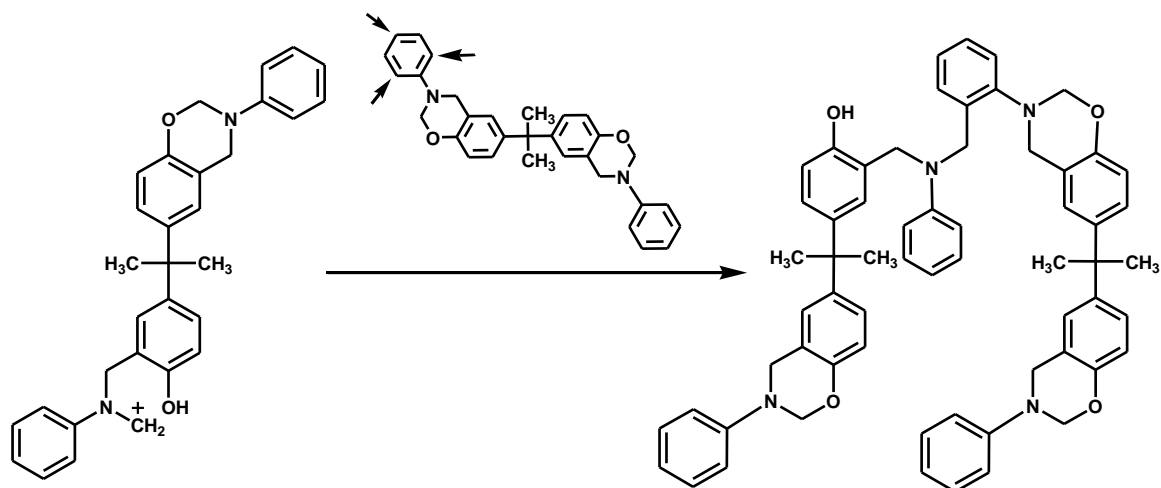
Scheme 1.11 Electrophonic substitution reaction of aniline moiety [143].

1.8 Gap in Existing Research

Although ferrite based ceramic materials exhibit interesting magnetic and electrical properties along with high thermal stability, their brittleness and lack of structural flexibility limit their usage in complex structured devices. Apart from that, high sintering temperature ($>1200\ ^{0}C$) is generally required for preparation of sintered ferrite bodies. Therefore, it is very difficult to prepare complex structures for specific high tech applications using pure ferrite nanopowders. Preparation of ferrite films or sheets, which can exhibit magnetic property as well as mechanical flexibility, is a major challenge. Moreover, preparation and characterization polybenzoxazine based magnetic nanocomposites have not yet explored well.

To address this issue, we have prepared ferrite-polymer nanocomposites. In these composites ferrite nanoparticles contribute the magnetic property of the composites, whereas, polymeric matrix provides the mechanical flexibility.

In this present work, we have used two types of ferrite nanoparticles as magnetic nanoparticles (MNPs): hard ferrite ($CoFe_2O_4$ (CF), $BaFe_{12}O_{19}$ (BHF)) and soft ferrite ($NiFe_2O_4$ (NF), $Ni_{0.8}Zn_{0.2}Fe_2O_4$ (NZF)). Polymeric matrix is composed of two polymers: linear low density polyethylene (LLDPE) and polybenzoxazine (PB). We have chosen polybenzoxazine as one of the components of polymeric matrix because it offers various advantages in comparison with traditional epoxy or novolac type resins such as (i) near zero volumetric change upon curing, (ii) low water absorption, (iii) no requirement of strong acid catalysts for curing and (iv) good thermal stability, etc [143, 205-217]. Various types of polybenzoxazine based composites have been reported in the literature [144, 145]. However,

not many reports are available on magnetic nanoparticles-polybenzoxazine composites [218-221]. Though polybenzoxazine offers various advantages, their inherent brittleness limits their applications [222]. To overcome this limitation we have blended benzoxazine with LLDPE. LLDPE was chosen because it possesses extraordinary flexibility, more elongation at break and puncture resistance property compared to other variety of polyethylene [223, 224]. Prepared composite materials can be useful for various strategic applications particularly as stealth materials in defense system.

1.9 Objectives

The objective of the present research work is the preparation of polybenzoxazine based flexible magnetic nanocomposite.

1. Preparation of the polybenzoxazine based flexible magnetic nanocomposite:

   (a) Preparation of magnetic nanoparticles (MNPs) by using EDTA precursor based method.

   (b) Preparation of benzoxazine-MNPs nanocomposite.

   (c) Preparation of flexible magnetic sheet by blending LLDPE-LgM-PB-MNPs.

2. Investigation on structural characterization of the prepared materials by using powder X-Ray diffractometer, particle size analyzer, scanning electron microscope and transmission electron microscope.

3. Investigation on the mechanical, thermal and magnetic properties of the nanocomposites.

1.10 Characterization Details

The as-synthesized nanopowders and their composites were characterized by the following techniques:

Thermal Analysis

Thermo gravimetric Analysis (TGA) and Differential Scanning Calorimetric (DSC) analyses were carried out for the precursors by using Shimadzu DTG-60 and Shimadzu DSC-60 respectively. The thermal analyses were performed in air at a constant heating rate of $10\ ^0C/min$ in the temperature range of 35 to 550 ^0C in aluminum pan for DSC and 35 to 800 ^0C in platinum pan for TGA respectively for all composite sample characterization.

X-Ray Diffraction (XRD) Analysis

Room temperature XRD spectra of the precursors and the calcined powders for all compositions were recorded by using a Rigaku Powder X-Ray Diffractometer (Mini Flex II) with Cu K_α (λ=0.15405 nm) radiation. The scan was performed between 10 to 70 degrees with a scanning speed of 2 degree per minute and sampling width of 0.01 degree. The slow scans were performed with a scanning speed of 1.2 degree per minute and a sampling width of 0.02 degree.

Particle Size Analysis (PSA)

The particle size distribution for the nanocomposite powder was determined by dynamic light scattering (DLS) technique using a particle size analyser (Delsa Nano S, Beckman Coulter, USA). For DLS experiment particles were dispersed in a dilute aqueous solution (10%) of TWEEN 20.

Scanning Electron Microscopy (SEM) Analysis

Microstructures of the calcined nanopowder and the morphology of the fractured surfaces of the composites were studied using SEM (JSM-6390LV, JEOL, Japan). In pellet holder tensile fractured sample were paste and fixed to sample holder. This sample holder was placed in sputter coating unit JEOL JFC-1600 and vacuum was created <5Pa then platinum was coated using sputtering method at 30mA. These coated sample were placed in SEM machine (JEOL JSM-6390 LV) and scanned at 5-10kV.

Transmission Electron Microscopy (TEM) Analysis

The particle size of the calcined powders was determined by using a Transmission Electron Microscope (TEM) (JEOL JEMS FEG-TEM-2100, Japan).

Fourier-Transform Infrared (FT-IR) Spectroscopy Analysis

Fourier transform infrared (FT-IR) spectra of the samples were acquired using a Shimadzu IR Prestige-21 Spectrometer (Shimadzu, Japan), equipped with a potassium bromide (KBr) beam-splitter. All spectra were recorded with 50 scans at resolution of 4 cm^{-1} and spectral range between 4000-400 cm^{-1}.

Mechanical Measurement

Tensile measurements were performed according to ASTM D638 standard using an universal testing machine (INSTRON 3366, USA). Type I dog bone specimens were tested for polybenzoxazine, LLDPE and composites. Room temperature tensile measurements were carried out at a constant crosshead speed of 5 mm/min. The flexural properties of polybenzoxazine, LLDPE and composites were determined in accordance with ASTM D790 using a universal testing machine (INSTRON 3366, USA) with 10 kN load cell. Specimens were tested in a three point loading with 50 mm support span at crosshead speed of 5 mm/min at room temperature.

Magnetization Measurement

Room temperature magnetization measurement was performed for pure ferrite nanopowder as well as the composites using a Vibrating Sample Magnetometer (VSM) (EV5, ADE Technology, USA). The M-H loops were obtained using applied field of 15000 Oe for $CoFe_2O_4$, $BaFe_{12}O_{19}$ nanopowder and their composites, whereas an applied field of 2000 Oe was used for $NiFe_2O_4$, $Ni_{0.8}Zn_{0.2}Fe_2O_4$ nanopowder and their composites.

1.11 Outlay of the Thesis

The thesis is divided into seven chapters and each chapter is followed by a summary.

In Chapter 1, the subject of nanocomposite, methods of polymer nanocomposite preparation, introduction to ferrite and their synthesis methods, introduction to benzoxazine monomer and their processibility, identification of research gaps based on literature review and the objective of the present research work have also been discussed.

Chapter 2 describes the preparation and characterization of flexible polybenzoxazine-LLDPE composites.

Chapter 3 describes the synthesis, characterization and properties of pure single phase $CoFe_2O_4$ and LLDPE-LgM-Polybenzoxazine-$CoFe_2O_4$ flexible magnetic nanocomposites.

Chapter 4 describes the synthesis, characterization and properties of pure single phase $BaFe_{12}O_{19}$ and LLDPE-LgM-Polybenzoxazine-$BaFe_{12}O_{19}$ flexible magnetic nanocomposites.

Chapter 5 describes the synthesis, characterization and properties of pure single phase $NiFe_2O_4$ and LLDPE-LgM-Polybenzoxazine-$NiFe_2O_4$ flexible magnetic nanocomposites.

Chapter 6 describes the synthesis, characterization and properties of pure single phase $Ni_{0.8}Zn_{0.2}Fe_2O_4$ and LLDPE-LgM-Polybenzoxazine-$Ni_{0.8}Zn_{0.2}Fe_2O_4$ flexible magnetic nanocomposites.

In Chapter 7, the conclusions and future scope of research work have been presented along with a comparative summary of results for the prepared composite.

The characterization of prepared magnetic nanopowder and their composites was done in collaboration with other institutes as follows:

Fourier-Transform Infrared (FT-IR) Spectroscopy Analysis

Fourier-transform infrared (FT-IR) spectra of the samples were acquired in Goa University, India.

Transmission Electron Microscopy (TEM) Analysis

TEM Analysis was performed in Lunghwa University of Science and Technology, Taiwan.

Scanning Electron Microscopy (SEM) Analysis

SEM Analysis was performed in collaboration with Birla Institute of Technology Mesra, Jharkhand, India.

Mechanical measurement

Mechanical measurements were performed in collaboration with Birla Institute of Technology Mesra, Jharkhand, India and National Chemical Laboratory Pune, India.

Magnetization Measurement

Magnetization Measurements were performed in collaboration with Defence Research and Development Organisation Lab Jodhpur, Rajasthan, India.

<div align="right">**CHAPTER 2**</div>

<div align="center">

Preparation and characterization

of flexible polybenzoxazine-LLDPE composites

</div>

2.1 Experimental procedure for material synthesis

2.1.1 Materials used

The chemicals used were aniline, paraformaldehyde, and bisphenol-A (99%, s. d. fine-chem limited, India), chloroform (99.7%, Qualigens Fine Chemicals, India). Linear low density polyethylene (LLDPE, R35A042), having a density of 0.935 gm/cm^3 and melt flow index (MFI) of 4.2 gm/10 min, was obtained from GAIL (India) Ltd., and LLDPE-*g*-Maleic anhydride (LgM) (OPTIM E-126, with 0.73% maleic anhydride content and MFI 2.16 gm/10 min) from Pluss Polymers Pvt, Ltd., India. All chemicals were used as received.

2.1.2 Synthesis of Benzoxazine monomer (BA)

Benzoxazine monomer (bis (3-phenyl-3, 4-dihydro-2H-1, 3-benzoxazinyl) isopropane) was synthesized using a solventless method by reacting bisphenol-A, aniline, and paraformaldehyde [225]. In a typical synthesis, bisphenol-A (0.02 mol, 4.48 gm), aniline (0.04 mol, 3.68 ml), paraformaldehyde (0.08 mol, 2.4 gm) were mixed in a round bottom flask and heated slowly at 90 ^{0}C in an oil bath for 90 min. After cooling, benzoxazine monomer was extracted from reaction mixture by dissolving in chloroform followed by filtration. Pure benzoxazine monomer was finally obtained by evaporating chloroform. Benzoxazine monomer was then dried in a vacuum oven for 24 h at 55 ^{0}C to remove traces of chloroform.

2.1.3 Preparation of LLDPE-LgM-PB composites (L-LgM-PB) [226]

The blending of LLDPE, LgM and BA was carried out in a custom made cylindrical mixing chamber (65 mm diameter x 65 mm height) using a two sided bled stirrer. The temperature of the mixture during mixing was maintained at 180 ^{0}C and the stirring speed was 80 rpm. LLDPE and LgM were first melted for 10 min then benzoxazine was added to this melt and mixed for 20 min. This hot mass was then transferred into a pot and heated at 200 ^{0}C for 30 min in an oven. The hot semi-viscous mixture thus obtained was immediately poured into a closed mold under hydraulic pressure through a 5 mm gate. The material was then allowed to

cool at room temperature inside the mold cavity. After cooling the mold was opened to get the final product. The overall process is presented in scheme 2.1. As per ASTM D638 standard specification Type I dog bone shaped specimens (with over all dimension 165 mm x 19 mm x 3.2 mm) of the composites were prepared by this method for mechanical testing. Blend, having different compositions, were prepared by blending benzoxazine with LLDPE and LgM with various amounts (Table 2.1).
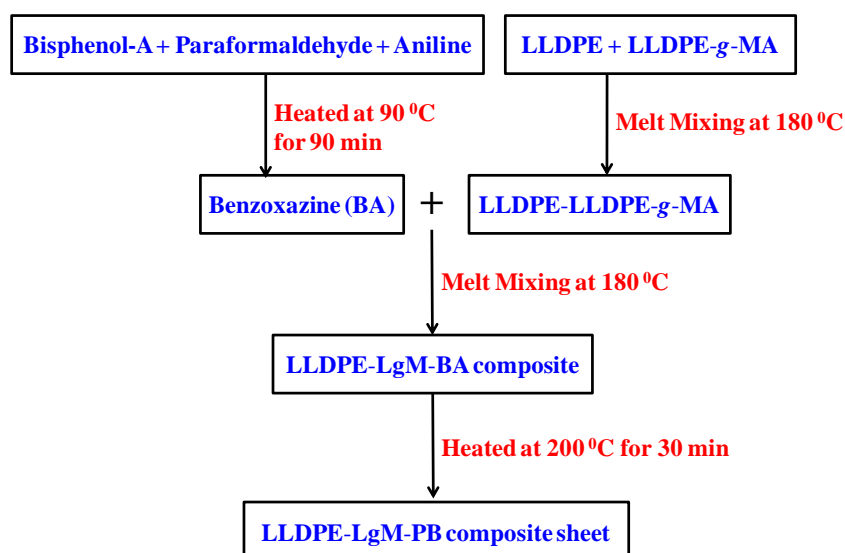
Scheme 2.1 Preparative route for LLDPE-LgM-PB composite sheets.

Table 2.1 Compositions of the LLDPE-LgM-PB composites.

Sample code	LLDPE (wt%)	LgM (wt%)	BA (wt%)
85.5L-5LgM-9.5PB	85.5	5	9.5
76.0L-5LgM-19.0PB	76.0	5	19.0
66.5L-5LgM-28.5PB	66.5	5	28.5
57.0L-5LgM-38.0PB	57.0	5	38.0
50.0L-0LgM-50.0PB	50.0	0	50.0
49.0L-2LgM-49.0PB	49.0	2	49.0
48.5L-3LgM-48.5PB	48.5	3	48.5
48.0L-4LgM 48.0PB	48.0	4	48.0
47.5L-5LgM-47.5PB	47.5	5	47.5
47.0L-6LgM-47.0PB	47.0	6	47.0
46.0L-8LgM-46.0PB	46.0	8	46.0

2.2 Results and Discussion

2.2.1 Characterization of L-LgM-PB composites

2.2.1.1 X-Ray Diffraction Analysis

Room temperature wide angle powder XRD spectra of pure LLDPE showed diffraction peaks at $2\theta = 21.6^0$, 23.8^0 and 36.3^0 corresponding to (110), (200) and (020) diffraction planes of the orthorhombic crystal planes of polyethylene [223, 224, 227] along with a broad amorphous peak in between $2\theta = 8$ and 12^0. Pure polybenzoxazine exhibited a broad peak from $2\theta = 11.7^0$ to 37.5^0 indicating its amorphous nature. XRD spectra of the prepared composites showed the presence of characteristic peaks of LLDPE along with amorphous broad peak of polybenzoxazine (Figure 2.1). The crystalline nature of LLPDE was remained preserved in the cured blend samples. However, with increasing amount of polybenzoxazine in the composites broadening of the peaks of LLDPE was observed. This indicates that blending of polybenzoxazine with LLDPE enhances the amorphous nature. The areas under the crystalline and amorphous portions were determined in arbitrary units, and the percentage of crystallinity (Xc) was measured with the following relation [227]:

$$Xc = \frac{Ic}{Ia + Ic}$$

Where Ia and Ic are the integral intensities corresponding to the amorphous and crystalline phases, respectively. The change of percentage of crystallinity of the composites with changing composition is summarized in Table 2.2.
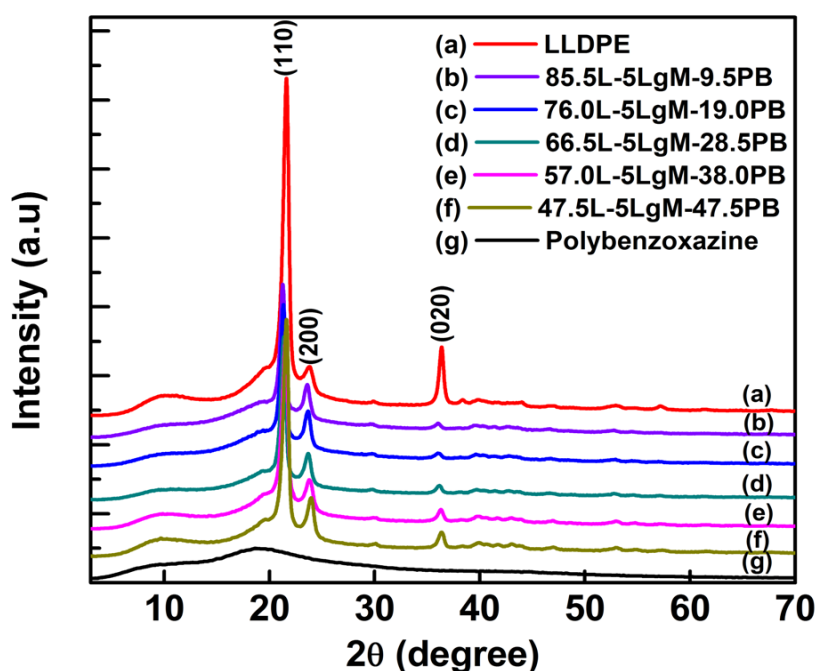
Fig 2.1 X-Ray Diffraction spectra of LLDPE, polybenzoxazine and composites.

Table 2.2 Amount of crystallinity present in the prepared composites.

Sample code	% crystallinity
LLDPE	69.23
85.5L-5LgM-9.5PB	63.87
76.0L-5LgM-19.0PB	62.23
66.5L-5LgM-28.5PB	61.90
57.0L-5LgM-38.0PB	59.69
47.5L-5LgM-47.5PB	56.65
Polybenzoxazine	21.85

2.2.1.2 Thermal Analysis

In the DSC theromgram of benzoxazine monomer an exothermic peak at ~205 ^{0}C was observed (Figure 2.2 A (a)), which corresponds to the ring opening polymerization of benzoxazine [228-231]. In case of pure LLDPE, (i) an endothermic peak at ~124 ^{0}C, corresponding to its melting temperature [227], and (ii) an exothermic peak at ~224 ^{0}C, which indicates its thermal-oxidative decomposition [232, 233], were observed (Figure 2.2 A (b)). Major decomposition of LLDPE occurred in the temperature range of ~390 to 480 ^{0}C, which indicated in DSC curve by the appearance of exothermic peaks at this temperature range (Figure 2.2 B (a)). In the DSC thermograms of LLDPE-polybenzoxazine composites the endothermic peak at ~124 ^{0}C was present but the exothermic ring opening polymerization peak of benzoxazine was absent (Figure 2.2 A (c)). This indicates that benzoxazine monomers were fully polymerized to polybenzoxazine during composite preparation as the melt blending was performed at 200 ^{0}C. An exothermic peak at ~283 ^{0}C, corresponding to the thermal-oxidative decomposition, was present in the DSC thermograms of the composites. It was observed that thermal-oxidative decomposition temperature of the composites shifted to higher temperatures with increasing amount of polybenzoxazine. Exothermic peaks for major decomposition of the composites were found to be in the temperature range of 430 to 530 ^{0}C (Figure 2.2 B (b)). This indicates that presence of polybenzoxazine enhances the thermal stability of the composites. Same observation was found in the TGA analysis of the composites. Thermal-oxidative decomposition of the composites was found to be started after ~250 ^{0}C. The temperatures at which 5 and 10 % weight loss was found to increase with increasing polybenzoxazine content in the composite and are listed in Table 2.3. Char yield of the all the composites was found to be zero at ~600 ^{0}C in air. Full decomposition

temperatures of the composites were also found to be increased with increasing amount of polybenzoxazine in the composition (Figure 2.3).
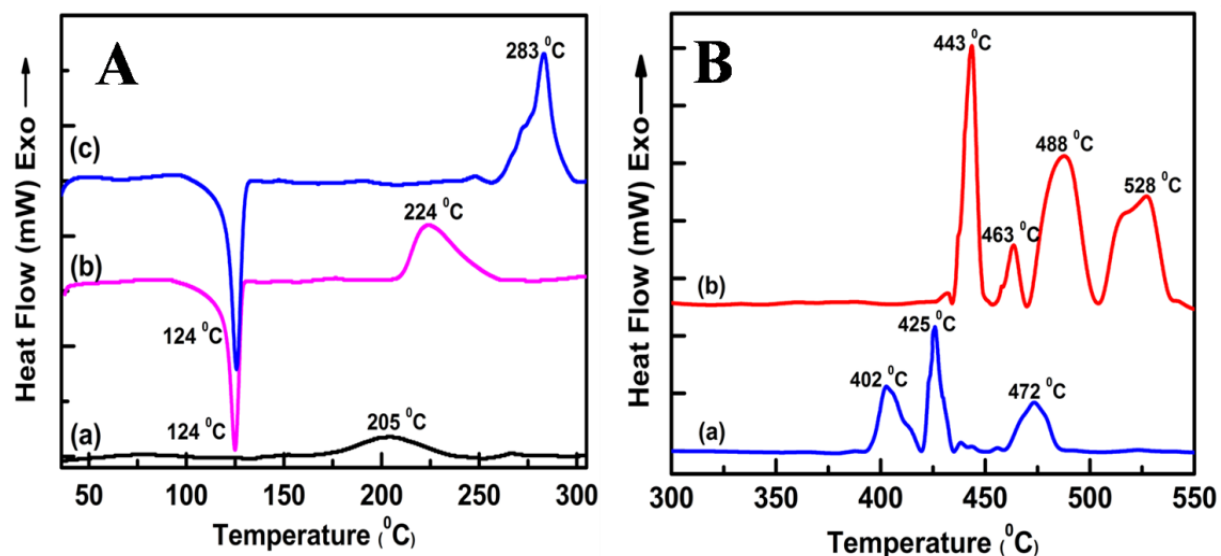
Fig 2.2 (A) DSC thermogram of (a) benzoxazine, (b) LLDPE, (c) 47.5L-5LgM-47.5PB composite. (B) DSC thermogram of (a) LLDPE, (b) 47.5L-5LgM-47.5PB composite in temperature range of 300 to 550 ^{0}C.
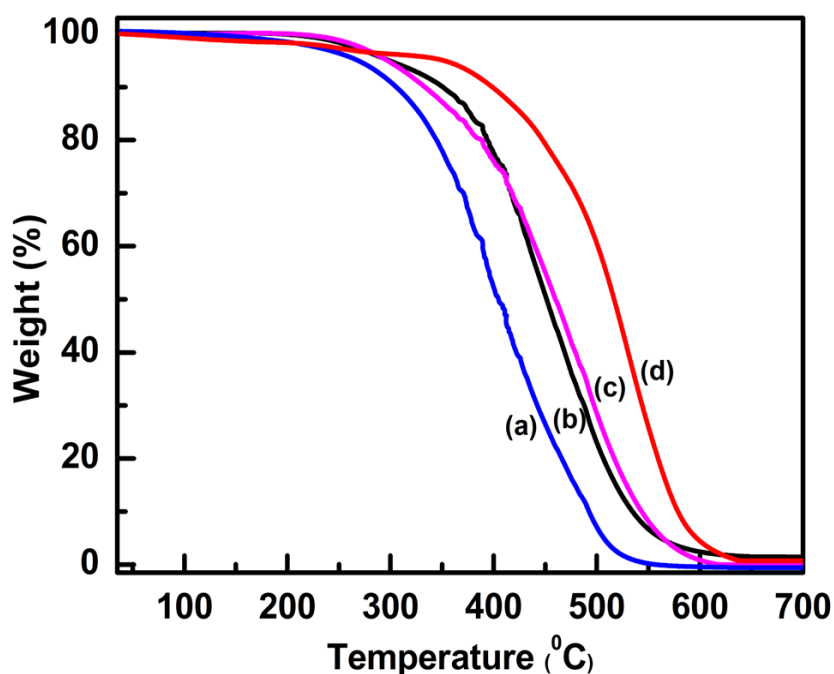
Fig 2.3 TGA thermograms of (a) LLDPE, (b) 57.0L-5LgM-38.0PB composite, (c) 47.5L-5LgM- 47.5PB composite, (d) Polybenzoxazine.

Table 2.3 Temperatures required for 5% and 10% weight loss of the composites due to thermal decomposition in air.

Sample code	$T_{5\%}$ (^{0}C)	$T_{10\%}$ (^{0}C)
Polybenzoxazine	350	400
LLDPE	267	305
85.5L-5LgM-9.5PB	272	306
76.0L-5LgM-19.0PB	281	329
66.5L-5LgM-28.5PB	286	331
57.0L-5LgM-38.0PB	302	343
47.5L-5LgM-47.5PB	306	345

2.2.1.3 FT-IR Analysis

FT-IR spectra of benzoxazine and 47.5L-5LgM-47.5PB blend are shown in Figure 2.4 (a) and 2.4 (b) respectively. In case of benzoxazine monomer, the peaks at 949 cm^{-1} and 1496 cm^{-1} assigned to the tri-substituted benzene ring and absorption at 1235 cm^{-1} for asymmetric stretching of C-O-C were observed [222, 234]. The methyl group vibration was found at 2962 cm^{-1} [235]. In the FT-IR spectra of composite (Figure 2.4 (b)) the characteristic peaks of LLDPE and polybenzoxazine were present. A strong peak around 2917 and 2843 cm^{-1}, associated with the C-H stretching vibration, along with peaks at 1364 cm^{-1} for -CH$_3$ symmetric vibration for LLDPE [227] were observed. It was also observed that the disappearance of peaks at 949 cm^{-1} and 1496 cm^{-1} peak (assigned for tri-substituted benzene ring of BA) and appearance of a peak at 1482 cm^{-1} (correspond to the tetra-substituted benzene ring of PB) [181] indicated that the ring opening polymerization of BA occurred during preparation of composites at 200 ^{0}C. This indicates the complete formation of polybenzoxazine from benzoxazine occurred during blend preparation.
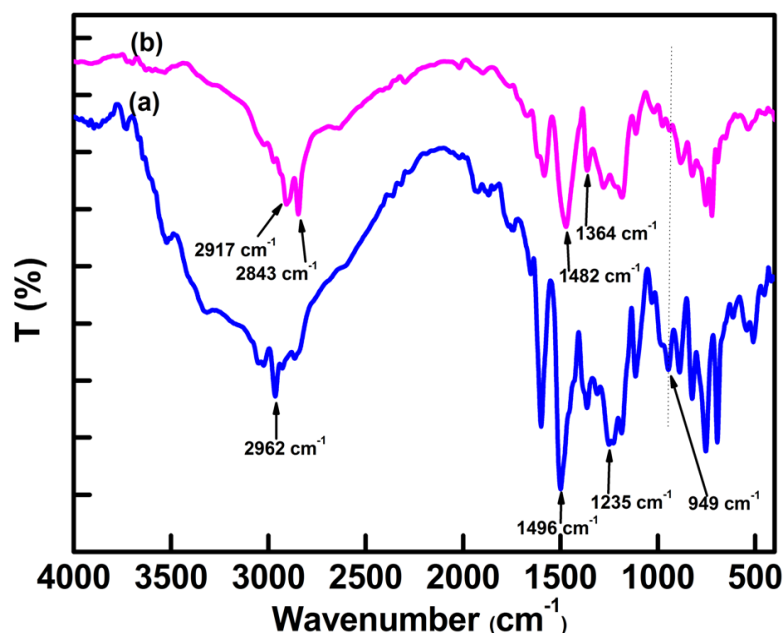
Fig 2.4 FT-IR spectra of (a) benzoxazine, (b) 47.5L-5LgM-47.5PB composite.

2.2.1.4 Mechanical Properties

In this study, composites were prepared by blending LLDPE with polybenzoxazine in presence of LgM compatibilizer. To determine the optimum amount of compatibilizer, required to achieve good mechanical property, samples were prepared by blending various amount of LgM (0 to 8 wt%) with LLDPE and PB and tensile and flexural tests were performed. It was observed that tensile strength and flexural strength of the composites increased with increasing amount of LgM (up to 5 wt%) and then started to decrease (Figure 2.5). Pure polybenzoxazine possessed high tensile strength (47.05 MPa) and less elongation at break (2.2%), whereas, LLDPE showed low tensile strength (16.75 MPa) and significantly more elongation at break (57.77%). Composites consist of LLDPE and PB with 5 wt% LgM (47.5L-5LgM-47.5PB) exhibited higher tensile strength (23.81 MPa) than pure LLDPE and more elongation at break (6.11%) than pure polybenzoxazine. The increase of tensile strength and flexural strength with increasing amount of LgM might be due to the fact that LgM molecules are placed at the interface of LLDPE and polybenzoxazine during melt blending processes. The polar functional groups of LgM interact with polar functional groups of polybenzoxazine while the LLDPE backbone of LgM molecules compatibilizer with the LLDPE matrix [236]. This interaction enhances the interfacial adhesion and helps to reduce the interfacial tension between the two distinct phases (LLDPE and polybenzoxazine). At 5 wt%, the concentration of LgM in the blend may reaches to the critical concentration value, where compatibilizer molecules already occupy most of the interfacial area. Beyond 5 wt%

excess LgM molecules form a third phase [236]. So, decrease in tensile strength and flexural strength of the composites was observed beyond 5 wt% LgM. Table 2.4 summarizes the tensile and flexural properties of the composites having various amount of LgM. As the composites containing 5 wt% LgM exhibited highest tensile and flexural strength, so, this concentration of LgM was chosen to prepare composites having various amount of LLDPE and polybenzoxazine to assess the effect of blending of LLDPE with polybenzoxazine.
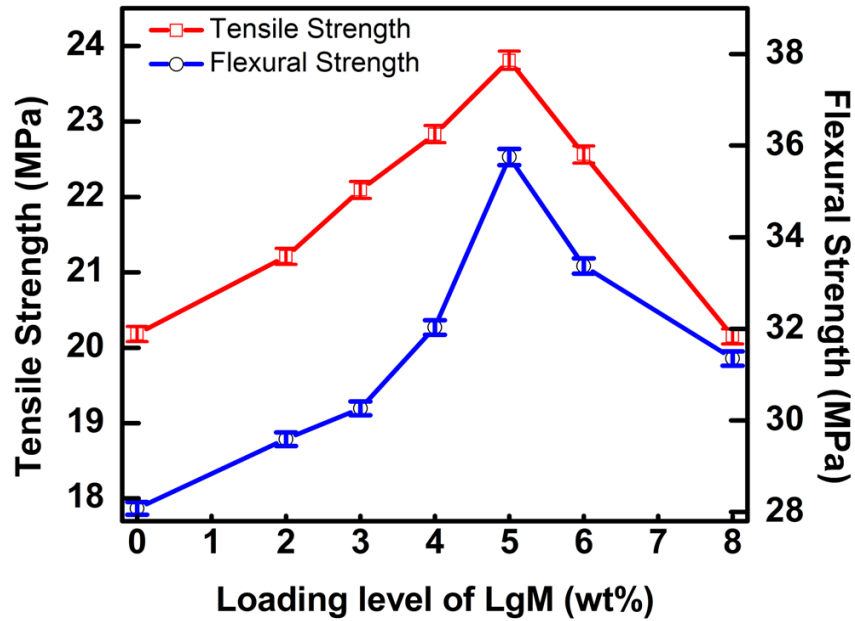
Fig 2.5 Change of tensile and flexural strength of the composites with the variation of LgM in the composition.

Table 2.4 Tensile and flexural properties of the composites having various amount of LgM.

Sample code	Tensile strength (MPa)	Tensile modulus (GPa)	Flexural strength (MPa)	Flexural modulus (GPa)
Polybenzoxazine	47.05	3.6	54.06	1.928
LLDPE	16.75	0.236	16.33	0.403
50.0L-0LgM-50.0PB	20.18	1.007	28.08	1.015
49.0L-2LgM-49.0PB	21.21	1.030	29.59	1.027
48.5L-3LgM-48.5PB	22.09	1.056	30.26	1.055
48.0L-4LgM-48.0PB	22.83	1.065	32.02	1.188
47.5L-5LgM-47.5PB	23.81	1.071	35.75	1.236
47.0L-6LgM-47.0PB	22.56	0.988	33.37	1.097
46.0L-8LgM-46.0PB	20.15	0.982	31.35	1.068

Tensile tests of the composites showed that blending of LLDPE with polybenzoxazine resulted in decrease of tensile strength and modulus with increasing amount of LLDPE. However, significant amount of increase of the elongation at break was observed due to blending of LLDPE with polybenzoxazine compare to pure polybenzoxazine (Figure 2.6). Flexural strength and modulus were also decreased with increasing amount of LLDPE in the composition of composites (Figure 2.7). However, toughness of the samples decreases very less with increasing amount of LLDPE in the composite. These facts indicate that blending of LLDPE with polybenzoxazine in presence of 5 wt% LgM compatibilizer increases the mechanical flexibility of the composites. The tensile and flexural properties of the composites are listed in Table 2.5.
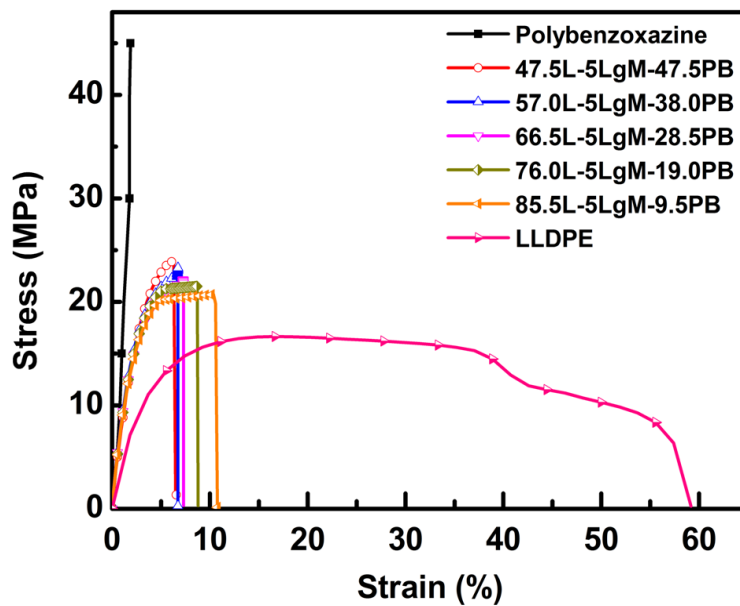
Fig 2.6 Tensile stress-strain curves of LLDPE-polybenzoxazine composites.
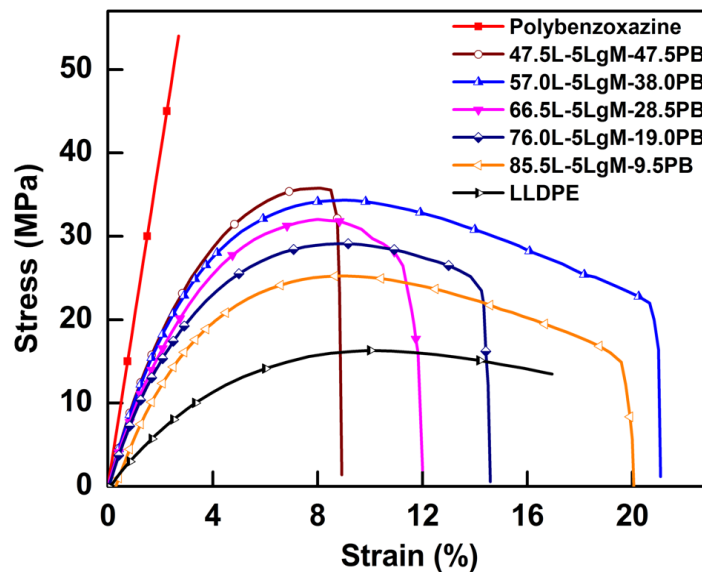
Fig 2.7 Flexural stress-strain curves of LLDPE-polybenzoxazine composites.

Table 2.5 Change of mechanical properties of the composites with the variation of LLDPE and polybenzoxazine in the composite.

Sample code	Tensile strength	Tensile modulus (GPa)	Elongation at break (%)	Flexural strength (MPa)	Flexural modulus (GPa)	Toughness (MPa)
Polybenzoxazine	47.05	3.6	2.2	54.06	1.928	0.439
47.5L-5LgM-47.5PB	23.81	1.071	6.11	35.75	1.236	0.244
57.0L-5LgM-38.0PB	23.07	1.012	6.66	34.07	1.169	0.476
66.5L-5LgM-28.5PB	22.16	0.986	7.30	32.10	1.108	0.291
76.0L-5LgM-19.0PB	21.50	0.951	8.77	29.01	0.988	0.341
85.5L-5LgM-9.5PB	20.85	0.910	10.82	25.10	0.860	0.394
LLDPE	16.75	0.236	57.77	16.33	0.403	0.274

2.2.1.5 SEM Analysis of Fractured Surfaces

The morphology of the fractured surfaces of the composites after tensile testing was investigated by SEM and is shown in Figure 2.8 (a)-(g). In case of 50.0L-0LgM-50.0PB composite (without compatibilizer) inhomogeneous matrix structure of fractured surface of blend was observed (Figure 2.8 (a)). This indicates the there is immiscibility between the two polymers (i.e. LLDPE and polybenzoxazine) without compatibilizer. It was observed that enhancement of homogeneity of LLDPE and polybenzoxazine phases with increasing amount of LgM (upto 5wt%) in the composite (i.e 49.0L-2LgM-49.0PB, 48.5L-3LgM-48.5PB, 48.5L-4LgM-48.5PB, 48.5L-5LgM-48.5PB) (Figure 2.8 (b), (c), (d), (e)). However, in case of the composites having more than 5wt% LgM (48.5L-6LgM-48.5PB, with 6wt% LgM) phase separation was observed and with increase of LgM concentration this effect was much more pronounced (Figure 2.8 (f) and (g)). This might be due to the high concentration of LgM acted as the third phase in the composite (Figure 2.8 (f) and (g)). This indicates the presence of 5wt% LgM compatibilizer in the blend enhances the interfacial adhesion.
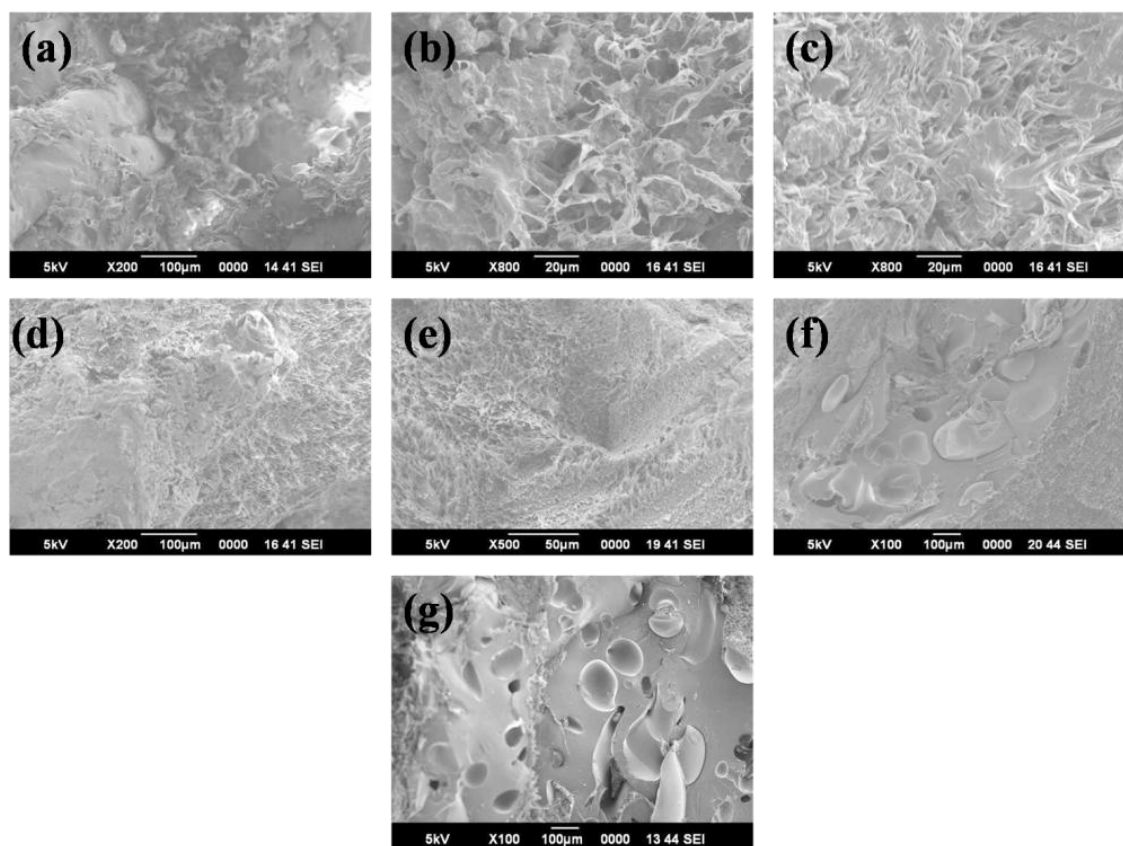
Fig 2.8 SEM micrograph of (a) 50.0L-0LgM-50.0PB composite, (b) 49.0L-2LgM-49.0PB composite, (c) 48.5L-3LgM-48.5PB composite, (d) 47.5L-4LgM-47.5PB composite, (e) 47.5L-5LgM-47.5PB composite, (f) 47.5L-6LgM-47.5PB composite, (g) 47.5L-8LgM-47.5PB composite.

Figure 2.9 demonstrates the flexibility of the composites, composed of 47.5 wt% LLDPE, 47.5 wt% polybenzoxazine and 5 wt% LgM.
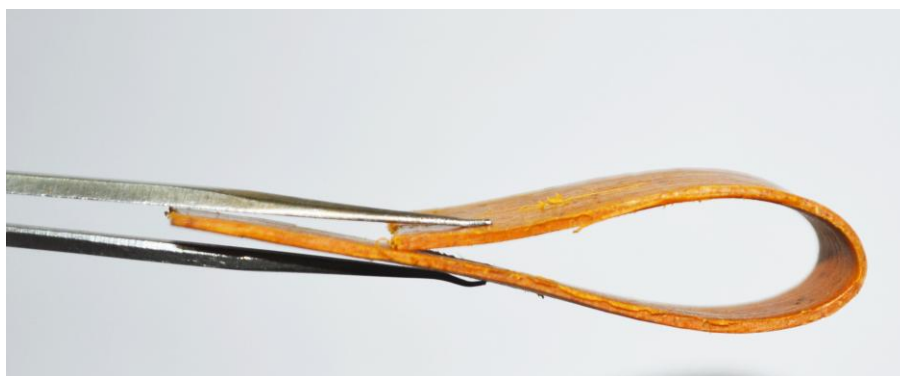
Fig 2.9 LLDPE-polybenzoxazine composite film (85 mm x 13 mm x 1 mm) showing mechanical flexibility.

2.3 Summary of Results

1. Polybenzoxazine-LLDPE based composites were prepared by blending LLDPE with polybenzoxazine in presence of a compatibilizer (LgM) by employing a simple melt blending method.

2. Thermal stability of the composites was found to be increased with increasing polybenzoxazine content in the blend. However, as the melting point of the LLDPE is ~124 ^{0}C, these composites should be used below this temperature.

3. Tensile and flexural testing of the composites revealed that 5 wt% is the optimum amount of compatibilizer that can be used in composite preparation.

4. Mechanical flexibility of the composites was found to be increased with increasing amount of LLDPE in the composition.

5. This method of composite preparation is simple and large scale composites can be prepared by employing this method. The prepared composites possess good mechanical flexibility along with good thermal stability; these composites have the potential to be used in preparation of complex structures.

CHAPTER 3

Synthesis, characterization and properties of pure single phase CoFe$_2$O$_4$ and LLDPE-LgM-Polybenzoxazine-CoFe$_2$O$_4$ flexible magnetic nanocomposites

3.1 Experimental procedure for material synthesis

3.1.1 Materials used

The chemicals used were Fe(NO$_3$)$_3$.9H$_2$O, Co(NO$_3$)$_2$.6H$_2$O, EDTA (99.9%, Merck, India). Aniline, paraformaldehyde and bisphenol-A (99%, s.d. fine chem limited, India), chloroform (99.7%, Qualigens Fine Chemicals, India). Linear low density polyethylene (LLDPE, R35A042) having a density of 0.935 gm/cm^3 and melt flow index (MFI) of 4.2 gm/10 min, was obtained from GAIL (India) Ltd., and LLDPE-*g*-Maleic anhydride (LgM) (OPTIM E-126) with a 0.73% maleic anhydride content and MFI 2.16 gm/10 min, from Pluss Polymers Pvt, Ltd., India. All chemicals were used as received.

3.1.2 Synthesis of CoFe$_2$O$_4$ (CF) nanopowder: [237]

CoFe$_2$O$_4$ nanopowder was prepared by using EDTA-precursor based method. In a typical synthesis, stoichiometric amounts of cobalt nitrate and ferric nitrate were dissolved in distilled water according to the molar ratio of 1:2. An aqueous solution of EDTA was prepared by dissolving EDTA in hot water with drop-wise addition of NH$_4$OH. After complete dissolution of EDTA, the solution was boiled to remove the excess NH$_3$. The pH of the solution was found to be ~6. Aqueous solutions of metal nitrates and EDTA were mixed in a molar ratio of 1:1 and stirred for 1 h at room temperature using a magnetic stirrer. The pH of the resulting mixture was ~2. Black-coloured precursor was formed when this reaction mixture was evaporated to dryness on a hot plate at ~110 ^{0}C. During drying, slight decomposition of the precursor was observed. Three to four drops of 10% NH$_4$NO$_3$ aqueous solution were added to the dried precursor powder and then precursor powders calcined in air for 2-4 h at specified temperatures ranging from 475 to 550 ^{0}C to obtain cobalt ferrite nanopowder. NH$_4$NO$_3$ was added to facilitate the oxidation of carbonaceous mass of the precursor.

3.1.3 Synthesis of Benzoxazine monomer (BA)

Benzoxazine monomer was synthesized as per the procedure described in the section 2.1.2 (Experimental procedure for material synthesis) of Chapter 2.

3.1.4 Preparation of benzoxazine-CoFe$_2$O$_4$ nanocomposites (BA-CF) [221]

For the synthesis of benzoxazine-CoFe$_2$O$_4$ nanocomposite, a solvent casting method was employed. Various compositions of nanocomposites using these powders were prepared by blending with BA as listed in Table 3.1. BA monomer was dissolved first in chloroform, followed by stepwise addition of cobalt ferrite nanopowder in desired weight ratio. During mixing, the mixture was ultrasonicated. After completion of mixing, the mixture was dried under reduced pressure in a vacuum oven at 80 ^{0}C for 12 h. Dynamic light scattering studies indicated the average sizes of these benzoxazine coated CoFe$_2$O$_4$ nanoparticles were in the range of 100-200 nm. The benzoxazine-cobalt ferrite nanocomposite powders thus obtained were used for further composite preparation.

3.1.5 Preparation of LLDPE-LgM-PB-CF composites (L-LgM-PB-CF) [221]

To prepare LLDPE-LgM-PB-CF composite sheets, benzoxazine-CoFe$_2$O$_4$ nanocomposite powders (BA-CF) were blended with LLDPE. LgM was used as compatibilizer between LLDPE and PB. 5 wt% LgM was used as compatibilizer between LLDPE and PB. 5 wt% LgM was chosen to prepare these composites because we have observed that mixing of 5 wt% LgM with LLDPE and PB helps to achieve best mechanical property of LLDPE-PB composite as discussed in chapter 2 (Section 2.2.1.4 Mechanical Properties) [226]. Nanocomposites having different compositions of CoFe$_2$O$_4$, PB and LLDPE were prepared as listed in Table 3.1. The blending of LLDPE, LgM and BA-CF nanopowders was carried out in a custom made cylindrical mixing chamber (65 mm diameter x 65 mm height) using a two sided blade stirrer. The temperature of mixing was set at 180 ^{0}C and the stirrer speed was 80 rpm. A mixture of LLDPE and LgM was first melted for 10 min then BA-CF powder was added and mixed for 20 min. The hot mass was then taken out from the mixing chamber and transferred into a pot and heated at 200 ^{0}C for 30 min in an oven. The hot semi-viscous mixture thus obtained was immediately poured into a closed mold under hydraulic pressure through a 5 mm gate. Then material inside the mold cavity was allowed to cool to room temperature and mold was opened to get the final product. The overall process is presented in

scheme 3.1. As per ASTM D638 standard specification Type I dog bone shaped specimens (with over all dimension 165 mm x 19 mm x 3.2 mm) of the composites were prepared by this method for mechanical testing.

| Benzoxazine Monomer + CF | | LLDPE + LLDPE-*g*-MA |

Mixing in CHCl₃ sonication for 30 min Drying

Melt Mixing at 180 ⁰C

| Benzoxazine + CF nanocomposite (BA-CF) | + | LLDPE-LLDPE-*g*-MA |

Melt Mixing at 180 ⁰C

| LLDPE-LgM-BA-CF composite |

Heated at 200 ⁰C for 30 min

| LLDPE-LgM-PB-CF composite sheet |
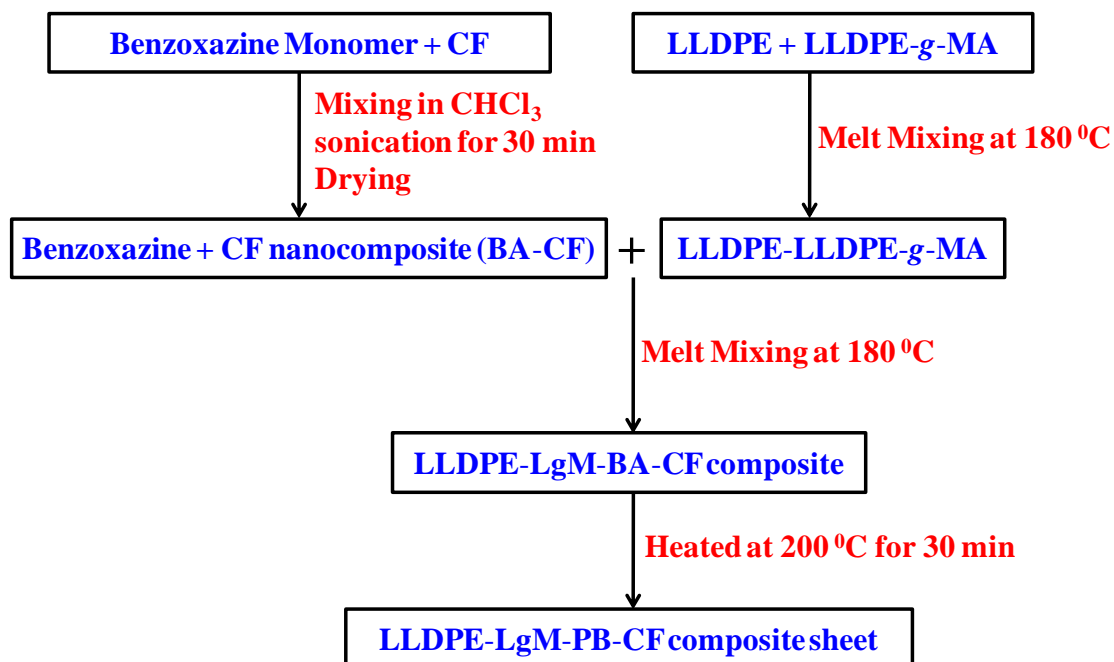
Scheme 3.1 Preparative route for LLDPE-LgM-PB-CF composite sheets.

Table 3.1 Compositions of prepared BA-CF and L-LgM-PB-CF composites.

Sample code	LLDPE (wt%)	LgM (wt%)	PB (wt%)	CoFe₂O₄ (wt%)
BA-CF (70:30)	--	--	70	30
BA-CF (50:50)	--	--	50	50
BA-CF (30:70)	--	--	30	70
47.5L-5LgM-47.5PB	47.5	5	47.5	--
47.5L-5LgM-33.25PB-14.25CF	47.5	5	33.25	14.25
47.5L-5LgM-23.75PB-23.75CF	47.5	5	23.75	23.75
47.5L-5LgM-14.25PB-33.25CF	47.5	5	14.25	33.25

SEM micrograph of the surface of a cross section of the composites (Figure 3.1) shows that polybenzoxazine coated CoFe$_2$O$_4$ nanoparticles are embedded within the polymeric matrix.
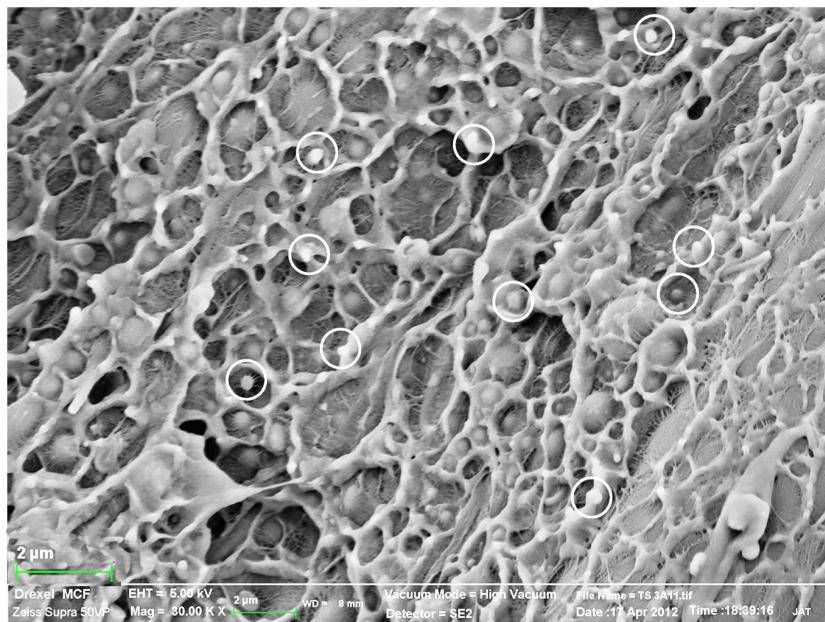
Fig 3.1 SEM micrograph of the composites shows that CoFe$_2$O$_4$ nanoparticles are dispersed within the polymeric matrix. Polybenzoxazine coated CoFe$_2$O$_4$ nanoparticles are within the marked circle.

3.2 Results and Discussion

3.2.1 Characterization of CoFe$_2$O$_4$ nanoparticles

3.2.1.1 Thermal Analysis

TGA and DSC analyses were performed to investigate the thermal decomposition behavior of precursor powder due to heat treatment in air and thermogram is shown in Figure 3.2. Thermogram of precursor powder revealed that a total weight loss of ~35% occurred in two steps when the precursor powder was heated from 35 to 800 ^{0}C in air. Initially, ~8% weight loss occurred in the region 35-180 ^{0}C due to the loss of moisture from the sample. 27% weight loss was observed in the temperature range 200-400 ^{0}C. This might be due to the oxidative decomposition of precursor and evolution of CO$_2$ and NO$_x$ gases. This decomposition was also reflected in the DSC thermogram as two exothermic peaks at 292 ^{0}C and 348 ^{0}C. No weight loss was observed in TGA when the sample was heated beyond 400 ^{0}C. This confirmed that full decomposition of carbonaceous mass of the precursor occurred within 400 ^{0}C.
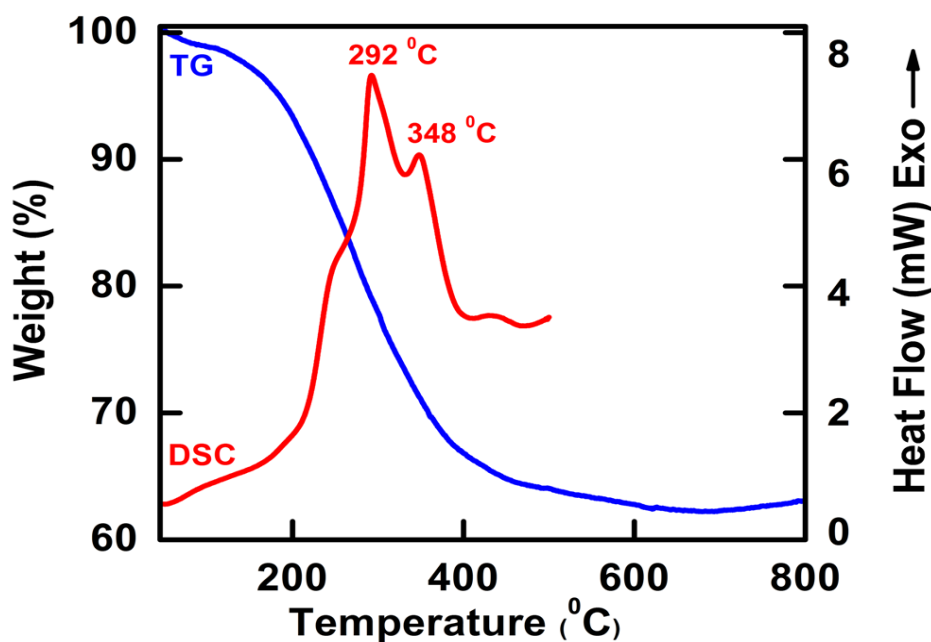
Fig 3.2 TGA-DSC thermogram of CoFe$_2$O$_4$ precursor.

3.2.1.2 X-Ray Diffraction Analysis

Room temperature XRD spectra of powder, calcined at different temperatures are shown in Figure 3.3 (a)-(e). It was observed that XRD spectra of the uncalcined precursor exhibited diffraction peaks for CoFe$_2$O$_4$ [JCPDS 22-1086]. However, intensity ratio (I/I_0) of the peaks did not exactly match with standard values. This indicated that partial decomposition of the uncalcined precursor, which occurred during the last stage of reaction mixture, resulted in the formation of CoFe$_2$O$_4$ phase but with poor crystallinity. XRD spectra of calcined powder (calcination temperature 475 ^{0}C) showed the formation of CoFe$_2$O$_4$ with better crystallinity. However, a small amount of impurity of α-Fe$_2$O$_3$ was also detected [JCPDS 84-0757]. Calcination of precursor at 550 ^{0}C for 4 h resulted in the formation of pure, single-phase CoFe$_2$O$_4$ and no impurity phase was detected. The increase in peak intensities with calcination temperature was due to the increase in crystallinity and particle size during the calcination process. The crystallite size of the calcined powders were calculated using X-ray peak-broadening of the diffraction peaks (311) and (440) using Scherrer's formula [238] and found to be ~18 nm.
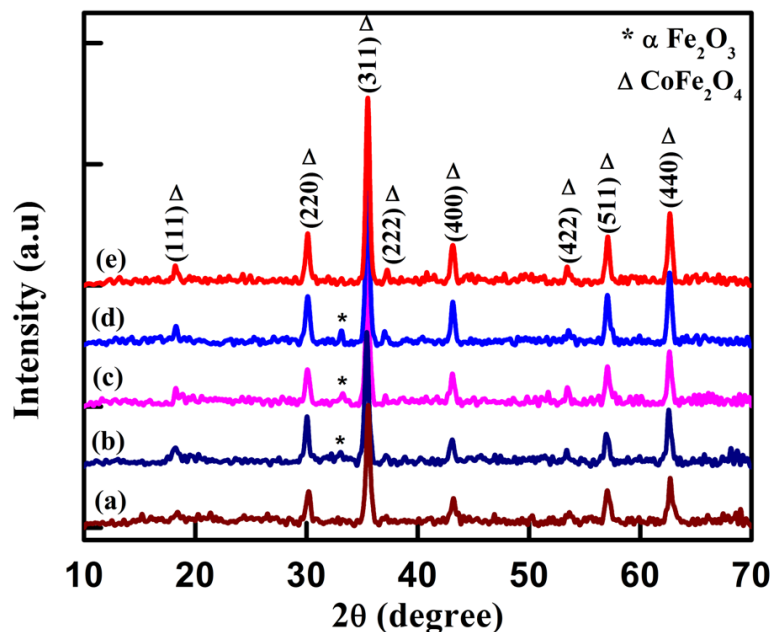
Fig 3.3 XRD patterns of $CoFe_2O_4$ (a) precursor and the powders obtained by calcining the precursor at (b) 475 ^{0}C for 2 h, (c) 475 ^{0}C for 4 h, (d) 550 ^{0}C for 2 h and (e) 550 ^{0}C for 4 h.

3.2.1.3 Particle Size and TEM Analysis of CoFe₂O₄ nanopowder

The intensity particle size distributions of the as-synthesized $CoFe_2O_4$ nanopowder obtained from DLS study at 30 ^{0}C (Figure 3.4 (a)) exhibited a single modal distribution with the main peak average around 15.1 $\pm$ 12.4 nm. The cumulant mean diameter of the particles was 11.9 nm with a polydispersity index of 0.013. The TEM micrograph for the powder calcined at 550 ^{0}C is shown in Figure 3.4 (b). The micrograph clearly indicated that average particle size of the calcined powder was ~20 nm. The particles were mostly round in shape and formed loose aggregates.
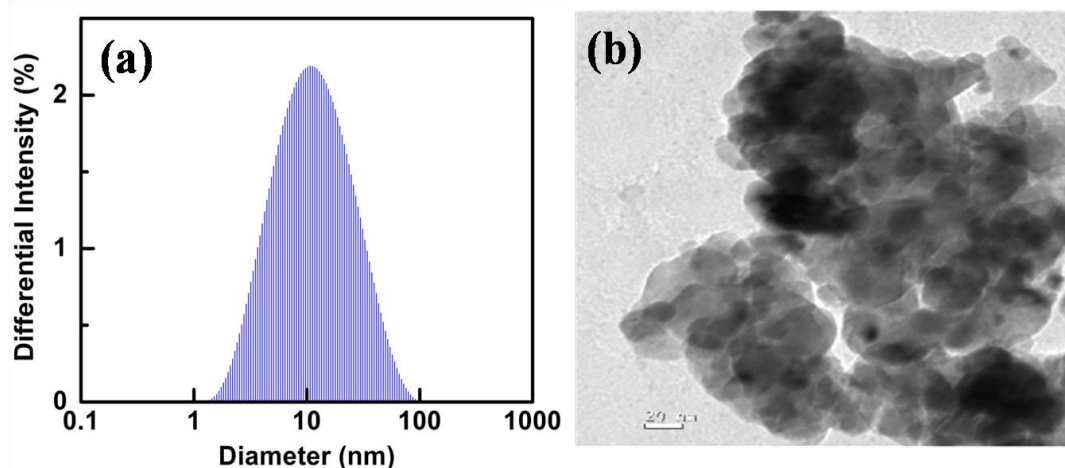
Fig 3.4 (a) Particle size distribution and (b) TEM micrograph of as-synthesized $CoFe_2O_4$ nanopowder.

3.2.1.5 Magnetization Measurement

Room temperature saturation magnetization (M_s) and coercivity (H_c) of the as-synthesized CoFe$_2$O$_4$ nanopowder was measured by using VSM and the hysteresis loop is shown in Figure 3.5. Ferromagnetic behavior was observed for the sample. The as-synthesized CoFe$_2$O$_4$ nanopowder possessed coercivity (H_c) of 1645.24 Oe and a saturation magnetization (M_s) of 67.55 emu/g. These values are comparable with the values reported by other authors using different preparation techniques, which are summarized in Table 3.2.
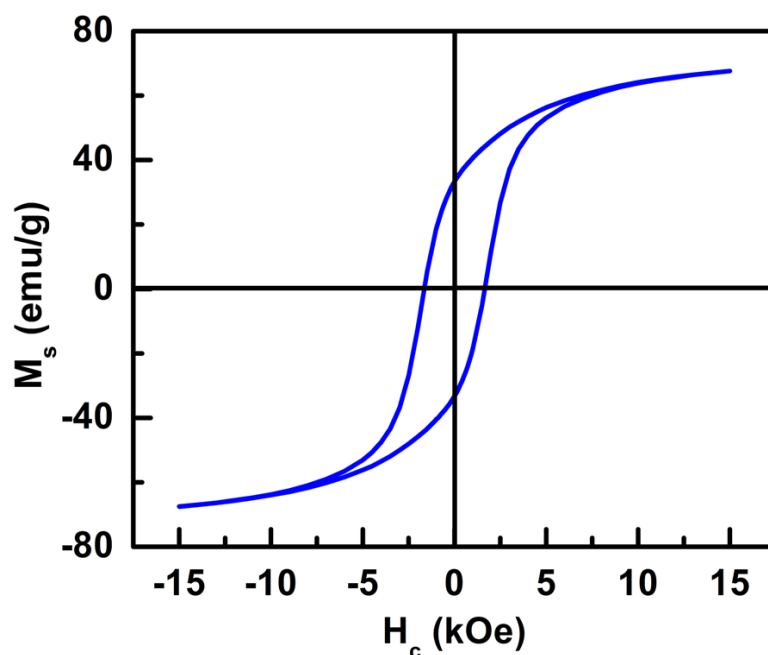
Fig 3.5 Room temperature hysteresis loop for CoFe$_2$O$_4$ nanopowder.

Table 3.2 Comparison of M_s and H_c of CoFe$_2$O$_4$ nanoparticles prepared by different synthesis methods.

Synthesis Methods	Calcination	M_S (emu/g)	H_C (Oe)	References
Co precipitation	900 ^{0}C for 1 h	74	1000	[239]
Co precipitation	700 ^{0}C for 2 h	58.52	-----	[240]
		Am^2/kg		
Co precipitation	800 ^{0}C for 1 h	66	66 mT	[241]
Sol-gel	800 ^{0}C	56	700	[242]
Sol-gel	850 ^{0}C for 3 h	76.5	2020	[243]
Organic acid precursor	400-1000 ^{0}C for 2 h	55.25-76.07	584-918.1	[244]

Polymer precursor based	400-800 ^{0}C for 2 h	67.5-100.1	1072-2091	[245]
Complexometric synthesis	850-1050 ^{0}C for 10 h	77.7-81.21 (Am^2/kg)	25-120.5 (kA/m)	[246]
Mechanical alloying	600-1000^{0}C for 6 h	38.7-47.25	1385-1982	[247]
Mechanical alloying	500-1000^{0}C for 4 h	23-48	500-1900	[248]
Mechanical milling	1000 ^{0}C for 4 h	82	1100	[249]
Wet chemical route	600 ^{0}C for 10 h	68	1205	[250]
EDTA precursor route	**550 ^{0}C for 4 h**	**67.55**	**1645.24**	**This Work [237]**

3.2.2 Characterization of BA-CF nanocomposite and L-LgM-PB-CF composite

3.2.2.1 X-Ray Diffraction Analysis

X-Ray diffraction spectra were recorded for pure BA-CF nanocomposites and L-LgM-PB-CF composites. In the X-ray diffratogram of BA-CF nanocomposite samples, all XRD peaks of CoFe$_2$O$_4$ were present and no additional peaks were detected (Figure 3.6 (b)). In the XRD spectra of L-LgM-PB-CF nanocomposite samples, XRD peaks of CoFe$_2$O$_4$ were present along with additional peaks at 2θ = 21.6^0 and 23.8^0. These two peaks corresponded to the (110) and (200) diffraction planes of LLDPE [223, 224, 227] and indicated that the crystalline structure of LLDPE remained unchanged upon blending in the nanocomposites. However, the intensity of the crystalline peaks of LLDPE varied with the compositions. These XRD spectra of the composites also confirmed that, the pure crystalline phase of CoFe$_2$O$_4$ was remained preserved in the composite with no impurity phase formation during the melt blending process.

Fig 3.6 XRD spectra of (a) CoFe₂O₄ powder, (b) BA-CF (50:50) nanocomposite, (c) 47.5L-5LgM-33.25PB-14.25CF composite, (d) 47.5L-5LgM-23.75PB-23.75CF composite, (e) 47.5L 5LgM-14.25PB-33.25CF composite.

3.2.2.2 Thermal Analysis

TGA and DSC analysis of the pure benzoxazine, BA-CF and L-LgM-PB-CF composites were performed to evaluate their thermal stability. In the DSC thermogram of benzoxazine monomer an exothermic peak at ~205 ^{0}C was observed, which was due to the ring opening polymerization of benzoxazine ring (Figure 3.7 (a)) [228-231]. In case of BA-CF nanocomposite this exothermic curing peak of benzoxazine shifted to the lower temperature at ~180 ^{0}C. This might be due to the catalytic effect of CoFe₂O₄ towards the thermal curing of benzoxazine [251, 252] (Figure 3.7 (b)). In the DSC thermogram of pure LLDPE (Figure 3.7 (c)) an endothermic peak at ~124 ^{0}C, corresponding to its melting temperature [227] and an exothermic peak at ~224 ^{0}C, which may be attributed to the beginning of the thermal oxidative decomposition of LLDPE were observed [232, 233]. In case of PB containing LLDPE composite (Figure 3.7 (d)) beginning of thermal oxidative decomposition occurred at ~283 ^{0}C, which is higher than that of pure LLDPE. For L-LgM-PB-CF composite samples an endothermic peak at ~124 ^{0}C corresponding to the melting temperature of LLDPE was observed [227]. The exothermic peak for ring opening polymerization of benzoxazine ring was absent in this thermogram (Figure 3.7 (e)). This result indicated that all benzoxazine monomers were fully polymerized to polybenzoxazine during composite preparation as the

melt blending was performed at 200 ^{0}C. An exothermic peak at ~249 ^{0}C was observed, which was due to the thermal-oxidative decomposition of LLDPE component of the L-LgM-PB-CF composite which is higher than the pure LLDPE (~224 ^{0}C) but lower than the LLDPE-LgM-PB matrix composite (~283 ^{0}C). This may be due the catalytic effect of CoFe₂O₄ on thermal degradation of polymeric matrix [251, 252].
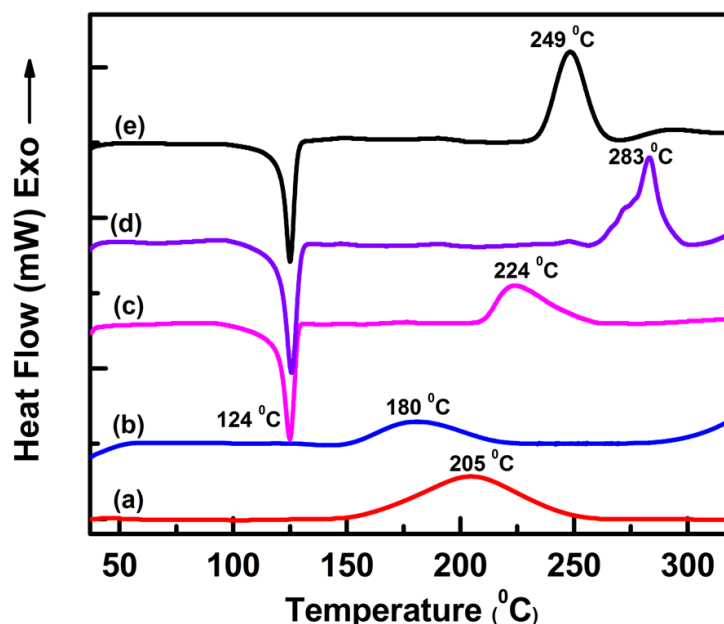
Fig 3.7 DSC thermogram of (a) benzoxazine, (b) BA-CF (50:50) nanocomposite, (c) LLDPE, (d) 47.5L-5LgM-47.5PB, (e) 47.5L-5LgM-23.75PB-23.75CF composite.

From TGA of pure PB, LLDPE and their composites, temperature for 5% weight loss ($T_{5\%}$), temperature for 10% weight loss ($T_{10\%}$) and char yield (%) at 800 ^{0}C in air were determined and listed in Table 3.3. It was observed that the temperature at 5 and 10% weight loss was found to be decrease with increasing CoFe₂O₄ content in the composites. This may be due catalytic effect of CoFe₂O₄ on thermal degradation of polymeric matrix [251, 252]. TGA thermograms of LLDPE, PB, BA-CF and L-LgM-PB-CF composite are shown in Figure 3.8. These thermograms revealed that presence of more thermally stable PB in the L-LgM-PB-CF composites enhances the overall thermal stability of the composites. The thermal stability of the composite was found to be more than pure LLDPE but less than pure polybenzoxazine. The degradation of all the composites was found in the temperature range of 350-550 ^{0}C. The char yield at 800 ^{0}C of the composite was found to increase with increasing CoFe₂O₄ content. However, as the melting temperature of LLDPE is ~124 ^{0}C the composites should be used below this temperature.
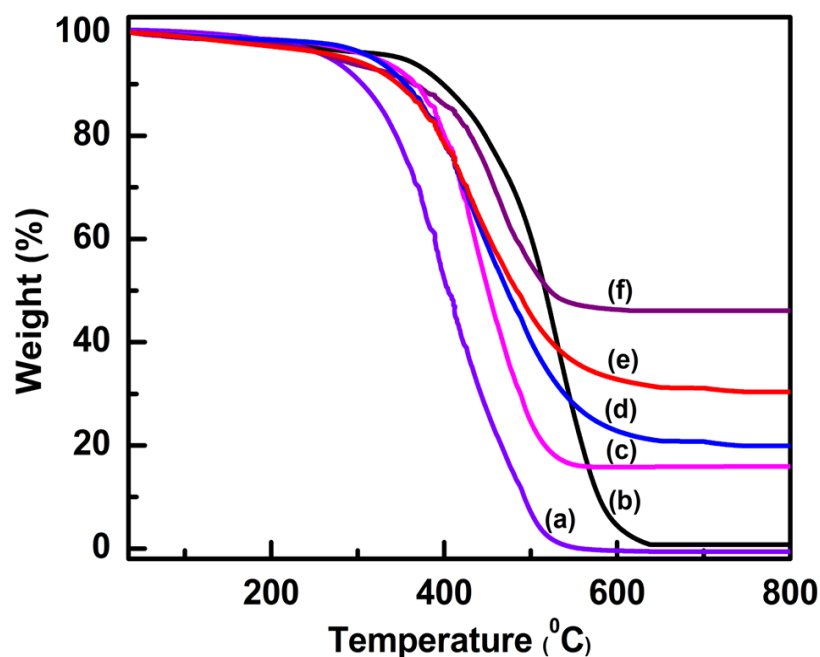
Fig 3.8 TGA thermograms of (a) LLDPE, (b) Polybenzoxazine, (c) 47.5L-5LgM-33.25PB-14.25CF composite, (d) 47.5L-5LgM-23.75PB-23.75CF composite, (e) 47.5L-5LgM-14.25PB-33.25CF composite, (f) PB-CF (50:50) nanocomposite.

Table 3.3 Thermal degradation properties of the BA-CF nanocomposite and L-LgM-PB-CF composites.

Sample code	$T_{5\%}$ (^{0}C)	$T_{10\%}$ (^{0}C)	char yield (%) at 800 ^{0}C
Polybenzoxazine	350	400	0
LLDPE	267	305	0
47.5L-5LgM-47.5PB	306	345	0
PB-CF(70:30)	301	375	25
PB-CF(50:50)	270	364	46
PB-CF(30:70)	265	362	63
47.5L-5LgM-33.25PB-14.25CF	316	365	14
47.5L-5LgM-23.75PB-23.75CF	310	354	20
47.5L-5LgM-14.25PB-33.25CF	288	343	30

3.2.2.3 FT-IR Analysis

In the FT-IR spectra of pure benzoxazine monomer (BA) (Figure 3.9 (a)), the peaks at 953 cm^{-1} and 1496 cm^{-1} assigned to the tri-substituted benzene ring and absorption at 1245 cm^{-1} for asymmetric stretching of C-O-C were observed [222, 234]. The methyl group vibration was found at 2969 cm^{-1} [235]. In case of BA-CF nanocomposite (Figure 3.9 (b)), all the characteristic bands of benzoxazine were present along with a peak at 568 cm^{-1} which corresponded to M-O stretching vibration mode of CoFe$_2$O$_4$ [253-255]. In the FT-IR spectra of L-LgM-PB-CF composites (Figure 3.9 (c)), the disappearance of peaks at 953 cm^{-1} and 1496 cm^{-1} peak (assigned to tri-substituted benzene ring of BA) and appearance of a peak at 1466 cm^{-1} (correspond to the tetra-substituted benzene ring of PB) indicated that the ring opening polymerization of BA occurred during preparation of composites at 200 ^{0}C [181]. Additionally, characteristic peaks of LLDPE at 1367 cm^{-1} (-CH$_3$ symmetric vibration) and peaks around 2925 and 2838 cm^{-1}, associated with the C-H stretching vibration [227], along with a peak around 568 cm^{-1} for CoFe$_2$O$_4$ were observed.
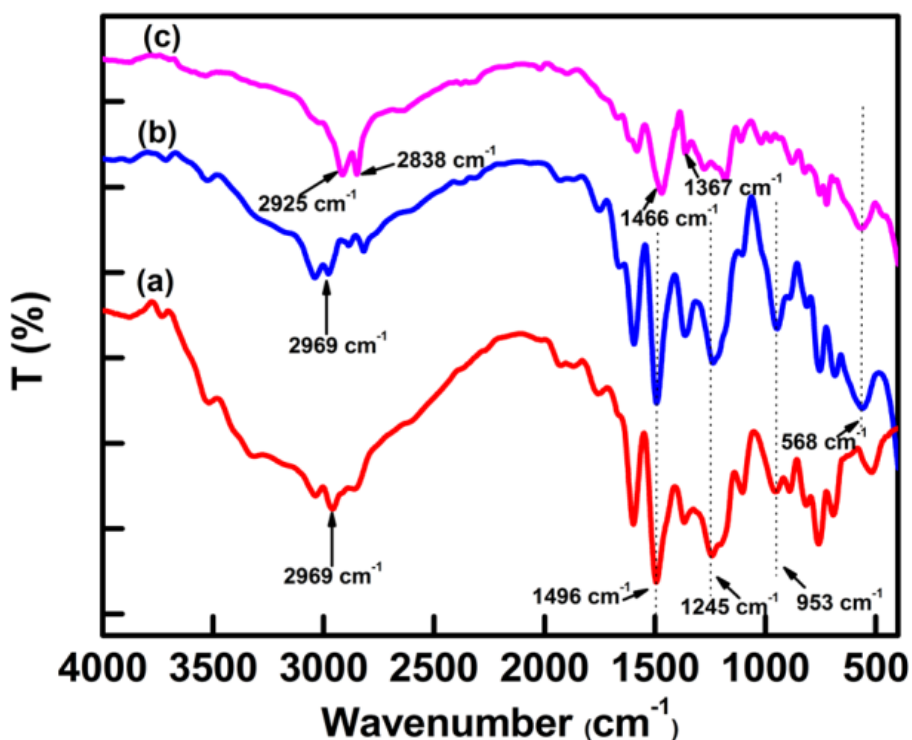
Figure 3.9 FT-IR spectra of (a) benzoxazine monomer, (b) BA-CF (70-30) nanocomposite, (c) 47.5L-5LgM-33.25PB-14.25CF composite.

3.2.2.4 Mechanical Properties

To evaluate the mechanical properties of the prepared L-LgM-PB-CF composites tensile tests and three point bending flexural tests were performed. Tensile stress-strain curves of PB, LLDPE, 47.5L-5LgM-47.5PB blend and L-LgM-PB-CF composite are shown in Figure 3.10. It was observed that pure polybenzoxazine while possessed high tensile strength (47.05 MPa) and less elongation at break (2.2%) LLDPE showed low tensile strength (16.75 MPa) and significantly more elongation at break (57.77%). Composites consists of LLDPE and PB with 5 wt% compatibilizer LgM (47.5L-5LgM-47.5PB) exhibited higher tensile strength (23.81 MPa) than pure LLDPE and more elongation at break (6.11%) than pure polybenzoxazine. This might be due to the binding role of compatibilizer (LgM), which enhanced chemical and physical interaction among the two separate phases (i.e. PB and LLDPE) [226, 236] and ultimately improved their interfacial adhesion by reducing the interfacial tension. SEM micrograph of the composite (Figure 3.11) showed the homogeneous polymeric matrix of the composite and no phase separation between PB and LLDPE in presence of LgM compatibilizer. Incorporation of CoFe$_2$O$_4$ nanoparticles in the L-LgM-PB-CF composites resulted in decrease in tensile strength of composites compare to that of 47.5L-5LgM-47.5PB blend (23.81 MPa). Tensile strength decreased slightly (from 19.92 to 18.55 MPa) with increasing CoFe$_2$O$_4$ loading (from 14.25 to 33.25 wt%) in the composition. This might be due to higher particle loading resulted in agglomeration of the particles, which caused to increase the interfacial tension. Therefore, loading stress was not easily transferred from polymer matrix to particles and ultimately tensile strength of the L-LgM-PB-CF composites decreased with increasing CoFe$_2$O$_4$ amount [256-259]. The elongation at break of the composites also decreased with increasing amount of CoFe$_2$O$_4$ nanoparticles in the composite composition. This might be the cause of decrease in tensile properties of the composites with increasing CoFe$_2$O$_4$ loading. However, tensile strengths of the composites were found to be higher than that of pure LLDPE. Tensile properties of the neat polymers and composites are summarized in Table 3.4.
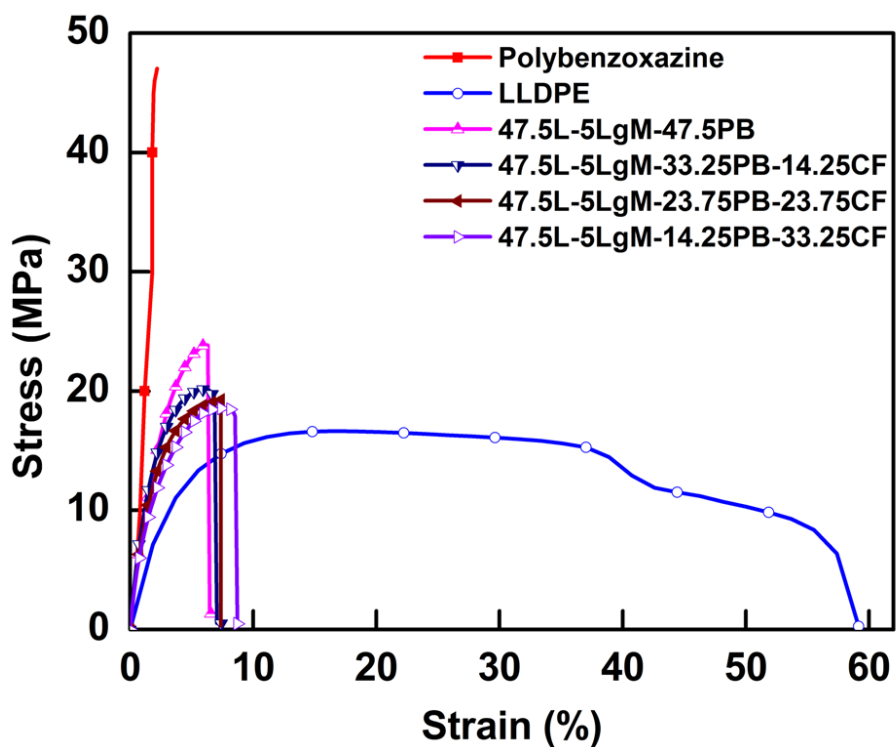
Fig 3.10 Tensile stress-strain curves of the neat polymer, blend and L-LgM-PB-CF composites.
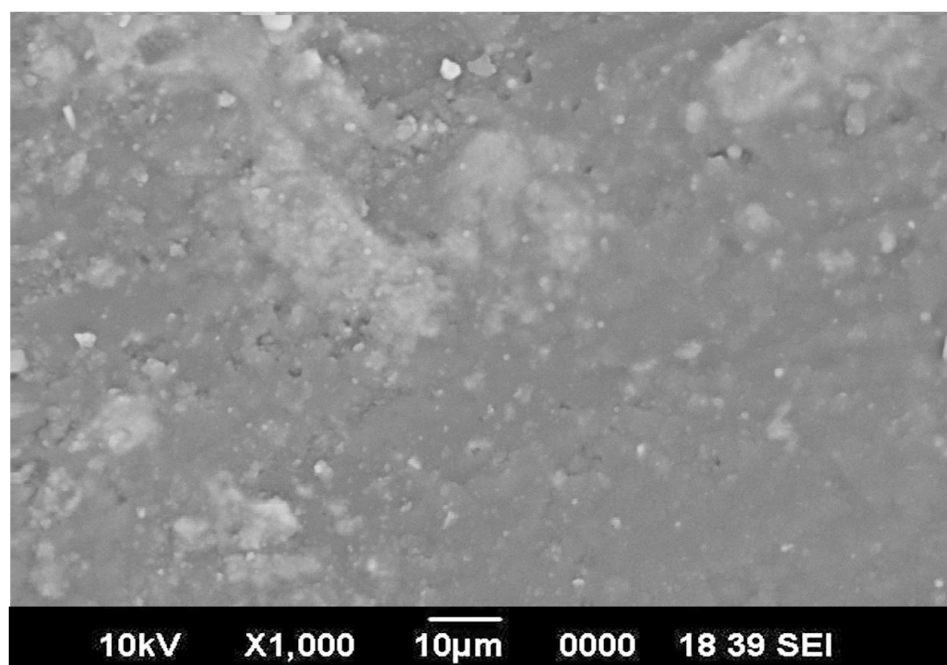
Fig 3.11 SEM micrograph of surface 47.5L-5LgM-23.75PB-23.75CF composite before tensile testing.

Table 3.4 Tensile properties of the neat polymer, blend and L-LgM-PB-CF composites.

Sample code	Tensile strength (MPa)	Tensile modulus (GPa)	Elongation at break (%)
LLDPE	16.75	0.236	57.77
Polybenzoxazine	47.05	3.6	2.2
47.5L-5LgM-47.5PB	23.81	1.071	6.11
47.5L-5LgM-33.25PB-14.25CF	19.92	1.110	8.7
47.5L-5LgM-23.75PB-23.75CF	19.16	0.981	7.4
47.5L-5LgM-14.25PB-33.25CF	18.55	0.973	6.11

From the flexural stress-strain curves (Figure 3.12) of PB, LLDPE, 47.5L-5LgM-47.5PB blend and L-LgM-PB-CF composites, it was observed that L-LgM-PB-CF composites possessed higher flexural strength than that of pure LLDPE but less than 47.5L-5LgM-47.5PB blend. However, toughness (area under the stress-strain curve) of the L-LgM-PB-CF composites was higher than that of pure polybenzoxazine, pure LLDPE, and 47.5L-5LgM-47.5PB blend. Flexural properties of the neat polymers and composites are summarized in Table 3.5.
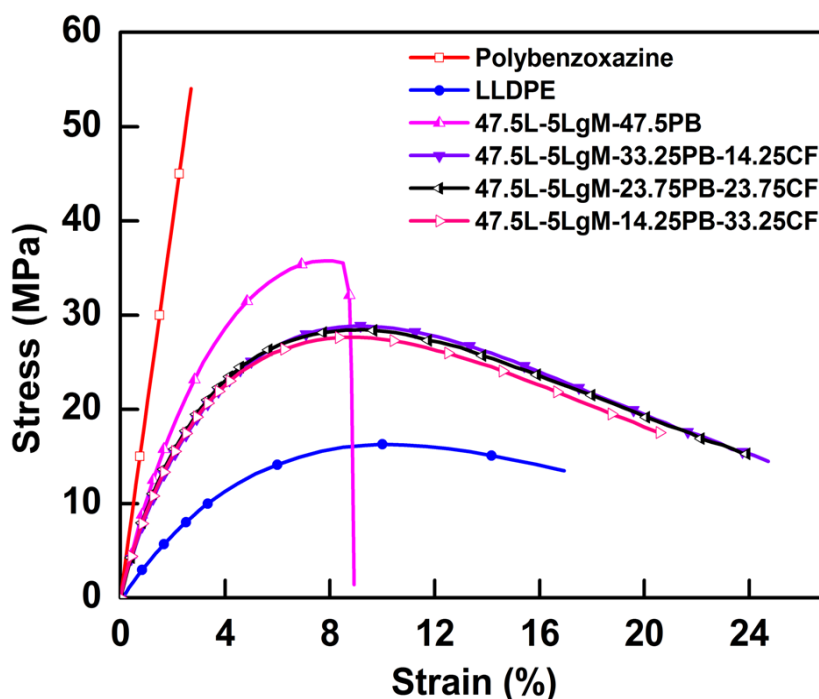
Fig 3.12 Flexural stress-strain curves of neat polymer, blend and L-LgM-PB-CF composite.

Table 3.5 Flexural properties of the neat polymer, blend and L-LgM-PB-CF composites.

Sample code	Flexural strength (MPa)	Flexural modulus (GPa)	Toughness (MPa)
LLDPE	16.33	0.403	0.274
Polybenzoxazine	54.06	1.928	0.439
47.5L-5LgM-47.5PB	35.75	1.236	0.244
47.5L-5LgM-33.25PB-14.25CF	28.70	1.184	0.535
47.5L-5LgM-23.75PB-23.75CF	28.43	1.126	0.524
47.5L-5LgM-14.25PB-33.25CF	27.67	1.102	0.479

3.2.2.5 SEM Analysis of Fractured Surfaces

The morphology of the fractured surfaces of the composites after tensile testing was investigated by SEM and is shown in Figure 3.13 (a)-(d). It was observed that for the sample composed of LLDPE, LgM and PB (47.5L-5LgM-47.5PB) fibril microstructure formed in the fractured surface during fracture under tensile strain (Figure 3.13 (a)). However, in case CoFe$_2$O$_4$ loaded composite samples, delamination of the nanoparticles from polymeric matrix occurred under tensile strain and formation of voids during breaking. This effect was pronounced for the composites having larger CoFe$_2$O$_4$ loading and large voids were observed in their fractured surfaces (Figure 3.13 (b), (c), (d)). This might be due to the high loading of CoFe$_2$O$_4$ in composite formed the agglomerates and these agglomerates pulled out from the polymeric matrix under tensile strain and formed the larger voids.
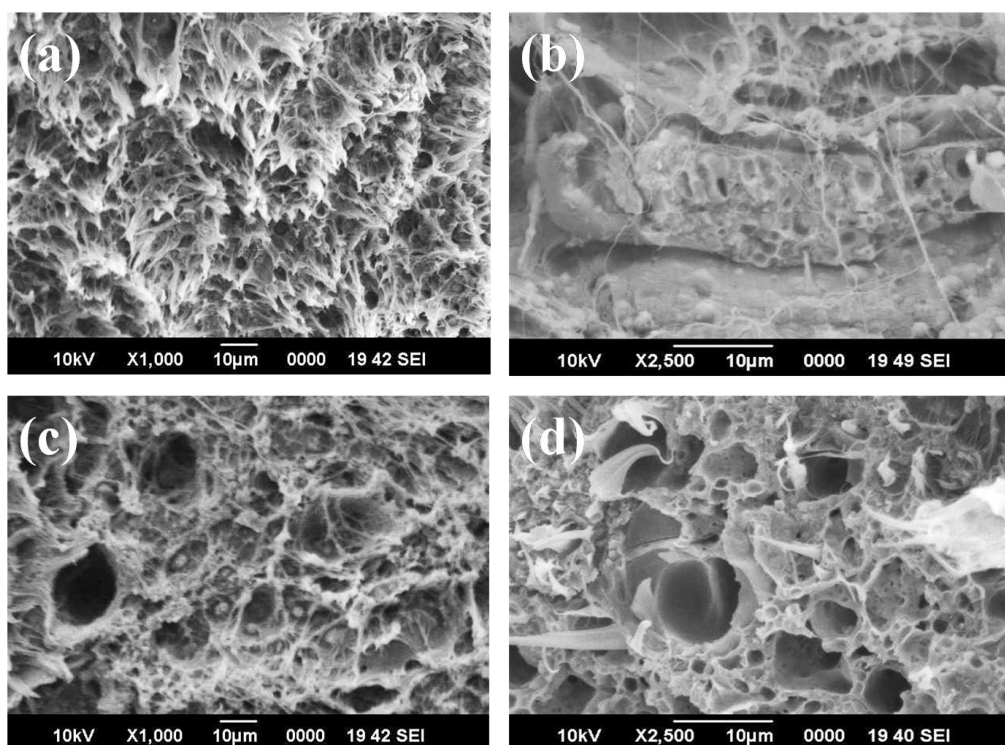
Fig 3.13 SEM micrographs of fractured surfaces of composites after tensile testing (a) 47.5L-5LgM-47.5PB composite, (b) 47.5L-5LgM-33.25PB-14.25CF composite, (c) 47.5L-5LgM-23.75PB-23.75CF composite, (d) 47.5L-5LgM-14.25PB-33.25CF composite.

3.2.2.6 Magnetization Measurement

The variation of magnetic properties, in terms of saturation magnetization (M_s) and coercivity (H_c), with the composition of composites were investigated by using a VSM at room temperature with an applied field of 15000 Oe. Figure 3.14 shows the hysteresis loops obtained for pure $CoFe_2O_4$ nanoparticles, BA-CF and series of L-LgM-PB-CF composites and the values of M_s and H_c are summarized in Table 3.6. The saturation magnetization (M_s) and coercivity (H_c) values of $CoFe_2O_4$ nanoparticles were 67.55 emu/g and 1645.24 Oe, respectively. It was observed that when $CoFe_2O_4$ nanoparticles were mixed with benzoxazine (BA-CF samples), M_s value of the samples were decreased. In the L-LgM-PB-CF composites the same trend was also observed. This decrease of M_s value with decreasing $CoFe_2O_4$ amount in the composite is quite obvious because the composites are composed of magnetic nanoparticles ($CoFe_2O_4$) and nonmagnetic polymeric matrix (LLDPE-LgM-PB). As magnetically dead polymeric matrix of the composites affect the magnetization of magnetic nanoparticles ($CoFe_2O_4$) due to quenching of the surface moment [260, 261] and also,

according to the equation $M_s = \varphi \, m_s$, where φ is the volume fraction of the CoFe$_2$O$_4$ and M_s is the saturation magnetization of pure CoFe$_2$O$_4$, the M_s of the composites depend on the loading of CoFe$_2$O$_4$ in the composite. Hence, due to the presence of nonmagnetic polymeric matrix (LLDPE-LgM-PB) the saturation magnetization of the composites has less magnetization than that of pure CoFe$_2$O$_4$ and M_s of the composites increased with increasing CoFe$_2$O$_4$ loading. Coercivity (H_c) value of the composite has found to be higher than that of pure CoFe$_2$O$_4$ nanoparticles. This might be due to the increased interparticle distance in the composite as compared to the close contact of the pure nanoparticles [262-264].

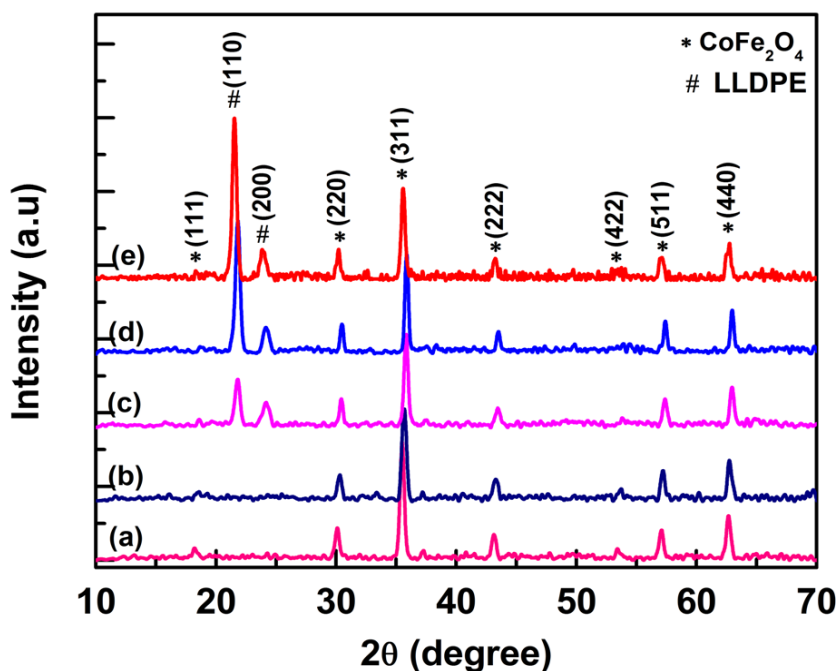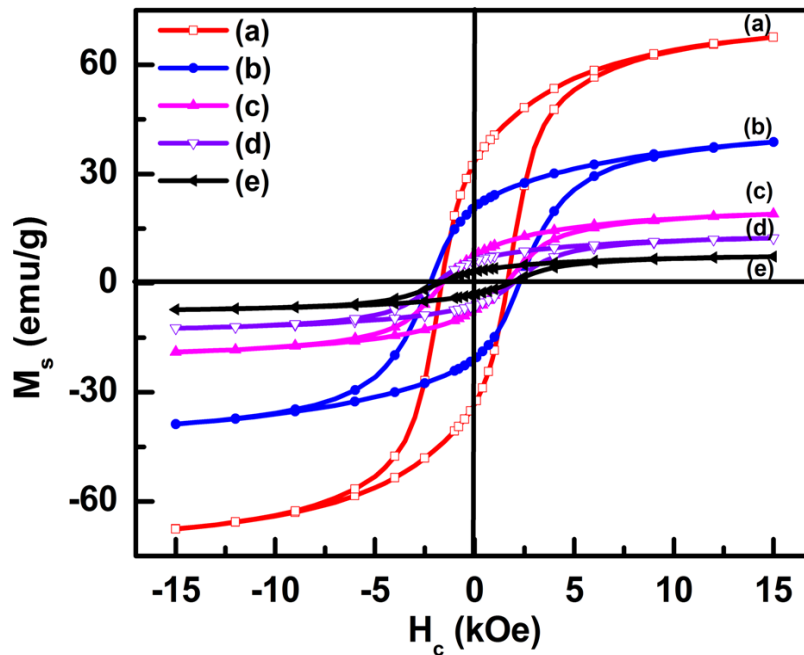Fig 3.14 Magnetization curves for (a) CoFe$_2$O$_4$ powder, (b) PB-CF (50:50) nanocomposite, (c) 47.5L-5LgM-14.25PB-33.25CF composite, (d) 47.5L-5LgM-23.75PB-23.75CF composite, (e) 47.5L-5LgM-33.25PB-14.25CF composite.

Table 3.6 Magnetic properties of BA-CF nanocomposite and L-LgM-PB-CF composites.

Sample code	M$_s$ (emu/g)	H$_c$ (Oe)
CoFe$_2$O$_4$	67.55	1645.24
PB-CF (70:30)	16.53	2056.16
PB-CF (50:50)	27.57	2134.84
PB-CF (30:70)	38.80	2243.51
47.5L-5LgM-33.25PB-14.25CF	7.24	1753.62
47.5L-5LgM-23.75PB-23.75CF	12.4	1931.95
47.5L-5LgM-14.25PB-33.25CF	18.9	1595.82

Figure 3.15 demonstrates that a sheet of L-LgM-PB-CF composite is attached with a bar magnet indicating its magnetic nature and both ends of the film can be gripped by a tweezer by easily bending it due to its mechanical flexibility. This shows that the composites reported here possess magnetic property along with mechanical flexibility.
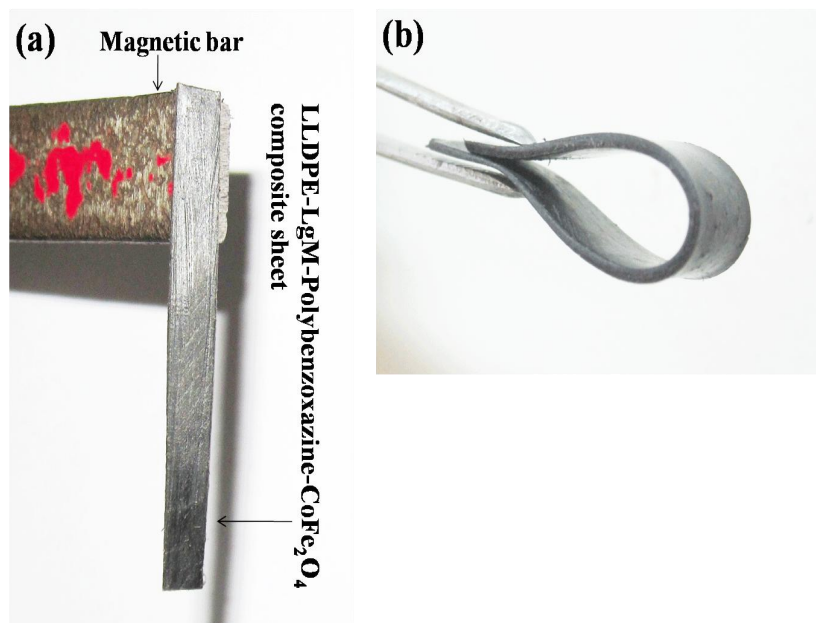
Fig 3.15 LLDPE-LgM-Polybenzoxazine-CoFe$_2$O$_4$ composite sheet exhibiting its (a) magnetic nature and (b) mechanical flexibility.

3.3 Summary of Results

1. CoFe$_2$O$_4$ nanopowder was successfully synthesized by using EDTA precursor based synthesis method.

2. Major thermal decomposition of the precursor was complete at ~400 ^{0}C.

3. Single phase CoFe$_2$O$_4$ was formed at a calcination temperature of 550 ^{0}C for 4 h in air atmosphere.

4. Average particle size of CoFe$_2$O$_4$ nanopowder was ~12 nm.

5. CoFe$_2$O$_4$ nanoparticles exhibited ferromagnetic behaviour with a coercivity (H$_c$) of 1645.24 Oe and a saturation magnetization (M$_s$) of 67.55 emu/g.

6. XRD analysis of the final composites confirmed the presence of single phase CoFe$_2$O$_4$ in the composite.

7. Prepared L-LgM-PB-CF composites showed better thermal stability than pure LLDPE.

8. Variation of CoFe$_2$O$_4$ nanoparticles loading (14.25 to 33.25 wt%) did not affect much in the tensile strength and tensile module of the composites.

9. Composites possessed higher flexural strength than that of pure LLDPE but lower than 47.5L-5LgM-47.5PB blend matrix.

10. Toughness of the L-LgM-PB-CF composites was higher than that of pure polybenzoxazine, pure LLDPE, and 47.5L-5LgM-47.5PB blend.

11. Saturation magnetization (M$_s$) value of composites decreased with decreasing CoFe$_2$O$_4$ content in the composites.

12. Value of coercivity (H$_c$) of the composites increased with decreasing amount of CoFe$_2$O$_4$ in the composites.

CHAPTER 4

Synthesis, characterization and properties of pure single phase BaFe$_{12}$O$_{19}$ and LLDPE-LgM-Polybenzoxazine-BaFe$_{12}$O$_{19}$ flexible magnetic nanocomposite

4.1 Experimental procedure for material synthesis

4.1.1 Materials used

BaCO$_3$ (99.9%), Fe(NO$_3$)$_3$·9H$_2$O (99.9%), EDTA (99.9%), NH$_4$NO$_3$ (99.9%), and nitric acid were purchased from Merck, India, and used without further purification. Ba(NO$_3$)$_2$ was prepared by dissolving BaCO$_3$ in aqueous nitric acid. Aniline, paraformaldehyde and bisphenol-A (99%, s.d. fine chem limited, India), chloroform (99.7%, Qualigens Fine Chemicals, India). Linear low density polyethylene (LLDPE, R35A042) having a density of 0.935 gm/cm^3 and melt flow index (MFI) of 4.2 gm/10 min, was obtained from GAIL (India) Ltd., and LLDPE-g-Maleic anhydride (LgM) (OPTIM E-126) with a 0.73% maleic anhydride content and MFI 2.16 gm/10 min, from Pluss Polymers Pvt, Ltd., India. All chemicals were used as received.

4.1.2 Synthesis of BaFe$_{12}$O$_{19}$ (BHF) nanopowder: [265]

BaFe$_{12}$O$_{19}$ nanoparticles were prepared by using EDTA-precursor based method. In a typical synthesis, stoichiometric amounts of barium nitrate and ferric nitrate were dissolved in distilled water according to a molar ratio of 1:12. An aqueous solution of EDTA was prepared by dissolving EDTA in hot water with dropwise addition of NH$_4$OH. After complete dissolution of EDTA, the solution was boiled to remove the excess NH$_3$. The pH of the solution was found to be ~6. To prepare precursors from various total metal ions: EDTA ratios, aqueous solutions of metal nitrates and EDTA were mixed in various molar ratios (ranging from 1:1 to 1:5). The mixtures were then stirred for 1 h at room temperature using a magnetic stirrer. Black precursors were formed when the mixtures were evaporated to dryness on a hot-plate at ~110 ^{0}C. Three to four drops of 10% NH$_4$NO$_3$ aqueous solution was added to the dried precursor powder and then the precursor powders were calcined in air for 4 h at different temperatures ranging from 450 to 850 ^{0}C to obtain barium hexaferrite

nanopowder. NH$_4$NO$_3$ was added to facilitate the oxidation of carbonaceous mass of the precursor.

4.1.3 Synthesis of Benzoxazine monomer (BA)

Benzoxazine monomer was synthesized as per the procedure described in the section 2.1.2 (Experimental procedure for material synthesis) of Chapter 2.

4.1.4 Preparation of benzoxazine-BaFe$_{12}$O$_{19}$ nanocomposites (BA-BHF) [266]

Benzoxazine-BaFe$_{12}$O$_{19}$ nanocomposite was prepared as per the procedure described in the section 3.1.4 (Experimental procedure for material synthesis) of Chapter 3. Dynamic light scattering studies indicated the average sizes of these benzoxazine coated BaFe$_{12}$O$_{19}$ nanoparticles were in the range of 121-160 nm. Various compositions of nanocomposites, prepared by using BA and BHF are listed in Table 4.1.

4.1.5 Preparation of LLDPE-LgM-PB-BHF composites (L-LgM-PB-BHF) [266]

LLDPE-LgM-PB-BHF composite was prepared as per the procedure described in the section 3.1.5 (Experimental procedure for material synthesis) of Chapter 3. Composites, having different compositions of BHF, PB and LLDPE, were prepared as listed in Table 4.1.

Table 4.1 Compositions of prepared BA-BHF and L-LgM-PB-BHF composites.

Sample code	LLDPE (wt%)	LgM (wt%)	PB (wt%)	BaFe$_{12}$O$_{19}$ (wt%)
BA-BHF (70:30)	--	--	70	30
BA-BHF (50:50)	--	--	50	50
BA-BHF (30:70)	--	--	30	70
47.5L-5LgM-47.5PB	47.5	5	47.5	--
47.5L-5LgM-33.25PB-14.25BHF	47.5	5	33.25	14.25
47.5L-5LgM-23.75PB-23.75BHF	47.5	5	23.75	23.75
47.5L-5LgM-14.25PB-33.25BHF	47.5	5	14.25	33.25

SEM micrograph of the surface of a cross section of the composites (Figure 4.1) shows that polybenzoxazine coated BaFe$_{12}$O$_{19}$ nanoparticles are embedded within the polymeric matrix.
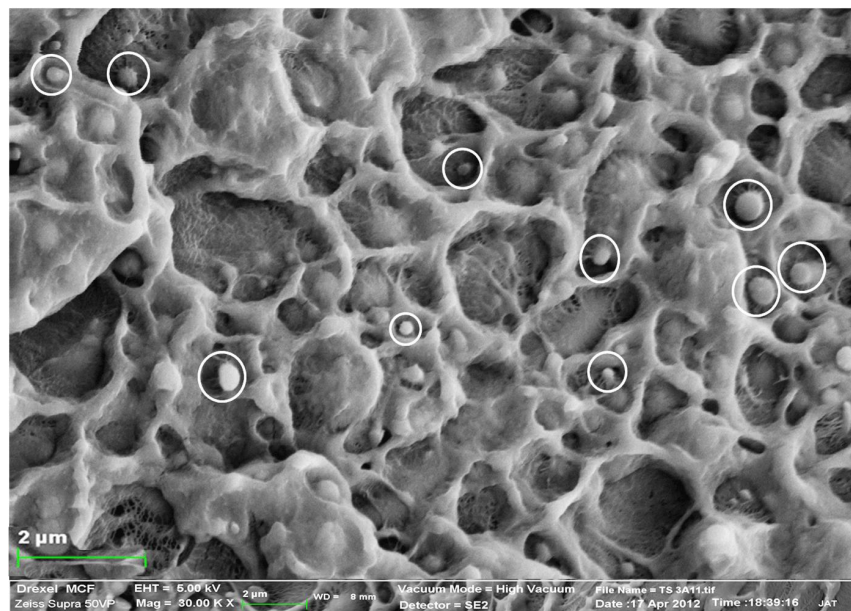
Fig 4.1 SEM micrograph of the composites shows that BaFe$_{12}$O$_{19}$ nanoparticles are dispersed within the polymeric matrix. Polybenzoxazine coated BaFe$_{12}$O$_{19}$ nanoparticles are marked within the circle.

4.2 Results and Discussion

4.2.1 Characterization of BaFe$_{12}$O$_{19}$ nanoparticles

4.2.1.1 Thermal Analysis

TGA and DSC analyses were performed to investigate the decomposition behavior of the precursor powder due to heat treatment in air and thermogram is shown in Figure 4.2. The TGA thermogram revealed that a total weight loss of ~88% occurred in two steps when the precursor powder was heated from 40 to 900 ^{0}C in air. Initially ~8% weight loss occurred between 40 and 180 ^{0}C due to the loss of moisture from the sample; ~80% weight loss was observed in the range of 200 to 450 ^{0}C. This may have been due to the thermo-oxidative decomposition of precursor and evolution of CO$_2$ and NO$_X$ gases. This decomposition was also reflected in the DSC thermogram, as shown in Figure 4.2, where an exothermic peak was observed at 435 ^{0}C. Heating the sample beyond 450 ^{0}C did not result in any further weight loss in TGA. Thus it can be assumed that decomposition of carbonaceous content of the precursor occurred in between 200 and 450 ^{0}C.
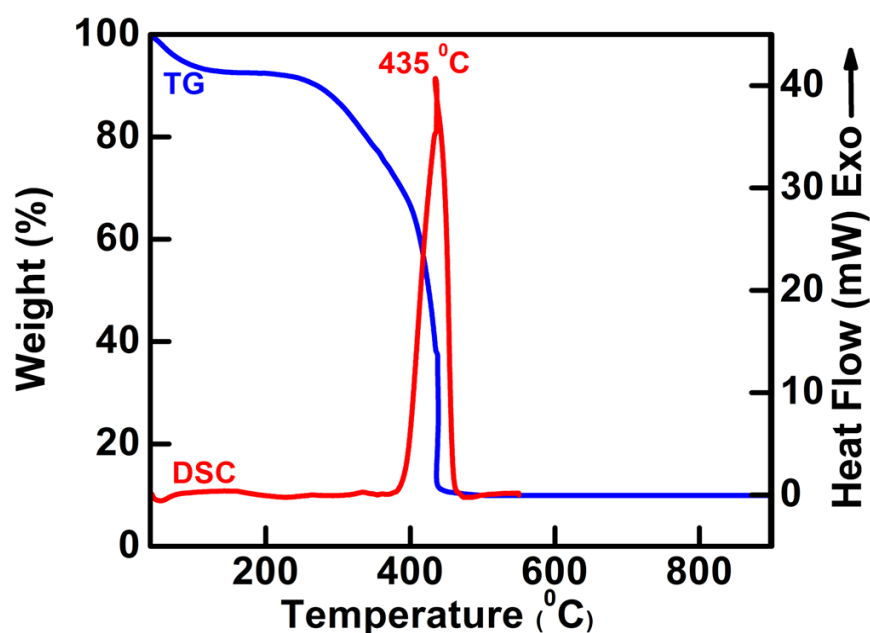
Fig 4.2 TGA-DSC thermograms of BaFe$_{12}$O$_{19}$ precursor.

4.2.1.2 X-Ray Diffraction Analysis

In order to determine the optimum condition (total metal ion: EDTA ratio and calcination temperature) to prepare single-phase nanosized BaFe$_{12}$O$_{19}$, room temperature powder XRD analysis of the calcined powders was performed. It was observed that, precursor powders were amorphous in nature and BaFe$_{12}$O$_{19}$ phase started to form when calcination temperature was 650 ^{0}C (Figure 4.3 (A)). For all the calcined powders the diffraction peaks corresponding to the (110), (008), (107), (114), (203), (205), (206), (217), (2011), (220), and (2014) diffraction planes of barium hexaferrite were present [JCPDS 84-0757] in the X-Ray diffractogram. The increase in peak intensities with increasing calcination temperature occurred due to the increase in crystallinity and crystallite size during the calcination process. The crystallite size of the calcined powders was calculated using X-ray peak broadening of the diffraction peaks (107) using Scherrer's formula [238] and are summarized in Table 4.2. It is important to note that peaks corresponding to α-Fe$_2$O$_3$ (hematite, as an impurity phase) were detected for the calcined powders obtained from the precursors prepared with total metal ions and EDTA molar ratio ranging from 1:1 to 1:4 (Figure 4.3 (B)) and when the calcination temperatures were lower than 850 ^{0}C (Figure 4.3 (A)). When the total metal ion: EDTA ratio was 1:5, formation of the pure single-phase barium hexaferrite occurred at a calcination temperature of 850 ^{0}C (Figure 4.3 (B)).
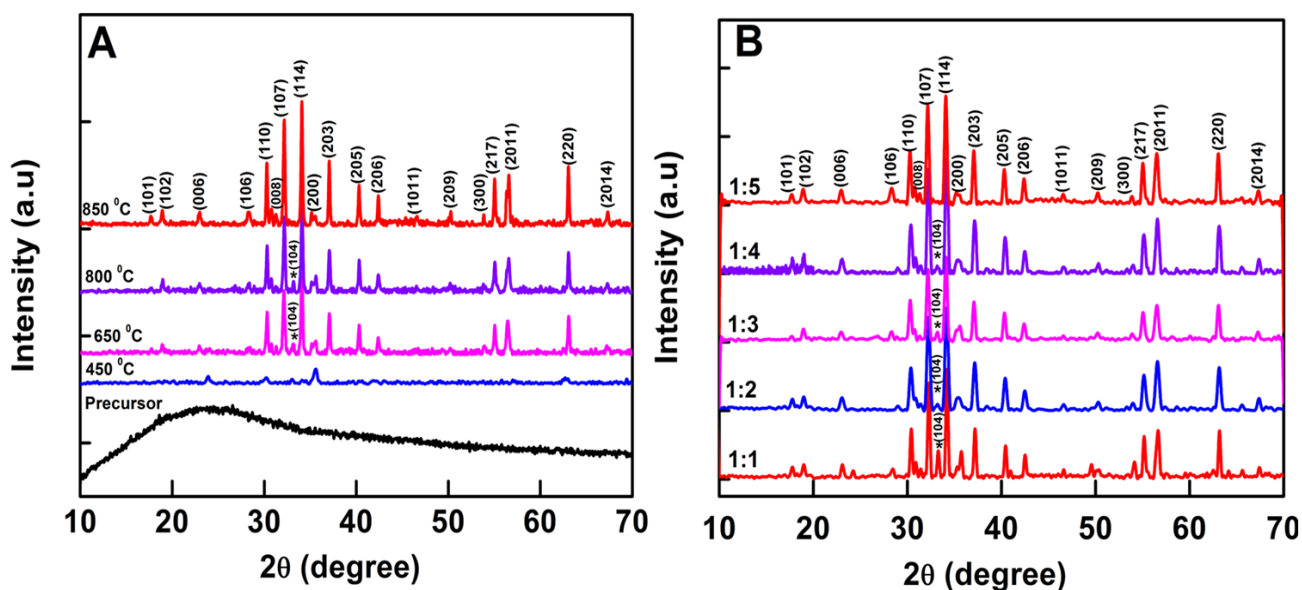
Fig 4.3 **(A)** XRD spectra of the barium hexaferrite powders obtained by using precursors with metal ion: EDTA molar ratio of 1:5 and calcined at specified temperatures. Impurity peak of hematite marked with asterisk [JCPDS 80-2377]. The absence of any impurity phase is clearly observed at 850 ^{0}C. **(B)** Room-temperature XRD spectra of the calcined powders prepared from different precursors (total metal ion: EDTA ratio ranging from 1:1 to 1:5) by calcining at 850 ^{0}C. Impurity peak of hematite marked with asterisk [JCPDS 80-2377]. The absence of any impurity phase is clearly observed for the 1:5 ratio.

Table 4.2 Crystallite size of BaFe$_{12}$O$_{19}$ at different calcination temperatures.

Calcination temperature (^{0}C)	Crystallite size (nm)
650	32.9
750	33.0
850	34.9

4.2.1.3 Particle Size and TEM Analysis of BaFe$_{12}$O$_{19}$ nanopowder

The intensity-weighted particle size distribution of the as-synthesized BaFe$_{12}$O$_{19}$ nanopowder (obtained by calcining the precursor at 850 ^{0}C), obtained from DLS study at 30 ^{0}C (Figure 4.4 (a)), exhibited a single particle size distribution with the peak average at 9.6 ± 3.9 nm and cumulant mean diameter 14.8 nm with a polydespersity index of 0.123. Figure 4.4 (b) illustrated an HRTEM micrograph of the calcined powder where the average particle size was estimated to be ~20 nm.
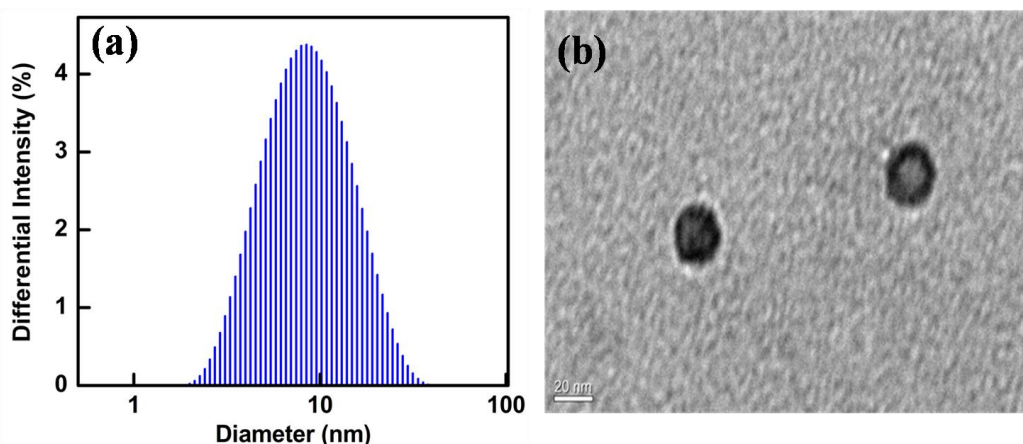
Fig 4.4 (a) Particle size distribution and (b) HRTEM micrograph of synthesized $BaFe_{12}O_{19}$ nanopowder.

4.2.1.4 Magnetization Measurement

Room-temperature magnetization curve for the synthesized $BaFe_{12}O_{19}$ nanopowder was obtained by using VSM with an applied field of 15000 Oe as shown in Figure 4.5. The magnetic property measurement yielded coercivity (H_c) of 4913.94 Oe and a saturation magnetization (M_s) of 56.50 emu/g. The coercivity and saturation magnetization values are comparable with the values reported by other authors using different $BaFe_{12}O_{19}$ preparation techniques. The variations in the magnetic properties of $BaFe_{12}O_{19}$, obtained by different synthesis routes, are summarized in Table 4.3. In the present case M_s (56.50 emu/g) and H_c (4913.94 Oe) values of the synthesized barium hexaferrite nanopowder were found to be lower than the theoretical values of M_s (72 emu/g) and H_c (6700 Oe) for the single crystal of $BaFe_{12}O_{19}$ [267, 268]. Several reasons, such as size effects, spincanting phenomenon, particle size effect, and others, have been proposed by Junliang et al. to explain the lowering of saturation magnetization values of nanoparticles [269]. The critical domain size of $BaFe_{12}O_{19}$, as estimated by several researchers, is ~1 μm [270-272]. In the current case, the smaller size of the synthesized $BaFe_{12}O_{19}$ nanoparticle (average particle size ~20 nm) plays a critical role for the observed lower values of M_s. However, the H_c value of the synthesized $BaFe_{12}O_{19}$ was found to be comparatively higher than that of most of the reported values (Table 4.3).
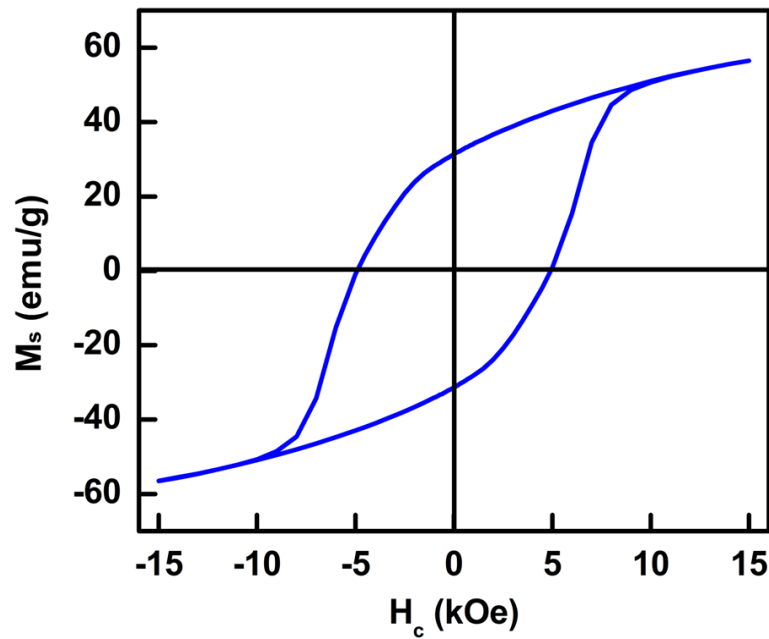
Fig 4.5 Room-temperature hysteresis loop for BaFe$_{12}$O$_{19}$ nanopowder.

Table 4.3 Comparison of M$_s$ and H$_c$ of BaFe$_{12}$O$_{19}$ particles prepared by different synthetic methods.

Synthesis Method	M$_s$ (emu/g)	H$_c$ (Oe)	Reference
Aerosol derived precursor	51.9-56.5	2000-2600	[273]
Microwave-assisted sol-gel Auto-combustion	64.1	1000	[274]
Sol-gel combustion	~ 60 Am^2/kg	------	[275]
Auto combustion	43-55	2587-5000	[276]
Sol-gel autocombustion	58.57-60.13 Am^2/kg	415-433 kA/m	[277]
Co precipitation	2.3-57	-----	[278]
Co precipitation	60.175	860	[279]
Acetate precursor method	52	2600	[280]
Sugar-nitrate precursor process	42.34	1624.9	[281]
Hydrothermal.	40 Am^2/kg	0.096x10^6 A/m	[282]
Reverse microemulsion	54.5-64.3	3357.2-5483.3	[283]
Aerosol pyrolysis	50	5600	[284]

Mechano-combustion	67.1	493.5 kA/m	[285]
Molten salt	65.8	5251	[286]
Solid state	34.44-59.38	2159-3598	[287]
Pyrolysis of aerosol	5.7-75.5	1325-5470	[288]
EDTA precursor route	**56.50**	**4913.94**	**This work [265]**

4.2.2 Characterization of BA-BHF nanocomposite and L-LgM-PB-BHF composites

4.2.2.1 X-Ray Diffraction Analysis

Room temperature XRD spectra of calcined powder and their different composition of composite are shown in Figure 4.6. X-Ray diffratogram of PB-BHF samples exhibited only the characteristic peaks of BHF were present in PB-BHF composites (Figure 4.6 (b)). X-Ray diffratogram of final composites, composed of LLDPE, PB, LgM and BHF (L-LgM-PB-BHF), showed the present of BHF peaks along with the peaks of LLDPE (at $2\theta = 21.6^0$ and 23.8^0 for (110) and (200) planes respectively [223, 224, 227]) (Figure 4.6 (c), (d), (e)). As in the X-Ray diffratograms of the final composites only the peaks, which are characteristics of the constituents BHF and LLDPE were present and no extra peak was observed, it was confirmed that during preparation of composite no impurity phase was formed by the interaction of polymeric matrix and ferrite nanoparticles.
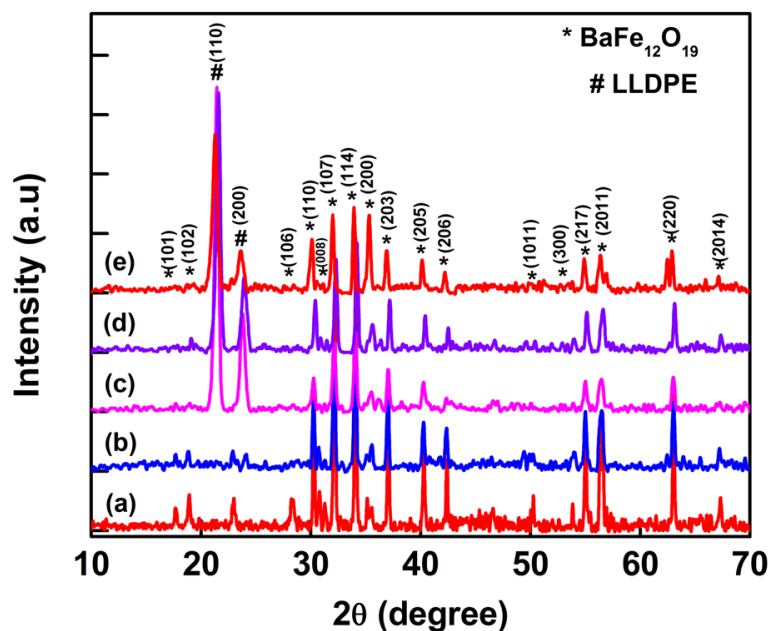
Fig 4.6 XRD spectra of (a) BaFe$_{12}$O$_{19}$ nanopowder, (b) PB-BHF (50:50) nanocomposite, (c) 47.5L-5LgM-14.25PB-33.25BHF composite, (d) 47.5L-5LgM-23.75PB-23.75BHF composite, (e) 47.5L-5LgM-33.25PB-14.25BHF composite. (* BaFe$_{12}$O$_{19}$ and # LLDPE)

4.2.2.2 Thermal Analysis

In the DSC thermogram of pure benzoxazine monomer (BA) (Figure 4.7 (a)) an exothermic peak (at ~205 ^{0}C) within the temperature range of 175 to 245 ^{0}C was observed indicating the thermal curing of BA occurred in this temperature [228-231]. When BHF were mixed with BA the exothermic curing peak of BA shifted to the lower temperature. For example, when 50 wt% BHF was mixed with 50 wt% BA this peak was found at ~181 ^{0}C (Figure 4.7 (b)). This fact indicated that BHF might catalyze the thermal curing of BA and lower the curing temperature [251, 252]. In the DSC thermogram of pure LLDPE (Figure 4.7 (c)) an endothermic peak at ~124 ^{0}C, corresponding to its melting temperature [227] and an exothermic peak at ~224 ^{0}C, which may be attributed to the beginning of the thermal oxidative decomposition of LLDPE were observed [232, 233]. In case of PB containing LLDPE composites (47.5L-5LgM-47.5PB) (Figure 4.7 (d)) beginning of thermal oxidative decomposition occurred at ~283 ^{0}C, which is higher than that of pure LLDPE. These facts indicated that the presence of PB enhanced the thermal stability of LLDPE-LgM-PB composites. However, presence of BHF slightly lowered the thermal oxidative decomposition temperature of the composite (~254 ^{0}C) (Figure 4.7 (e)). This might be due to the catalytic effect of BHF on thermal degradation of polymeric matrix [251, 252]. In the DSC curves of final composites (L-LgM-PB-BHF) (Figure 4.7 (e)), the endothermic peak at ~124 ^{0}C, corresponding to the melting temperature of LLDPE was present. The exothermic peak of thermal curing of BA was not observed, which indicated that in the final composites all BA monomers polymerized to PB during processing at 200 ^{0}C.
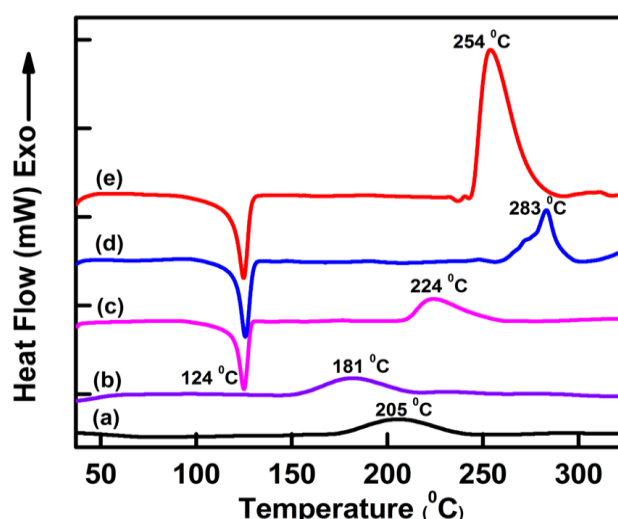
Fig 4.7 DSC thermogram of (a) benzoxazine monomer, (b) BA-BHF (50:50) nanocomposite, (c) LLDPE, (d) 47.5L-5LgM-47.5PB composite, (e) 47.5L-5LgM-23.75PB-23.75BHF composite.

71

From TGA thermal stability of the composites was determined. Temperatures for 5% weight loss (T$_{5\%}$), 10% weight loss (T$_{10\%}$) and char yields (%) at 800 ^{0}C in air for pure PB, LLDPE and composites are listed in Table 4.4 It was observed that the temperature at 5 and 10% weight loss was found to be decrease with increasing BaFe$_{12}$O$_{19}$ content in the composites. This may be due catalytic effect of BaFe$_{12}$O$_{19}$ on thermal degradation of polymeric matrix [251, 252]. TGA thermograms of LLDPE, PB, BA-BHF and L-LgM-PB-BHF composite are shown in Figure 4.8. These thermograms revealed that presence of PB enhances the overall thermal stability of the composites. The thermal stability of the composite was found to be more than pure LLDPE but less than pure polybenzoxazine. The degradation of all the L-LgM-PB-BHF composites was found in the temperature range of 325-525 ^{0}C. The char yield at 800 ^{0}C of the composite was found to increase with increasing BaFe$_{12}$O$_{19}$ content. However, as the melting temperature of LLDPE is ~124 ^{0}C the composites should be used below this temperature.
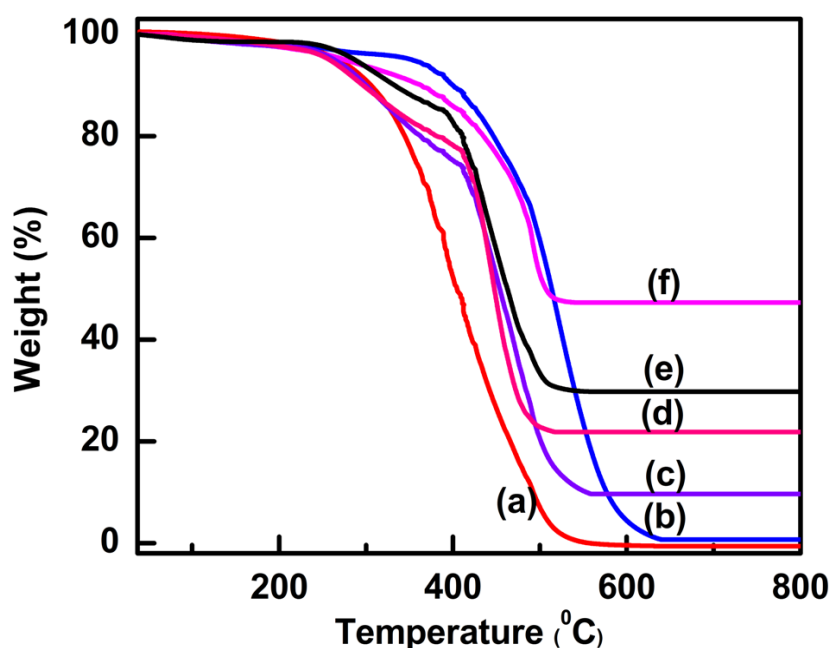
Fig 4.8 Thermograms (TGA) of (a) LLDPE, (b) Polybenzoxazine, (c) 47.5L-5LgM-33.25PB-14.25BHF composite, (d) 47.5L-5LgM-23.75PB-23.75BHF composite, (e) 47.5L-5LgM-14.25PB-33.25BHF composite, (f) PB-BHF (50:50) nanocomposite.

Table 4.4 Thermal properties of neat polymer and BA-BHF nanocomposite and L-LgM-PB-BHF composite.

Sample code	T$_{5\%}$ (^{0}C)	T$_{10\%}$ (^{0}C)	char yield (%) at 800 ^{0}C
Polybenzoxazine	350	400	0
LLDPE	267	305	0
47.5L-5LgM-47.5PB	306	345	0
PB-BHF (70:30)	313	378	26
PB-BHF (50:50)	299	369	45
PB-BHF (30:70)	290	358	65
47.5L-5LgM-33.25PB-14.25BHF	286	318	10
47.5L-5LgM-23.75PB-23.75BHF	272	316	22
47.5L-5LgM-14.25PB-33.25BHF	265	310	30

4.2.2.3 FT-IR Analysis

In the FT-IR spectra of pure BA (Figure 4.9 (a)) the characteristic peaks for tri-substituted benzene ring at 945 and 1497 cm^{-1} and the asymmetric stretching band of C-O-C at 1238 cm^{-1} were observed [222, 234]. The methyl group vibration was found at 2971 cm^{-1} [235]. In case of BA-BHF nanocomposite (Figure 4.9 (b)) a peak at ~588 cm^{-1}, corresponding to M-O stretching of BHF was observed [253-255] along with the characteristic peaks of BA. In the FT-IR spectra of final composites (Figure 4.9 (c)), L-LgM-PB-BHF following features were observed (i) disappearance of the characteristic peaks of benzoxazine monomer (at 945 and 1497 cm^{-1}) and appearance of a peak at 1474 cm^{-1}, which can be attributed to the tetra-substituted benzene ring of polybenzoxazine (PB) [181]. This fact indicated that BA monomer of BA-BHF polymerized to PB during preparation of final composite at 200 ^{0}C, (ii) peaks at 1364 cm^{-1} (-CH$_3$ stretching vibration) and 2898 and 2839 cm^{-1} (C-H symmetric vibration), which are characteristic peaks of LLDPE were present [227], (iii) a peak at ~588 cm^{-1} for M-O stretching of BHF was present.
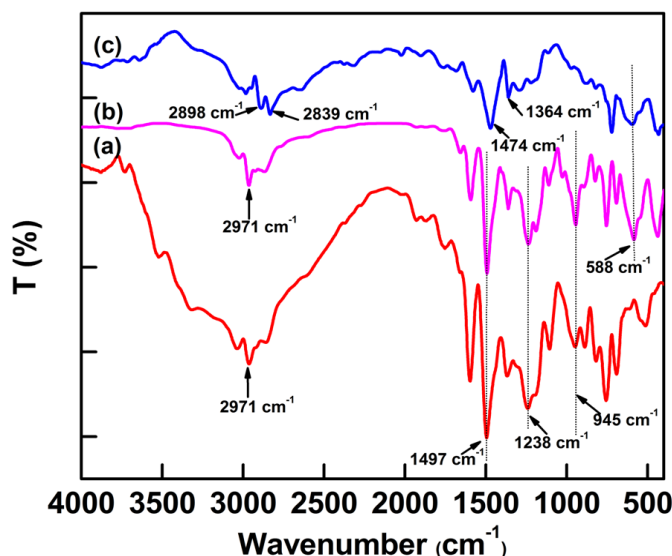
Fig 4.9 FT-IR spectra of (a) benzoxazine monomer, (b) BA-BHF (70-30) nanocomposite, (c) 47.5L-5LgM-33.25PB-14.25BHF composite.

4.2.2.4 Mechanical Properties

Tensile tests and three point bending flexural tests were performed to determine the mechanical properties of the composites. From tensile tests it was observed that, pure polybenzoxazine possessed higher tensile strength (47.05 MPa) and lesser elongation at break (2.2%) in comparison with LLDPE (with tensile strength of 16.75 MPa and 57.77% elongation at break). The blend, composed of 47.5 wt% LLDPE, 47.5 wt% PB and 5 wt% LgM compatibilizer (47.5L-5LgM-47.5PB) exhibited higher tensile strength (23.81 MPa) than pure LLDPE and more elongation at break (6.11%) than pure polybenzoxazine (Figure 4.10). In our previous study we have observed that, presence of an optimum amount of 5 wt% compatibilizer LgM in the blend of 47.5 wt% PB and 47.5 wt% LLDPE significantly enhances the tensile and flexural strength of composites [226]. This might be due to the fact that in the composites polar functional groups of LgM interact with polar functional groups of PB while the LLDPE backbone of LgM compatibilize with LLDPE [236]. This interaction improves the interfacial adhesion between the two separate phases (i.e. PB and LLDPE). SEM micrograph of the composite (Figure 4.11) also showed the homogenous polymeric matrix of composite and no phase separation between PB and LLDPE in presence of LgM compatibilizer. From tensile stress-strain graphs of the final composites their tensile properties were determined (Figure 4.10). Tensile properties of pure LLDPE, pure PB and BaFe$_{12}$O$_{19}$ nanoparticle containing composites are summarized in Table 4.5. It was observed that loading of 14.25 wt% BaFe$_{12}$O$_{19}$ nanoparticle in polymeric matrix (47.5L-5LgM-

33.25PB-14.25BHF) resulted in increase of elongation at break in comparison with 47.5L-5LgM-47.5PB, but decrease in tensile strength. When $BaFe_{12}O_{19}$ nanoparticle content in the composite is high, nanoparticles act as defects [289] and the higher concentration of defects caused by the higher concentration of $BaFe_{12}O_{19}$ nanoparticles resulted in decrease in tensile strength. However, variation of loading level of $BaFe_{12}O_{19}$ nanoparticle (from 14.25 to 33.25 wt%) did not affect much in the tensile strength (varies from 18.50 to 17.55 MPa) and tensile modulus of the composites (0.892 to 0.803 GPa). This might be due to the fact that in the present case the amount of nanoparticle loading in the polymeric matrix of composite is very high.
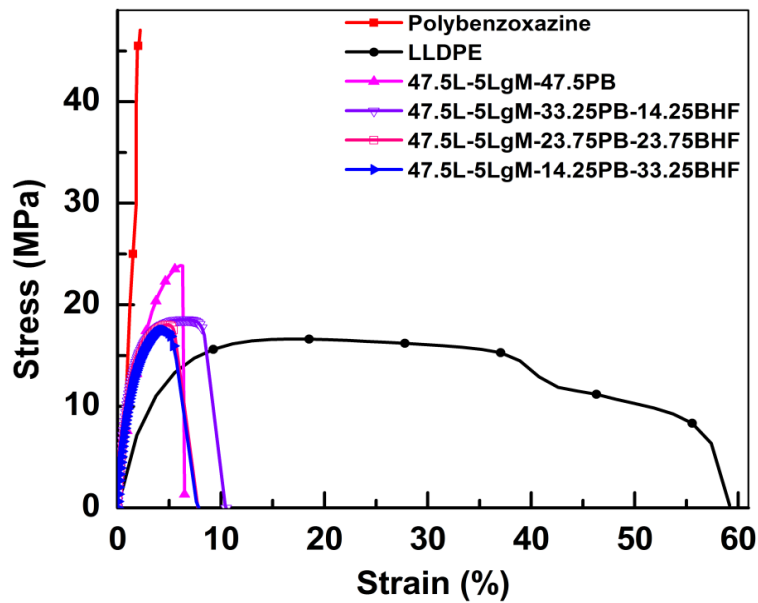
Fig 4.10 Tensile stress-strain curves of neat polymer, blend and L-LgM-PB-BHF composites.
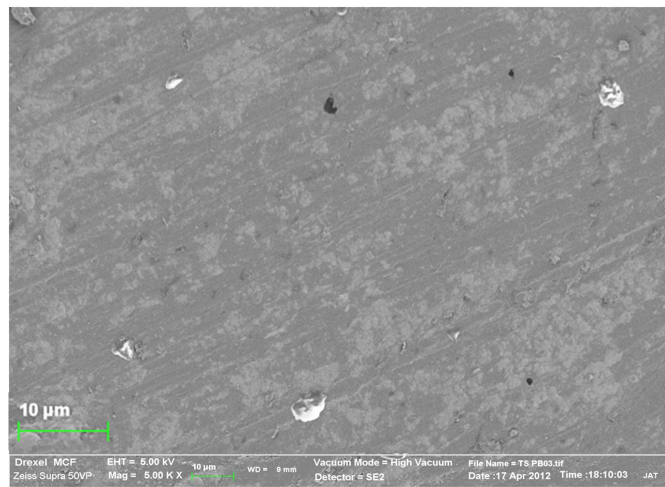
Fig 4.11 SEM micrograph of surface 47.5L-5LgM-23.75PB-23.75BHF composite before tensile testing.

Table 4.5 Tensile properties of the neat polymer and L-LgM-PB-BHF composite.

Sample code	Tensile strength (MPa)	Tensile modulus (GPa)	Elongation at break (%)
LLDPE	16.75	0.236	57.77
Polybenzoxazine	47.05	3.6	2.2
47.5L-5LgM-47.5PB	23.81	1.071	6.11
47.5L-5LgM-33.25PB-14.25BHF	18.50	0.892	10.41
47.5L-5LgM-23.75PB-23.75BHF	18.00	0.864	7.7
47.5L-5LgM-14.25PB-33.25BHF	17.55	0.803	7.6

Flexural strength and flexural modulus of the BaFe$_{12}$O$_{19}$ incorporated composites have been found to be higher than that of pure LLDPE but less than that of pure polybenzoxazine and 47.5L-5LgM-47.5PB (Figure 4.12). Flexural properties of composites are listed in Table 4.6. L-LgM-PB-BHF composites possess higher flexural strength than that of pure LLDPE but less than 47.5L-5LgM-47.5PB. However, toughness (i.e. area under the stress-strain curve) of the L-LgM-PB-BHF composites was found to be higher than that of pure LLDPE, pure polybenzoxazine and 47.5L-5LgM-47.5PB. Decrease in flexural strength (28.20 to 25.41 MPa) was observed with increasing loading level of BaFe$_{12}$O$_{19}$ nanoparticle (14.25 to 33.25 wt%) in the composite, where as slight decrease in flexural modulus (1.035 to 0.917 GPa) and toughness (0.533 to 0.460 MPa) was observed (Table 4.6).
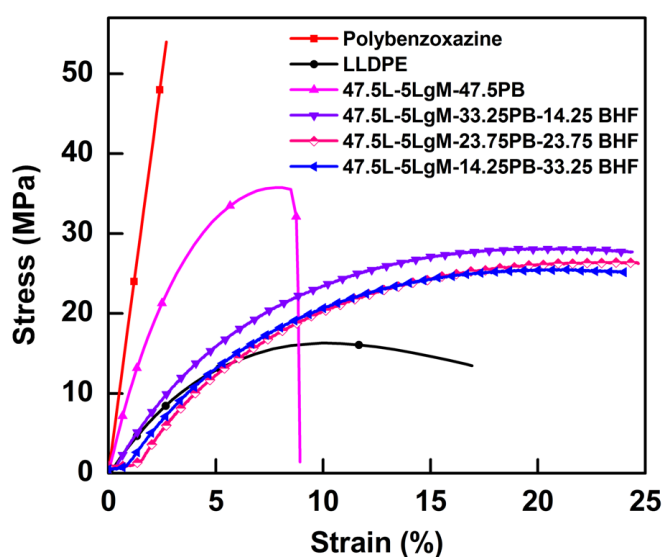
Fig 4.12 Flexural stress-strain curves of neat polymer, blend and L-LgM-PB-BHF composites.

Table 4.6 Flexural properties of the neat polymer and L-LgM-PB-BHF composites.

Sample code	Flexural strength (MPa)	Flexural modulus (GPa)	Toughness (MPa)
LLDPE	16.33	0.403	0.274
Polybenzoxazine	54.06	1.928	0.439
47.5L-5LgM-47.5PB	35.75	1.236	0.244
47.5L-5LgM-33.25PB-14.25BHF	28.20	1.035	0.533
47.5L-5LgM-23.75PB-23.75BHF	26.31	0.955	0.473
47.5L-5LgM-14.25PB-33.25BHF	25.41	0.917	0.460

4.2.2.5 SEM Analysis of Fractured Surfaces

Figure 4.13 represents the micrographs of fractured surfaces of the composites after tensile test. It was observed that for the sample composed of LLDPE, LgM and PB (47.5L-5LgM-47.5PB), fibril microstructure formed in the fractured surface during fracture under tensile strain (Figure 4.13 (a)). But for BaFe$_{12}$O$_{19}$ loaded composite samples voids were formed due to delamination of BHF from polymeric matrix (Figure 4.13 (b), (c), (d)). With increasing BaFe$_{12}$O$_{19}$ content in the composites larger void formation (~10µm) occurred. This might be due to the fact that when BHF loading is high in the composite, they formed agglomerates and when these agglomerates pulled out from polymeric matrix large voids formed. This type of void formation was not observed for the samples (47.5L-5LgM-47.5PB) which did not contain any BaFe$_{12}$O$_{19}$.
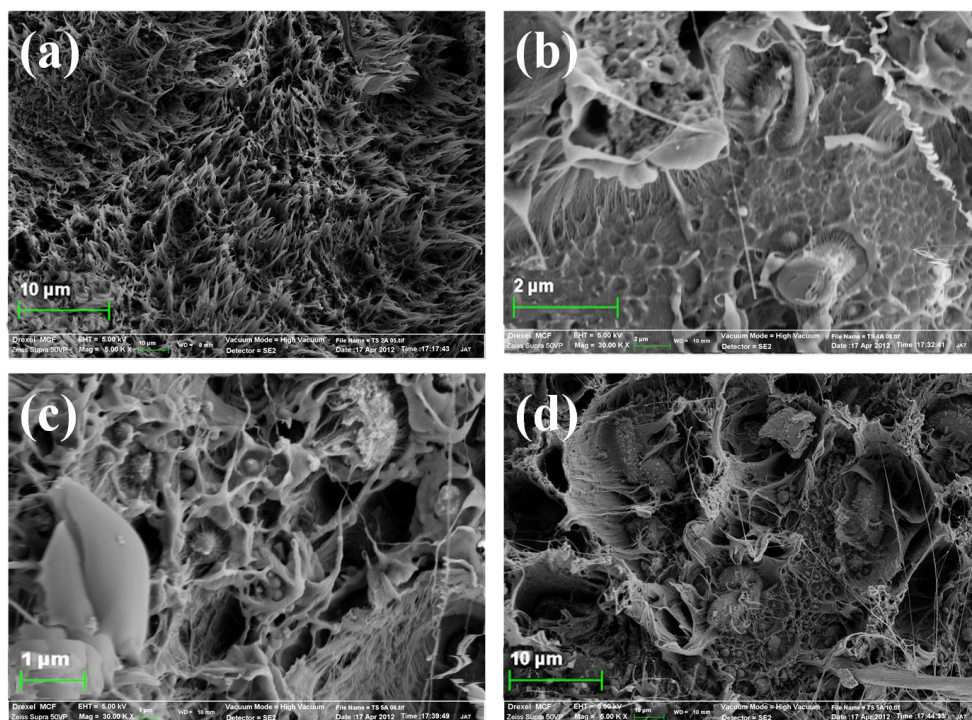
Fig 4.13 SEM micrographs of fractured surfaces of composites after tensile testing (a) 47.5L-5LgM-47.5PB composite, (b) 47.5L-5LgM-33.25PB-14.25BHF composite, (c) 47.5L-5LgM-23.75PB-23.75BHF composite, (d) 47.5L-5LgM-14.25PB-33.25BHF composite.

4.2.2.6 Magnetization Measurement

The variations of magnetic properties, such as saturation magnetization (M_s) and coercivity (H_c) with changing composition of the composites were investigated by VSM at room temperature with applied field of 15000 Oe. The M_s and H_c values of the pure BaFe$_{12}$O$_{19}$ and their composites are listed in Table 4.7. In general it was observed that in BaFe$_{12}$O$_{19}$ containing composites the values of M_s decreased with decreasing BaFe$_{12}$O$_{19}$ loading. This is quite obvious, because the composites are composed of magnetic nanoparticles (BaFe$_{12}$O$_{19}$) and nonmagnetic polymeric matrix (LLDPE-LgM-PB). As magnetically dead polymeric matrix of the composites affect the magnetization of magnetic nanoparticles (BaFe$_{12}$O$_{19}$) due to quenching of the surface moment [260, 261] and also, according to the equation $M_s = \varphi \, m_s$, where φ is the volume fraction of the BaFe$_{12}$O$_{19}$ and M_s is the saturation magnetization of pure BaFe$_{12}$O$_{19}$, the M_s of the composites depend on the loading of BaFe$_{12}$O$_{19}$ in the composite. Hence, due to the presence of nonmagnetic polymeric matrix (LLDPE-LgM-PB) the saturation magnetization of the composites has less magnetization than that of pure BaFe$_{12}$O$_{19}$ and M_s of the composites increased with increasing BaFe$_{12}$O$_{19}$ loading. Magnetic

78

hysteresis loops of pure BaFe$_{12}$O$_{19}$ their composites are shown in Figure 4.14. Interestingly it was observed that BaFe$_{12}$O$_{19}$ containing composites the value of H$_c$ decreased with decreasing amount of BHF in the composites. For example, H$_c$ of pure BaFe$_{12}$O$_{19}$ and 14.25 wt% BaFe$_{12}$O$_{19}$ containing composites are 4913.94 and 2992.39 Oe respectively. This might be due to the fact that as coercivity is dependent on surface anisotropy and interparticle interactions, the coating of polymeric matrix on the BaFe$_{12}$O$_{19}$ nanoparticles affects the participation of these anisotropy mechanisms [290] and reduces the effective magnetocrytalline anisotropy. Therefore, H$_c$ values were found to be decreased with increasing polymer contact in BaFe$_{12}$O$_{19}$ containing composites. Similar effect was also reported by Farghali et al. for polyaniline/Co$_{1-x}$Mg$_x$Fe$_2$O$_4$ nanocomposite [261].
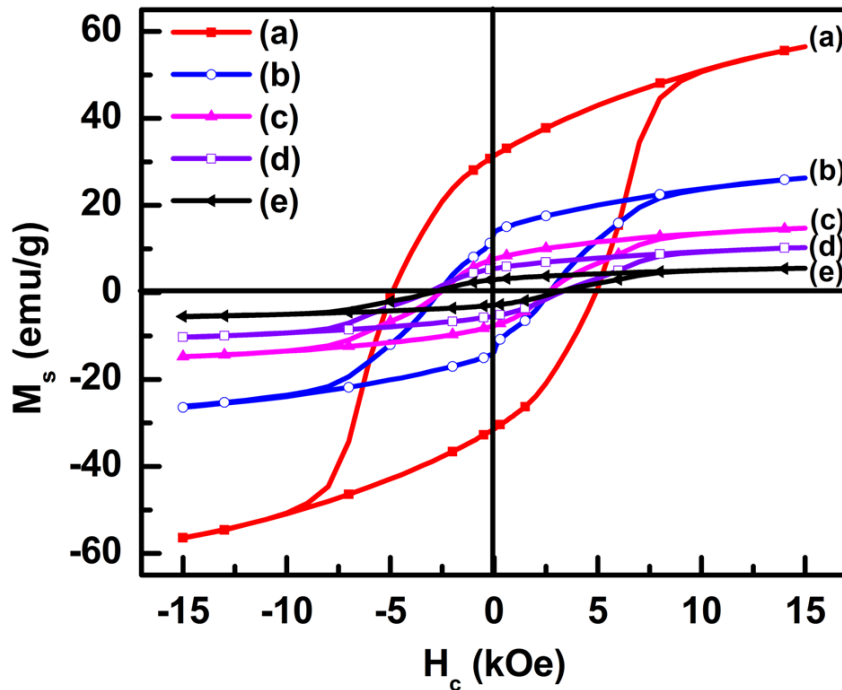
Fig 4.14 Magnetization curves for (a) BaFe$_{12}$O$_{19}$ powder, (b) PB-BHF (50:50) nanocomposite, (c) 47.5L-5LgM-14.25PB-33.25BHF composite, (d) 47.5L-5LgM-23.75PB-23.75BHF composite, (e) 47.5L-5LgM-33.25PB-14.25BHF composite.

Table 4.7 Magnetic properties of PB-BHF nanocomposite and L-LgM-PB-BHF composites.

Sample code	M$_s$ (emu/g)	H$_c$ (Oe)
BaFe$_{12}$O$_{19}$	56.50	4913.94
PB-BHF (70:30)	13.82	2956.25
PB-BHF (50:50)	26.36	2669.40
PB-BHF (30:70)	32.74	2557.39
47.5L-5LgM-33.25PB-14.25BHF	5.56	2992.39
47.5L-5LgM-23.75PB-23.75BHF	10.31	3208.47
47.5L-5LgM-14.25PB-33.25BHF	14.79	2587.51

Figure 4.15 demonstrates that a sheet of L-LgM-PB-BHF composite is attached with a bar magnet indicating its magnetic nature and both ends of the sheet can be gripped by a tweezer by bending it easily due to its mechanical flexibility. This shows that the composites reported here possess magnetic property as well as mechanical flexibility.
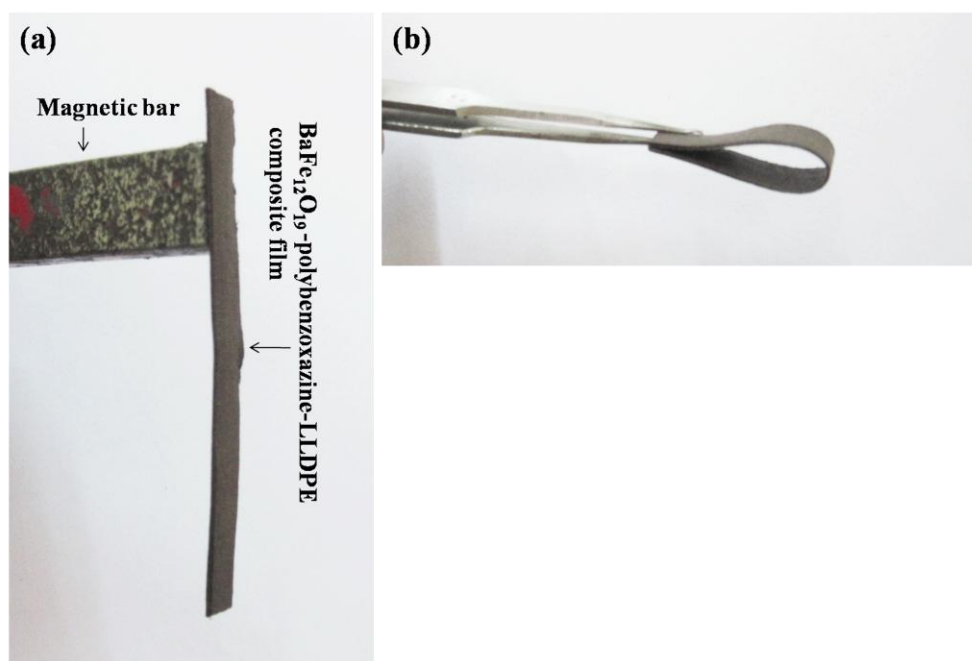
Fig 4.15 LLDPE-LgM-Polybenzoxazine-BaFe$_{12}$O$_{19}$ composite sheet showing (a) magnetic nature, (b) mechanical flexibility.

4.3 Summary of Results

1. BaFe$_{12}$O$_{19}$ nanopowder was successfully synthesized by using EDTA precursor based synthesis method.

2. Major thermal decomposition of the precursor was complete at ~450 ^{0}C.

3. Single phase BaFe$_{12}$O$_{19}$ was formed at a calcination temperature of 850 ^{0}C for 4 h in air atmosphere.

4. Average particle size of BaFe$_{12}$O$_{19}$ nanopowder was ~15 nm.

5. BaFe$_{12}$O$_{19}$ nanoparticles exhibited ferromagnetic behaviour with a coercivity (H$_c$) of 4913.94 Oe and a saturation magnetization (M$_s$) of 56.50 emu/g.

6. XRD analysis of the final composites confirmed the presence of single phase BaFe$_{12}$O$_{19}$ in the composite.

7. Prepared L-LgM-PB-BHF composites showed better thermal stability than pure LLDPE.

8. Variation of BaFe$_{12}$O$_{19}$ nanoparticles loading (14.25 to 33.25 wt%) did not affect much in the tensile strength and tensile module of the composites.

9. Composites possessed higher flexural strength than that of pure LLDPE but lower than 47.5L-5LgM-47.5PB blend matrix.

10. Toughness of the L-LgM-PB-BHF composites was higher than that of pure polybenzoxazine, pure LLDPE, and 47.5L-5LgM-47.5PB blend.

11. Saturation magnetization (M$_s$) value of composites decreased with decreasing BaFe$_{12}$O$_{19}$ content in the composites.

12. Value of coercivity (H$_c$) of the composites decreased with decreasing amount of BaFe$_{12}$O$_{19}$ in the composites.

CHAPTER 5

Synthesis, characterization and properties of pure single phase $NiFe_2O_4$ and LLDPE-LgM-Polybenzoxazine-$NiFe_2O_4$ flexible magnetic nanocomposites

5.1 Experimental procedure for material synthesis

5.1.1 Materials used

The chemicals used were $Fe(NO_3)_3.9H_2O$, $Ni(NO_3)_2.6H_2O$, EDTA (99.9%, Merck, India). Aniline, paraformaldehyde and bisphenol-A (99%, s.d. fine chem limited, India), chloroform (99.7%, Qualigens Fine Chemicals, India). Linear low density polyethylene (LLDPE, R35A042) having a density of 0.935 gm/cm^3 and Melt flow index (MFI) of 4.2 gm/10 min, was obtained from GAIL (India) Ltd., and LLDPE-g-Maleic anhydride (LgM) (OPTIM E-126) with a 0.73% maleic anhydride content and MFI 2.16 gm/10 min, from Pluss Polymers Pvt, Ltd., India. All chemicals were used as received.

5.1.2 Synthesis of $NiFe_2O_4$ (NF) nanopowder: [291]

$NiFe_2O_4$ nanopowder was prepared by using EDTA-precursor based method. In a typical synthesis, stoichiometric amounts of nickel nitrate and ferric nitrate were dissolved in distilled water according to the molar ratio of 1:2. An aqueous solution of EDTA was prepared by dissolving EDTA in hot water with drop wise addition of dilute NH_4OH solution. After complete dissolution of EDTA, the solution was boiled to remove excess NH_3. The pH of the solution was found to be ~6. Aqueous solutions of the metal nitrates and EDTA were mixed in a molar ratio of 1:1 and stirred for 1 h at room temperature using a magnetic stirrer. The pH of the resulting mixture was ~2. Black coloured precursor was formed when this reaction mixture was evaporated to dryness on a hot plate at ~110 ^{0}C. 3-4 drops of 10% NH_4NO_3 aqueous solution was added to the dried precursor powder which was then calcined in air for 2-4 h at different temperatures ranging from 450 to 550 ^{0}C to obtain nickel ferrite nanopowder. Aqueous NH_4NO_3 solution was added to the precursor before calcination to facilitate the oxidation of the carbonaceous mass.

5.1.3 Synthesis of Benzoxazine monomer (BA)

Benzoxazine monomer was synthesized as per the procedure described in the section 2.1.2 (Experimental procedure for material synthesis) of Chapter 2.

5.1.4 Preparation of benzoxazine-NiFe$_2$O$_4$ nanocomposites (BA-NF) [292]

Benzoxazine-NiFe$_2$O$_4$ nanocomposite was prepared as per the procedure described in the section 3.1.4 (Experimental procedure for material synthesis) of Chapter 3. Dynamic light scattering studies indicated the average sizes of these benzoxazine coated NiFe$_2$O$_4$ nanoparticles were in the range of 111-134 nm. Various compositions of nanocomposites, prepared by using BA and NF are listed in Table 5.1.

5.1.5 Preparation of LLDPE-LgM-PB-NF composites (L-LgM-PB-NF) [292]

LLLDPE-LgM-PB-NF composite was prepared as per the procedure described in the section 3.1.5 (Experimental procedure for material synthesis) of Chapter 3. Composites, having different compositions of NF, PB and LLDPE, were prepared as listed in Table 5.1.

Table 5.1 Compositions of prepared BA-NF and L-LgM-PB-NF composites.

Sample code	LLDPE (wt%)	LgM (wt%)	PB (wt%)	NiFe$_2$O$_4$ (wt%)
BA-NF (70:30)	--	--	70	30
BA-NF (50:50)	--	--	50	50
BA-NF (30:70)	--	--	30	70
47.5L-5LgM-47.5PB	47.5	5	47.5	--
47.5L-5LgM-33.25PB-14.25NF	47.5	5	33.25	14.25
47.5L-5LgM-23.75PB-23.75NF	47.5	5	23.75	23.75
47.5L-5LgM-14.25PB-33.25NF	47.5	5	14.25	33.25

SEM micrograph of the surface of a cross section of the composites (Figure 5.1) shows that polybenzoxazine coated $NiFe_2O_4$ nanoparticles are embedded within the polymeric matrix.
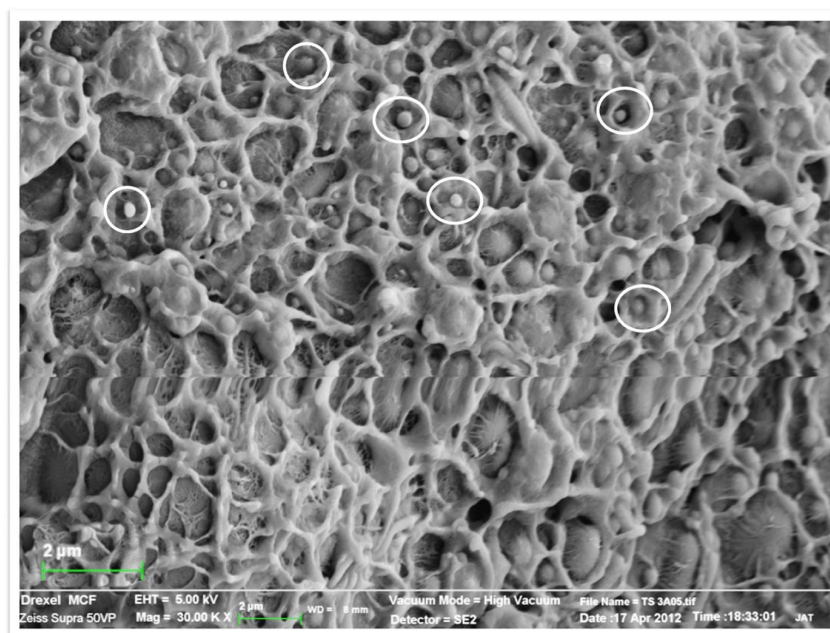
Fig 5.1 SEM micrograph of the composites shows that $NiFe_2O_4$ nanoparticles are dispersed within the polymeric matrix. Polybenzoxazine coated $NiFe_2O_4$ nanoparticles are marked within the circle.

5.2 Results and Discussion

5.2.1 Characterization of $NiFe_2O_4$ nanoparticles

5.2.1.1 Thermal Analysis

TGA and DSC analyses were performed to investigate the decomposition behavior of the precursor powder due to heat treatment in air and thermogram is shown in Figure. 5.2. The TGA thermogram revealed that a total weight loss of ~28% occurred when the precursor powder was heated from 30 ^{0}C to 600 ^{0}C in air. Initially ~5% weight loss occurred between 30 ^{0}C and 100 ^{0}C due to the loss of moisture from the sample. Approximately 23% weight loss was observed up to 450 ^{0}C. This may have been due to the thermo-oxidative decomposition of the precursor and evolution of CO_2 and NO_x gases. This decomposition was also reflected in DSC thermogram, as shown in Figure 5.2, where exothermic peaks were observed at 295 ^{0}C and 388 ^{0}C. Heating the sample beyond 450 ^{0}C did not result in any further weight loss in TGA or formation of any new peak in DSC thermogram. Thus it can be assumed that decomposition of carbonaceous content of the precursor occurred up to 450 ^{0}C.
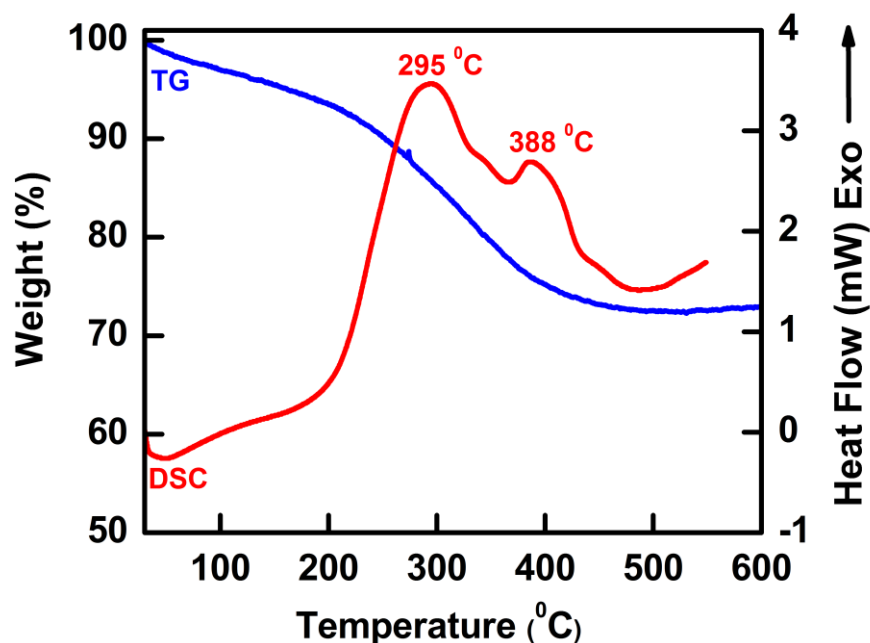
Fig 5.2 TGA-DSC thermograms of NiFe$_2$O$_4$ precursor.

5.2.1.2 X-Ray Diffraction Analysis

Room temperature powder X-Ray diffraction spectra of the precursor and its calcined powder were performed to investigate phase formation due to calcination of the precursor powder (Figure 5.3). The uncalcined precursor exhibited XRD diffraction peaks Figure 5.3(a) for NiFe$_2$O$_4$ [ICDD 54-0964]. However, intensity ratio (I/I$_0$) of the peaks did not exactly match standard values, indicating the effect of the small crystallite size. The notable feature is that the formation of pure NiFe$_2$O$_4$ phase was observed in the precursor. To the best of our knowledge, precursor containing NiFe$_2$O$_4$ has not been reported for any other precursor based method. What this study shows is that precursor powder calcined at 550 ^{0}C for 4 h did show the formation of single phase NiFe$_2$O$_4$ nanopowder, as corroborated by the presence of (111), (220), (311), (222), (400), (422), (511) and (440) diffraction planes in the XRD spectra of single phase spinel nickel ferrite nanopowder. The intensities of the peaks increased with increasing calcination temperature, due to the increase of crystallinity and crystallite size. The crystallite size was calculated using X-ray peak-broadening of the diffraction peak for (311) using Scherrer's formula [238] to be 26.4 and 38.4 nm for precursor and calcined powder respectively. The values of lattice parameter (a=b=c) of synthesized NiFe$_2$O$_4$ was found to be 8.34 Å, which agreed well with the standard value of 8.33 Å for NiFe$_2$O$_4$ [293]. TGA-DSC and XRD analyses of the synthesized precursor and calcined powders confirm that the oxidative decomposition of precursor led to the formation of single phase NiFe$_2$O$_4$

nanopowder. The chemical process starts from a homogeneous aqueous solution of metal nitrates and EDTA, which, after evaporation, produces a fluffy, voluminous, carbon rich "precursor" powder. Calcination of the precursor results in the formation of pure single phase $NiFe_2O_4$ nanopowders. EDTA, a chelating agent, plays a critical role in the formation of $NiFe_2O_4$ nanopowder: it not only prevents the segregation or intermittent precipitation of metal ions from the reaction mixture during evaporation by forming water soluble complex with metal ions but also acts as a fuel to provide the heat of combustion for forming the metal oxide phase. During decomposition, the precursor produces gases (such as CO_2, NO_x) that help to dissipate the heat of combustion and thus inhibit the sintering of fine particles during the process to form nanosized oxides.
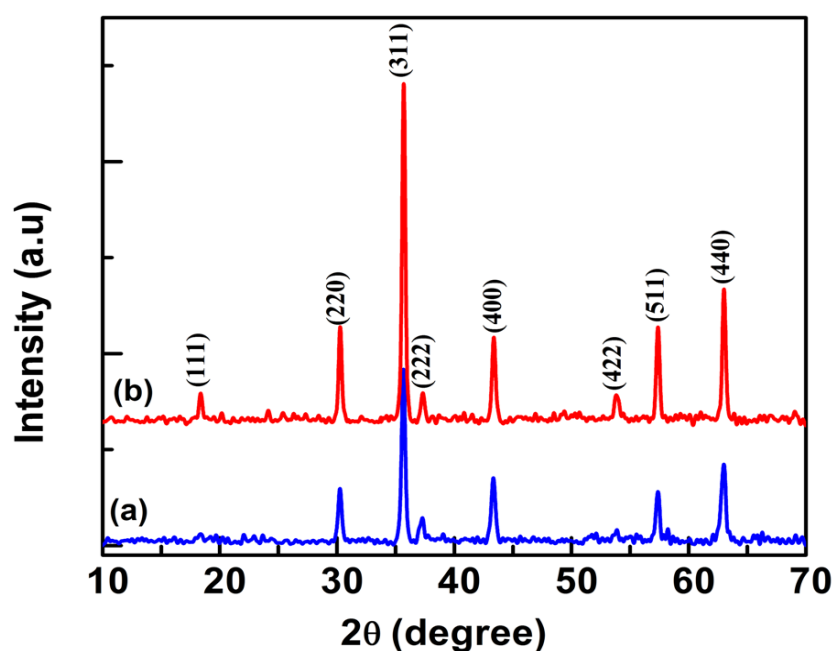
Fig 5.3 XRD patterns of (a) precursor and the powders obtained by calcining the precursor at 550 ^{0}C for 4 h (b).

5.2.1.3 Particle Size and TEM analysis of NiFe₂O₄ nanopowder

The differential intensity related to particle size distributions of the as-synthesized $NiFe_2O_4$ nanopowder obtained from DLS study at 30 ^{0}C as shown in Figure 5.4(a) exhibited a double nodal distribution with the main peak averages around 10.5 ± 6.7 nm and 189.8 ± 48.5 nm. The cumulant mean diameter of the particles was 23 nm with a polydespersity index of 0.297. The TEM micrograph of the powder calcined at 550 ^{0}C is shown in Figure 5.4(b). It is clearly indicated that average particle size of the calcined powder was ~35 nm. The particles were mostly round in shape and formed loose aggregates.
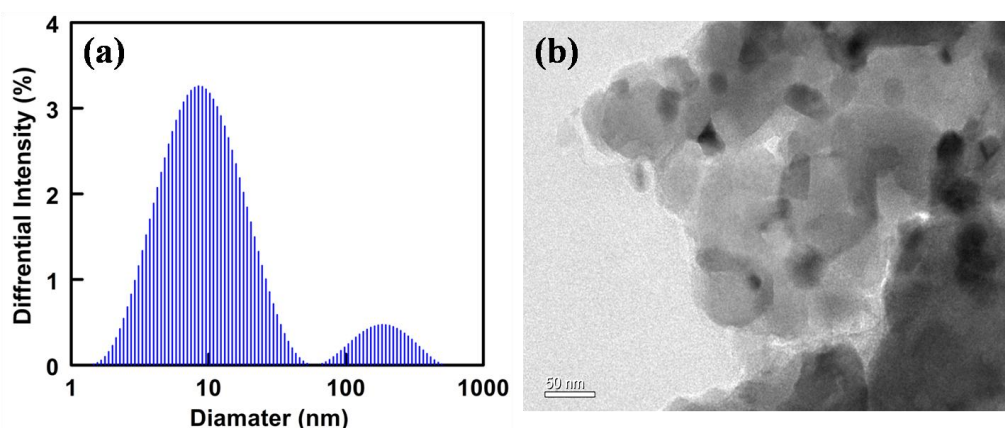
Fig 5.4 (a) Particle size distribution and (b) TEM micrograph of as-synthesized $NiFe_2O_4$ nanopowder.

5.2.1.4 Magnetization Measurement

Room temperature magnetization of the as-synthesized $NiFe_2O_4$ nanoparticles was measured using VSM with an applied field of 2000 Oe, as shown in Figure 5.5. $NiFe_2O_4$ nanoparticles exhibited ferromagnetic behavior with a coercivity (H_c) of 158.30 Oe and a saturation magnetization (M_s) of 30.70 emu/g. It was observed that the synthesized $NiFe_2O_4$ nanoparticles possessed a relatively high coercivity as compared to reported values. Particle size, surface morphology, microstructure of the final nanoparticle change with the method of synthesis. These factors affect the magnetic properties of the synthesized materials. Table 5.2 summarizes saturation magnetization (M_s) and coercivity (H_c) of $NiFe_2O_4$ nanopowders prepared by different synthesis methods.
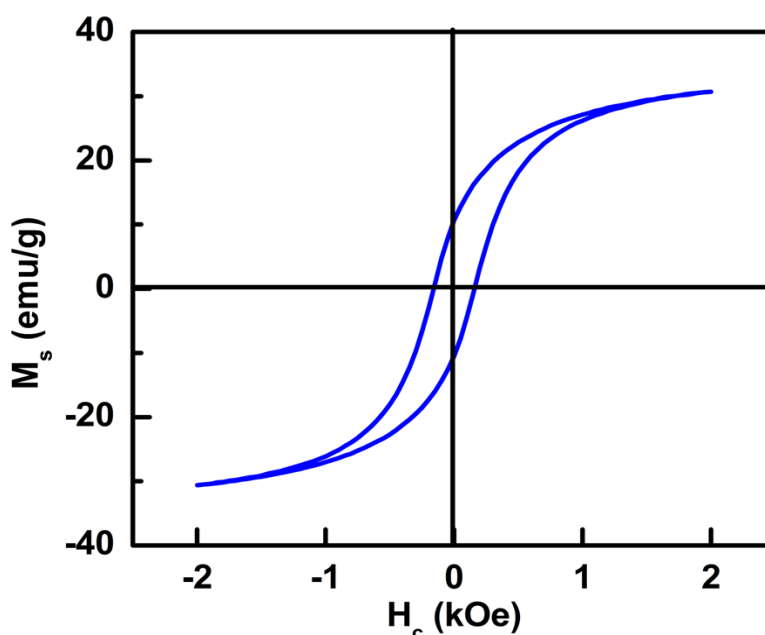
Fig 5.5 Room temperature magnetic hysteresis loop for $NiFe_2O_4$ nanopowder.

Table 5.2 Comparison of saturation magnetization M$_s$ and coercivity H$_c$ of NiFe$_2$O$_4$ particles prepared by different synthetic methods.

Synthesis Method	M$_s$ (emu/g)	H$_c$ (Oe)	Reference
Facile hydrothermal	30.4	87.4	[294]
Pulsed laser deposition	~45	29.3	[295]
EDTA-assisted hydrothermal	---	70	[296]
Egg white based process	34.5	85	[297]
Conventional ceramic	24	---	[293]
High-energy milling	34.55	0.107 (T)	[83]
Sonochemical	25	---	[298]
Hydrothermal	54.02	54.1 (kA/m)	[299]
EDTA precursor route	**30.70**	**158.30**	**This work [291]**

5.2.2 Characterization of BA-NF nanocomposite and L-LgM-PB-NF composites

5.2.2.1 X-Ray Diffraction Analysis

The room temperature wide angle powder X-Ray diffraction spectra were recorded for pure NiFe$_2$O$_4$ nanopowder, BA-NF nanocomposites and L-LgM-PB-NF composites. In case of BA-NF nanocomposite samples, all the XRD peaks of NiFe$_2$O$_4$ were present and no additional peaks were detected (Figure. 5.6 (b)). For L-LgM-PB-NF nanocomposite samples, XRD peaks of NiFe$_2$O$_4$ were present along with additional peaks at $2\theta = 21.6^0$ and 23.8^0. These two peaks correspond to the (110) and (200) diffraction planes of LLDPE [223, 224, 227] and indicated that the crystalline structure of LLDPE remained unchanged upon blending in the nanocomposites (Figure 5.6 (c-e)). However, the intensity of the crystallite peaks of LLDPE varied with compositions. These XRD spectra of the composite conformed that the pure crystalline phases of NiFe$_2$O$_4$ remained preserved in the composite with no impurity phase generation during melt blending process.
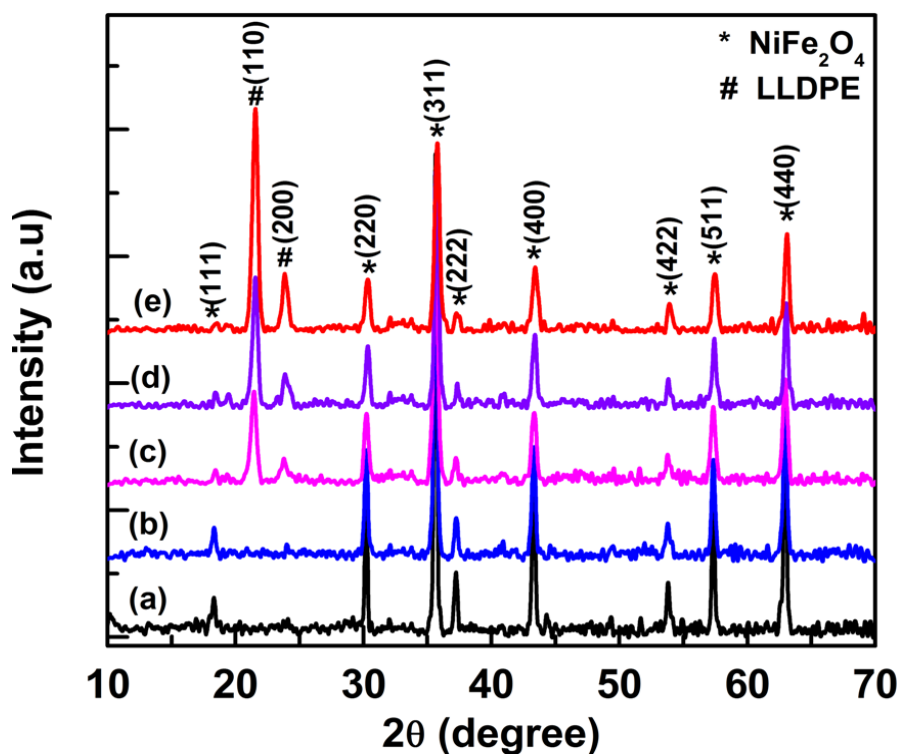
Fig 5.6 XRD spectra of (a) $NiFe_2O_4$ powder, (b) PB-NF (50:50) nanocomposite, (c) 47.5L-5LgM-14.25PB-33.25NF composite, (d) 47.5L-5LgM-23.75PB-23.75NF composite, (e) 47.5L-5LgM-33.25PB-14.25NF composite. (* $NiFe_2O_4$ and # LLDPE)

5.2.2.2 Thermal Analysis

Thermo gravimetric (TGA) and differential scanning calorimetric (DSC) analysis of pure benzoxazine monomer, polybenzoxazine, LLDPE, PB-NF and L-LgM-PB-NF composites were performed to evaluate their thermal stability. In the DSC thermogram of pure benzoxazine monomer an exothermic peak at ~205 ^{0}C was observed, which was attributed to the ring opening polymerization of benzoxazine ring (Figure 5.7 (a)) [228-231]. In case of PB-NF nanocomposites, this exothermic curing peak of benzoxazine shifted from ~205 to ~194 ^{0}C (Figure 5.7 (b)). This decrease in curing temperature of benzoxazine might be due to the catalytic effect of $NiFe_2O_4$ towards the thermal curing of benzoxazine monomer [251, 252]. In DSC thermogram of pure LLDPE an endothermic peak at ~124 ^{0}C due to its melting [227] and an exothermic peak at ~224 ^{0}C for its beginning of thermal oxidative decomposition [232, 233] were observed (Figure 5.7 (c)). In case of PB containing LLDPE composites (47.5L-5LgM-47.5PB) (Figure 5.7 (d)) beginning of thermal oxidation decomposition occurred at ~283 ^{0}C, which is higher than that of pure LLDPE. In case of L-LgM-PB-NF composite samples, an endothermic peak at ~124 ^{0}C, corresponding to the

melting temperature of LLDPE was observed. It was observed that for composite samples the exothermic peak for thermal oxidative decomposition shifted to higher temperature (~254 ^{0}C) compare to pure LLDPE (~224 ^{0}C) but lower than the LLDPE-LgM-PB matrix composite (~283 ^{0}C). This may be due to the catalytic effect of NiFe$_2$O$_4$ towards the thermal degradation of polymeric matrix [251, 252]. Another important observation was that the exothermic peak for ring opening polymerization of benzoxazine ring was absent in the thermograms of final composite samples (Figure 5.7 (d)). This result confirmed that all benzoxazine monomers were fully polymerized to polybenzoxazine during composite preparation at 200 ^{0}C.
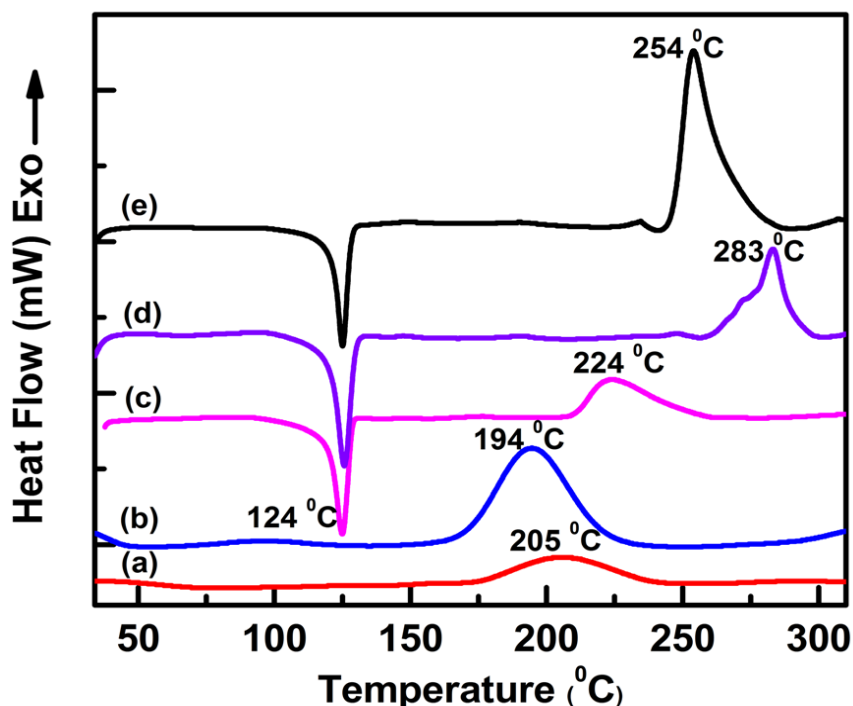
Fig 5.7 DSC thermogram of (a) benzoxazine monomer, (b) BA-NF (70:30) nanocomposite, (c) LLDPE, (d) 47.5L-5LgM-47.5PB composite, (e) 47.5L-5LgM-23.75PB-23.75NF composite.

From TGA of pure PB, LLDPE and L-LgM-PB-NF composites, temperatures for 5% weight loss (T$_{5\%}$), 10% weight loss (T$_{10\%}$) and char yield (%) at 800 ^{0}C in air were determined and listed in Table 5.3. It was observed that the temperature at 5 and 10% weight loss was found to be decrease with increasing NiFe$_2$O$_4$ content in the composites. This may be due catalytic effect of NiFe$_2$O$_4$ on thermal degradation of polymeric matrix [251, 252]. TGA thermograms of LLDPE, PB, BA-NF and L-LgM-PB-NF composite are shown in Figure 4.8. These thermograms revealed that, presence of more thermally stable PB in L-LgM-PB-NF

composites enhances the overall thermal stability of the composites. The thermal stability of the composite was found to be more than pure LLDPE but less than pure polybenzoxazine. The degradation of all the L-LgM-PB-NF composites was found in the temperature range of 350-550 ^{0}C. The char yield at 800 ^{0}C of the composite was found to increase with increasing NiFe₂O₄ content. However, as the melting temperature of LLDPE is ~124 ^{0}C, the composites should be used below this temperature.
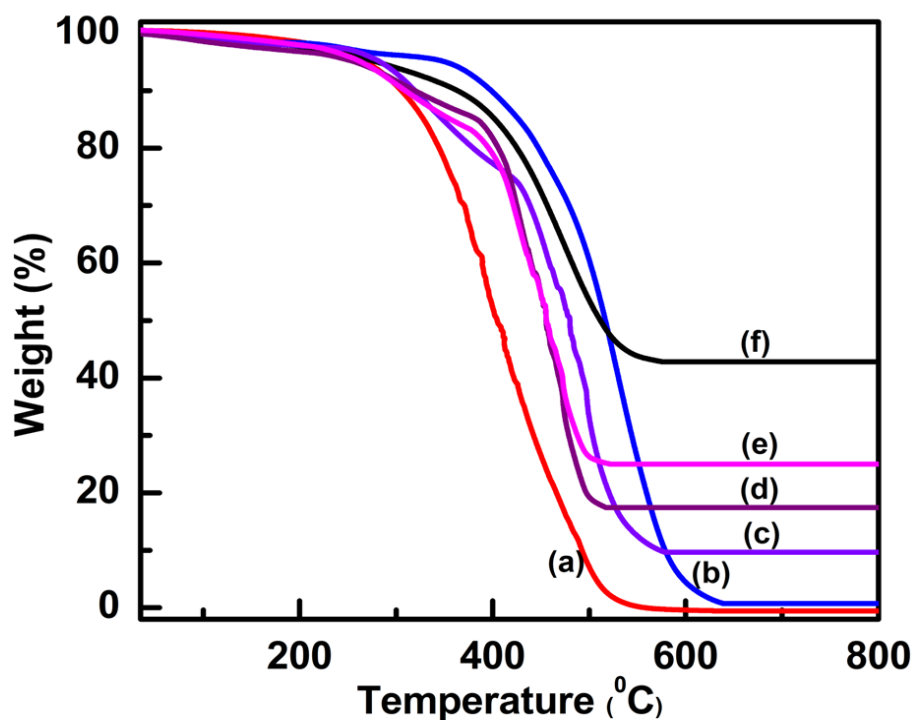
Fig 5.8 Thermograms (TGA) of (a) LLDPE, (b) Polybenzoxazine, (c) 47.5L-5LgM-33.25PB-14.25NF composite, (d) 47.5L-5LgM-23.75PB-23.75NF composite, (e) 47.5L-5LgM-14.25PB-33.25NF composite, (f) PB-NF (50:50) nanocomposite.

Table 5.3 Thermal properties of neat polymer and BA-NF nanocomposite and L-LgM-PB-NF composite.

Sample code	T$_{5\%}$ (^{0}C)	T$_{10\%}$ (^{0}C)	char yield (%) at 800 ^{0}C
Polybenzoxazine	350	400	0
LLDPE	267	305	0
47.5L-5LgM-47.5PB	306	345	0
PB-NF (70:30)	319	381	29
PB-NF (50:50)	261	348	43
PB-NF (30:70)	222	338	60
47.5L-5LgM-33.25PB-14.25NF	258	296	9
47.5L-5LgM-23.75PB-23.75NF	255	318	17
47.5L-5LgM-14.25PB-33.25NF	254	303	25

5.2.2.3 FT-IR Analysis

In the FT-IR spectra of pure benzoxazine monomer (BA) (Figure 5.9 (a)), the peaks at 949 cm^{-1} and 1496 cm^{-1} assigned to the tri-substituted benzene ring and absorption at 1235 cm^{-1} for asymmetric stretching of C-O-C were observed [222, 234]. The methyl group vibration was found at 2967 cm^{-1} [235]. In case of BA-NF nanocomposite (Figure 5.9 (b)), all the characteristic bands of benzoxazine were present along with a peak at 586 cm^{-1}, which corresponded to M-O stretching vibration mode of NiFe$_2$O$_4$ [253-255]. In the FT-IR spectra of L-LgM-PB-NF composites (Figure 5.9 (c)), following features were observed (i) the disappearance of peaks at 949 cm^{-1} and 1496 cm^{-1} peak (assigned for tri-substituted benzene ring of BA) and appearance of a peak at 1482 cm^{-1} (correspond to the tetra-substituted benzene ring of PB) indicated that the ring opening polymerization of BA occurred during preparation of composites at 200 ^{0}C [181]. (ii) characteristic peaks of LLDPE at 1364 cm^{-1} (-CH$_3$ symmetric vibration) and peaks around 2907 and 2849 cm^{-1}, associated with the C-H stretching vibration [227], (iii) a peak around 549 cm^{-1} for NiFe$_2$O$_4$.
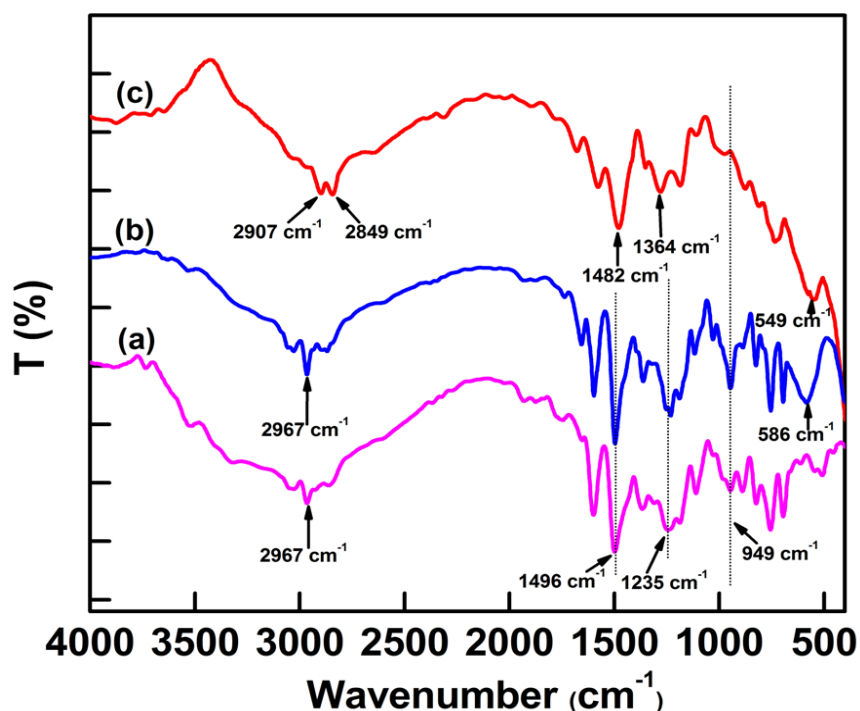
Fig 5.9 FT-IR spectra of (a) benzoxazine monomer, (b) BA-NF (70-30) nanocomposite, (c) 47.5L-5LgM-33.25PB-14.25NF composite.

5.2.2.4 Mechanical Properties

To evaluate the mechanical properties of the L-LgM-PB-NF composites tensile tests and three point bending flexural tests were performed. From tensile tests it was observed that pure polybenzoxazine possessed high tensile strength (47.05 MPa) and less elongation at break (2.2%), while LLDPE showed low tensile strength (16.75 MPa) and significantly more elongation at break (57.77%). The blend, composed of LLDPE, PB and 5 wt% compatibilizer LgM (47.5L-5LgM-47.5PB), exhibited higher tensile strength (23.81 MPa) than pure LLDPE and more elongation at break (6.11%) than pure polybenzoxazine (Figure 5.10). This might be due to the binding role of compatibilizer (LgM), which enhanced chemical and physical interaction among the two separate phases (i.e. PB and LLDPE) and ultimately improved their interfacial adhesion by reducing the interfacial tension [236, 226]. SEM micrograph of the 47.5L-5LgM-23.75PB-23.75NF composite (Figure 5.11) also showed the homogeneous polymeric matrix of the composite and no phase separation between PB and LLDPE in presence of LgM compatibilizer. From tensile stress-strain graph (Figure 5.10) it was observed that due to loading of 14.25 wt% $NiFe_2O_4$ nanoparticle in polymeric blend (47.5L-5LgM-47.5PB) tensile strength decreased from 23.81 MPa to 19.45 MPa but % of elongation at break increased from 6.11% to 15.5%. However, variation of $NiFe_2O_4$ nanoparticles

loading (14.25 to 33.25 wt%) did not affect much in the tensile strength and tensile module of the composite. But, elongation at break was found to be decreased from 15.5 to 8.52% with increasing NiFe$_2$O$_4$ loading in the composite. This might be due to the higher loading level of NiFe$_2$O$_4$ nanoparticles might acts as defects under the extension by causing stress concentrations [256-259]. Tensile properties of the neat LLDPE, polybenzoxazine and composites are summarized in Table 5.4.
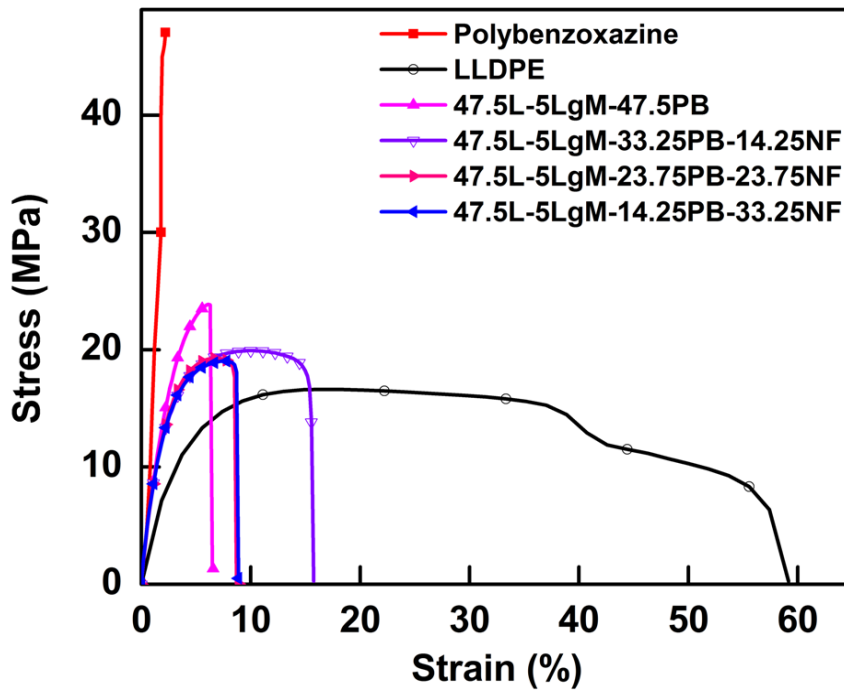
Fig 5.10 Tensile stress-strain curves of neat polymer, blend and L-LgM-PB-NF composites.
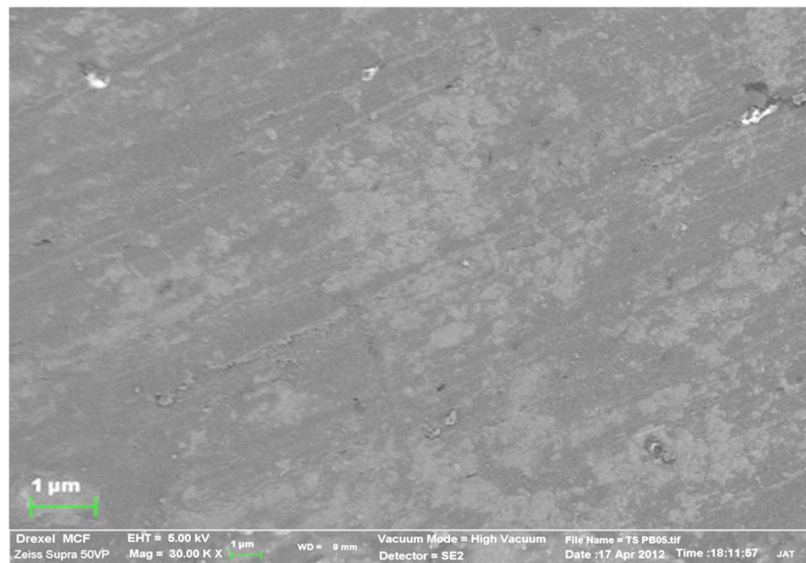
Fig 5.11 SEM micrograph of surface 47.5L-5LgM-23.75PB-23.75NF composite before tensile testing.

Table 5.4 Tensile properties of the neat polymer, blend and L-LgM-PB-NF composite.

Sample code	Tensile strength (MPa)	Tensile modulus (GPa)	Elongation at break (%)
LLDPE	16.75	0.236	57.77
Polybenzoxazine	47.05	3.6	2.2
47.5L-5LgM-47.5PB	23.81	1.071	6.11
47.5L-5LgM-33.25PB-14.25NF	19.45	0.997	15.5
47.5L-5LgM-23.75PB-23.75NF	19.20	0.956	9.06
47.5L-5LgM-14.25PB-33.25NF	19.00	0.900	8.52

From the flexural stress-strain curves of PB, LLDPE, 47.5L-5LgM-47.5PB blend and L-LgM-PB-NF composite (Figure 5.12), it was observed that L-LgM-PB-NF composites possessed greater flexural strength than that of pure LLDPE but lesser than 47.5L-5LgM-47.5PB blend. However, it is important to note that the toughness (area under the stress-strain curve) of the composites was higher than that of pure polybenzoxazine, pure LLDPE, and 47.5L-5LgM-47.5PB blends. Flexural properties of the neat LLDPE, polybenzoxazine and composites are summarized in Table 5.5.
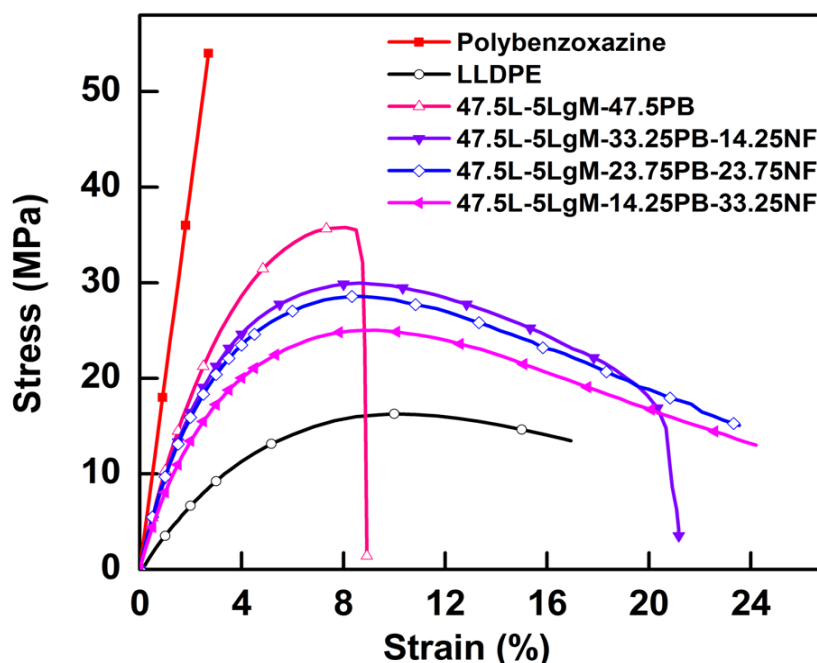
Fig 5.12 Flexural stress-strain curves of neat polymer, blend and L-LgM-PB-NF composites.

Table 5.5 Flexural properties of the neat polymer, blend and L-LgM-PB-NF composite.

Sample code	Flexural strength (MPa)	Flexural modulus (GPa)	Toughness (MPa)
LLDPE	16.33	0.403	0.274
Polybenzoxazine	54.06	1.928	0.439
47.5L-5LgM-47.5PB	35.75	1.236	0.244
47.5L-5LgM-33.25PB-14.25NF	30.01	1.369	0.530
47.5L-5LgM-23.75PB-23.75NF	28.22	1.139	0.512
47.5L-5LgM-14.25PB-33.25NF	25.04	0.998	0.502

5.2.2.5 SEM Analysis of Fractured Surfaces

The morphology of the fractured surfaces of the composites after tensile testing was investigated by SEM and is shown in Figure 5.13 (a)-(d). It was observed that for the sample composed of LLDPE, LgM and PB (47.5L-5LgM-47.5PB), fibril microstructure formed in the fractured surface during fracture under tensile strain (Figure 5.13 (a)). In case of NiFe$_2$O$_4$ containing composites it was observed that, delamination of the nanoparticles from polymeric matrix occurred under tensile strain and formation of voids during breaking. This effect was pronounced for the composites having higher NiFe$_2$O$_4$ loading and large voids were observed in their fractured surfaces (Figure 5.13 (c), (d)). This might be due to the formation of large NiFe$_2$O$_4$ agglomerates in the composites with high NiFe$_2$O$_4$ loading, as nanoparticles tend to form agglomerates.
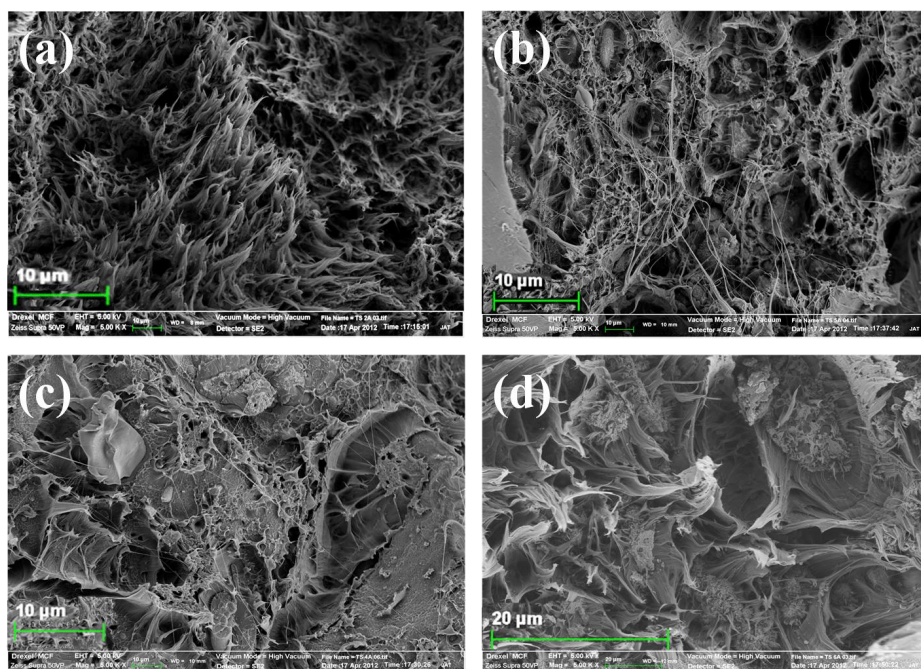
Fig 5.13 SEM micrographs of fractured surfaces of composites after tensile testing (a) 47.5L-5LgM-47.5PB composite, (b) 47.5L-5LgM-33.25PB-14.25NF composite, (c) 47.5L-5LgM-23.75PB-23.75NF composite, (d) 47.5L-5LgM-14.25PB-33.25NF composite.

5.2.2.6 Magnetization Measurement

The variation of magnetic properties, in terms of saturation magnetization (M_s) and coercivity (H_c), with the composition of composites were investigated by using a VSM at room temperature with an applied field of 2000 Oe. Figure 5.14 shows the hysteresis loops of the as synthesized pure $NiFe_2O_4$ nanoparticles, BA-NF, L-LgM-PB-NF composite and the values of M_s and H_c are summarized in Table 5.6. The saturation magnetization (M_s) and coericivity (H_c) values of $NiFe_2O_4$ nanoparticles were found to be 30.70 emu/g and 158.30 Oe respectively. It was observed that, when $NiFe_2O_4$ nanoparticles were mixed with benzoxazine (BA-NF), M_s value of the samples were decreased with increasing PB content. In the L-LgM-PB-NF composites the same trend was also observed. This decrease of M_s value with decreasing $NiFe_2O_4$ loading in the composition of composite is quite obvious because the composite is composed of magnetic $NiFe_2O_4$ nanoparticles and non-magnetic polymer. Interestingly, it was observed that Coercivity (H_c) value of the composites was found to be higher than that of pure $NiFe_2O_4$ nanoparticles. For example, H_c of pure NF is 158.30 Oe and for composite containing 14.25 wt% of NF H_c is 253.14 Oe. This might be due to the fact that dispersion of NF nanoparticles within the polymeric matrix caused decrease in interparticle dipolar interaction arising from the increased interparticle distance within the single domain

as compared to the close contact of the pure NF nanoparticles, and also due to the polymer-particle interfacial effect [262-264]. Similar effect was also reported by Guo et al., for Fe$_2$O$_3$ nanoparticle reinforced vinyl-ester resin nanocomposites [300].
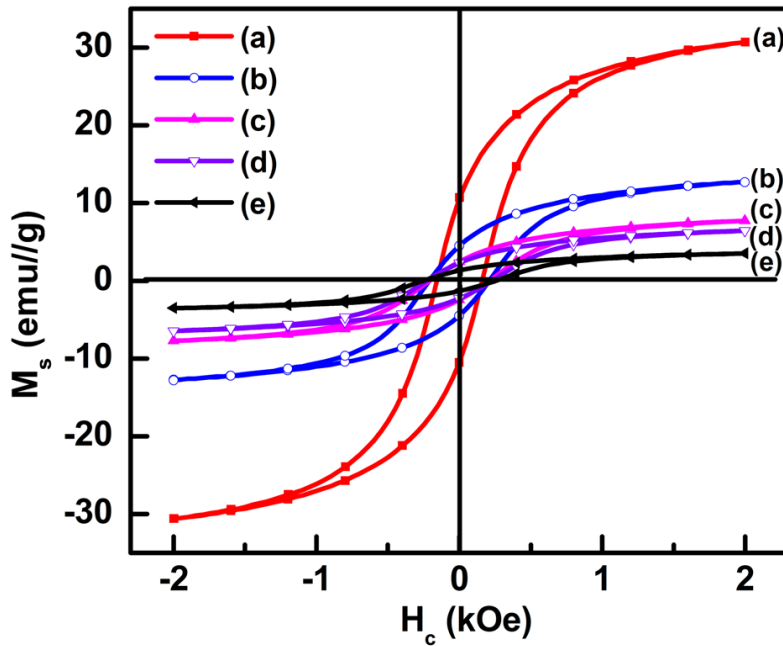
Fig 5.14 Magnetization curves for (a) NiFe$_2$O$_4$ powder, (b) PB-NF (50:50) nanocomposite, (c) 47.5L-5LgM-14.25PB-33.25NF composite, (d) 47.5L-5LgM-23.75PB-23.75NF composite, (e) 47.5L-5LgM-33.25PB-14.25NF composite.

Table 5.6 Magnetic properties of PB-NF nanocomposite and L-LgM-PB-NF composite.

Sample code	M_s (emu/g)	H_c (Oe)
NiFe$_2$O$_4$	30.70	158.30
PB-NF (70:30)	7.53	187.35
PB-NF (50:50)	12.57	210.55
PB-NF (30:70)	18.05	205.14
47.5L-5LgM-33.25PB-14.25NF	3. 51	253.14
47.5L-5LgM-23.75PB-23.75NF	6.44	230.46
47.5L-5LgM-14.25PB-33.25NF	7.72	210.32

Figure 5.15 demonstrates that a film of L-LgM-PB-NF composite is attached with a bar magnet indicating its magnetic nature and both ends of the sheet can be gripped by a tweezer by bending it easily due to its mechanical flexibility. This shows that the composites reported here possess magnetic property as well as mechanical flexibility.
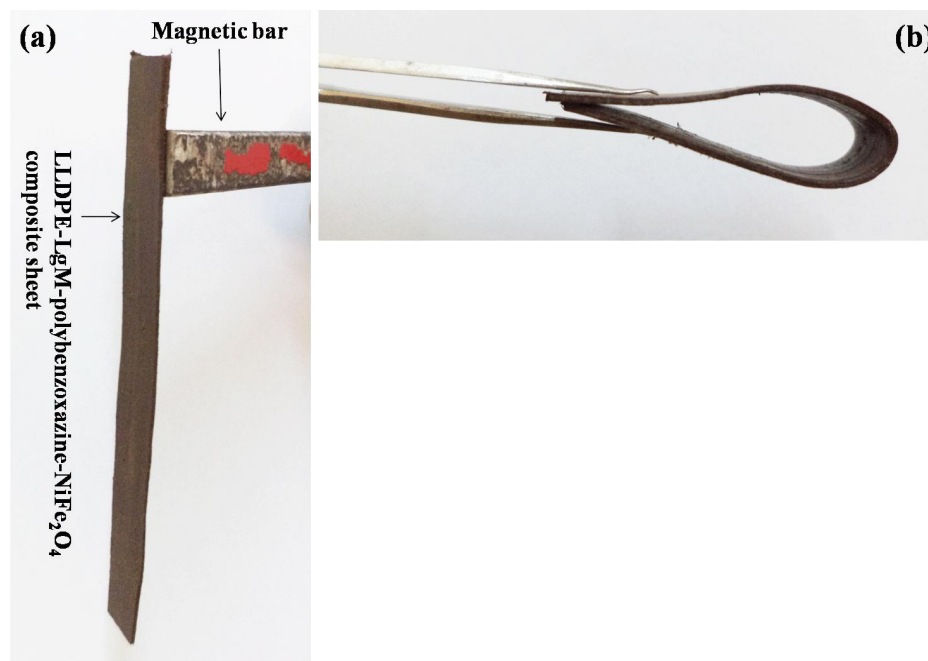
Fig 5.15 LLDPE-LgM-Polybenzoxazine-NiFe$_2$O$_4$ composite sheets exhibiting (a) magnetic nature, (b) mechanical flexibility.

5.3 Summary of Results

1. NiFe$_2$O$_4$ nanopowder was successfully synthesized by using EDTA precursor based synthesis method.

2. Major thermal decomposition of the precursor was complete at ~450 ^{0}C.

3. Single phase NiFe$_2$O$_4$ was formed at a calcination temperature of 550 ^{0}C for 4 h in air atmosphere.

4. Average particle size of NiFe$_2$O$_4$ nanopowder was ~23 nm.

5. NiFe$_2$O$_4$ nanoparticles exhibited ferromagnetic behaviour with a coercivity (H$_c$) of 158.30 Oe and a saturation magnetization (M$_s$) of 30.70 emu/g.

6. XRD analysis of the final composites confirmed the presence of single phase NiFe$_2$O$_4$ in the composite.

7. Prepared L-LgM-PB-NF composites showed better thermal stability than pure LLDPE.

8. Variation of NiFe$_2$O$_4$ nanoparticles loading (14.25 to 33.25 wt%) did not affect much in the tensile strength and tensile module of the composites.

9. Composites possessed higher flexural strength than that of pure LLDPE but lower than 47.5L-5LgM-47.5PB blend matrix.

10. Toughness of the L-LgM-PB-NF composites was higher than that of pure polybenzoxazine, pure LLDPE, and 47.5L-5LgM-47.5PB blend.

11. Saturation magnetization (M$_s$) value of composites decreased with decreasing NiFe$_2$O$_4$ content in the composites.

12. Value of coercivity (H$_c$) of the composites increased with decreasing amount of NiFe$_2$O$_4$ in the composites.

CHAPTER 6

Synthesis, characterization and properties of pure single phase Ni$_{0.8}$Zn$_{0.2}$Fe$_2$O$_4$ and LLDPE-LgM-Polybenzoxazine-Ni$_{0.8}$Zn$_{0.2}$Fe$_2$O$_4$ flexible magnetic nanocomposites

6.1 Experimental procedure for materials synthesis

6.1.1 Materials used

The chemicals used were Fe(NO$_3$)$_3$.9H$_2$O, Ni(NO$_3$)$_2$.6H$_2$O, Zn dust, ethylene diamine tetra acetic acid (EDTA), NH$_4$NO$_3$, nitric acid (99.9%, Merck, India), aniline, paraformaldehyde and bisphenol-A (99%, s.d. fine-chem limited, India), chloroform (99.7%, Qualigens Fine Chemicals, India). Linear low-density polyethylene (LLDPE, R35A042) having a density of 0.935 gm/cm^3 and melt flow index (MFI) of 4.2 gm/10 min, was obtained from GAIL (India) Ltd., and LLDPE-*g*-Maleic anhydride (LgM) (OPTIM E-126) with 0.73% maleic anhydride content and MFI 2.16 gm/10 min, from Pluss Polymers Pvt, Ltd., India. All chemicals were used without further purification.

6.1.2 Synthesis of Ni$_{0.8}$Zn$_{0.2}$Fe$_2$O$_4$ (NZF) nanopowder: [301]

Ni$_{0.8}$Zn$_{0.2}$Fe$_2$O$_4$ nanopowder was prepared by using EDTA-precursor based method. In a typical synthesis, aqueous solutions of metal nitrates were mixed in a stoichiometric amount to prepare Ni$_{0.8}$Zn$_{0.2}$Fe$_2$O$_4$ nanopowder. Then, aqueous solutions of metal nitrates and EDTA were mixed in a molar ratio of total metal ions: EDTA 1:1. The mixture was then evaporated to dryness on a hot plate at ~110 ^{0}C to obtain precursor powder. The precursor powder thus obtained was then calcined in air at 450 ^{0}C for 2:30 h to obtain pure Ni$_{0.8}$Zn$_{0.2}$Fe$_2$O$_4$ nanopowder. Before calcination, 3-4 drops of 10% aqueous solution of NH$_4$NO$_3$ was mixed with the precursor to facilitate the oxidation of the carbonaceous mass during calcination.

6.1.3 Synthesis of benzoxazine monomer (BA)

Benzoxazine monomer was synthesized as per the procedure described in the section 2.1.2 (Experimental procedure for material synthesis) of Chapter 2.

6.1.4 Preparation of benzoxazine-Ni$_{0.8}$Zn$_{0.2}$Fe$_2$O$_4$ nanocomposites (BA-NZF) [220, 266]

Benzoxazine-Ni$_{0.8}$Zn$_{0.2}$Fe$_2$O$_4$ nanocomposite was prepared as per the procedure described in the section 3.1.4 (Experimental procedure for material synthesis) of Chapter 3. Various compositions of nanocomposites, prepared by using BA and NZF are listed in Table 6.1. Dynamic light scattering studies indicated that the average sizes of these benzoxazine coated Ni$_{0.8}$Zn$_{0.2}$Fe$_2$O$_4$ nanoparticles were in the range of 74-119 nm. TEM micrograph of the nanocomposite (Figure 6.1) clearly shows that coating of polybenzoxazine over Ni$_{0.8}$Zn$_{0.2}$Fe$_2$O$_4$ nanoparticle.
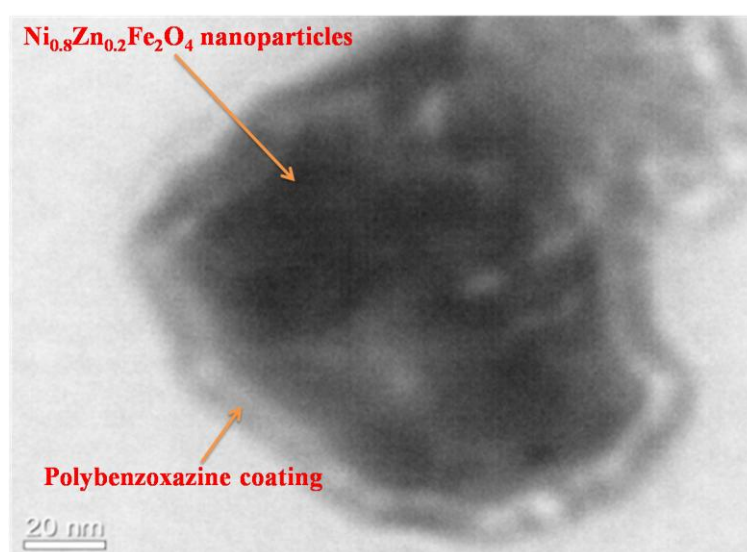
Fig 6.1 TEM micrograph of Ni$_{0.8}$Zn$_{0.2}$Fe$_2$O$_4$-polybenzoxazine (50:50) nanocomposite.

6.1.5 Preparation of LLDPE-LgM-PB-NZF composites (L-LgM-PB-NZF) [266]

LLDPE-LgM-PB-NZF composite was prepared as per the procedure described in the section 3.1.5 (Experimental procedure for material synthesis) of Chapter 3. Composites, having different compositions of NZF, PB and LLDPE were prepared as listed in Table 6.1.

Table 6.1 Compositions of prepared BA-NZF and L-LgM-PB-NZF composites.

Sample code	LLDPE (wt%)	LgM (wt%)	PB (wt%)	Ni$_{0.8}$Zn$_{0.2}$Fe$_2$O$_4$ (wt%)
BA-NZF (70:30)	--	--	70	30
BA-NZF (50:50)	--	--	50	50
BA-NZF (30:70)	--	--	30	70
47.5L-5LgM-47.5PB	47.5	5	47.5	--
47.5L-5LgM-33.25PB-14.25NZF	47.5	5	33.25	14.25
47.5L-5LgM-23.75PB-23.75NZF	47.5	5	23.75	23.75
47.5L-5LgM-14.25PB-33.25NZF	47.5	5	14.25	33.25

SEM micrograph of the surface of a cross section of the composites (Figure 6.2) shows that polybenzoxazine coated Ni$_{0.8}$Zn$_{0.2}$Fe$_2$O$_4$ nanoparticles are embedded within the polymeric matrix.

Fig 6.2 SEM micrograph of the composites shows that Ni$_{0.8}$Zn$_{0.2}$Fe$_2$O$_4$ nanoparticles are dispersed within the polymeric matrix. Polybenzoxazine coated Ni$_{0.8}$Zn$_{0.2}$Fe$_2$O$_4$ nanoparticles are marked by the circles.

6.2 Results and Discussion

6.2.1 Characterization of Ni$_{0.8}$Zn$_{0.2}$Fe$_2$O$_4$ nanoparticles

6.2.1.1 X-Ray Diffraction Analysis

A room temperature X-Ray diffraction spectrum of Ni$_{0.8}$Zn$_{0.2}$Fe$_2$O$_4$ is shown in Figure 6.3. Prepared precursor was calcined at 450 ^{0}C for 2:30 h for producing pure single-phase Ni$_{0.8}$Zn$_{0.2}$Fe$_2$O$_4$ nanopowder. In the X-Ray diffraction spectra of calcined Ni$_{0.8}$Zn$_{0.2}$Fe$_2$O$_4$ nanopowder, the presence of peaks at 2θ = 18.50^0, 30.10^0, 35.5^0, 36.1^0, 43.3^0, 53^0, 57.3^0 and 62^0 corresponding to (111), (220), (311), (222), (400), (422), (511), and (440) diffraction planes confirmed the formation of a single-phase Ni$_{0.8}$Zn$_{0.2}$Fe$_2$O$_4$, with a spinal structure (JCPDS 08-0234) [301]. The crystallite size of the powder was determined by using Scherrer's equation [238], and it was found that the average crystallite size is ~24 nm.
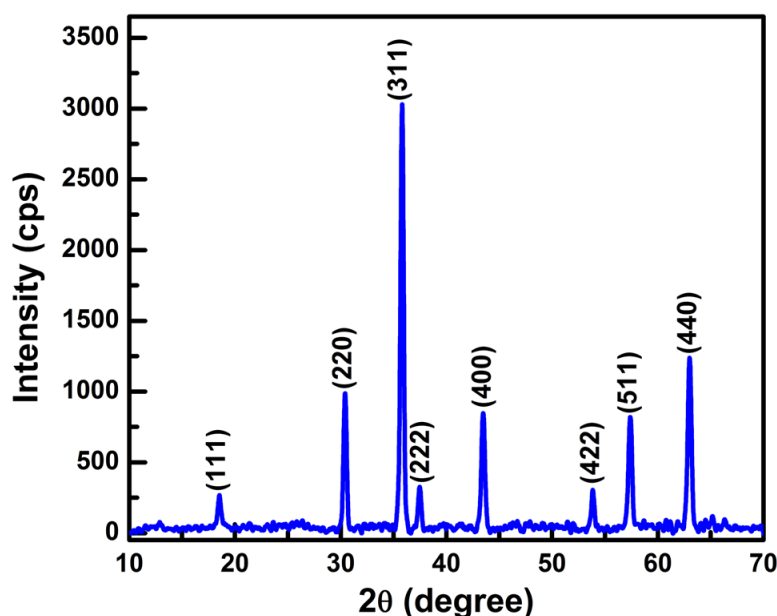
Fig 6.3 XRD patterns of Ni$_{0.8}$Zn$_{0.2}$Fe$_2$O$_4$ powder obtained by calcining the precursor at 450 ^{0}C for 2:30 h.

6.2.1.2 Particle Size and TEM Analysis of Ni$_{0.8}$Zn$_{0.2}$Fe$_2$O$_4$ nanopowder

The differential intensity related to particle size distributions of the as-synthesized Ni$_{0.8}$Zn$_{0.2}$Fe$_2$O$_4$ nanopowder obtained from DLS study at 30 ^{0}C is shown in Figure 6.4 (a). It is clearly indicate that Ni$_{0.8}$Zn$_{0.2}$Fe$_2$O$_4$ nanoparticles exhibited a single nodal distribution with the main peak averages around 10.6 ± 7.1 nm. The cumulant mean diameter of the particles was 30 nm with a polydespersity index of 0.128. Figure 6.4 (b) illustrated a TEM micrograph of the calcined powder where the average particle size was estimated to be ∼35 nm.
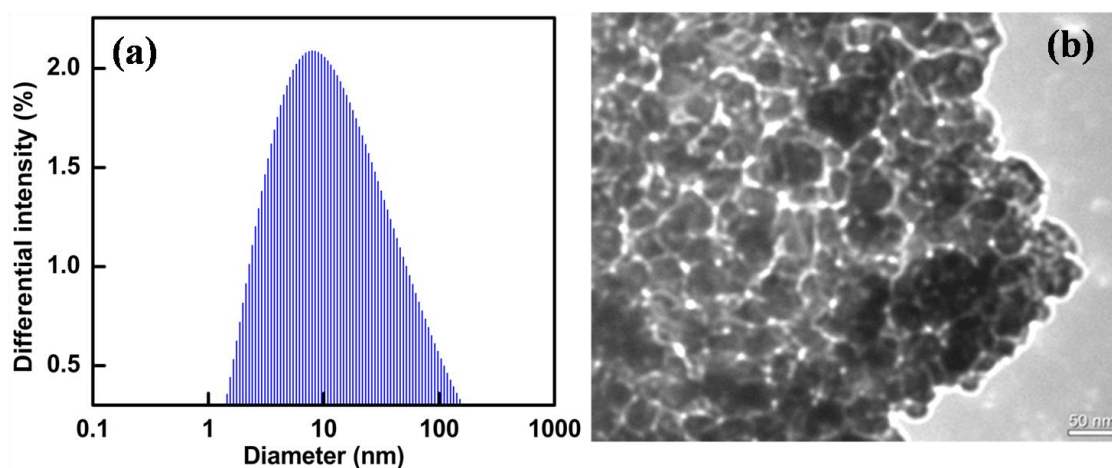
Fig 6.4 (a) Particle size distribution and (b) TEM micrograph of synthesized Ni$_{0.8}$Zn$_{0.2}$Fe$_2$O$_4$ nanopowder.

6.2.1.3 Magnetization Measurement

Room temperature saturation magnetization (M$_s$) and coercivity (H$_c$) of the as-synthesized Ni$_{0.8}$Zn$_{0.2}$Fe$_2$O$_4$ nanoparticles was measured and the hysteresis loop is shown in Figure 6.5. Ni$_{0.8}$Zn$_{0.2}$Fe$_2$O$_4$ nanoparticles exhibited ferromagnetic behavior with a coercivity (H$_c$) of 125.17 Oe and a saturation magnetization (M$_s$) of 38.31 emu/g. These values are comparable with the values reported by other authors using different preparation techniques which are summarized in Table 6.2 [302].
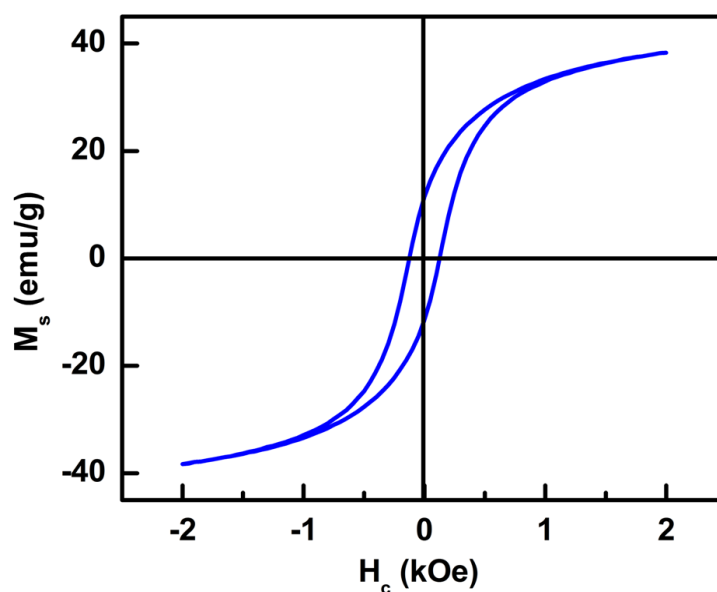
Fig 6.5 Room-temperature hysteresis loop for Ni$_{0.8}$Zn$_{0.2}$Fe$_2$O$_4$ nanopowder.

Table 6.2 Comparison of saturation magnetization M_s and coercivity H_c of $Ni_{1-x}Zn_xFe_2O_4$ particles prepared by different synthesis methods [302].

Synthesis Method	Composition	M_s (emu/g or G)	H_c (Oe)	Reference
Conventional ceramic method (Bulk sample)	$Ni_{1-x}Zn_xFe_2O_4$ ($0.20 \leq x \leq 0.67$)	283-292 G	0.40-6.8	[89]
Coprecipitation	$Ni_{0.50}Zn_{0.50}Fe_2O_4$	SPM	----	[303]
Glyoxylate Precursor	$Ni_{0.35}Zn_{0.65}Fe_2O_4$	30-60	10-41	[304]
Reverse Micelle	$Ni_{0.20}Zn_{0.44}Fe_{2.36}O_4$	SPM	----	[305]
Reverse Micelle	$Ni_{0.50}Zn_{0.50}Fe_2O_4$	SPM	----	[306]
Autocombustion	$Ni_{0.50}Zn_{0.50}Fe_2O_4$	25-75	$\sim$35-100	[307]
Citrate based Sol-gel	$Ni_{1-x}Zn_xFe_2O_4$ ($0.20 \leq x \leq 0.60$)	63-73	1.77-6.2	[308]
Sol-gel autocombustion	$Ni_xZn_{1-x}Fe_2O_4$ ($0.20 \leq x \leq 1$)	20-69	33-158	[309]
Combustion	$Ni_{1-x}Zn_xFe_2O_4$ ($0 \leq x \leq 0.70$)	39-47	0-6990	[310]
EDTA-based precursor method	$\mathbf{Ni_{0.8}Zn_{0.2}Fe_2O_4}$	**38.31**	**125.17**	**This work** [266]

6.2.2 Characterization of PB-NZF nanocomposite and L-LgM-PB-NZF composites

6.2.2.1 X-Ray Diffraction Analysis

The room temperature wide angle powder X-Ray diffraction spectra of as-synthesized NZF nanopowder, PB-NZF nanocomposite and L-LgM-PB-NZF composite are shown in Figure 6.6. The XRD spectra of PB-NZF nanocomposite the presence of all characteristic peaks of NZF conforms that the spinel phase of NZF remain preserved in the PB-NZF nanocomposite (Figure 6.6 (b)). The XRD spectra of L-LgM-PB-NZF show all characteristic peaks of NZF along with two strong diffraction peaks of LLDPE at $2\theta = 21.36^0$ and 23.63^0 assigned to orthoromphic crystallites diffraction planes (110) and (200), respectively (Figure 6.6 (c), (d), (e)) [223, 220, 227]. The presence of these characteristic peaks of LLDPE in the composite clearly indicates that the crystalline structure of LLDPE remain unchanged upon blending with different weight percent of PB-NZF nanocomposite. However, the intensity of the crystalline peaks of LLDPE varied with compositions. These XRD spectra of the composites also confirmed that, the pure crystalline phase of NZF remained preserved in the composite with no impurity phase formation during the melt blending process.
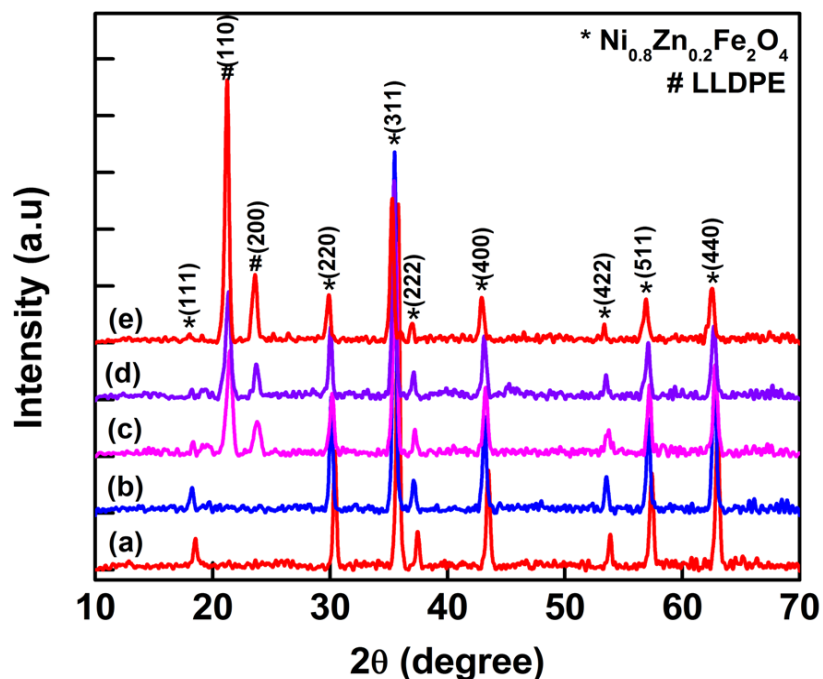
Fig 6.6 XRD spectra of (a) Ni$_{0.8}$Zn$_{0.2}$Fe$_2$O$_4$ powder, (b) PB-NZF (50:50) nanocomposite, (c) 47.5L-5LgM-14.25PB-33.25NZF composite, (d) 47.5L-5LgM-23.75PB-23.75NZF composite, (e) 47.5L-5LgM-33.25PB-14.25NZF composite. (* NZF and # LLDPE)

6.2.2.2 Thermal Analysis

In the DSC thermogram of benzoxazine monomer (BA) an exothermic peak at ~205 ^{0}C was observed, which was due to ring opening polymerization of benzoxazine ring (Figure 6.7 (a)) [228-231]. In case of PB-NZF this exothermic curing peak of benzoxazine shifted to the lower temperature at ~182 ^{0}C (Figure 6.7 (b)). This may due to the catalytic effect of NZF towards the thermal curing of benzoxazine [251, 252]. In the DSC thermogram of pure LLDPE (Figure 6.7 (c)) an endothermic peak at ~124 ^{0}C, corresponding to its melting temperature [227] and an exothermic peak at ~224 ^{0}C, which may be attributed to the beginning of the thermal oxidative decomposition [232, 233] of LLDPE were observed (Figure 6.7 (c)). In case of PB containing LLDPE composites (47.5L-5LgM-47.5PB) (Figure 6.7 (d)) beginning of thermal oxidative decomposition occurred at ~283 ^{0}C, which is higher than that of pure LLDPE. These facts indicated that the presence of PB enhanced the thermal stability of LLDPE-LgM-PB composites. However, presence of NZF slightly lowered the thermal oxidative decomposition temperature of the composite (~257 ^{0}C) (Figure 6.7 (e)). This might be due to the catalytic effect of NZF on thermal degradation of polymeric matrix [251, 252]. In the DSC curves of final composites (L-LgM-PB-NZF) (Figure 6.7 (e)), the endothermic peak at ~124 ^{0}C, corresponding to the melting temperature of LLDPE was

present. The exothermic peak of thermal curing of BA was not observed, which indicated that in the final composites all BA monomers polymerized to PB during processing at 200 ^{0}C.
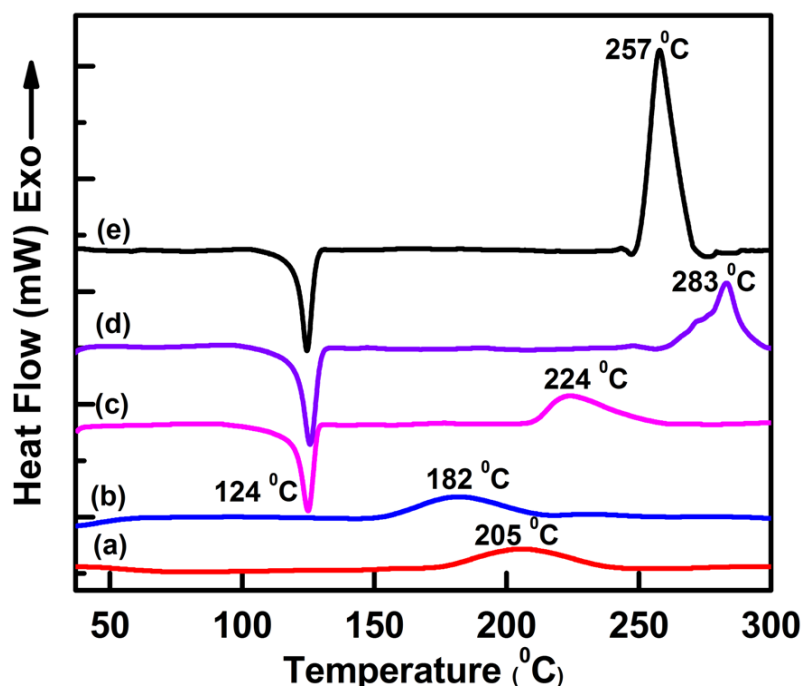
Fig 6.7 DSC thermogram of (a) benzoxazine, (b) BA-NZF (50:50) nanocomposite, (c) LLDPE, (d) 47.5L-5LgM-23.75PB-23.75NZF composite.

From TGA of pure LLDPE, PB and their L-LgM-PB-NZF composites, temperature at 5% weight loss (T$_{5\%}$), 10% weight loss (T$_{10\%}$) and char yield (%) at 800 ^{0}C were determined and summarized in Table 6.3. It was observed that the temperature at 5 and 10% weight loss was found to be decrease with increasing NZF content in the composites. This may be due catalytic effect of NZF on thermal degradation of polymeric matrix [251, 252]. TGA thermogram of LLDPE, PB, PB-NZF, and L-LgM-PB-NZF composite are shown in Figure 6.8. These thermograms revealed the presence of thermally stable PB in L-LgM-PB-NZF composites enhances the overall thermal stability of the composites. The thermal stability of the composite was found to be higher than pure LLDPE but lower than pure PB. The degradation of all the composites was found in the temperature range of 300-500 ^{0}C. The char yield at 800 ^{0}C of the composite was found to increase with increasing NZF content. However, as the melting temperature of LLDPE is ~124 ^{0}C the composites should be used below this temperature.
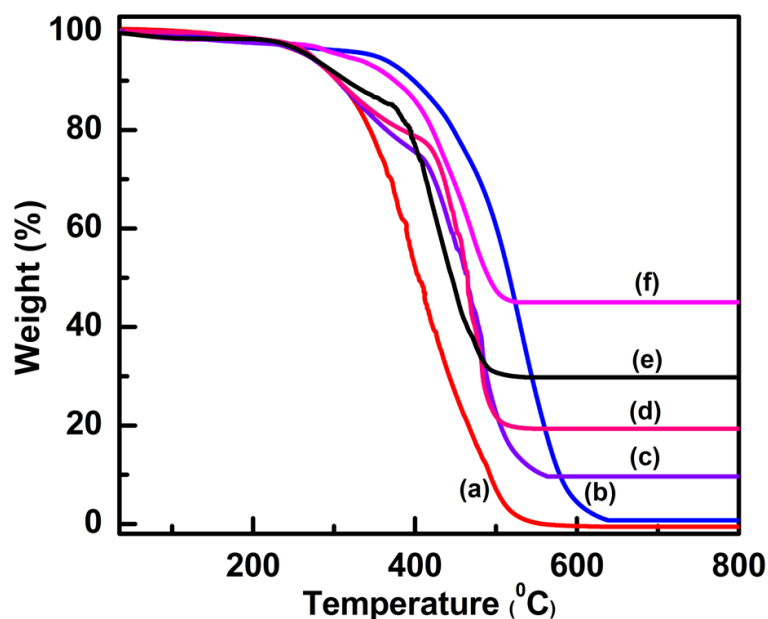
Fig 6.8 Thermograms (TGA) of (a) LLDPE, (b) polybenzoxazine, (c) 47.5L-5LgM-33.25PB-14.25NZF composite, (d) 47.5L-5LgM-23.75PB-23.75NZF composite, (e) 47.5L-5LgM-14.25PB-33.25NZF composite, (f) PB-NZF (50:50) nanocomposite.

Table 6.3 Thermal degradation properties of the neat polymer, PB-NZF nanocomposite and L-LgM-PB-NZF composites.

Sample code	T$_{5\%}$ (^{0}C)	T$_{10\%}$ (^{0}C)	char yield (%) at 800 ^{0}C
Polybenzoxazine	350	400	0
LLDPE	267	305	0
47.5L-5LgM-47.5PB	306	345	0
PB-NZF (70:30)	323	380	25
PB-NZF (50:50)	306	371	44
PB-NZF (30:70)	273	362	66
47.5L-5LgM-33.25PB-14.25NZF	278	312	10
47.5L-5LgM-23.75PB-23.75NZF	272	306	19
47.5L-5LgM-14.25PB-33.25NZF	269	304	30

6.2.2.3 FT-IR Analysis

In the FT-IR spectra of pure benzoxazine monomer (BA) (Figure 6.9 (a)), the peaks at 945 cm^{-1} and 1493 cm^{-1} assigned to the tri-substituted benzene ring and absorption at 1233 cm^{-1} for asymmetric stretching of C-O-C were observed [222, 234]. The methyl group vibration

was found at 2960 cm^{-1} [235]. In case of BA-NZF nanocomposite (Figure 6.9 (b)), all the characteristic bands of benzoxazine were present along with a peak at 559 cm^{-1}, which corresponded to M-O stretching vibration mode of Ni$_{0.8}$Zn$_{0.2}$Fe$_2$O$_4$ [253-255]. In the FT-IR spectra of L-LgM-PB-NZF composites (Figure 6.9 (c)), the disappearance of peaks at 945 cm^{-1} and 1493 cm^{-1} peak (assigned to tri-substituted benzene ring of BA) and appearance of a peak at 1468 cm^{-1} (correspond to the tetra-substituted benzene ring of PB) indicated that the ring opening polymerization of BA occurred during preparation of composites at 200 ^{0}C [181]. Characteristic peaks of LLDPE at 1364 cm^{-1} (-CH$_3$ symmetric vibration) and peaks around 2928 and 2851 cm^{-1}, associated with the C-H stretching vibration [227], along with a peak around 559 cm^{-1} for Ni$_{0.8}$Zn$_{0.2}$Fe$_2$O$_4$ were observed.
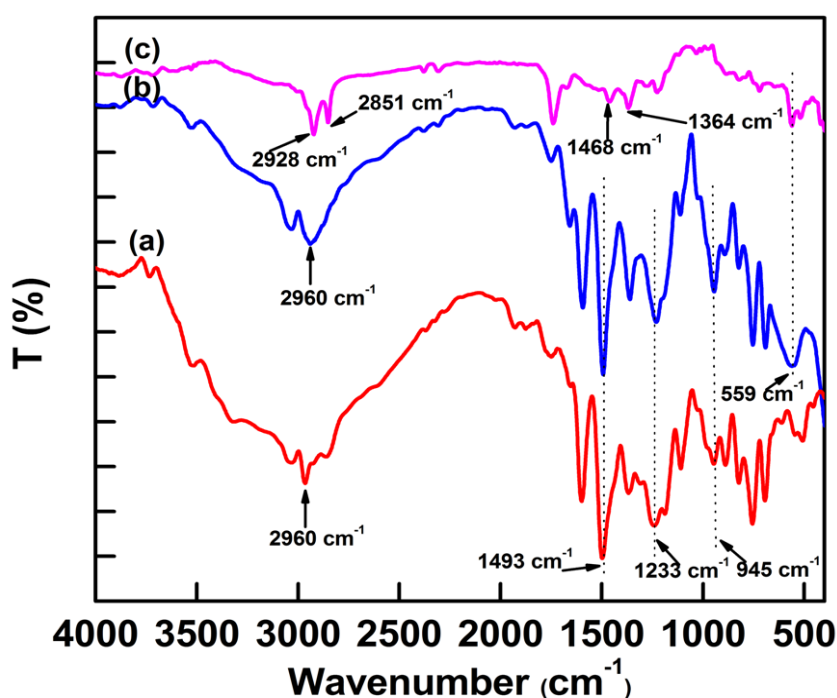
Fig 6.9 FT-IR spectra of (a) benzoxazine monomer, (b) BA-NZF (70-30) nanocomposite, (c) 47.5L-5LgM-33.25PB-14.25NZF composite.

6.2.2.4 Mechanical Properties

To evaluate the mechanical properties of the prepared L-LgM-PB-NZF composites we have performed tensile tests and three point bending flexural tests. Tensile stress-strain curves of PB, LLDPE, 47.5L-5LgM-47.5PB blend and L-LgM-PB-NZF composite are shown in Figure 6.10. It was observed that, pure polybenzoxazine possessed high tensile strength (47.05 MPa) and less elongation at break (2.2%), while LLDPE showed low tensile strength (16.75 MPa) and significantly more elongation at break (57.77%). The blend, composed of LLDPE and PB

with additional LLDPE-*g*-MA (47.5L-5LgM-47.5PB), exhibited higher tensile strength (23.81 MPa) than pure LLDPE and more elongation at break (6.11%) than pure polybenzoxazine. This may be due to the fact that the presence of compatibilizer on the interface allows a better stress transfer across the phase boundary and provides better dispersion of the applied stress which leads to enhanced mechanical properties [236, 226]. SEM micrograph of the 47.5L-5LgM-23.75PB-23.75NZF composite before tensile testing (Figure 6.11) showed the homogeneous polymeric matrix of the composite and no phase separation between PB and LLDPE in presence of LgM compatibilizer. It was observed that loading of 14.25 wt% NZF nanoparticle in polymeric matrix (47.5L-5LgM-33.25PB-14.25NZF) resulted in increase of elongation at break in comparison with 47.5L-5LgM-47.5PB, but decrease in tensile strength. When NZF nanoparticle content in the composite is high, nanoparticles act as defects and the higher concentration of defects caused by the higher concentration of NZF nanoparticles resulted in agglomeration of the particles, which causes to increase the interfacial tension. Therefore, loading stress was not easily transferred from matrix to particles and ultimately tensile strength of the L-LgM-PB-NZF composites decreased with increasing NZF content [256-259]. However, the tensile strength of the composites was higher than that of pure LLDPE. Tensile properties of L-LgM-PB-NZF composites are listed in Table 6.4.
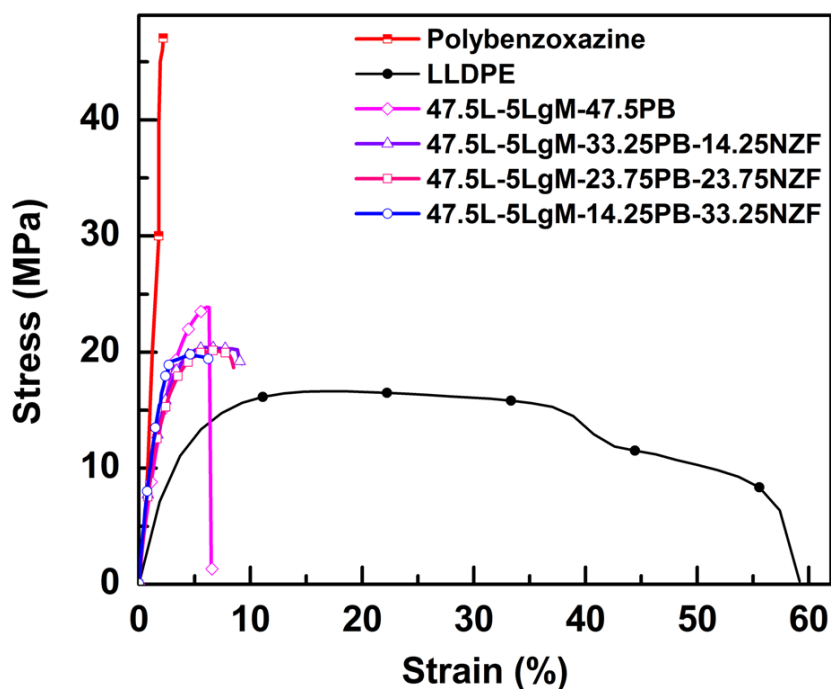
Fig 6.10 Tensile stress-strain curves of neat polymer, blend and L-LgM-PB-NZF composites.
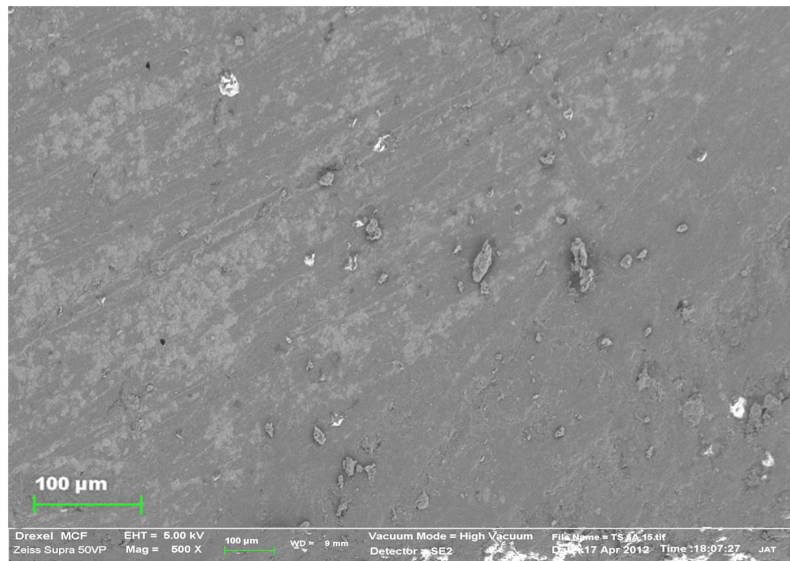
Fig 6.11 SEM micrograph of surface 47.5L-5LgM-23.75PB-23.75NZF composite before tensile testing.

Table 6.4 Tensile properties of the neat polymer, blend and L-LgM-PB-NZF composites.

Sample code	Tensile strength (MPa)	Tensile modulus (GPa)	Elongation at break (%)
LLDPE	16.75	0.236	57.77
Polybenzoxazine	47.05	3.6	2.2
47.5L-5LgM-47.5PB	23.81	1.071	6.11
47.5L-5LgM-33.25PB-14.25NZF	20.38	0.954	9.20
47.5L-5LgM-23.75PB-23.75NZF	20.20	0.937	8.48
47.5L-5LgM-14.25PB-33.25NZF	19.80	0.912	6.26

From the flexural stress-strain curves of PB, LLDPE, 47.5L-5LgM-47.5PB blend and L-LgM-PB-NZF composite are shown in Figure 6.12, it was observed that L-LgM-PB-NZF composites possessed higher flexural strength than pure LLDPE but less than 47.5L-5LgM-47.5PB blend. However, it is important to note that the toughness (area under the stress-strain curve) of the composites was higher than that of pure polybenzoxazine, pure LLDPE, and 47.5L-5LgM- 47.5PB blend. This finding revealed that L-LgM-PB-NZF composites have the potential to be used in structural applications. Flexural properties of the neat polymers and composites are summarized in Table 6.5.
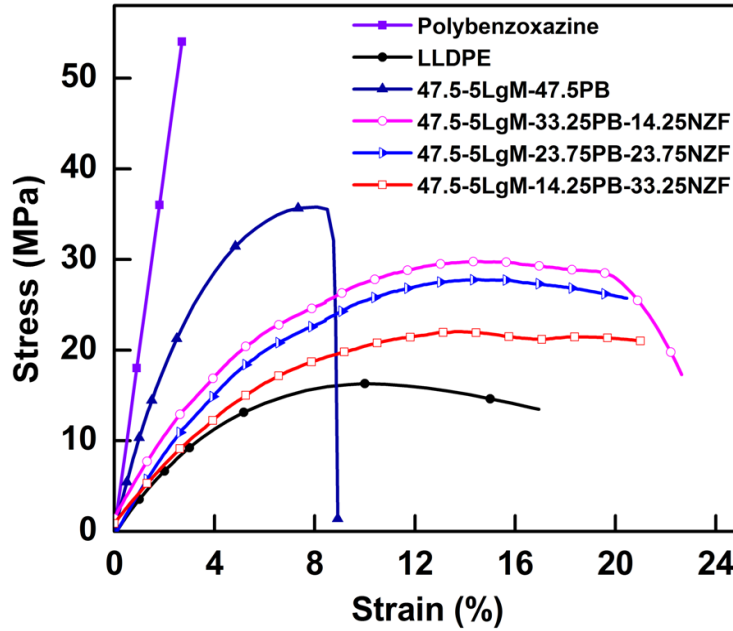
Fig 6.12 Flexural stress-strain curves of neat polymer, blend and L-LgM-PB-NZF
composites.

Table 6.5 Flexural properties of the neat polymer, blend and L-LgM-PB-NZF composites.

Sample code	Flexural strength (MPa)	Flexural modulus (GPa)	Toughness (MPa)
LLDPE	16.33	0.403	0.274
Polybenzoxazine	54.06	1.928	0.439
47.5L-5LgM-47.5PB	35.75	1.236	0.244
47.5L-5LgM-33.25PB-14.25NZF	29.76	0.951	0.538
47.5L-5LgM-23.75PB-23.75NZF	27.85	0.937	0.496
47.5L-5LgM-14.25PB-33.25NZF	22.15	0.915	0.448

6.2.2.5 SEM Analysis of Fractured Surfaces

The morphology of the fractured surface of the samples was also investigated by SEM.
Figure 6.13 represents the micrographs of fractured surfaces of the composites after tensile
test. It was observed that for the sample composed of LLDPE, LgM and PB (47.5L-5LgM-
47.5PB), fibril microstructure formed in the fractured surface during fracture under tensile
strain (Figure 6.13 (a)), but for NZF loaded composite samples voids were formed due to
delamination of NZF from polymeric matrix (Figure 6.13 (b), (c), (d)). With increasing NZF
content in the composites larger void formation occurred. This might be due to the fact that

when NZF loading is high in the composite, they formed agglomerates and when these agglomerates pulled out from polymeric matrix large voids formed. This effect was pronounced for the composites having larger NZF loading and large voids were observed in their fractured surfaces (Figure 6.13 (c), (d)). This type of void formation was not observed for the samples (47.5L-5LgM-47.5PB) which did not contain any NZF.
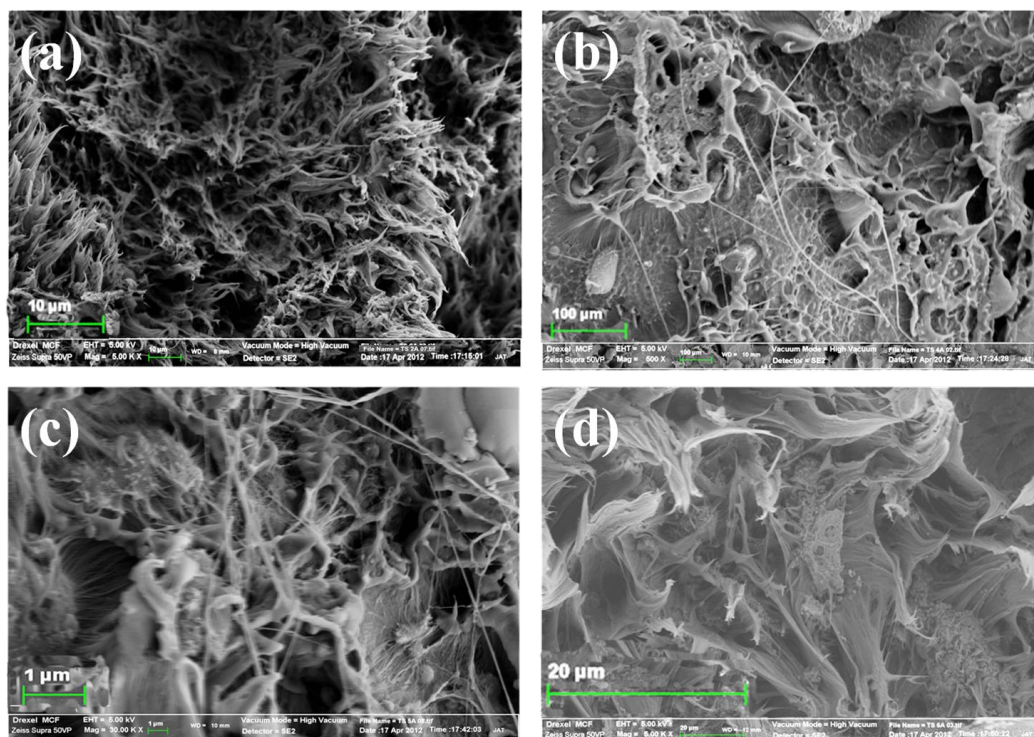
Fig 6.13 SEM micrographs of fractured surfaces of composites after tensile testing (a) 47.5L-5LgM-47.5PB composite, (b) 47.5L-5LgM-33.25PB-14.25NZF composite, (c) 47.5L-5LgM-23.75PB-23.75NZF composite, (d) 47.5L-5LgM-14.25PB-33.25NZF composite.

6.2.2.6 Magnetization Measurement

The variation of magnetic properties, in terms of saturation magnetization (M_s) and coercivity (H_c), with the composition of composites were investigated by using a VSM at room temperature with an applied field of 2000 Oe. Figure 6.14 shows the hysteresis loops obtained for pure Ni$_{0.8}$Zn$_{0.2}$Fe$_2$O$_4$ nanoparticles, BA-NZF and series of L-LgM-PB-NZF composites and the values of M_s and H_c are summarized in Table 6.6. The saturation magnetization (M_s) and coericivity (H_c) values of Ni$_{0.8}$Zn$_{0.2}$Fe$_2$O$_4$ nanoparticles were 38.31 emu g^{-1} and 125.17 Oe, respectively. It was observed that when Ni$_{0.8}$Zn$_{0.2}$Fe$_2$O$_4$ nanoparticles were mixed with benzoxazine (BA-NZF samples), M_s value of the samples were decreased.

In the L-LgM-PB-NZF composites the same trend was also observed. This decrease of M$_s$ value with decreasing Ni$_{0.8}$Zn$_{0.2}$Fe$_2$O$_4$ loading in the composition of composite is quite obvious because the composite is composed of pure magnetic nanoparticles and non-magnetic polymer. Interestingly, it was observed that in all cases of composites the value of H$_c$ increased with decreasing amount of NZF in the composites. For example, H$_c$ of pure Ni$_{0.8}$Zn$_{0.2}$Fe$_2$O$_4$ is 125.17 Oe and H$_c$ of 14.25 wt% NZF composites is 170.64 Oe. This might be due to the fact that dispersion of Ni$_{0.8}$Zn$_{0.2}$Fe$_2$O$_4$ nanoparticles within the polymeric matrix caused to decrease interparticle dipolar interaction arising from the increased interparticle distance within the single domain as compared to the close contact of the pure NZF nanoparticles, and also due to the polymer-particle interfacial effect [262-264]. Similar effect was also reported by Guo et al., for Fe$_2$O$_3$ nanoparticle reinforced vinyl-ester resin nanocomposites [300].
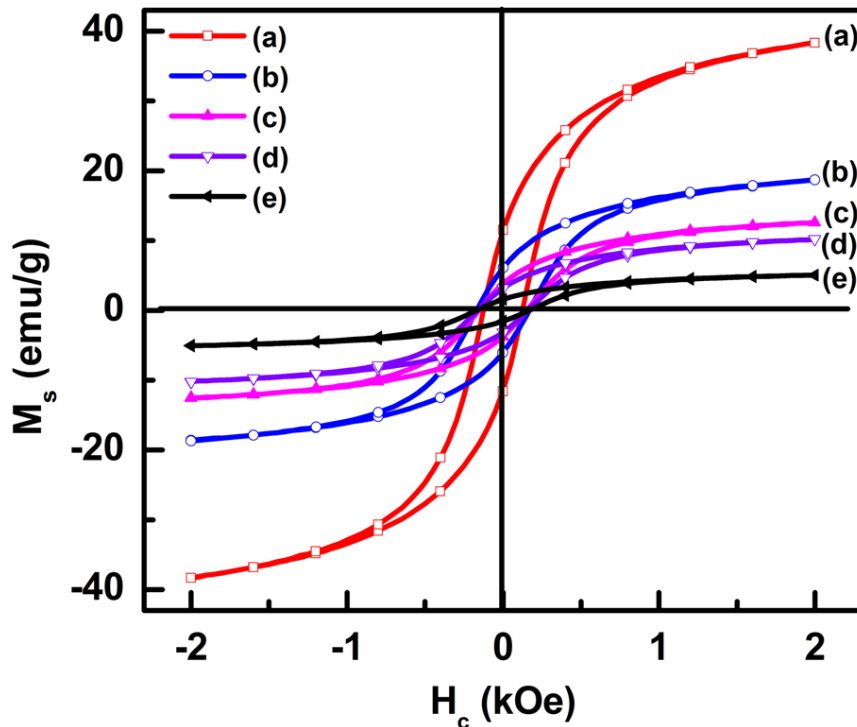
Fig 6.14 Magnetization curves for (a) Ni$_{0.8}$Zn$_{0.2}$Fe$_2$O$_4$ powder, (b) PB-NZF (50:50) nanocomposite, (c) 47.5L-5LgM-14.25PB-33.25NZF composite, (d) 47.5L-5LgM-23.75PB-23.75NZF composite, (e) 47.5L-5LgM-33.25PB-14.25NZF composite.

Table 6.6 Magnetic properties of PB-NZF and L-LgM-PB-NZF composite.

Sample code	M_s (emu/g)	H_c (Oe)
$Ni_{0.8}Zn_{0.2}Fe_2O_4$	38.31	125.17
PB-NZF (70:30)	12.01	154.64
PB-NZF (50:50)	18.67	167.50
PB-NZF (30:70)	25.49	143.18
47.5L-5LgM-33.25PB-14.25NZF	5.05	170.64
47.5L-5LgM-23.75PB-23.75NZF	10.16	161.61
47.5L-5LgM-14.25PB-33.25NZF	12.58	153.58

Figure 6.15 demonstrates that a film of L-LgM-PB-NZF composite is attached with a bar magnet indicating its magnetic nature and both ends of the film can be gripped by a tweezer by easily bending it due to its mechanical flexibility. This shows that the composites reported here possess magnetic property along with mechanical flexibility.
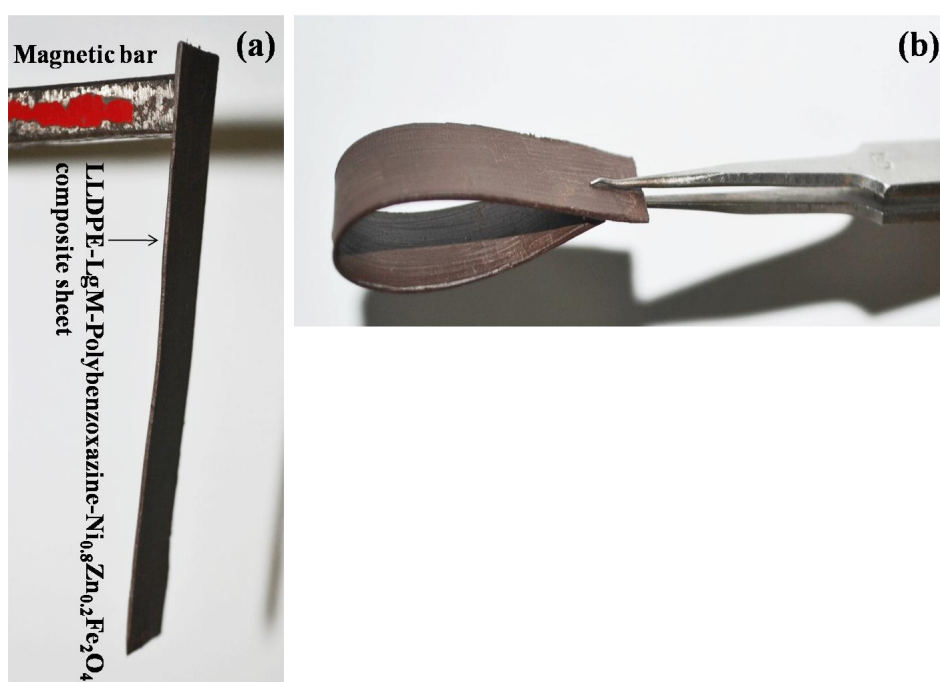
Fig 6.15 LLDPE-LgM-Polybenzoxazine-$Ni_{0.8}Zn_{0.2}Fe_2O_4$ composite sheets exhibiting (a) magnetic nature, (b) mechanical flexibility.

6.3 Summary of Results

1. $Ni_{0.8}Zn_{0.2}Fe_2O_4$ nanopowder was successfully synthesized by using EDTA precursor based synthesis method.

2. Major thermal decomposition of the precursor was complete at ~450 ^{0}C.

3. Single phase $Ni_{0.8}Zn_{0.2}Fe_2O_4$ was formed at a calcination temperature of 450 ^{0}C for 2:30 h in air atmosphere.

4. Average particle size of $Ni_{0.8}Zn_{0.2}Fe_2O_4$ nanopowder was ~30 nm.

5. $Ni_{0.8}Zn_{0.2}Fe_2O_4$ nanoparticles exhibited ferromagnetic behaviour with a coercivity (H_c) of 125.17 Oe and a saturation magnetization (M_s) of 38.31 emu/g.

6. XRD analysis of the final composites confirmed the presence of single phase $Ni_{0.8}Zn_{0.2}Fe_2O_4$ in the composite.

7. Prepared L-LgM-PB-NZF composites showed better thermal stability than pure LLDPE.

8. Variation of $Ni_{0.8}Zn_{0.2}Fe_2O_4$ nanoparticles loading (14.25 to 33.25 wt%) did not affect much in the tensile strength and tensile module of the composites.

9. Composites possessed higher flexural strength than that of pure LLDPE but lower than 47.5L-5LgM-47.5PB blend matrix.

10. Toughness of the L-LgM-PB-NZF composites was higher than that of pure polybenzoxazine, pure LLDPE, and 47.5L-5LgM-47.5PB blend.

11. Saturation magnetization (M_s) value of composites decreased with decreasing $Ni_{0.8}Zn_{0.2}Fe_2O_4$ content in the composites.

12. Value of coercivity (H_c) of the composites increased with decreasing amount of $Ni_{0.8}Zn_{0.2}Fe_2O_4$ in the composites.

<div align="right">

CHAPTER 7

</div>

<div align="center">

Conclusions and

Future Scope of Work

</div>

7.1 Comparative Summary of Results of synthesized single phase nanopowders and their Composites

We have successfully prepared different types of magnetic nanoparticles (such as $CoFe_2O_4$, $BaFe_{12}O_{19}$, $NiFe_2O_4$ and $Ni_{0.8}Zn_{0.2}Fe_2O_4$) by using an aqueous solution based EDTA precursor method. These magnetic nanoparticles were blended with polybenzoxazine and LLDPE to prepare nanocomposites which possessed structural flexibility as well as magnetic properties. The important results have been summarized in Table 7.1 and Table 7.2.

Table 7.1 Comparative summary of results for nanostructured $CoFe_2O_4$, $BaFe_{12}O_{19}$, $NiFe_2O_4$ and $Ni_{0.8}Zn_{0.2}Fe_2O_4$ synthesized by EDTA precursor based method.

Characterization Techniques	Synthesized Material	Obtained Results
Thermal analysis	$CoFe_2O_4$ nanopowder	Complete decomposition of carbonaceous mass of the precursor occurred within 400 ^{0}C in air atmosphere.
	$BaFe_{12}O_{19}$ nanopowder	Complete decomposition of carbonaceous content of the precursor occurred in between 300 and 450 ^{0}C.
	$NiFe_2O_4$ nanopowder	Complete decomposition of carbonaceous content of the precursor occurred up to 450 ^{0}C.
	$Ni_{0.8}Zn_{0.2}Fe_2O_4$ nanopowder	Complete decomposition of the precursor occurred at ~450 ^{0}C in air atmosphere.
XRD Analysis		Formation of single phase ferrite nanopowders occurred due to calcination of precursors in air.
	$CoFe_2O_4$ nanopowder	at 550 ^{0}C for 4 h
	$BaFe_{12}O_{19}$ nanopowder	at 850 ^{0}C for 4 h
	$NiFe_2O_4$ nanopowder	at 550 ^{0}C for 4 h
	$Ni_{0.8}Zn_{0.2}Fe_2O_4$ nanopowder	at 450 ^{0}C for 2:30 h
		Average particle size (nm) ($\pm$ 5 nm)
	$CoFe_2O_4$ nanopowder	~12 nm

Particle size analysis	$BaFe_{12}O_{19}$ nanopowder	~15 nm	
	$NiFe_2O_4$ nanopowder	~23 nm	
	$Ni_{0.8}Zn_{0.2}Fe_2O_4$ nanopowder	~30 nm	
Magnetic Measurements		M_s (emu/g)	H_c (Oe)
	$CoFe_2O_4$ nanopowder	67.55	1645.24
	$BaFe_{12}O_{19}$ nanopowder	56.50	4913.94
	$NiFe_2O_4$ nanopowder	30.70	158.30
	$Ni_{0.8}Zn_{0.2}Fe_2O_4$ nanopowder	38.31	125.17

Table 7.2 Comparative summary of results for flexible magnetic nanocomposite composed of LLDPE, Polybenzoxazine and ferrite nanoparticles.

Characterization techniques	Material	Results	
XRD Analysis	L-LgM-PB matrix composite	XRD spectra of the composites conformed that characteristic peak of LLDPE are presents along with amorphous broad peak of polybenzoxazine.	
	L-LgM-PB-CF composite	XRD spectra of the composites conformed that single phase nanosized ferrite particles are present in the composites.	
	L-LgM-PB-BHF composite		
	L-LgM-PB-NF composite		
	L-LgM-PB-NZF composite		
Thermal analysis	L-LgM-PB matrix blend	Thermal analysis showed that presence of polybenzoxazine enhanced the thermal stability of the composites. In presence of ferrite nanoparticles, the exothermic curing peak of benzoxazine monomer shifted to a lower temperature.	
	L-LgM-PB-CF composite		
	L-LgM-PB-BHF composite		
	L-LgM-PB-NF composite		
	L-LgM-PB-NZF composite		
Particle size analysis		Average particle size (nm) (± 5 nm)	
	PB-CF nanocomposite	100 to 200 nm	Average particle size of prepared polybenzoxazine-ferrite nanocomposite varies with the composition of the composites.
	PB-BHF nanocomposite	121 to 160 nm	
	PB-NF nanocomposite	111 to 134 nm	
	PB-NZF nanocomposite	74 to 119 nm	
FT-IR analysis	L-LgM-PB matrix blend	FT-IR spectra indicate that the complete formation of polybenzoxazine from benzoxazine occurred during	
	L-LgM-PB-CF composite		
	L-LgM-PB-BHF		

	composite	blend preparation.
	L-LgM-PB-NF composite	
	L-LgM-PB-NZF composite	
Mechanical testing	L-LgM-PB matrix composite	Tensile and flexural testing of the composites revealed that 5 wt% is the optimum amount of compatibilizer that can be used in composite preparation.
	L-LgM-PB-CF composite	From tensile and flexural testing of the composites it was observed that the composites possessed higher tensile and flexural strength than pure LLDPE and grater elongation at break than pure polybenzoxazine. Toughness of the composites was higher than that of pure polybenzoxazine, pure LLDPE, and L-LgM-PB blend.
	L-LgM-PB-BHF composite	
	L-LgM-PB-NF composite	
	L-LgM-PB-NZF composite	
SEM Study	L-LgM-PB matrix composite	SEM micrographs of the composites also showed the enhancement of homogeneity of LLDPE and polybenzoxazine phases with increasing amount of LgM.
	L-LgM-PB-CF composite	SEM micrograph of the surface of a cross section of the composite shows that polybenzoxazine coated ferrite nanoparticles are embedded within the polymeric matrix.
	L-LgM-PB-BHF composite	
	L-LgM-PB-NF composite	
	L-LgM-PB-NZF composite	
Magnetic Measurement	L-LgM-PB-CF composite	Magnetic property measurement of the composites indicated that the magnetic property of the composites varied with the nature of MNPs as well as amount of MNPs present in the composites. With increase of MNPs amount in the composite M_s was found to be increased.
	L-LgM-PB-BHF composite	
	L-LgM-PB-NF composite	
	L-LgM-PB-NZF composite	

7.2 Conclusions:

(a)   A simple aqueous solution based EDTA precursor method has been employed for preparation of pure hard ferrite (e.g. $CoFe_2O_4$, $BaFe_{12}O_{19}$) and soft ferrite ($NiFe_2O_4$, $Ni_{0.8}Zn_{0.2}Fe_2O_4$) nanopowders. This method offers following advantages:

(i)   metal alkoxides or complex metal compounds, which are expensive, difficult to handle, synthesize, and sometimes toxic were not used in the developed method.

(ii) strong bases as precipitating agent or organic solvents, etc were not used in this method.

(iii) use of cheap metal nitrates as starting materials and water as solvent helps in reducing the processing cost as compared to other reported wet chemical methods.

(iv) moreover, any elaborate experimental setup is not required for the synthesis of nanopowders by these methods.

(b) A simple method has been developed for preparation of LLDPE-LgM-polybenzoxazine-ferrite nanocomposite. This method is applicable for preparation of hard ferrite as well as soft ferrite nanoparticles containing nanocomposites.

(c) XRD analysis shows that pure ferrite nanoparticles are present in the composite after processing the final composites.

(d) Thermal analysis of the composites indicates that presence of polybenzoxazine enhances the thermal stability of the composites.

(e) Presence of 5wt% LgM in the composite enhances the compatibility between LLDPE and polybenzoxazine, which was reflected in the SEM micrographs analysis and mechanical property study of the composites.

(f) Investigation on magnetic properties of the composites shows that saturation magnetization (M_s) of the composites increases with increasing ferrite nanoparticles loading. Same trend was observed for all types of ferrite nanoparticles containing composites.

(g) Incorporation of MNPs in the composites resulted in decrease in the tensile properties of composites, but variation of loading of MNPs (from 14.25 wt% to 33.25 wt%) did not affect much in the tensile properties. Nature of MNPs (hard or soft ferrite) does not affect much in the mechanical properties of the composite. $CoFe_2O_4$, $BaFe_{12}O_{19}$, $NiFe_2O_4$, $Ni_{0.8}Zn_{0.2}Fe_2O_4$ containing composites exhibited similar type of mechanical properties.

(h) The magnetic properties of these composites can easily be tuned by the judicious choice of the nature of MNPs and their loading level in the composition of the composites.

7.3 Limitations of the Composites:

Though it has been observed that presence of polybenzoxazine enhances the thermal stability of the composites but as the melting temperature of LLDPE is ~124 ^{0}C, the composites should be used below this temperature.

Future Scope of work

(i)   Investigations on the microwave absorption properties of the synthesized nanocomposites, so that they can be used as radar absorbing materials (RAM) in military applications.

(ii) Modification of these composites so that they can be used as coating.

(iii) Investigations on the enhancement of the thermal stability of the composites so that they can be used above 124 ^{0}C.

References:

[1]   Pinnavia T. J., Beall G. W. Polymer-Clay nanocomposites. John Wiley & Sons Ltd, Chichester, West Sussex, England, 2000.

[2]   Harris P. J. F. Carbon nanotube composites. International Materials review. 2204, 49: 31-43.

[3]   Ajayan P. M., Schadler L. S., Braun P. V. Nanocomposite Science and Technology. Wiley: New York, NY, USA, 2003.

[4]   Jordan J., Jacob K. I., Tannenbaum R., Sharaf M. A., Jasiuk I. Experimental trends in polymer nanocomposites-A review. Materials Science and Engineering: A. 2005, 393: 1-11.

[5]   Work W. J., Horie K., Hess M., Stepto R. F. T. Definitions of Terms Related To Polymer Blends, Composites, and Multiphase Polymeric Materials. Pure and Applied Chemistry. 2004, 76: 1985-2007.

[6]   Kawasumi M., Hasegawa N., Kato M., Usuki A., Okada A. Preparation and Mechanical Properties of Polypropylene-Clay Hybrids. Macromolecules. 1997, 30: 6333-6338.

[7]   Sanchez C., Lebeau B., Chaput F., Boilot J. P. Optical Properties of Functional Hybrid Organic-Inorganic Nanocomposites. Advanced Materials. 2003, 15: 1969-1994.

[8]   Zhan G. D., Mukherjee A. K. Carbon Nanotube Reinforced Alumina-Based Ceramics with Novel Mechanical, Electrical, and Thermal Properties. International Journal of Applied Ceramic Technology. 2004, 1: 161-171.

[9]   Alam J., Riaz U., Ahmad S. Effect of Ferro fluid concentration on electrical and magnetic properties of Fe_3O_4/PANI Nanocomposites. Journal of Magnetism and

Magnetic Materials, 2007, 314: 93-99.

[10]   Yeh J. M., Chen C. L., Chen Y. C., Ma C. Y., Lee K. R., Wei Y., Li S. Enhancement of corrosion protection effect of poly(o-ethoxyaniline) via the formation of poly(o-ethoxyaniline)-clay nanocomposite materials. Polymer. 2002, 43: 2729-2736.

[11]   Nowosielski R., Wysłocki J. J., Wnuk I., Sakiewicz P., Gramatyka P. Ferromagnetic properties of polymer nanocomposites containing $Fe_{78}Si_9B_{13}$ powder particles. Journal of Materials Processing Technology. 2005, 162-163: 242-247.

[12]   Lobez J. M., Swager T. M. Radiation Detection: Resistivity Responses in Functional Poly(Olefin Sulfone)/Carbon Nanotube Composites. Angewandte Chemie International Edition. 2010, 49: 95-98.

[13]   Pandey P., Singh S. P., Arya S. K., Sharma A., Datta M., Malhotra B. D. Gold Nanoparticle-Polyaniline Composite films for glucose sensing. Journal of Nanoscience and Nanotechnology. 2008, 8: 3158-3163.

[14]   Giannelis E. P. Polymer Layer Silicate Nanocomposites. Advanced Materials. 1996, 8: 29-35.

[15]   Kojima Y., Usuki A., Kawasumi M., Okada A., Kurauchi T., Kamigaito O. Synthesis of nylon 6-clay hybrid by montmorillonite intercalated with ε-caprolactam. Journal of Polymer Science Part A: Polymer Chemistry. 1993, 31: 983-986.

[16]   Riaz U., Ahmad S. A., Ahmad S., Ashraf S. M. A comparative study on camphorsulphonic acid modified montmorillonite clay based conducting polymer nanocomposites. Polymer Composites. 2009, 31: 906-912.

[17]   Usuki A., Kojima Y., Kawasumi M., Okada A., Fukushima Y., Kurauchi T., Kamigaito O. Synthesis of nylon 6-clay hybrid. Journal of Materials Research. 1993, 8: 1179-1184.

[18]   Kovalchuk A. A., Shchegolikhin A. N., Shevchenko V. G., Nedorezova P. M., Klyamkina A. N., Aladyshev A. M. Synthesis and Properties of Polypropylene/Multiwall Carbon Nanotube Composites. Macromolecules. 2008, 41: 3149-3156.

[19]   Zafar F., Ashraf S. M., Ahmad S. In-situ Development of Zn/Cd-Incorporated Poly (esteramide-urethane) from renewable resource. Journal of Applied Polymer Science, 2008, 110: 584-593.

[20]   Ahmad S., Ahmad S., Agnihotry S. A. Synthesis and characterization of insitu prepared poly(Methylmethacrylate) nanocomposites. Bulletin Material Science. 2007, 30: 31-35.

[21]   Jia Z. J., Wang Z. Y., Xu C. L., Liang J., Wei B. Q., Wu D. H., Zhu S. W. Study on poly(methyl methacrylate)/carbon nanotube composites. Materials Science and Engineering: A. 1999, 271: 395-400.

[22]   Li X. F., Lau K. T., Yin Y. S. Mechanical properties of epoxy-based composites using coiled carbon nanotubes. Composites Science and Technology, 2008, 68: 2876-2881.

[23]   Lan T., Pinnavaia T. J. Clay-Reinforced Epoxy Nanocomposites. Chemistry of Materials. 1994, 6: 2216-2219.

[24]   Gao J. B., Itkis M. E., Yu A. P., Bekyarova E., Zhao B., Haddon R. C. Continuous Spinning of a Single-Walled Carbon Nanotube-Nylon Composite Fiber. Journal of the American Chemical Society. 2005, 127: 3847-3854.

[25]   Fu K. F., Huang W. J., Lin Y., Riddle L. A., Carroll D. L., Sun Y. P. Defunctionalization of Functionalized Carbon Nanotubes. Nano Letters. 2001, 1: 439-441.

[26]   Singhal R., Datta M. Synthesis and characterization of novel poly(o-toluidine) montmorillonite nanocomposites: Effect of surfactant on intercalation. Journal of Applied Polymer Science. 2007, 106: 1909-1916.

[27]   Liu M. H., Zhu T., Li Z. C., Liu Z. F. One-Step in Situ Synthesis of Poly(methyl methacrylate)-Grafted Single-Walled Carbon Nanotube Composites. The Journal of Physical Chemistry C. 2009, 113: 9670-9675.

[28]   Novak B. M. Hybrid Nanocomposite Materials-between inorganic glasses and organic polymers. Advanced Materials. 1993, 5: 422-433.

[29]   Liu Y., Lee J. Y., Hong L. Morphology, Crystallinity, and Electrochemical Properties of In Situ Formed Poly(ethylene oxide)/TiO$_2$ Nanocomposite Polymer Electrolytes. Journal of Applied Polymer Science. 2003, 89: 2815-2822.

[30]   Kim K. M and Chujo Y. Polymer Hybrids with Functionalized Silsesquioxanes via Two Physical Interactions in One System. Journal of Polymer Science Part A: Polymer Chemistry. 2003, 41: 1306-1315.

[31]   Huang X., Brittain W. J. Synthesis and Characterization of PMMA Nanocomposites by Suspension and Emulsion Polymerization. Macromolecules, 2001, 34: 3255-3260.

[32]   Wang G. A., Wang C. C., Chen C. Y. The disorderly exfoliated LDHs/PMMA nanocomposites synthesized by in situ bulk polymerization: The effects of LDH-U on thermal and mechanical properties. Polymer Degradation and Stability. 2006, 91: 2443-2450.

[33]   Liu T. X., Phang I. Y., Shen L., Chow S. Y., Zhang W. D. Morphology and Mechanical Properties of Multiwalled Carbon Nanotubes Reinforced Nylon-6 Composites Macromolecules. 2004, 37: 7214-7222.

[34]   Gorga R. E., Cohen R. E. Toughness Enhancements in Poly(methyl methacrylate) by Addition of Oriented Multiwall Carbon Nanotubes. Journal of Polymer Science Part B: Polymer Physics. 2004, 42: 2690-2702.

[35]   Yuan J. M., Fan Z. F., Chen X. H., Wu Z. J., He L. P. Preparation of polystyrene-multiwalled carbon nanotube composites with individual-dispersed nanotubes and strong interfacial adhesion. Polymer. 2009, 50: 3285-3291.

[36]   Pascual J., Fages E., Fenollar O., Garcia D., Balart R. Influence of the compatibilizer/nanoclay ratio on final properties of polypropylene matrix modified with montmorillonite-based organoclay. Polymer Bulletin. 2009, 62: 367-380.

[37]   Ray S. S., Okamoto M. Polymer/layered silicate nanocomposites: a review from preparation to processing. Progress in Polymer Science. 2003, 28: 1539-1641.

[38]   Nguyen Q. T., Baird D. G. An improved technique for exfoliating and dispersing nanoclay particles into polymer matrices using supercritical carbon dioxide. Polymer. 2007, 48: 6923-6933.

[39]   Nguyen Q. T., Baird D. G. Preparation of Polymer-Clay Nanocomposites and Their Properties. Advances in Polymer Technology. 2006, 25: 270-285.

[40]   Hotta S., Paul D. R. Nanocomposites formed from linear low density polyethylene and organoclays. Polymer. 2004, 45: 7639-7654.

[41]   Santanu R., Surekha D. High solids content semicontinuous microemulsion copolymerization of methylmethacrylate and butylacrylate. Polymer. 1997, 38: 3325-3331.

[42]   Michael D., Bemd T. Polymerization of Styrene in Ternary Microemulsion Using Cationic Gemini Surfactants. Langmuir. 1998, 14: 800-807.

[43]   Xu X. J., Siow K. S., Wong M. K., Gan L. M. Microemulsion Polymerization of styrene using a polymerizable nonionic surfactant and cationic surfactant. Colloid and Polymer Science. 2001, 279: 879-886.

[44]   Papp S., Dekany I. Structural Properties of Palladium nanoparticles embedded in inverse microemulsion. Colloid and Polymer Science. 2001, 279: 449-458.

[45]   Bhawa S., Pokhriyal N. K., Devi S. Translucent nanolatexes through emulsion polymerisation of ethyl acrylate. European Polymer Journal. 2002, 38: 735-744.

[46]   Du H., Chen P., Lin F., Meng F. D., Li N., Tang X. Y. Preparation and assembly of nanosized polymer latex. Materials Chemistry and Physics. 1997, 51: 277-282.

[47]   Pant P., Bhuvaneswari S., Ghosh N. N. Chemical methodologies for preparation of micron and nanometer scale ferrites-A minireview of patents. Recent Patents Nanotechnology. 2008, 2: 8-18.

[48]   Agag T., Takeichi T. Preparation and cure behaviour of organoclay modified ally-functional benzoxazine resin and the properties of their nanocomposites. Polymer Composites. 2008, 29: 750-757.

[49]   Phiriyawirut P., Magaraphan R., Ishida H. Preparation and characterization of polybenzoxazine-clay immiscible nanocomposite. Material Research Innovation. 2001, 4: 187-196.

[50]   Agag T., Takeichi T. Polybenzoxazine-montmorillonite hybrid nanocomposites synthesis and characterization. Polymer. 2000, 41: 7083-7090.

[51]   Agag T., Tsuchiya H., Takeichi T. Novel organic-inorganic hybrids prepared from polybenzoxazine and titania using sol-gel process. Polymer. 2004, 45: 7903-7910.

[52]   Wilson J. L., Poddar P., Frey N. A., Srikanth H., Mohomed K., Harmon J. P. Synthesis and magnetic properties of polymer nanocomposites with embedded

iron nanoparticles. Journal of Applied Physics. 2004, 95: 1439-1443.

[53]   Fang J., Tung L. D., Stokes K. L., He J., Caruntu D., Zhou W. L. Synthesis and magnetic properties of CoPt-poly(methylmethacrylate) nanostructured composite material. Journal of Applied Physics. 2002, 91: 8816-8818.

[54]   Gangopadhyay R., De A. Polypyrrole-ferric oxide conducting nanocomposites: I. Synthesis and characterization. European Polymer Journal. 1999, 35: 1985-1992.

[55]   Prabhakaran T., Hemalatha J. Synthesis and characterization of magnetoelectric polymer nanocomposites. Journal of Polymer Science: B Polymer Physics. 2008, 46: 2418-2422.

[56]   Chen Y. J., Gao P., Zhu C. L., Wang R. X., Wang L. J., Cao M. S. Synthesis, magnetic and electromagnetic wave absorption properties of porous $Fe_3O_4/Fe/SiO_2$ core/shell nanorods. Journal of Applied Physics. 2009, 106: 54303-54304.

[57]   Kim D. K., Toprak M. S., Mikhaylova M., Jo Y. S., Savage S., Lee H. B. Polymeric nanocomposites of complex ferrite. Solid State Phenomena. 2003, 165: 99-100.

[58]   Yang Y. L., Gupta M. C. Novel carbon nanotubepolystyrene foam composites for electromagnetic interference shielding. Nano Letters. 2005, 5: 2131-2134.

[59]   Lopatin A. V., Kazantseva N. E., Yu N., Kazantsev O. A., Dyakonova J., Vil A., Saha P. The Efficiency of Application of Magnetic Polymer Composites as Radio-Absorbing Materials. Journal of Communications Technology and Electronics. 2008, 53: 487-496.

[60]   Srikanth H., Hajndl R., Chirinos C., Sanders J., Sampath A., Sudershan T. S. Magnetic studies of polymer-coated Fe nanoparticles synthesized by microwave plasma polymerization. Applied Physics Letter. 2001, 79: 3503-3505.

[61]   Malini K. A., Anantharaman M. R., Gupta A. Low temperature Mossbauer studies on magnetic nanocomposites. Bulletin of Materials Science. 2004, 27: 361-366.

[62]   Kiskan B., Demirel A. L., Kamer O., Yagci Y. Synthesis and Characterization of Nanomagnetite Thermosets Based on Benzoxazines. Journal of Polymer Science Part A: Polymer Chemistry. 2008, 46: 6780-6788.

[63]   Anantharaman M. R., Malini K. A., Sindhu S., mohammed E. M., Date S. K., Kulkarni S. D., Joy P. A., Kurian P. Tailoring magnetic and dielectric properties of rubber ferrite composites containing mixed ferrites. Bulletin Material Science. 2001, 24: 623-631.

[64]   Jiang J., Ai L. H., Liu L. Y. Poly(aniline-co-o-toluidine)/BaFe$_{12}$O$_{19}$ composite: Preparation and characterization. Materials Letters. 2010, 64: 888-890.

[65]   Ting T. H, Wu K. H. Synthesis, characterization of polyaniline/BaFe$_{12}$O$_{19}$ composites with microwave-absorbing properties. Journal of Magnetism and Magnetic Materials. 2010, 322: 2160-2166.

[66]   Deng J., Ding X., Zhang W., Peng Y., Wang J., Long X., Li P., Chan A. S. C. Magnetic and conducting Fe$_3$O$_4$-cross-linked polyaniline nanoparticles with core-shell structure. Polymer. 2002, 43: 2179-2184.

[67]   Xu P., Han X., Jiang J., Wang X., Li X., Wen A. Synthesis and Characterization of Novel Coralloid Polyaniline/BaFe$_{12}$O$_{19}$ Nanocomposites. Journal of Physical Chemistry C. 2007, 111: 12603-12608.

[68]   Shannigrahin S. R., Pramoda K. P., Nugroho F. A. A. Synthesis and characterizations of microwave sintered ferrite powders and their composite films for practical applications. Journal of Magnetism and Magnetic Materials. 2012, 324: 140-145.

[69]   Boon M. S., Serena Saw W. P., Mariatti M. Magnetic, dielectric and thermal stability of Ni-Zn ferrite-epoxy composite thin films for electronic applications. Journal of

Magnetism and Magnetic Materials. 2012, 324: 755-760.

[70]   Sunny V., Kurian P., Mohanan P., Joy P. A., Anantharaman M. R. A flexible microwave absorber based on nickel ferrite nanocomposite. Journal of Alloys and Compounds. 2010, 489: 297-303.

[71]   Verma A., Saxena A. K., Dube D. C. Microwave permittivity and permeability of ferrite-polymer thick films. Journal of Magnetism and Magnetic Materials. 2003, 263: 228-234.

[72]   Ma R. T., Zhao H. T., Zhang G. Preparation, characterization and microwave absorption properties of polyaniline/$Co_{0.5}Zn_{0.5}Fe_2O_4$ nanocomposite. Materials Research Bulletin. 2010, 45: 1064-1068.

[73]   Dosoudil R., Usakova M., Franek J., Slama J., Olah V. RF electromagnetic wave absorbing properties of ferrite polymer composite materials. Journal of Magnetism and Magnetic Materials. 2006, 304: 755-757.

[74]   Hosseinia S. H., Mohsenib S. H., Asadniac A., Kerdarid H. Synthesis and microwave absorbing properties of polyaniline/$MnFe_2O_4$ nanocomposite. Journal of Alloys and Compounds. 2011, 509: 4682-4687.

[75]   Bayrakdar H. Complex permittivity, complex permeability and microwave absorption Properties of ferrite-paraffin polymer composites. Journal of Magnetism and Magnetic Materials. 2011, 323: 1882-1885.

[76]   Wang Z., Bi H., Liu J., Sun T., Wu X. Magnetic and microwave absorbing properties of polyaniline/γ-Fe_2O_3 nanocomposite. Journal of Magnetism and Magnetic Materials. 2008, 320: 2132-2139.

[77]   Lisjak D., Lintunen P., Hujanen A., Varis T., Bolelli G., Lusvarghi L., Drofenik M. J. M. Hexaferrite/polyethylene composite coatings prepared with flame spraying. Materials Letters. 2011, 65: 534-536.

[78]   Snelling E. C. Soft Ferrites Properties and Applications. ILIFFE Books Ltd., London, 1969.

[79]   Sarangi P. P. Development of Chemical Methodologies for Synthesis of α-Fe$_2$O$_3$ and Ni$_{1-x}$Zn$_x$Fe$_2$O$_4$ ($0 < x < 1$) Nanopowders and Study of their Structural and Physical Properties, Ph.D. Thesis, Birla Institute of Technology and Science, Pilani (Rajasthan), India. 2010.

[80]   Angelakos D. J., Korman M. M. Radiation from Ferrite-Filled Apertures. Proceedings of the Institute of Radio Engineers. 1956, 44: 1463.

[81]   Tyras G., Held G. Radiation from a Rectangular waveguide Filled with Ferrite. Microwave Theory and Techniques, IRE Transactions on. 1958, 6: 268-277.

[82]   Liu Q., Huang H., Lai L., Sun J., Shang T., Zhou Q., Xu Z. Hydrothermal synthesis and magnetic properties of NiFe$_2$O$_4$ nanoparticles and nanorods. Journal of Material Science. 2009, 44: 1187-1191.

[83]   Sepelak V., Bergmann I., Feldhoff A., Heitjans P., Krumeich F., Menzel D. Nanocrystalline nickel ferrite, NiFe$_2$O$_4$: Mechanosynthesis, nonequilibrium cation distribution, canted spin arrangement, and magnetic behavior. Journal of Physical Chemistry C. 2007, 111: 5026-5033.

[84]   Nelson C. E. Ferrite-Tunable Microwave Cavities and the Introduction of a New Reflectionless, Tunable Microwave Filter. Proceedings of the Institute of Radio Engineers. 1956, 44: 1449-1455.

[85]   Smit J. Magnetic Properties of Material. (Inter University Electronics series). McGraw Hill Company, 13, 29: 1971.

[86]   DeMaw D. Ferromagnetic-Core Design and Application Handbook. Prentice-Hall, Englewood Cliffs, New Jersey, 1981.

[87]   Soloman M. A. Evaluation of Magnetic, Dielectric and Mechanical Properties of Rubber Ferrite Composites, Ph.D. Thesis, Cochin University of Science and Technology, Cochin. India. July 2002.

[88]   Sugimoto M. The Past, Present, and Future of Ferrites. Journal of the American Ceramic Society. 1999, 82: 269-280.

[89]   Smit J., Wijn H. P. J., Physical properties of ferromagnetic oxides in relation to their technical applications, Phillip's Technical Library, New York, USA, 1959.

[90]   Snelling. E. C., Giles A. D. Ferries for Inductors and Transformers. Research Studies press Ltd, John Wiley & Sons Inc. New York, 1983.

[91]   Barten P. G., Kaashoek J. 30AX Self-Aligning 1100 In-Line Color TV Display. IEEE Transactions on Consumer Electronics. CE-24, 3 (1978) 481-488.

[92]   Benito G., Morales M. P., Reequena J., Raposo V., Vazquez M., Moya S. Barium hexaferrite monodispersed nanoparticles prepared by the ceramic method. Journal of Magnetism and Magnetic Materials. 2001, 234: 65-72.

[93]   Broek C. A. M., Stuijts A. L. Ferroxdure. Philips Technical Review. 1977, 37: 157-175.

[94]   Verma A., Chatterjee R. Effect of zinc concentration on the structural, electrical and magnetic properties of mixed Mn-Zn and Ni-Zn ferrites synthesized by the citrate precursor technique. Journal of Magnetism and Magnetic Materials. 2006, 306: 313-320.

[95]   Suh J. J., Han Y. H. Quantative analysis of zinc vaporization from manganese zinc ferrites. Journal of the American Ceramic Society. 2003, 85: 765-768.

[96]   Verma A., Goel T. C., Mendiratta R. G., Alam M. I. Dielectric properties of Ni-Zn ferrites prepared by the citrate precursor method. Materials Science and Engineering

B. 1999, 60: 156-162.

[97]   Zhang H., Wang W. W., Li H., Meng S., Li D. A strategy to prepare ultrafine dispersed Fe_2O_3 nanoparticles. Materials Letters. 2008, 62: 1230-1233.

[98]   Upadhyay C., Verma H. C., Anand S. Cation distribution in nanosized Ni-Zn ferrites. Journal of Applied Physics. 2004, 95: 5746-5751.

[99]   Mendoza M. E., Donado F., Silva R., Perez M. A., Carrillo J. L. Magnetite microcrystals for magneto-rheological fluids. Journal of Physics and Chemistry of Solids. 2005, 66: 927-931.

[100]   Nair S. S., Rajesh S., Abraham V. S., Anantharaman M. R., Nampoori V. P. N. Magnetic field-induced cluster formation and variation of magneto-optical signals in zinc-substituted ferrofluids. Journal of Magnetism and Magnetic Materials. 2006, 305: 28-34.

[101]   Gul I. H., Ahmed W., Maqsood A. Electrical and magnetic characterization of nanocrystalline Ni-Zn ferrite synthesis by coprecipitation route. Journal of Magnetism and Magnetic Materials. 2008, 320: 270-275.

[102]   Rao B. P., Caltun O., Cho W. S., Kim C. O., Kim C. G. Synthesis and characterization of mixed ferrite nanoparticles. Journal of Magnetism and Magnetic Materials. 2007, 310: 812-814.

[103]   Banerjee M., Verma N., Prasad R. Structural and catalytic properties of $Zn_{1-x}Cu_xFe_2O_4$ nanoparticles. Journal of Materials Science. 2007, 42: 1833-1837.

[104]   Suwalka O., Sharma R. K., Varkey S., Lakshmi N., Venugopalan K. A study of nanosized Ni substituted Co-Zn ferrite prepared by coprecipitation. Journal of Magnetism and Magnetic Materials. 2007, 313: 198-203.

[105]   Date S. K., Joy P. A., Anil Kumar P. S., Sahoo B., Keune W. Structural, magnetic and Mossbauer studies on nickel-zinc ferrites synthesized via a precipitation route. Physica Status Solidi (C). 2004, 1: 3495-3498.

[106]   Modak S., Ammar M., Mazaleyrat F., Das S., Chakrabarti P. K. XRD, HRTEM and magnetic properties of mixed spinel nanocrystalline Ni-Zn-Cu-ferrite. Journal of Alloys and Compounds. 2009, 473: 15-19.

[107]   Suri K., Annapoorni S., Tandon R. P. Phase change induced by polypyrrole in ironoxide polypyrrole nanocomposite. Bulletin of Materials Science. 2001, 24: 563-567.

[108]   Popovici M., Savii C., Niznansky D., Subrt J., Bohacek J., Becherescu D., Caizer C., Enach C., Ionescu C. Nanocrystalline Ni-Zn Ferrites Prepared By Sol-Gel Method. Journal of Optoelectronics and Advanced Materials. 2003, 5: 251-256.

[109]   Yan S., Yin J., Zhou E. Study on the synthesis of NiZnCu ferrite nanoparticles by PVA sol-gel method and their magnetic properties. Journal of Alloys and Compounds. 2008, 450: 417-420.

[110]   Lee S. W., Kim C. S. Superparamagnetic properties of Ni-Zn ferrite for nano-bio fusion applications. Journal of Magnetism and Magnetic Materials. 2006, 304: 418-420.

[111]   Pradeep A., Chandrasekaran G. FTIR study of Ni, Cu and Zn substituted nanoparticles of $MgFe_2O_4$. Materials Letters. 2006, 60: 371-374.

[112]   Roy P. K., Bera J. Characterization of nanocrystalline NiCuZn ferrite powders synthesized by sol-gel auto-combustion method. Journal of Materials Processing Technology. 2008, 197: 279-283.

[113]   Azadmanjiri J. Structural and electromagnetic properties of Ni-Zn ferrites prepared by sol-gel combustion method. Materials Chemistry and Physics. 2008, 109: 109-112.

[114]   Wang S. B., Min Y. L., Yu S. H. Synthesis and Magnetic Properties of Uniform Hematite Nanocubes. Journal of Physical Chemistry C. 2007, 3: 3551-3554.

[115]   Wang H. W., Kung S. C. Crystallization of nanosized Ni-Zn ferrite powders prepared by hydrothermal method. Journal of Magnetism and Magnetic Materials. 2004, 270: 230-236.

[116]   Li X., Li Q., Xia Z., Yan W. Effects on direct synthesis of large scale mono-disperse $Ni_{0.5}Zn_{0.5}Fe_2O_4$ nanosized particles. Journal of Alloys and Compounds. 2008, 458: 558-563.

[117]   Liu X., Qiu G., Yan A., Wang Z., Li X. Hydrothermal synthesis and characterization of α-FeOOH and α-Fe$_2$O$_3$ uniform nanocrystallines. Journal of Alloys and Compounds. 2007, 433: 216-220.

[118]   Zhang X., Li Q. Microwave assisted hydrothermal synthesis and magnetic property of hematite nanorods. Materials Letters. 2008, 62: 988-990.

[119]   Verma S., Joy P. A., Khollam Y. B., Potdar H. S., Deshpande S. Synthesis of nanosized $MgFe_2O_4$ powders by microwave hydrothermal method. Materials Letters. 2004, 58: 1092-1095.

[120]   Upadhyay C., Mishra D., Verma H. C., Anand S., Das R. P. Effect of preparation conditions on formation of nanophase Ni-Zn ferrites through hydrothermal technique. Journal of Magnetism and Magnetic Materials. 2003, 260: 188-194.

[121]   Hwang C. S., Wang N. C. Preparation and characteristics of ferrite catalysts for reduction of CO_2. Materials Chemistry and Physics. 2004, 88: 258-263.

[122]   Li X., Wang G. Low-temperature synthesis and growth of superparamagnetic $Zn_{0.5}Ni_{0.5}Fe_2O_4$ nanosized particles. Journal of Magnetism and Magnetic Materials. 2009, 321:1276-1279.

[123]   Sato T., Sue K., Suzuki W., Suzuki M., Matsui K., Hakuta Y., Hayashi H., Arai K., Kawasaki S., Kawai-Nakamura A., Hiaki T. Rapid and Continuous Production of Ferrite Nanoparticles by Hydrothermal Synthesis at 673 K and 30 Mpa. Industrial and Engineering Chemistry Research. 2008, 47: 1855-1860.

[124]   Satyanarayana L., Reddy K. M., Manorama S. V. Nanosized spinel $NiFe_2O_4$: A novel material for the detection of liquefied petroleum gas in air. Materials Chemistry and Physics. 2003, 82: 21-26.

[125]   Buenoa A. R., Gregori M. L., Nobrega M. C. S. Effect of Mn substitution on the microstructure and magnetic properties of $Ni_{0.50-x}Zn_{0.50-x}Mn_{2x}Fe_2O_4$ ferrite prepared by the citrate-nitrate precursor method. Materials Chemistry and Physics. 2007, 105: 229-233.

[126]   Chikate R. C., Jun K. W., Rode C. V. Nonaqueous synthesis and characterization of capped α-Fe_2O_3 nanoparticles from iron(III) hydroxyoleate precursor. Polyhedron. 2008, 27: 933-938.

[127]   Iijima M., Sato K., Kurashima K., Ishigaki T., Kamiya H. Low-temperature synthesis of redispersible iron oxide nanoparticles under atmospheric pressure and ultradense reagent concentration. Powder Technology. 2008, 181: 45-50.

[128]   Keluskar S. H., Tangsali R. B., Naik G. K., Budkuley J. S. High permeability of low loss Mn-Zn ferrite obtained by sintering nanoparticle Mn-Zn ferrite. Journal of Magnetism and Magnetic Materials. 2006, 305: 296-303.

[129]   Zhang D., Zhang X. J., Nia X. M., Song J. M., Zheng H. Synthesis and characterization of $CoFe_2O_4$ octahedrons via an EDTA-assisted route. Journal of Magnetism and Magnetic Materials. 2006, 305: 68-70.

[130] Ghodake S. A., Ghodake U. R., Sawant S. R., Suryavanshi S. S., Bakare P. P. Magnetic properties of NiCuZn ferrites synthesized by oxalate precursor method. Journal of Magnetism and Magnetic Materials. 2006, 305: 110-119.

[131] Verma A., Thakur O. P., Prakash C., Goel T. C., Mendiratta R. G. Temperature dependence of electrical properties of nickel-zinc ferrites processed by the citrate precursor technique. Materials Science and Engineering B. 2005, 116: 1-6.

[132] Yang J. M., Yen F. S. Evolution of intermediate phases in the synthesis of zinc ferrite nanopowders prepared by the tartrate precursor method. Journal of Alloys and Compounds. 2008, 450: 387-394.

[133] Mouallem-Bahout M., Bertrand S., Pena O. Synthesis and characterization of $Zn_{1-x}Ni_xFe_2O_4$ spinels prepared by a citrate precursor. Journal of Solid State Chemistry. 2005, 178:1080-1086.

[134] Costa A. C. F. M., Leite A. M. D., Ferreira H. S., Kiminami R. H. G. A., Cavac S., Gama L. Brown pigment of the nanopowder spinel ferrite prepared by combustion reaction. Journal of the European Ceramic Society. 2008, 28: 2033-2037.

[135] Jasinski J., Pinkerton K. E., Kennedy I. M., Leppert V. J. Surface oxidation state of combustion-synthesized γ-Fe_2O_3 nanoparticles determined by electron energy loss spectroscopy in the transmission electron microscope. Sensors and Actuators B: Chemical. 2005, 109: 19-23.

[136] Costa A. C. F. M., Tortella E., Morelli M. R., Kiminami R. H. G. A. Synthesis, microstructure and magnetic properties of Ni-Zn ferrites. Journal of Magnetism and Magnetic Materials. 2003, 256: 174-182.

[137] Mangalaraja R. V., Lee S. T., Ananthakumar S., Manohar P., Camurri C. P. Effect of composition on initial permeability of $Ni_{1-x}Zn_xFe_2O_4$ by flash combustion technique. Materials Science and Engineering: A. 2008, 476: 234-239.

[138]   Fu Y. P., Pan K. Y., Lin C. H. Microwave-induced combustion synthesis of $Ni_{0.25}Cu_{0.25}Zn_{0.5}$ ferrite powders and their characterizations. Materials Letters. 2002, 57: 291-296.

[139]   Hwang C. C., Wu T. Y., Wan J., Tsai J. S. Development of a novel combustion synthesis method for synthesizing of ceramic oxide powders. Materials Science and Engineering B. 2004, 111: 49-56.

[140]   Gama L., Diniz A. P., Costa A. C. F. M., Rezende S. M., Azevedoa A., Cornejoc D. R., Magnetic properties of nanocrystalline Ni-Zn ferrites doped with samarium. Physica B. 2006, 384: 97-99.

[141]   Morrison S. A., Cahill C. L., Carpenter E. E., Calvin S., Swaminathan R., McHenry M. E., Harris V. G. Magnetic and structural properties of nickel zinc ferrite nanoparticles synthesized at room temperature. Journal of Applied Physics. 2004, 95: 6392-6395.

[142]   Gubbala S., Nathani H., Koizol K., Mishra R. D. K. Magnetic properties of nanocrystalline Ni-Zn, Zn-Mn and Ni-Mn ferrites synthesized by reverse micelle technique. Physica B, 2004, 348: 317-328.

[143]   Ghosh N. N., Kiskan B., Yagci Y. Polybenzoxazines-New high performance thermosetting resins: Synthesis and properties. Progress in Polymer Science. 2007, 32: 1344-1391.

[144]   Kiskan B., Ghosh N. N., Yagci Y. Polybenzoxazine-based composites as high-performance materials. Polymer International. 2011, 60: 167-177.

[145]   Yagci Y., Kiskan B., Ghosh N. N. Recent Advancement on Polybenzoxazine-A Newly Developed High Performance Thermoset. Journal of Polymer Science Part A: Polymer Chemistry. 2009, 47: 5565-5576.

[146]   Ishida H., Low H. Y. A study on the volumetric expansion of benzoxazine-based phenolic resin. Macromolecules. 1997, 30: 1099-1106.

[147]   Maggana C., Pissis P. Water sorption and diffusion studies in an epoxy resin system. Journal of Polymer Science Part B: Polymer Physics. 1999, 37: 1165-1182.

[148]   Wirasate S., Dhumrongvaraporn S., Allen D. J., Ishida H. Molecular origin of unusual physical and mechanical properties in novel phenolics materials based on benzoxazine chemistry. Journal of Applied Polymer Science. 1998, 70: 1299-1306.

[149]   Higginbottom H. P. Polymerizable compositions comprising polyamines and poly(dihydrobenzoxazines), U.S. Pat. 4,501,864, 1985.

[150]   Walters R. N., Lyon R. L. Molar group contributions to polymer flammability. Journal of Applied Polymer Science. 2003, 87: 548-563.

[151]   Holly F. W., Cope A. C. Condensation products of aldehydes and ketones with o-aminobenzyl alcohol and o-hydroxy-benzylamine. Journal of the American Chemical Society. 1944, 66: 1875-1879.

[152]   Burke W. J. 3,4-dihydro-1,3,2 H-benzoxazines reaction of p-substituted phenols with N,N-dimethylolamines. Journal of the American Chemical Society. 1949, 71: 609-612.

[153]   Riess G., Schwob M., Guth G., Roche M., Lande B. In Advances in Polymer Synthesis, Culbertson, B. M. and McGrath, J. E., Eds.; Plenum: New York, 1985.

[154]   Ishida H. U.S. Patent 5,543,516, May 18, 1996.

[155]   Ning X., Ishida H. Phenolic materials via ring-opening polymerization of benzoxazines-effect of molecular-structure on mechanical and dynamic-mechanical properties. Journal of Polymer Science Part A: Polymer Chemistry. 1994, 32: 1121-1129.

[156] Kim H. J., Brunovska Z, Ishida H. Molecular characterization of the polymerization of acetylene-functional benzoxazine resins. Polymer 1999, 40: 1815-1822.

[157] Kim H. J., Brunovska Z, Ishida H. Dynamic mechanical analysis on highly thermally stable polybenzoxazines with an acetylene functional group. Journal of Applied Polymer Science. 1999, 73: 857-862.

[158] Brunovska Z., Ishida H. Thermal study on the copolymers of phthalonitrile and phenylnitrile-functional benzoxazines. Journal of Applied Polymer Science. 1999, 73: 2937-49.

[159] Agag T., Takeichi T. Novel benzoxazine monomers containing p-phenyl propargyl ether: polymerization of monomers and properties of polybenzoxazines. Macromolecules. 2001, 34: 7257-7263.

[160] Agag T., Takeichi T. Synthesis and characterization of novel benzoxazine monomers containing allyl groups and their high performance thermosets. Macromolecules. 2003, 36: 6010-6017.

[161] Kim H. J., Brunovska Z., Ishida H. Synthesis and thermal characterization of polybenzoxazines based on acetylene functional monomers. Polymer. 1999, 40: 6565-6573.

[162] Lee Y. H., Allen D. J., Ishida H. Effect of rubber reactivity on the morphology of polybenzoxazine blends investigated by atomic force microscopy and dynamic mechanical analysis. Journal of Applied Polymer Science. 2006, 100: 2443-2454.

[163] Ishida H., Allen D. J. Physical and mechanical characterization of near-zero shrinkage polybenzoxazines. Journal of Polymer Science Part B: Polymer Physics. 1996, 34: 1019-1030.

[164] Ishida H., Ohba S. Synthesis and characterization of maleimide and norbornene functionalized benzoxazines. Polymer. 2005, 46: 5588-5595.

[165]   Kiskan B., Yagci Y. Thermally curable benzoxazine monomer with a photodimerizable coumarin group. Journal of Polymer Science Part A: Polymer Chemistry. 2007, 45: 1670-1676.

[166]   Liu Y. L, Chou C. I. High performance benzoxazine monomers and polymers containing furan groups. Journal of Polymer Science Part A: Polymer Chemistry. 2005, 43: 5267-82.

[167]   Kiskan B., Demiray G., Yagci Y. Thermally curable polyvinylchloride via click chemistry. Journal of Polymer Science Part A: Polymer Chemistry. 2008, 46: 3512-3518.

[168]   Ergin M., Kiskan B., Gacal B., Yagci Y. Thermally curable polystyrene via click chemistry. Macromolecules. 2007, 40: 4724-4727.

[169]   Kukut M., Kiskan B., Yagci Y. Self-Curable Benzoxazine Functional Polybutadienes Synthesized by Click Chemistry. Designed Monomers and Polymers. 2009, 12: 167-176.

[170]   Kiskan B., Colak D., Muftuoglu A. E., Cianga I., Yagci Y. Synthesis and Characterization of Thermally Curable Benzoxazine-Functionalized Polystyrene Macromonomers. Macromolecular Rapid Communications. 2005, 26: 819-824.

[171]   Kiskan B., Yagci Y. Synthesis and characterization of naphthoxazine functional poly(ε-caprolactone). Polymer. 2005, 46: 11690-11697.

[172]   Liu J. Synthesis, Characterization, Reaction Mechanism and Kinetics of 3,4-Dihydro-2H-1,3-benzoxazine and its Polymers, Ph.D. Thesis, Case Western University, Cleveland, OH, May 1995.

[173]   Takeichi T., Kano T., Agag T. Synthesis and thermal cure of high molecular weight polybenzoxazine precursors and the properties of the thermosets. Polymer. 2005, 46: 12172-12180.

[174]   Chernykh A., Liu J. P., Ishida H. Synthesis and properties of a new crosslinkable polymer containing benzoxazine moiety in the main chain. Polymer. 2006, 47: 7664-7669.

[175]   Yeganeh H, Nouri M. R., Ghaffari M. Synthesis and Properties of Polybenzoxazine Modified Polyurethanes as a New Type of Electrical Insulators With Improved Thermal Stability. Polymer Engineering and Science. 2008, 48: 1329-1338.

[176]   Kimura H., Matsumoto A., Hasegawa K., Ohtsuka K., Fukuda A. Epoxy resin cured by bisphenol A based benzoxazine. Journal of Applied Polymer Science. 1998, 68:1903-1910.

[177]   Ishida H., Lee Y. H. Infrared and thermal analyses of polybenzoxazine and polycarbonate blends. Journal of Applied Polymer Science. 2001, 81: 1021-1034.

[178]   Ishida H., Lee Y. H. Study of hydrogen bonding and thermal properties of polybenzoxazine and poly-(epsilon-caprolactone) blends. Journal of Polymer Science Part B: Polymer Physics. 2001, 39: 736-749.

[179]   Jang J., Seo D. Performance improvement of rubber modified polybenzoxazine. Journal of Applied Polymer Science. 1998, 67: 1-10.

[180]   Kumar K. S. S., Nair C. P. R., Ninan K. N. Effect of fiber length and composition on mechanical properties of carbon fiber-reinforced polybenzoxazine. Polymers for Advance Technologies. 2008, 19: 895-904.

[181]   Agag T., Tsuchiya H., Takeichi T. Novel organic-inorganic hybrids prepared from polybenzoxazine and titania using sol-gel process. Polymer. 2004, 45: 7903-7910.

[182] Agag T., Takeichi T. Polybenzoxazine-montmorillonite hybrid nanocomposites: synthesis and characterization. Polymer. 2000, 41: 7083-7090.

[183] Kumar K. S. S, Nair C. P. R., Ninan K. N. Silica Fiber-Polybenzoxazine-Syntactic Foams; Processing and Properties. Journal of Applied Polymer Science. 2008, 107: 1091-1099.

[184] Burke W. J., Bishop J. L., Glennie E. L. M., Bauer W. N. A new aminoalkylation reaction. Condensation of phenols with dihydro-1,3-aroxazines. Journal of Organic Chemistry. 1965, 30: 3423-3427.

[185] Wang Y. X., Ishida H. Cationic ring-opening polymerization of benzoxazines. Polymer. 1999, 40: 4563-4570.

[186] Wang Y. X., Ishida H. Synthesis and properties of new thermoplastic polymers from substituted 3,4-dihydro-2H-1,3-benzoxazines. Macromolecules. 2000, 33: 2839-2847.

[187] Riess G., Schwob M., Guth G., Roche M., Lande B. In: Culbertson BM, McGrath, editors. Advances in polymer synthesis. New York: Plenum; 1985.

[188] Dunkers J., Ishida H. Reaction of benzoxazine-based phenolic resins with strong and weak carboxylic acids and phenols as catalysts. Journal of Polymer Science A: Polymer Chemistry. 1999, 37: 1913-1921.

[189] Ishida H., Rodriguez Y. Catalyzing the curing reaction of a new benzoxazine-based phenolic resin. Journal of Applied Polymer Science. 1995, 58: 1751-1760.

[190] Ishida H., Rodriguez Y. Curing kinetics of a new benzoxazine-based phenolic resin by differential scanning calorimetry. Polymer. 1995, 36: 3151-3158.

[191] Kiskan B., Yagci Y., Sahmetlioglu E. L. T. Preparation of conductive polybenzoxazines by oxidative polymerization. Journal of Polymer Science Part A: Polymer Chemistry. 2007, 45: 999-1006.

[192]   Liu X., Gu Y. Study on the volumetric expansion of benzoxazine curing with different catalysts. Journal of Applied Polymer Science. 2002, 84: 1107-1113.

[193]   Hayakawa T., Osanai Y., Niizeki K., Haba O., Ueda M. The curing reaction of 3-aryl substituted benzoxazine. High Performance Polymers. 2000, 12: 237-246.

[194]   McDonagh A. F., Smith H. E. Ring-chain tautomerism of derivatives of o-hydroxybenzylamine with aldehydes and ketones. Journal of Organic Chemistry. 1968, 33:1-8.

[195]   Kasapoglu F., Cianga I., Yagci Y., Takeichi T. Photoinitiated cationic polymerization of monofunctional benzoxazine. Journal of Polymer Science A: Polymer Chemistry. 2003, 41: 3320-3328.

[196]   Ning X., Ishida H. Phenolic materials via ring-opening polymerization-synthesis and characterization of bisphenol-A based benzoxazines and their polymers. Journal of Polymer Science A: Polymer Chemistry. 1994, 32: 1121-1129.

[197]   Shen S. B., Ishida H. Dynamic mechanical and thermal characterization of high-performance polybenzoxazines. Journal of Polymer Science Part B: Polymer Physics. 1999, 37: 3257-68.

[198]   Schreiber H. German Patent 2 255 504.

[199]   Ishida H., Allen D. J. Rheological characterization during cure of near-zero shrinkage polybenzoxazines. Abstracts of Papers of the American Chemical Society. 1995, 210 272-PMSE.

[200]   Agag T., Takeichi T. Synthesis and characterization of novel benzoxazine monomers containing allyl groups and their high performance thermosets. Macromolecules. 2003, 36: 6010-6017.

[201]   Xiang H., Ling H., Wang J., Song L., Gu Y. A novel high performance RTM resin based on benzoxazine. Polymer Composites. 2005, 26: 563-571

[202]   Lee Y. H., Allen D. J., Ishida H. Effect of rubber reactivity on the morphology of polybenzoxazine blends investigated by atomic force microscopy and dynamic mechanical analysis. Journal of Applied Polymer Science. 2006, 100: 2443-2454.

[203]   Ning X., Ishida H. Phenolic materials via ring-opening polymerization-synthesis and characterization of bisphenol- a based benzoxazines and their polymers. Journal of Polymer Science A: Polymer Chemistry. 1994, 32: 1121-1129.

[204]   Takeichi T., Kano T., Agag T. Synthesis and thermal cure of high molecular weight polybenzoxazine precursors and the properties of the thermosets. Polymer. 2005, 46: 12172-12180.

[205]   Russell V. M., Koenig J. L., Low H. Y., Ishida H. Study of the characterization and curing of benzoxazines using C-13 solid-state nuclear magnetic resonance. Journal of Applied Polymer Science. 1998, 70: 1413-1425.

[206]   Russell V. M., Koenig J. L., Low H. Y., Ishida H. Study of the characterization and curing of a phenyl benzoxazine using N-15 solid-state nuclear magnetic resonance spectroscopy. Journal of Applied Polymer Science. 1998, 70: 1401-1411.

[207]   Su Y. C., Yei D. R., Chang F. C. The kinetics of B-a and P-a type copolybenzoxazine via the ring opening process. Journal of Applied Polymer Science. 2005, 95: 730-737.

[208]   Yu D. S., Chen H., Shi Z. X., Xu R. W. Curing kinetics of benzoxazine resin by torsional braid analysis. Polymer. 2002, 43: 3163-3168.

[209]   Ishida H., Allen D. J. Gelation behavior of near-zero shrinkage polybenzoxazines. Journal of Applied Polymer Science. 2001, 79: 406-417.

[210]   Zhang X. Q., Potter A. C., Solomon D. H. The chemistry of novolac resins. 5. Reactions of benzoxazine intermediates. Polymer. 1998, 39: 399-404.

[211]   Zhang X. Q., Solomon D. H. The chemistry of novolac resins .6. Reactions between benzoxazine intermediates and model phenols. Polymer. 1998, 39: 405-412.

[212]   Macko J. A., Ishida H. Effects of phenolic substitution on the photooxidative degradation of polybenzoxazines. Macromolecular Chemistry and Physics. 2001, 202: 2351-2359.

[213]   Macko J. A., Ishida H. Structural effects of amines on the photooxidative degradation of polybenzoxazines. Polymer. 2001, 42: 6371-6383.

[214]   Macko J. A., Ishida H. Behavior of a bisphenol-A-based polybenzoxazine exposed to ultraviolet radiation. Journal of Polymer Science B: Polymer Physics. 2000, 38: 2687-2701.

[215]   Huang M. T., Ishida H. Investigation of the boron nitride/polybenzoxazine interphase. Journal of Polymer Science B: Polymer Physics. 1999, 37: 2360-2372.

[216]   Kumar K. S. S., Nair C. R. P., Ninan K. N. Mechanical Properties of Polybenzoxazine Synthetic Foams. Journal of Applied Polymer Science. 2008, 108: 1021-1028.

[217]   kumar K. S. S., Nair C. R. P., Ninan K. N. Effect of fiber length and composition on mechanical properties of carbon fiber-reinforced polybenzoxazine. Polymers for Advanced Technologies. 2008, 19: 895-904.

[218]   Kiskan B., Demirel L., Kamer O., Yagci Y. Synthesis and Characterization of Nanomagnetite Thermosets Based on Benzoxazines. Journal of Polymer Science Part A: Polymer Chemistry. 2008, 46: 6780-6788.

[219]   Sarangi P. P., Naik B., Vadera S. R., Patra M. K., Prakash C., Ghosh N. N. Preparation of polybenzoxazine-Ni-Zn ferrite magnetic nanocomposite and its magnetic property. Materials Technology Advanced Performance Materials. 2010, 25: 271-275.

[220]   Ghosh N. N., Rajput A. B. Preparation of Polybenzoxazine-Ni-Zn Ferrite Nanocomposites and Their Magnetic Property. In: H. Ishida, T. Agag (Eds.), Handbook of Benzoxazine Resins, Elsevier, Amsterdam, 2011, 641-650.

[221]   Rajput A. B., Rahaman S. J., Sarkhel G., Patra M. K., Vadera S. R., Singru P. M., Yagci Y., Ghosh N. N. Synthesis, Characterization, and Properties of Flexible Magnetic Nanocomposites of Cobalt Ferrite-Polybenzoxazine-Linear Low-Density Polyethylene. Journal of Applied Polymer Science. 2013, 128: 3726-3733.

[222]   Ishida H. Overview and Historical Background of Polybenzoxazine Research. In: H. Ishida, T. Agag (Eds.), Handbook of Benzoxazine Resins, Elsevier, Amsterdam, 2011, 3-69.

[223]   Bhadrakumari S., Predeep P. PTCR Characteristics in $YBa_2Cu_3O_7$-x-Linear Low Density Polyethylene (LLDPE) Composite Materials. Journal of Superconductivity and Novel Magnatism. 2008, 21: 313-316.

[224]   Bhadrakumari S., Predeep P. High-T_c superconductor/linear low density polyethylene (LLDPE) composite materials for diamagnetic applications. Superconductor Science and Technology. 2006, 19: 808-812.

[225]   Brunovska Z., Liu J. P., H. Ishida. 1,3,5-Triphenylhexahydro-1,3,5-triazine-active intermediate and precursor in the novel synthesis of benzoxazine monomers and oligomers. Macromolecular Chemistry and Physics. 1999, 200: 1745-1751.

[226]   Rajput A. B., Seikh J. R., Sarkhel G., Ghosh N. N. Preparation and characterization of flexible Polybenzoxazine-LLDPE composites. Designed Monomers and Polymers. 2012, 16: 177-184.

[227] Borah J. S., Chaki T. K. Dynamic mechanical, thermal, physico-mechanical and morphological properties of LLDPE/EVA blends. Journal of Polymer Research. 2011, 18: 569-578.

[228] Rajput A. B., Ghosh N. N. Preparation and Characterization of Novel Polybenzoxazine-Polyester Resin Blends. International Journal of Polymeric Materials. 2011, 60: 27-39.

[229] Liu Y-L., Hsu C-W., Chou C-I. Silicon-Containing Benzoxazines and Their Polymers: Copolymerization and Copolymer Properties. Journal of Polymer Science: Part A: Polymer Chemistry. 2007, 45: 1007-1015.

[230] Huang K-W., Kuo S-W. High-Performance Polybenzoxazine Nanocomposites Containing Multifunctional POSS Cores Presenting Vinyl-Terminated Benzoxazine Groups. Macromolecular Chemistry and Physics. 2010, 211: 2301-2311.

[231] Takeichi T., Kano T., Agag T., Kawauchi T., Furukawa N. Preparation of High Molecular Weight Polybenzoxazine Prepolymers Containing Siloxane Unites and Properties of Their Thermosets. Journal of Polymer Science: Part A: Polymer Chemistry. 2010, 48: 5945-5952.

[232] Iring M., Foldes E., Barabas K., Kelen T., Tudos F. Thermal oxidation of Linear Low Density Polyethylene. Polymer Degradation and Stability. 1986, 14: 319-332.

[233] Schmid M., Affolter S. Interlaboratory tests on polymers by differential scanning calorimetry (DSC): determination and comparison of oxidation induction time (OIT) and oxidation induction temperature (OIT∗). Polymer Testing. 2003, 22: 419-428.

[234] Tekeichi T., Guo Y., Agag T. Synthesis and Characterization of Poly(urethanebenzoxazine) Films as Novel Type of Polyurethane/Phenolic Resin Composites. Journal of Polymer Science: Part A: Polymer Chemistry. 2000, 38: 4165-4176.

[235] Rimdusit S., Ramsiri B., Jubsilp C., Dueramae I. Characterizations of polybenzoxazine modified with isomeric biphenyl tetracarboxylic dianhydrides. eXPRESS Polymer Letters. 2012, 6: 773-782.

[236] Borah J. S., Chaki T. K. Dynamic mechanical, thermal, physico-mechanical and morphological properties of LLDPE/EVA blends. Journal of Polymer Research. 2011, 18: 569-578.

[237] Rajput A. B., Hazra S., Ghosh N. N. Synthesis and characterisation of pure single-phase $CoFe_2O_4$ nanopowder via a simple aqueous solution-based EDTA-precursor route. Journal of Experimental Nanoscience. 2013, 8: 629-639.

[238] Cullity B. D. Elements of X-ray Diffraction, Addison-Wesley, New York, 1978, p. 99.

[239] Kumar V., Rana A., Yadav M. S., Pant R. P. Size-induced effect on nano-crystalline $CoFe_2O_4$. Journal of Magnetism and Magnetic Materials. 2008, 320: 1729-1734.

[240] Chen Y., Ruan M., Jiang Y. F., Cheng S. G., Li W. The synthesis and thermal effect of $CoFe_2O_4$ nanoparticles. Journal of Alloys and Compounds. 2010, 493: 36-38.

[241] Veverka M., Veverka P., Kaman O., Lancok A., Zaveta K., Pollert E., Knizek K., Boha cek J., Benes M., Kaspar P., Duguet E., Vasseur S. Magnetic heating by cobalt ferrite nanoparticles. Nanotechnology. 2007, 18: 345704-345711.

[242] Gopalan E. V., Joy P. A., Al-Omari I. A., Kumar D. S., Yoshida Y., Anantharaman M. R., On the structural, magnetic and electrical properties of sol-gel derived nanosized cobalt ferrite. Journal of Alloys and Compounds. 2009, 485: 711-717.

[243] Lee J. G., Park J. Y., Kim C. S. Growth of ultra-fine cobalt ferrite particles by a sol-gel method and their magnetic properties. Journal of Material Science. 1998, 33: 3965-3968.

[244]   Mohamed R. M., Rashad M. M., Haraz F. A., Sigmund W. Structure and magnetic properties of nanocrystalline cobalt ferrite powders synthesized using organic acid precursor method. Journal of Magnetism and Magnetic Materials. 2010, 322: 2058-2064.

[245]   Gharagozlou M. Synthesis, characterization and influence of calcination temperature on magnetic properties of nanocrystalline spinel Co-ferrite prepared by polymeric precursor method. Journal of Alloys and Compounds. 2009, 486: 660-665.

[246]   Thang P. D., Rijnders G., Blank D. H. A. Spinel cobalt ferrite by complexometric synthesis. Journal of Magnetism and Magnetic Materials. 2005, 295: 251-256.

[247]   Waje S. B., Hashim M., Yusoff W. D. W., Abbas Z. Physical and magnetic characterization of polycrystalline cobalt ferrite ($CoFe_2O_4$) materials prepared via mechanically alloyed nanoparticles. Journal of Applied Science Research. 2009, 5: 1440-1444.

[248]   Waje S. B., Hashim M., Yusoff W. D. W., Abbas Z. X-ray diffraction studies on crystallite size evolution of $CoFe_2O_4$ nanoparticles prepared using mechanical alloying and sintering. Applied Surface Science. 2010, 256: 3122-3127.

[249]   Wang Y. C., Ding J., Yin J. H., Liu B. H., Yi J. B., Yu S. Effects of heat treatment and magneto annealing on nanocrystalline Co-ferrite powders. Journal of Applied Physics. 2005, 98: 124306-124312.

[250]   Maaz K., Mumtaz A., Hasanain S. K., Ceylan A. Synthesis and magnetic properties of cobalt ferrite ($CoFe_2O_4$) nanoparticles prepared by wet chemical route. Journal of Magnetism and Magnetic Materials. 2007, 308: 289-295.

[251]   Chiang P., Whang W. The synthesis and morphology characteristic study of BAO-ODPA polyimide/TiO_2 nano hybrid films. Polymer. 2003, 44: 2249-2254.

[252]   Sawada T., Ando S. Synthesis, Characterization, and Optical Properties of Metal-Containing Fluorinated Polyimide Films. Chemistry of Materials. 1998, 10: 3368-3378.

[253]   Akl J., Ghaddar T., Ghanem A., El-Rassy H. Cobalt ferrite aerogels by epoxide sol-gel addition: Efficient catalysts for the hydrolysis of 4-nitrophenyl phosphate. Journal of Molecular Catalysis A: Chemical. 2009, 312: 18-22.

[254]   Zhao L., Zhang H., Xing Y., Song S., Yu S., Shi W., Guo X., Yang J., Lei Y., Cao F. Studies on the magnetism of cobalt ferrite nanocrystals synthesized by hydrothermal method. Journal of Solid State Chemistry. 2008, 181: 245-252.

[255]   Waldron R. D. Infrared Spectra of Ferrites. Physical Review letters. 1955, 99: 1727-1735.

[256]   Chae D. W., Lee K. H., Kim B. C. Rheological Properties of Ferrite Nanocomposites Based on Nylon-66. Journal of Polymer Science: Part B: Polymer Physics. 2006, 44: 371-377.

[257]   Guo Z. H., Liang X. F., Pereira T., Scaffaro R., Hahn H. T. CuO nanoparticle filled vinyl-ester resin nanocomposites: Fabrication, characterization and property analysis. Composites Science and Technology. 2007, 67: 2036-2044.

[258]   Guo Z. H., Lei, K., Li, Y. T., Ng, H. W., Prikhodko, S., Hahn, H. T. Fabrication and characterization of iron oxide nanoparticles reinforced vinyl-ester resin nanocomposite. Composites Science and Technology. 2008, 68: 1513-1520.

[259]   Fu S. Y., Feng, X. Q., Lauke, B., Mai, Y. W. Effects of particle size, particle/matrix interface adhesion and particle loading on mechanical properties of particulate-polymer composites. Composites Part B: Engineering. 2008, 39: 933-961.

[260]   Kaiser R., Miskolczy G. Magnetic Properties of Stable Dispersions of Sub domain Magnetite Particles. Journal of Applied Physics. 1970, 41: 1064-1072.

[261]   Farghali A. A., Moussa M., Khedr M. H. Synthesis and characterization of novel conductive and magnetic nano-composites. Journal of Alloys and Compounds. 2010, 499: 98-103.

[262]   Guo Z. H., Park, S., Wei, S. Y., Pereira, T., Moldovan, M., Karki, A. B., Young, D. P., Hahn, H. T. Flexible high-loading particle-reinforced polyurethane magnetic nanocomposite fabrication through particle-surface-initiated polymerization. Nanotechnology. 2007, 18: 335704-335711.

[263]   Zhang D., Klabunde, K. J., Sorensen, C. M., Hadjipanayis, G. C. Magnetization temperature dependence in iron nanoparticles. Physical Review B. 1998, 58: 14167-14170.

[264]   Sorensen C. M. In Nanoscale Materials in Chemistry; Klabunde, K. J., Ed.; Wiley-Interscience: New York, 2001; Chapter 6, p 169.

[265]   Rajput A. B., Hazra S., Fernando G. F., Ghosh N. N. Synthesis of Single-Phase Barium Hexaferrite Nanopowder via a Novel EDTA Precursor-Based Route and its DC Resistivity and Magnetic Property. Synthesis and Reactivity in Inorganic, Metal-Organic, and Nano-Metal Chemistry, 41: 1-8, 2011.

[266]   Rajput A. B., Sharifi M., Pol H. V., Patra M. K., Vadera S. R., Singru P. M., Ghosh N. N. Preparation of flexible magnetic nanocomposites of linear low-density polyethylene-polybenzoxazine-magnetic nanoparticles and their mechanical and magnetic properties. Journal of Nanoscience Letters. 2013, 3: 26-36.

[267]   Xu P., Han, X., Wang, M. Synthesis and magnetic properties of $BaFe_{12}O_{19}$ hexaferrite nanoparticles by a reverse microemulsion technique. The Journal of Physical Chemistry C. 2007, 111: 5866-5870.

[268]   Pillai V., Kumar P., Multani M. S., Shah D. O. Structure and magnetic properties of nanoparticles of barium ferrite synthesized using microemulsion processing. Colloids and Surfaces A. 1993, 80: 69-75.

[269] Junliang L., Yanwei Z., Cuijing G., Wei Z., Xiaowei Y. One-step synthesis of barium hexaferrite nano-powders via microwave-assisted sol-gel auto-combustion. Journal of the European Ceramic Society. 2010, 30: 993-997.

[270] Haneda K., Morrish A. H. Magnetic properties of $BaFe_{12}O_{19}$ small particles. IEEE Transactions on Magnetics. 1989, 25: 2597-2601.

[271] Kittle C. Physical theory of ferromagnetic domains. Reviews of Modern Physics. 1949, 21: 541-583.

[272] Goto K., Ito M., Sakurai T. Studies on magnetic domains of small particles of barium ferrite by colloid-SEM method. Japanese Journal of Applied Physics. 1980, 19: 1339-1346.

[273] Yu H., Lin H. Preparation and thermal behavior of aerosol-derived $BaFe_{12}O_{19}$ nanoparticles. Journal of Magnetism and Magnetic Materials. 2004, 283: 190-198.

[274] Junliang L., Yanwei Z., Cuijing G., Wei Z., Xiaowei Y. One-step synthesis of barium hexaferrite nano-powders via microwave-assisted sol-gel auto-combustion. Journal of the European Ceramic Society. 2010, 30: 993-997.

[275] Ataie A., Mali A. Characteristics of barium hexaferrite nanocrystalline powders prepared by a sol-gel combustion method using inorganic agent. Journal of Electroceramics. 2008, 21: 357-360.

[276] Bahadur D., Rajakumar S., Kumar A. Influence of fuel ratios on auto combustion synthesis of barium ferrite nano particles. Journal of Chemical Sciences. 2006, 118: 15-21.

[277] Xu G., Ma H., Zhong M., Zhou J., Yue Y., He Z. Influence of pH on characteristics of $BaFe_{12}O_{19}$ powder prepared by sol-gel auto-combustion. Journal of Magnetism and Magnetic Materials. 2006, 301: 383-388.

[278]   Lisjak D., Drofenik M. The mechanism of the low-temperature formation of barium hexaferrite. Journal of the European Ceramic Society. 2007, 27: 4515-4520.

[279]   Shepherd P., Mallick K. K., Green R. J. Magnetic and structural properties of M-type barium hexaferrite prepared by co-precipitation. Journal of Magnetism and Magnetic Materials. 2007, 311: 683-692.

[280]   Ataie A., Heshmati-Manesh S., Kazempour H. Synthesis of barium hexaferrite by the co-precipitation method using acetate precursor. Journal of Materials Science. 2002, 37: 2125-2128.

[281]   Tang X., Zhao B. Y., Hu K. A. Preparation of M-Ba-ferrite fine powders by sugar-nitrates process. Journal of Materials Science. 2006, 41: 3867-3871.

[282]   Drofenik M., Kristl M., Znidarsic A., Hanmel D., Lisjak D. Hydrothermal synthesis of Ba-hexaferrite nanoparticles. Journal of the American Ceramic Society. 2007, 90: 2057-2061.

[283]   Xu P., Han X., Wang M. Synthesis and magnetic properties of $BaFe_{12}O_{19}$ hexaferrite nanoparticles by a reverse microemulsion technique. The Journal of Physical Chemistry C. 2007, 111: 5866-5870.

[284]   Gonzalez-Carreno T., Morales M. P., Serna C. J. Barium ferrite nanoparticles prepared directly by aerosol pyrolysis. Materials Letters. 2000, 43: 97-101.

[285]   Ataie A., Zojaji S. E. Synthesis of bariumhexaferrite nano-particles via mechano-combustion route. Journal of Alloys and Compounds. 2007, 431: 331-336.

[286]   Yu J., Tang S., Zhai L., Shi Y., Dua Y. Synthesis and magnetic properties of single-crystalline $BaFe_{12}O_{19}$ nanoparticles. Physica B. 2009, 404: 4253-4256.

[287]   Sozeri H. Simple recipe to synthesize single-domain $BaFe_{12}O_{19}$ with high saturation magnetization. Journal of Magnetism and Magnetic Materials. 2009, 321: 2717-2722.

[288]   Cabanas M. V., Gonzalez-Calbet J. M., Vallet-Regi M. Synthesis of barium hexaferrite by pyrolysis of aerosol. Journal of Materials Research. 1994, 9: 712-716.

[289]   Krupa I., Novak I., Chodak I. Electrically and thermally conductive polyethylene/graphite composites and their mechanical properties. Synthetic Metals. 2004, 145: 245-252.

[290]   Wu K. H., Shin Y. M., Yang C. C., Ho W. D., Hsuj J. S. Preparation and Ferromagnetic Properties of $Ni_{0.5}Zn_{0.5}Fe_2O_4$/Polyaniline Core-Shell Nanocomposites. Journal of Polymer Science: Part A: Polymer Chemistry. 2006, 44: 2657-2664.

[291]   Rajput A. B., Hazra S., Krishna N. B., Chavali P., Datla S., Ghosh N. N. Preparation of $NiFe_2O_4$ nanopowder via EDTA precursor and study of its properties. Particuology. 2012, 10: 29-34.

[292]   Rajput A. B., Seikh J. R., Sarkhel G, Patra M. K., Vadera S. R., Ghosh N. N. Preparation, characterization and properties of flexible magnetic nanocomposites of $NiFe_2O_4$-polybenzoxazine-LLDPE. Polymer-Plastics Technology and Engineering. 2012 (Aceepted).

[293]   Nabiyouni G., JafariFesharaki M., Mozafari M., Amighian J. Characterization and magnetic properties of nickel ferrite nanoparticles prepared by ball milling technique. Chinese Physics Letters. 2010, 27: 126401.

[294]   Liu Q., Huang H., Lai L., Sun J., Shang T., Zhou Q., et al. Hydrothermal synthesis and magnetic properties of $NiFe_2O_4$ nanoparticles and nanorods. Journal of Materials Science. 2009, 44: 1187-1191.

[295]   Dixit G., Singh J. P., Srivastava R. C., Agrawal H. M., Choudhary R. J., Gupta A. Structural and magnetic behaviour of $NiFe_2O_4$ thin film grown by pulsed laser deposition. Indian Journal of Pure and Applied Physics. 2010, 48: 287-291.

[296] Kasapoglu N., Baykal A., Toprak M. S., Koseoglu Y., Bayrakdar H. Synthesis and characterization of $NiFe_2O_4$ nano-octahedrons by EDTA-assisted hydrothermal method. Turkish Journal of Chemistry. 2007, 31: 659-666.

[297] Maensiri S., Masingboon C., Boonchomb B., Seraphinc S. A simple route to synthesize nickel ferrite ($NiFe_2O_4$) nanoparticles using egg white. Scripta Materialia. 2007, 56: 797-800.

[298] Shafi K. V. P. M., Koltypin Y., Gedanken A., Prozorov R., Balogh J., Lendvai J., Felner I. Sonochemical preparation of nanosized amorphous $NiFe_2O_4$ particles. Journal of Physical Chemistry B. 1997, 101: 6409-6414.

[299] Zhao Y. T., Chen D. H., Chen D. R., Jiao X. L. Synthesis of $NiFe_2O_4$ powders well defined in size and morphologies. Chinese Chemical Letters. 2002, 13: 389-392.

[300] Guo Z., Lei K., Li Y., Ng H. W., Prikhodko S., Hahn H. T. Fabrication and characterization of iron oxide nanoparticles reinforced vinyl-ester resin nanocomposite. Composites Science and Technology. 2008, 68: 1513-1520.

[301] Sarangi P. P., Naik B. D., Vadera S. R., Patra M. K., Prakash C., Ghosh, N. N. Development of a simple chemical method for synthesis of single-phase Ni-Zn ferrite nano-powders. Materials Technology: Advanced Performance Materials. 2009, 24: 97-99.

[302] Sarangi P. P., Vadera S. R., Patra M. K., Prakash C., Selvin R., Ghosh N. N. Development of a Novel Aqueous Solution Based Chemical Methodology for Synthesis of $Ni_{(1-x)}Zn_xFe_2O_4$ Nanopowders and their Electrical and Magnetic Property. Integrated Ferroelectrics. 116: 327-341, 2010.

[303] Albuquerque A. S., Ardisson J. D., Macedo W. A. A. Nanosized powders of NiZn ferrites: Synthesis, structure and magnetism. Journal of Applied Physics. 2000, 87: 4352-4357.

[304]   Caizer C., Stefanescu M. Magnetic characterization of nanocrystalline Ni-Zn ferrite powder prepared by the glyoxylate precursor method. Journal of Physics D: Applied Physics. 2002, 35: 3035-3040.

[305]   Morrison S. A., Cahill C. L., Carpenter E. E., Calvin S., Swaminathan R., McHenry M. E., Harris V. G. Magnetic and structural properties of nickel zinc ferrite nanopartilces synthesized at room temperature. Journal of Applied Physics. 2004, 95: 6392-6395.

[306]   Gubbala S., Nathani H., Koizol K., Mishra R. D. K. Magnetic properties of nanocrystalline Ni-Zn, Zn-Mn and Ni-Mn ferrites synthesized by reverse micelle technique. Physica B. 2004, 348: 317-328.

[307]   Deka S., Joy P. A. Characterization of nanosized NiZn ferrite powders synthesized by an autocombustion method. Materials Chemistry and Physics. 2006, 100: 98-101.

[308]   Pathak A., Pramanik P. Nanoparticles of oxides through chemical methods. Proceedings of the Indian National Science Academy. 2001, 67A: 47-70.

[309]   Zhang H. E., Zhang B. F., Wang G. F., Dong X. H., Gao Y. The structure and magnetic properties of $Zn_{1-x}Ni_xFe_2O_4$ ferrite nanoparticles prepared by sol-gel autocombustion. Journal of Magnetism and Magnetic Materials. 2007, 312: 126-130.

[310]   Costa A. C. F. M., Silva V. J., Cornejo D. R., Morelli M. R., Kiminami R. H. G. A., Gama L. Magnetic and structural properties of $NiFe_2O_4$ ferrite nanopowder doped with Zn^{2+}. Journal of Magnetism and Magnetic Materials. 2008, 320: 370-372.

List of Publications:

International Journals

1. Rajput A., Hazra S., Ghosh N. N. Synthesis and characterization of pure single-phase $CoFe_2O_4$ nanopowder via a simple aqueous solution based EDTA-precursor route. The Journal of Experimental Nanoscience. 2013, 8: 629-639.

2. Rajput A. B., Hazra S., Fernando G. F., Ghosh N. N. Synthesis of single-phase barium hexaferrite nanopowder via a novel EDTA-precursor based route and its DC resistivity and magnetic property. Synthesis and Reactivity in Inorganic, Metal-Organic, and Nano-Metal Chemistry. 2011, 41: 1114-1121.

3. Rajput A. B., Hazra S., Krishna N. B., Chavali P., Datla S., Ghosh N. N. Preparation of $NiFe_2O_4$ nanopowder via EDTA precursor and study of its properties. Particuology. 2012, 10: 29-34.

4. Rajput A. B., Seikh J. R., Sarkhel G., Ghosh N. N. Preparation and characterization of flexible Polybenzoxazine-LLDPE composites. Designed Monomers and Polymers. 2012, 16: 177-184.

5. Rajput A. B., Seikh J. R., Sarkhel G., Patra M. K., Vadera S. R., Singru P. M., Yagci Y., Ghosh N. N. Synthesis, Characterization, and Properties of Flexible Magnetic Nanocomposites of Cobalt Ferrite-Polybenzoxazine-Linear Low-Density Polyethylene. Journal of Applied Polymer Science. 2013, 128: 3726-3733.

6. Rajput A. B., Sharifi M., Pol H. V., Patra M. K., Vadera S. R., Singru P. M., Ghosh N. N. Preparation of flexible magnetic nanocomposites of linear low-density polyethylene-polybenzoxazine-magnetic nanoparticles and their mechanical and magnetic properties. Journal of Nanoscience Letters. 2013, 3: 26-36.

7. Rajput A. B., Seikh J. R., Sarkhel G, Patra M. K., Vadera S. R., Ghosh N. N. Preparation, characterization and properties of flexible magnetic nanocomposites of $NiFe_2O_4$-polybenzoxazine-LLDPE. Polymer-Plastics Technology and Engineering. 2012 (Accepted).

8. Rajput A. B., Ghosh N. N. Preparation and Characterization of Novel Polybenzoxazine-Polyester resin Blends. International Journal of Polymeric Materials. 2010, 59: 1-13.

9. Waigaonkar S. D., Babu B. J. C., Rajput A. B. Parametric optimization to enhance impact strength of rotationally molded products: A six sigma approach. Journal of Manufacturing Technology Research. 2010, 3: 1-3.

10. Waigaonkar S. D., Babu B. J. C., Rajput A. B. Six Sigma DOE approach: a case study of rotational moulding process. International Journal of Six Sigma and Competitive Advantage. 2011, 6: 256-277.

11. Waigaonkar S. D., Babu B. J. C., Rajput A. B. Experimental investigations and parametric optimization of curing of unsaturated polyester resin. Indian Journal of Engineering and Material Sciences. 2011, 18: 31-3.

12. Babu B. J. C., Waigaonkar S. D., Rajput A. B. Experimental investigations and optimization of processibility of sheet moulding compound. Journal of Polymer Engineering. 2011, 31: 309-317.

Book Chapter

1. Ghosh N. N., Rajput A. B. Preparation of polybenzoxazine-Ni-Zn Ferrite nanocomposites and their magnetic property. Handbook of Benzoxazine Resin. Eds. Ishida H., Agag T. Elsevier, Amsterdam, 2011.

Conferences
International (09) and National (01)

1. Rajput A. B., Ghosh N. N. Preparation and Characterization of Novel Polybenzoxazine-Polyester Composite. ICCE-18, Anchorage, Alaska, USA, July 4-10, 2010.

2. Rajput A. B., Ghosh N. N. Preparation and characterization of Polybenzoxazine-Ni-Zn Ferrite nanocomposites and their magnetic property. Proceedings of DAE-BRNS 3rd International Symposium on Materials Chemistry (ISMC-2010), pp 290, BARC Mumbai, India, December 7-11, 2010.

3. Rajput A. B., Ghosh N. N. Preparation of Polybenzoxazine-Ni-Zn Ferrite nanocomposites and their magnetic property. Proceedings of 3rd International Conference on Recent Advances in Composite Materials (ICRACM), ENSIL-University of Limoges and ENSCI, France, December 13-15, 2010.

4. Babu B. J. C., Waigaonkar S. D., Rajput A. Experimental investigations and optimization of processibility of glass fiber-polyester resin molding compound. Proceedings of 2nd International Conference on Polymer Processing and Characterization. pp. 60-66, Institute of Macromolecular Science and Engineering, Kottayam, Kerala, India, January 15-17, 2010.

5. Waigaonkar S. D., Babu B. J. C., Rajput A. Investigating impact strength of roto-molded products: a comparison of DOE with Shainin Variable Search Technique. Proceedings of 2nd International Conference on Polymer Processing and Characterization. pp. 156-162, Institute of Macromolecular Science and Engineering, Kottayam, Kerala, India, January 15-17, 2010.

6. Naik B., Rajput A. B., Chandrashekhar A., Iyer A., Ghosh N. N. Development of an aqueous solution based method for preparation of TiO_2 and Ag-doped TiO_2 nano catalysts and their photocatalytic activity. National Conference on Green and Sustainable Chemistry-2010, BITS Pilani, India, February 19-21, 2010.

7. Rajput A. B., Premchandani R., Nallabati V., Ghosh N. N. Preparation and Characterization of Polybenzoxazine-LLDPE-Ferrite based Flexible Magnetic Nanocomposites. International Conference on Advances in Polymer Science and Rubber Technology (APSRT). IIT Kharagpur, March 3- 5, 2011.

8. Ghosh N. N., Rajput A. B., Hazra S., Choudhury S. Synthesis and Characterization of pure single-phase $ZnFe_2O_4$ nanopowder via a simple aqueous solution based EDTA-precursor route. International Conference on Nanoscience and Nanotechnology. University of Delhi, India, December 18-21, 2011.

9. Rajput A. B., Choudhury S., Hazra S. Ghosh N. N. Preparation and Characterization of Pure Single-Phase $ZnFe_2O_4$ Nanopowder via a Simple Aqueous Solution Based EDTA-Precursor Method. International Conference on Emerging Technologies: Micro to Nano 2013 (ETMN-2013). BITS Pilani, K. K. Birla Goa Campus, India, February 23-24, 2013.

10. Ghosh N. N., Rajput A. B., Hazra S., Singru P. M., Vadera S. R., Patra M. K., Pol H. V. Preparation, characterization and properties of flexible magnetic nanocomposite sheets of MNPs-polybenzoxazine-LLDPE. International Conference on Emerging Technologies: Micro to Nano 2013 (ETMN-2013). BITS Pilani, K. K. Birla Goa Campus, India, February 23-24, 2013.

BIO-DATA OF CANDIDATE

Personal details:

Name	Amit Balsing Rajput
Date of Birth	29-06-1984
Education	M.Sc. (Polymer Chemistry)
	Solapur University, Solapur (2006).
	B.Sc. (Chemistry)
	Shivaji University, Kolhapur (2004).
Email	amit.rajput337@gmail.com

Scholarships and Awards:

1. Junior Research Fellowship, from the "Department of Science and Technology" (DST), July 2008-July 2010.

2. Senior Research Fellowship, from the "BITS Pilani, K. K. Birla Goa campus", August 2010.

Publications during Ph.D. Programme:

Listed in Appendix I.

BIO-DATA OF SUPERVISOR

Name   Dr. Narendra Nath Ghosh

Current Position   Associate Professor
                                  Department of Chemistry
                                  Birla Institute of Technology and Science Pilani,
                                  K. K. Birla Goa Campus.
                                  City: Zuarinagar, State: Goa-403 726, India.

Date of Birth: 01-01-1970

Education   Ph.D. (Chemistry): IIT-Kharagpur (1999).

                                  M.Sc. (Chemistry): 1st Class, IIT-Kharagpur (1994).

Areas of Research (i)   Nonmaterial's (Chemical Synthesis Methodologies, Characterizations and Applications in Catalysis, Sensors, Separations, etc).
   (ii) Mesoporous Materials (Particularly catalysts).
   (iii) Nanocomposite (Polymer-fiber, Polymer-ceramic), Polymer (Polybenzoxazine, Epoxy).

No. of Sponsored Research Projects

   (i) As PI: 05 (DRDO, DST, BRNS)

   (ii) As Co-PI: 03

No. of International Journal Publications   49

No. of Conference Proceedings   11

No. of Invited Talks   07

Honors/Awards/Recognition

1. Visiting Scientist Fellowship Award by "The Scientific and Technological Research Council of Turkey (TUBITAK)" 2006, 2009.

2. Member Expert in Chemistry for selection of candidates for Commonwealth Scholarship., UK Nominated by Ministry of Human Resource Development, Government of India.

3. Best Poster paper award "A Simple Chemical Technique for Synthesis of High

Surface Area Mesoporous Silica Matrix and Iron-Oxide Incorporated Silicates" International Congress of Environmental Research (ICER 08) 2008.

4. Invited as Chairperson (for NANO-O9 and NANO-11 Sessions) in the 16th International Conference on Composites or Nano Engineering, ICCE-16, July 20-26, 2008 in Kunming, China.

5. Travel Grant Awards received from Indian National Science Academy, New Delhi, BITS- Pilani, Rajasthan, CSIR New Delhi, DST New Delhi. Appendix III.

6. Outstanding Scientist of 21st Century medal: Cambridge UK 2005.

7. Honorary appointment to the Research Board of Advisors of "The American Biographical Institute", USA. 2003.

8. Eminent Scientists of Today Medal by International Biographical Center Cambridge, U.K, 2002.

9. Biography has published in several Who's Who in Science and Engineering from USA, UK.

10. The Royal Academy Of Engineering for Research Exchanges with China And India-Short Award for 2010.

11. Receives a prestigious research grant under the DST UKIERI Thematic Partnership Scheme.

Reviewer of International Journals:

Thin Solid Films, Materials Research Society, American Ceramic Society, Macromolecular Symposia, Journal of Surface Coating and Technology, Powder Technology, Journal of Microporous and Mesoporous Materials, International Journal of the Physical Sciences, etc.

BIO-DATA OF CO-SUPERVISOR

Name	Dr. Pravin Madanrao Singru
Current Position	Associate Professor Department of Mechanical Engineering Birla Institute of Technology and Science Pilani, K. K. Birla Goa Campus. City: Zuarinagar, State: Goa-403 726, India.
Education	Ph.D.: VNIT-Nagpur. M. Tech.: IIT-Kharagpur.

Areas of Research
(i)   Machine Dynamics and Control
(ii) Nonlinear Dynamics and Chaos
(iii) Optimization using Genetic Algorithms
(iv) Experimental and Theoretical Vibration Analysis
(v)   MEMS Sensor

No. of International Journal Publications   18

No. of Conference Proceedings   35

Honors/Awards/Recognition

1. Organizer of Indo-Russian workshop on Topical Problems in Solid Mechanics, sponsored by DST and Russian Academy of Sciences in November, 2008.

2. Member of organizing committee of International Conference on Emerging Miniaturized Technology Micro to Nano (EMTM2N-2013), in February 2013.

3. Delivered talks on invitation from various Institutions in India.

Reviewer of International Journals:

He is Reviewer of five International Journals.